Supramolecular Approaches for Water Oxidation Catalysis with Ruthenium Complexes

Dissertation zur Erlangung des
naturwissenschaftlichen Doktorgrades
der Julius-Maximilians-Universität Würzburg

vorgelegt von
Valentin Kunz
aus Berlin

Würzburg 2017

Eingereicht bei der Fakultät für Chemie und Pharmazie am:
7. September 2017

Gutachter der schriftlichen Arbeit:

1. Gutachter: Prof. Dr. Frank Würthner
2. Gutachter: Prof. Dr. Udo Radius

Prüfer des öffentlichen Promotionskolloquiums:

1. Prüfer: Prof. Dr. Frank Würthner
2. Prüfer: Prof. Dr. Udo Radius
3. Prüfer: Prof. Dr. Roland Mitrić
4. Prüfer: Prof. Dr. Jürgen Seibel
5. Prüfer: Priv.-Doz. Dr. Florian Beuerle

Datum des öffentlichen Promotionskolloquiums:
27. Oktober 2017

Doktorurkunde ausgehändigt am:

____

ABBREVIATIONS

#	article number
Ac	acetyl
ADP	adenosine diphosphate
AFM	atomic force microscopy
Ala	alanine
aq.	aqueous
Asp	aspartic acid
ATP	adenosine triphosphate
a.u.	arbitrary units
bda	2,2'-bipyridine-6,6'-dicarboxylate
Bn	benzyl
bp	3,3'-bipyridine
bpaH$_2$	2,2'-bipyridine-6,6'-diylbis(hydrogen phosphonate)
bpb	1,4-bis(pyridin-3'-yl)benzene
bpbp	4,4'-bis(pyridin-3''-yl)-1,1'-biphenyl
bpe	1,2-bis(pyridin-3'-yl)ethyne
bpm	2,2'-bipyrimidine
bpy	2,2'-bipyridine
bpyms	2,2'-bipyridine-5,5'-bis(methane sulfonate)
brs	broad singlet
Bu	butyl
CAN	cerium(IV) ammonium nitrate
cat.	catalyst
CCD	charge-coupled device
Chl a	chlorophyll a
cryo	cryogenic

CV	cyclic voltammetry
d	doublet
dba	dibenzylideneacetone
DBU	1,8-diazabicycloundec-7-ene
DCM	dichloromethane
DCTB	*trans*-2-[3-(4-*tert*-butylphenyl)-2-methyl-2-propenylidene]malononitrile
DFT	density functional theory
DMF	dimethylformamide
DMSO	dimethyl sulfoxide
dmso	dimethyl sulfoxide as ligand
DPV	differential pulse voltammetry
Em.	emission
EPR	electron paramagnetic resonance
eq.	equation
equiv.	equivalent
ESI	electrospray ionization
Et	ethyl
Fc	ferrocene
Fd	ferredoxin
Fl.	fluorescence
g	gaseous
GC	gas chromatography
Glu	glutamine
GPC	gel permeation chromatography
Hbpp	bis-(2-pyridyl)pyrazole
His	histidine
HOMO	highest occupied molecular orbital
HOPG	highly oriented pyrolytic graphite
HPLC	high-performance liquid chromatography
HR	high resolution

I2M	interaction of two metal oxyl radicals (mechanism)
IPCE	incident-photon-to-electron conversion-efficiency
KIE	kinetic isotope effect
L	ligand
l	liquid
LC	ligand centered
LHC	light-harvesting complex
LF	ligand field
LFSE	ligand field stabilization energy
LMCT	ligand to metal charge transfer
LUMO	lowest unoccupied molecular orbital
m	multiplet
m_c	centered multiplet
MALDI	matrix assisted laser desorption ionization
MC	macrocycle
MD	molecular dynamics
Me	methyl
MLCT	metal to ligand charge transfer
MM	molecular mechanics
M.W.	molecular weight
NADP	nicotinamide adenine dinucleotide phosphate
n.d.	not determined
NEXAFS	near edge X-ray absorption fine structure
NHE	normal hydrogen electrode
NMR	nuclear magnetic resonance
npm	4-*tert*-butyl-2,6-di-(10,80-naphthyrid-20-yl)-pyridine
NTO	natural transition orbital
Δ_O	octahedral field splitting energy
OEC	oxygen evolving complex
ORTEP	Oak Ridge Thermal Ellipsoid Plot

P	photosensitizer
PBI	perylene bisimide
PC	plastocyanine
PCET	proton-coupled electron transfer
pda	1,10-phenanthroline-2,9-dicarboxylate
PEC	photoelectrochemical cell
Ph	phenyl
pic	4-picoline
ppm	parts per million
PQ	plastoquinone
PS	photosystem
psi	pounds per square inch
ptz	phthalazine
py	pyridine
pynap	2-(pyrid-2'-yl)-1,8-naphthyridine
PyO	4-(2-(2-(2-methoxyethoxy)ethoxy)ethoxy)pyridine
QE	quantum efficiency
QM	quantum mechanical
Quant.	quantitative
RDS	rate-determining step
ref.	reference
rpm	rotations per minute
r.t.	room temperature
s	singlet
SEM	scanning electron microscopy
t	triplet
TCD	thermal conductivity detector
tda	2,2':6',2''-terpyridine-6,6''-dicarboxylate
TFE	2,2,2-trifluoroethanol
THF	tetrahydrofuran

TON	turnover number
TOF	turnover frequency
ToF	time-of-flight
tpy	2,2':6',2''-terpyridine
Ts	*p*-toluenesulfonyl
Tyr	tyrosine
UV	ultraviolet
VE	valence electron
Vis	visible
vs.	versus
w	weight
WNA	water nucleophilic attack (mechanism)
WOC	water oxidation catalyst
WOK	Wasseroxidationskatalysator
XANES	X-ray absorption near edge structure
XFEL	X-ray free electron laser

VARIABLES AND CONSTANTS

ε	extinction coefficient
δ	chemical shift
h	Planck constant (4.136×10^{-15} eV s)
λ	wavelength
ρ	density
υ	frequency
% v/v	volume concentration
% w/w	mass fraction
A	absorbance
c	concentration
d	path length
E	potential
E_a	activation energy
I	current
pH	potential of hydrogen
k	rate constant
m	mass
n	amount of substance
p	pressure
R	ideal gas constant (8.314 J K^{-1} mol^{-1})
T	temperature
t	time
z	charge

TABLE OF CONTENT

CHAPTER 1 AIM OF THE THESIS

About 2.4 billion years ago, an evolutional leap changed the face of our planet forever. The emergence of oxygenic photosynthesis established the basis for higher life and is responsible for the formation of almost the entire biomass present on earth today.[1, 2] This was achieved by nature's development of a sophisticated supramolecular machinery, called the photosystem. It uses sunlight to produce large energy-rich biomolecules, the carbohydrates, with carbon dioxide (CO_2) and water serving as nearly inexhaustible feedstock. The electrons required for the reduction of CO_2 are extracted from water at a Mn_4CaO_5 cluster leading to the release of molecular oxygen as the by-product. Interestingly, almost all oxygen present in the earth's atmosphere today, which makes up 21% of the entire atmospheric composition, was generated by this evolutionary highly conserved catalyst named oxygen evolving complex (OEC).[3] Photosynthesis is furthermore responsible for the generation of all fossil fuels, such as coal, oil, and natural gas, that we are using today. Those resources have been generated by the geological anaerobic decomposition of the biomass formed by photosynthetic processes. However, humankind is consuming those resources in only a few centuries, whereas it took nature billions of years to create them. Since the beginning of the "industrial revolution" at the end of the 19th century, society's energy demand has continuously increased (in the last decade by 2.1% per year), and is expected to double until 2050.[3, 4] It is therefore assumed that the reservoir of fossil fuels will be consumed until the end of the 21st century,[5] which makes the transformation towards a sustainable society, driven by renewable fuels, inevitable.[4-8]

In principal, renewable energy sources (solar, wind, biomass, hydro, and tidal) have a strong potential to cover our energy needs in the future. That becomes obvious by comparing the annual global energy consumption with the energy that could be generated from those sources within one year, and with the energy that could be generated by exploiting all fossil fuel resources present on earth (**Figure 1**).[9] Particularly solar energy would be most promising, since sunlight provides in one year more energy than what could be extracted from all fossil fuels available.[10]

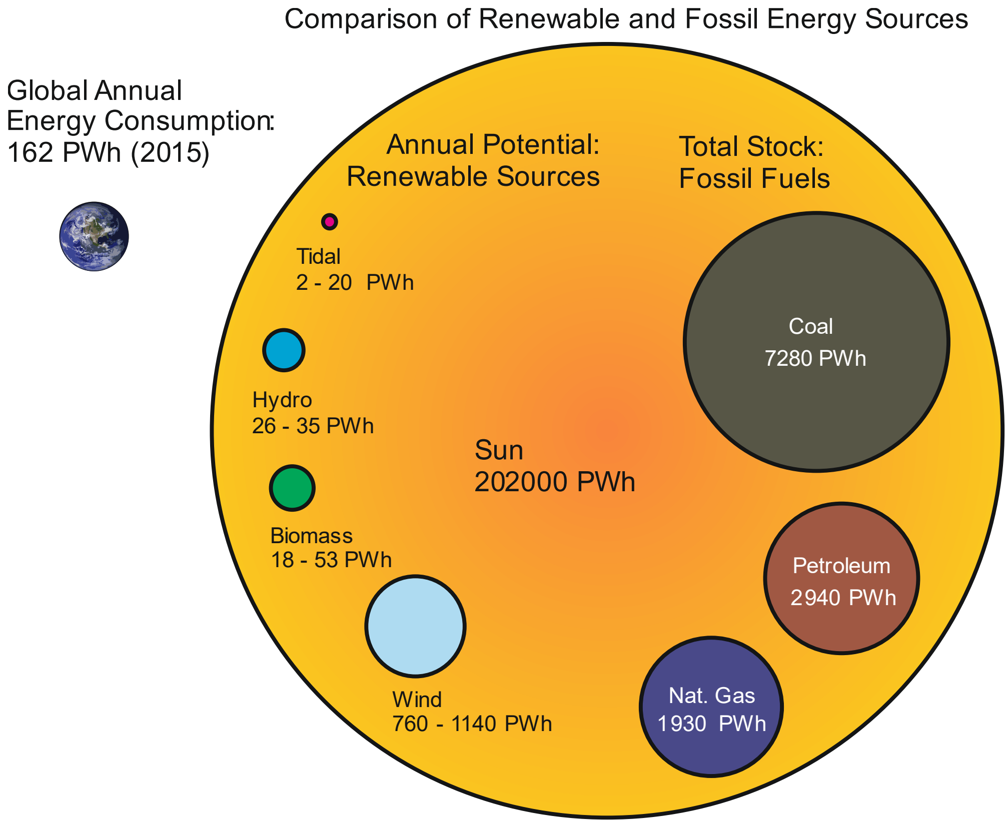

Figure 1: Comparison of the potential of different energy carriers with the global annual energy consumption based on numbers for 2015.[9]

An already well-established way to use solar energy is the direct conversion into electricity using silicon photovoltaic cells, which nowadays can reach solar-to-electricity efficiencies with record values up to 27%.[11-13] Recently, the levelized cost of electricity generated by photovoltaics in Germany (8–14 Eurocent/kWh, 2013)[14] becomes competitive to electricity generated traditionally from hard coal (6–8 Eurocent/kWh, 2013).[14, 15] In 2014, Germany already produced 27% of its energy from renewable sources, mainly wind and solar power. In course of the "Energiewende", a political project to reshape the German energy landscape, it is planned to increase this portion to 80% by 2050.[16-18] However, wind and sunlight are intermittent and not evenly distributed on earth, which makes it difficult to produce the energy close to the site of consumption. Therefore, in order to achieve this ambitious goal, efficient ways to store and transport energy have to be developed to deal with the unsteady energy production capacity and its occasional peaks.[19] Although, a huge progress has been achieved in battery technology over the last decade,[20, 21] batteries still possess considerably lower energy densities compared to liquid fuels.[7, 22, 23] Furthermore, batteries are very inefficient for the long-term storage of energy due to discharging phenomena, and thus, it is desirable to store solar energy directly in chemical bonds by the creation of energy rich molecules, so called "solar fuels".[24-33] On one hand, the production of fuel from biomass would be one viable option, but this approach is clearly limited due to the low overall solar to biomass efficiency of natural photosynthesis, which lies in the range of 1–2%.[34] On the other hand, the photocatalytic generation of molecular hydrogen is highly promising because it allows: (i) fine-tuned engineering of the catalytic system, (ii) long-term energy storage with a very high gravimetric energy density, and (iii) a clean combustion process that does not lead to the release of greenhouse gases. The hydrogen can be used directly in fuel-cells,[35, 36] or it can serve as a reductant to produce methane, methanol or other hydrocarbons from CO_2, which can be achieved either by chemical [37-42] or biochemical catalysis.[43, 44]

The desired hydrogen can preferably be generated from water, which provides the required electrons and protons.[45-48] Generally, it is possible to split water into its elements electrochemically by applying a voltage of at least 1.23 V in an electrolyzer at pH 0 (eq. 3).[49] This reaction consists of two half-reactions. At the anode the oxidation of water to molecular oxygen occurs (eq. 1), whereas the protons, which are released during this process, are reduced to molecular hydrogen at the cathode (eq. 2).

$$\begin{array}{lclcll} & & & & \multicolumn{2}{l}{E \text{ vs. NHE (pH 0)}} \\ 2\,H_2O\,(l) & \rightarrow & O_2\,(g) + 4\,H^+ + 4\,e^- & (1) & E^0_{\text{anode:}} & +\,1.23\text{ V} \\ 4\,H^+ + 4\,e^- & \rightarrow & 2\,H_2\,(g) & (2) & E^0_{\text{cathode:}} & 0.00\text{ V} \\ \hline 2\,H_2O\,(l) & \rightarrow & O_2\,(g) + 2\,H_2\,(g) & (3) & E^0_{\text{cell:}} & -\,1.23\text{ V} \end{array}$$

The development of a photocatalytic system that is capable of performing this reaction solely using sunlight has been defined as one of the “Holy Grails” of chemical research.[50] One of the major challenges to achieve this goal is the oxidation of water. The complexity of this four-electron process and the resulting high overpotentials make the catalyst development for this reaction very demanding.[48, 51-53] The first molecular catalyst for water oxidation has been discovered in 1982 by T. J. Meyer.[54] Since then, a huge progress has been accomplished with the development of homogeneous metalorganic water oxidation catalysts based on various transition metals (Mn, Fe, Co, Cu, Ir, and Ru).[28, 55-63] The best homogeneous water oxidation catalysts known so far are mononuclear complexes based on the {Ru(bda)} complex fragment (bda = 2,2'-bipyridine-6,6'-dicarboxylate) developed by Sun and co-workers,[57] of which some can already compete with the performance of the natural oxygen evolving cluster (OEC).[64] Generally, two different mechanisms to form the O–O bond are known for these catalysts,[51, 65-68] and sometimes even small structural alterations can lead to a complete change from one mechanism to the other.[69-73] The performance of the water oxidation reaction catalyzed by ruthenium complexes has been successfully enhanced by various supramolecular strategies, depending on the respective reaction mechanisms, which have been inspired by biological enzymes.[74] As demonstrated by nature, the activity of a catalytic center can greatly be improved by supramolecular interactions in the surrounding matrix of the respective catalyst. In many metallo-enzymes the protein matrix plays a crucial role for the overall catalytic activity.[75] For example, mimicking only the metal oxide cluster of the OEC leads to complexes with considerably high overpotentials due to the absence of a redox-levelling matrix, and thus only negligible water oxidation activities.[76, 77] Consequently, the field of supramolecular catalysis tries to transfer those natural concepts to the development of artificial catalytic systems. This can be achieved by tuning the second coordination sphere of the catalyst, meaning the ligand structure that is not in direct contact to the metal center,[78-85] or by generating defined cavities that resemble the binding pockets of enzymatic reaction centers.[86-91]

The aim of the present thesis is to establish novel supramolecular approaches to improve the water oxidation catalysis using the catalytically active {Ru(bda)} fragment as key motive. The {Ru(bda)} moiety can be regarded as a linear coordination building block for the construction of metallosupramolecular structures. Within this work, two approaches for the incorporation of multiple catalytic centers into supramolecular assemblies are investigated. The catalytic {Ru(bda)} fragments are either incorporated into metallosupramolecular macrocycles, or are embedded in extended supramolecular aggregates. The macrocyclic structures can be obtained by using ditopic ligands of the right geometry facilitating the connection of several ruthenium centers. For the generation of extended aggregates, the {Ru(bda)} complex fragment can be equipped with axial ligand systems that contain strongly aggregating subunits, such as perylene bisimides (PBIs). The first approach is based on the work of Dr. Marcus Schulze that has recently been summarized in a publication on a metallosupramolecular macrocycle gathering three {Ru(bda)} centers.[92, 93] It has been shown that the incorporation of {Ru(bda)} fragments into such a trinuclear macrocycle has a beneficial effect on the stability and activity of the catalytic system, which was attributed to the chelate effect and a prevented self-oxidation. Detailed mechanistic studies have been performed for this novel catalyst, and it was observed that the incorporation into a cyclic assembly strongly influences the O–O bond formation mechanism. Furthermore, novel emergent properties have been observed, which indicated interactions between the ruthenium centers. Preliminary density functional theory (DFT) calculations suggested that those centers might be connected through a hydrogen-bonded water network inside the macrocyclic cavity.[93] Accordingly, the distance between the {Ru(bda)} fragments should strongly affect important molecular properties. A series of differently sized macrocycles has therefore been developed by using bridging ligands of various lengths, as it is described in **chapter 3.1**. To identify trends within the catalyst series, the macrocycles were studied with regard to their catalytic performance and important optical and electrochemical properties. In a cooperation with the group of Prof. Mitrić, DFT calculations on a high-level of theory were applied in a molecular dynamics (MD) framework, which allows to freely explore the potential energy surface of the system, to rationalize the experimental findings. Since the solubility in water becomes significantly reduced with increasing molecular size of the macrocyclic assemblies, organic co-solvents are therefore always needed to perform the water oxidation catalysis for the larger macrocycles. To overcome the limited water solubility of the best performing macrocyclic system, and to enable water oxidation catalysis in pure water, derivatives of the initial bridging ligand were synthesized that bear hydrophilic side-chains. The effect of the different solubilizing groups on the overall solubility and the catalytic activity of the functionalized macrocycles is summarized in **chapter 3.2**.

The second approach, described in **chapter 3.3**, pursues the idea of incorporating {Ru(bda)} fragments into more "loose" supramolecular aggregates. The soft-matter environment is supposed to act as a stabilizing matrix, because the axial ligand dissociation, which is regarded as the major catalyst deactivation pathway, might be suppressed. Perylene bisimides (PBIs) were chosen as an aggregating unit since their aggregation behavior is well-investigated, and their molecular properties can be tuned easily.[94] Consequently, different pyridyl functionalized PBI derivatives were synthesized as axial ligands for the coordination of the {Ru(bda)} fragment. The influence of the different PBI containing ligands on the aggregation behavior of the respective complexes was examined using UV/Vis spectroscopy and microscopic techniques. Moreover, the impact of the different aggregate morphologies on the catalytic performance has been studied. The insights thus obtained will help to develop novel design principles for supramolecular catalytic systems that go beyond pure catalyst optimization.

CHAPTER 2 LITERATURE SURVEY

2.1 Natural Photosynthesis

2.1.1 Photosynthesis and Photosystem II

In nature, the splitting of water is accomplished by oxygenic photosynthetic organisms such as green plants, algae and cyanobacteria.[95] Photosynthesis basically consists of a series of light reactions in which electrons are extracted from water and used to create NADPH that can be considered as the biological equivalent to molecular hydrogen. During the electron extraction from water (water oxidation), a proton gradient is created across a membrane, which acts as the driving force for the ATP synthase to convert ADP into ATP, the energy carrier of living cells. In a following set of dark reactions, described by the Calvin cycle, ATP and NADPH are used to build up carbohydrates starting from CO_2 as a feedstock (**Figure 2**).

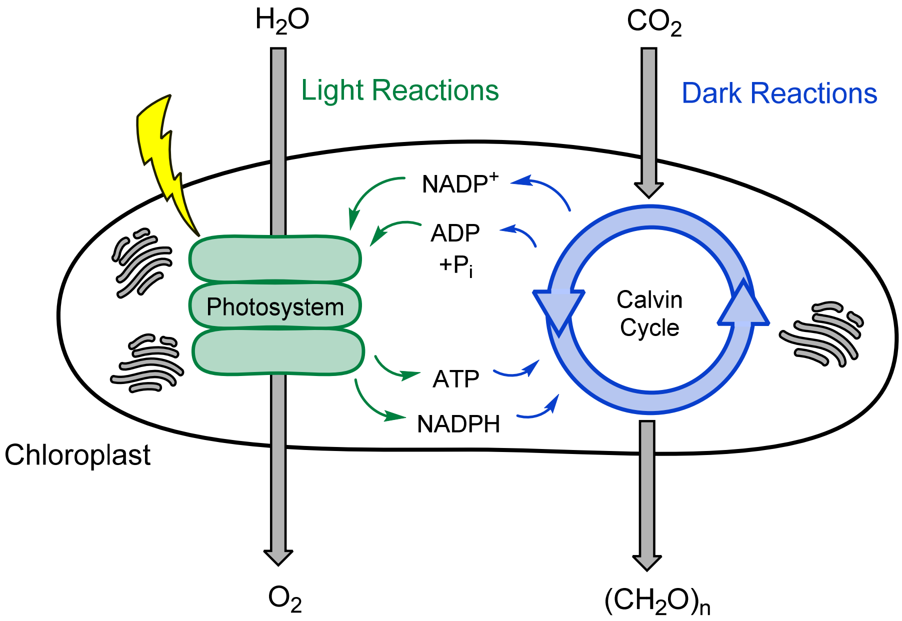

Figure 2: Schematic representation of chemical conversions performed in a chloroplast under irradiation and in the dark and how those cycles are interconnected.

The highly sophisticated molecular machinery, responsible for the transformation of sunlight into chemical energy, is called photosystem. Depending on the species, the photosystem differs structurally and can be located in different parts of the cell. In the following section, only the photosynthetic apparatus of green plants will be discussed in detail. Here, the photosystem is placed in the thylakoid membranes of cell organelles known as chloroplasts. It consists of two subunits, namely the photosystem I and II, which are each capable of absorbing different parts of the visible-light spectrum (**Figure 3**). Both photosystems are surrounded by chromophore assemblies called light-harvesting complexes (LHCs).[24] They are responsible for absorbing light and funneling the photons to the reaction centers, which is usually accomplished with quantum efficiencies over 90%.[96] There is a great structural variety among LHCs of different species, however, they usually consist of arrays of dye molecules, such as carotenoid and chlorophyll derivatives.[97-99] Inside each photosystem, the special pair, which is composed of two exciton-coupled chromophores, is responsible for the initial charge separation. The first charge separation takes place in the photosystem II upon oxidation of the chlorophyll a (Chl a) dimer P680, which creates an electron/hole pair. The generated hole is filled by an electron that is extracted from the oxygen evolving Mn_4CaO_5 cluster using a pendant tyrosine (Tyr) as a redox shuttle. The corresponding excited electron is transferred *via* several plastoquinones (PQ) to the membrane bound cytochrome b_6f protein. There it is used to reduce the copper center of a mobile plastocyanine (PC), concomitantly creating a proton gradient along the membrane that is later used as the driving force for the ATP synthase to produce the cellular energy carrier adenosine triphosphate (ATP). The plastocyanine transports the electron to the photosystem I, where it is used to fill the hole that has been generated by a second excitation process at the special pair P700. The excited electron from P700 is transferred to a ferredoxin (Fd), which is responsible for the transportation of the electron to the NADP reductase, where NADPH is generated by reduction of NADP (NADP = Nicotinamide adenine dinucleotide phosphate). Finally, the NADPH and the ATP are utilized for the construction of carbohydrates by reduction of CO_2 in a series of dark reactions described by the Calvin cycle.[100] The holes which are accumulated during this entire process at the oxygen evolving cluster become filled with electrons obtained from water oxidation. Consequently, each absorbed photon leads to the extraction of one electron from a water molecule. After the extraction of overall four electrons from two water molecules, elemental oxygen is released as a by-product during the photosynthetic light reactions at the Mn_4CaO_5 cluster (*vide infra*).

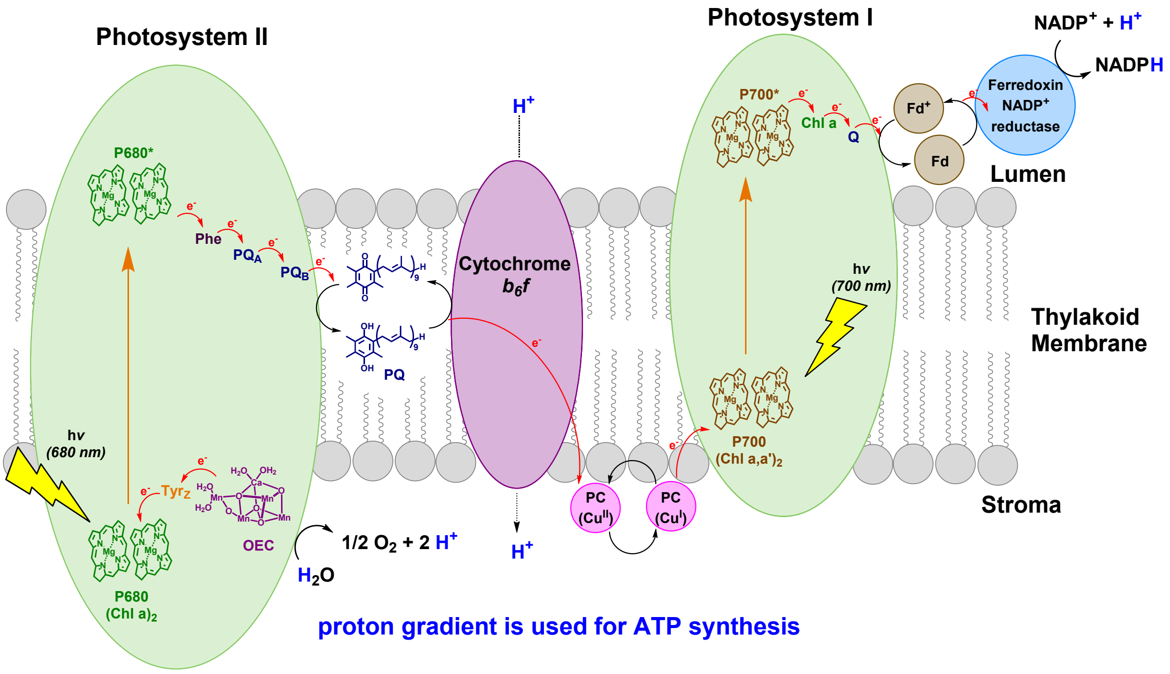

Figure 3: Schematic representation of the photosystem of green plants and the electron transfer processes.

2.1.2 The Oxygen Evolving Cluster (OEC)

The successive absorption of four photons, together with the transfer of four electrons and protons, makes the oxygen generation a very challenging chemical process. It is therefore regarded to be the bottleneck for the development of artificial photosynthetic systems. In the natural photosystem II (PSII), a tetramanganese-calcium cluster (Mn_4CaO_5), composed of a Mn_3CaO_4 heterocubane and a pendant oxo-bridged manganese, realizes biological water oxidation while being embedded into a complex proteinoic environment.[51, 77, 101] Whereas the Ca^{2+} can be replaced with Sr^{2+} to yield catalytically still active analogues of the OEC, the Mn centers seem to be indispensable.[102] Most probably, nature chose this element because it provides the most diverse redox chemistry of the highly abundant first-row transition metals.[2, 103, 104] Particularly important is the capability of the transition metal to stabilize O^{2-} by π-bonding, and thus the ability to form metal-oxo species as important intermediates. The OEC can produce oxygen with a turnover frequency (TOF) of 500 cycles s^{-1} and is stable for 30 minutes.[75] Therefore, it can achieve 10^6 turnovers until it has to be replaced.[105] Based on a theory of Kok and co-workers, the oxygen evolving complex passes four distinct redox states before liberating oxygen. Those states are commonly described by the S_n-state cycle (**Figure 4a**), with n being the number of stored oxidizing equivalents ($n = 0-4$).[106, 107] Each oxidation step follows on the absorption of one photon by the photosystem II, which initiates an electron transfer chain (*vide supra*). The hole which is thus created at the special pair P680, is filled by the proton-coupled oxidation of a pendant tyrosine residue, which acts as a redox shuttle and is finally extracting electrons from the Mn_4CaO_5 cluster. In such a way, starting from the S_0 state with one Mn(IV) and three Mn(III) ions, the OEC becomes successively oxidized by partially proton-coupled electron transfer processes (PCET) to the S_3 intermediate with all manganese ions in the oxidation state IV.[108] After the generation of the S_4-state, O–O-bond formation takes place followed by liberation of dioxygen eventually closing the catalytic cycle.

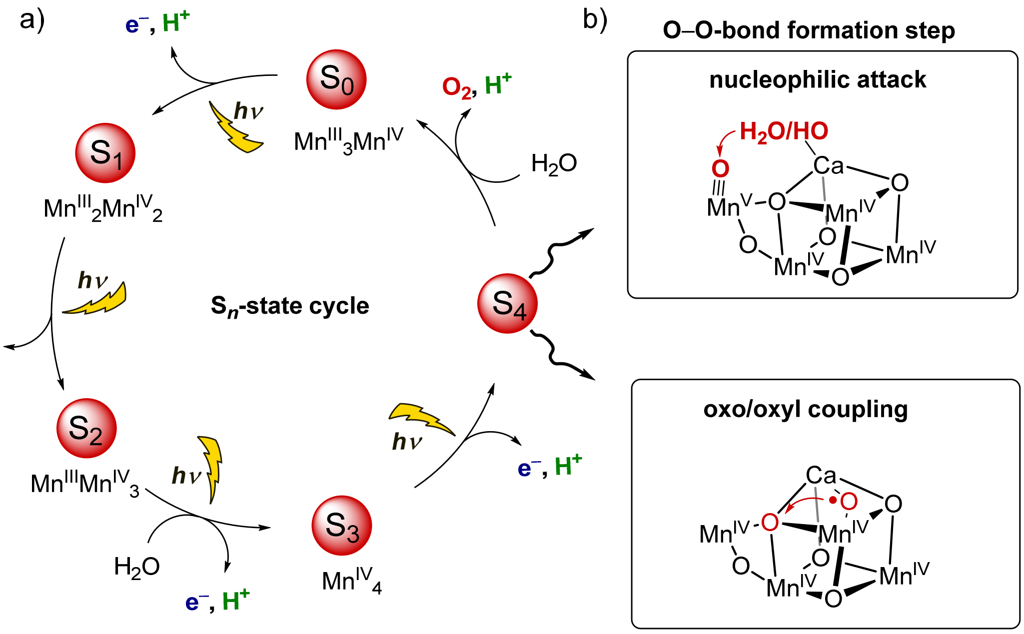

Figure 4: (a) Schematic representation of the S_n-state cycle developed by Kok *et al.* for biological water oxidation of the oxygen evolving complex of photosystem II. (b) Possible pathways for the O–O bond formation (Adapted with permission from ref. [74]; copyright (2017) Wiley-VCH).

The states S_0–S_3 can be prepared specifically and were studied in great detail, whereas the generation of the transient S_4 state is extremely challenging since it quickly liberates oxygen and reforms the S_0 state. First X-ray crystallographic data for the PSII was obtained in 2001,[109] but it took ten additional years until Kamiya *et al.* were able to elucidate the structure of the dark-stable S_1 state of OEC with a resolution of 1.9 Å (**Figure 5a** and **Figure 5b**).[110, 111] Further studies on the S_2 state revealed that the oxygen atom 5 (O5) shows dynamic behavior and an equilibrium exists between the closed cubane structure and an open structure. Sophisticated NMR experiments on ^{17}O-labelled samples and ammonia binding experiments furthermore revealed that the oxygen atom in this bridge is easily exchangeable, and that it is one of the sites where water enters the catalytic cycle.[112, 113] Although, much effort has been spent on elucidating the structure of the final oxidation state (S_4) and the mechanism of O–O-bond formation, there are still two major pathways discussed in literature that significantly differ from each other (**Figure 4b**),[51, 77, 101, 114] as recently summarized by J. Barber.[115] The first discussed mechanism involves the intermediate formation of a highly electrophilic manganese oxo species that is nucleophilically attacked by a calcium bound water molecule/hydroxide before dioxygen formation.[115-119] In contrast, in the oxo/oxyl radical coupling mechanism, proposed by Siegbahn *et al.*, a terminal bound oxyl radical is likely to be formed in the S_4-state that attacks the adjacent μ-oxo bridge to eliminate elemental oxygen.[120-122] A powerful tool to gain further insights into this O–O bond formation step might be time-resolved serial femtosecond crystallography using a X-ray free electron laser (XFEL).[123, 124] This technique allows to follow dynamic processes in crystals upon absorption of light flashes. Although first studies using this technique on the photosystem II have been reported, the resolution has still to be increased for conclusive results.[123, 124]

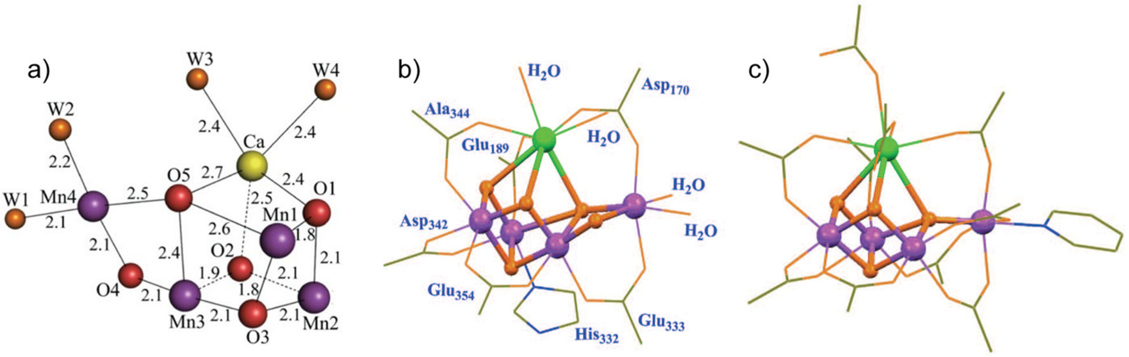

Figure 5: (a) X-ray crystal structure and bond lengths of the natural oxygen evolving cluster (Mn_4CaO_5) at a resolution of 1.9 Å (Reproduced with permission from ref. [110]; copyright (2011) Nature Publishing Group). (b) Coordination environment of the natural OEC, and (c) of the mimic by Zhao *et al.* in which the natural amino acids are replaced by small organic ligands such as acetate and pyridine (Reproduced with permission from ref. [125]; copyright (2015) American Association for the Advancement of Science).

Independent on the precise mechanism, adjacent amino acid residues facilitate proton-coupled electron transfer processes and deprotonation of substrate water molecules by pre-organizing them appropriately in a hydrogen bonding network.[126-128] The importance of such highly cooperative supramolecular interactions becomes even more evident by a recent study of Zhang, Dong and Dau who accomplished the synthesis of an artificial Mn_4CaO_4 mimic that closely resembles the structure of the native OEC (**Figure 5c**).[125] In this structure all the amino acids are replaced by simple organic ligands such as acetate and pyridine. Although, this artificial model system readily cycles the S-states up to S_3, no oxygen evolution could be detected presumably due to the absence of the smart protein matrix that would help to reduce the overpotential by pre-organizing water molecules and acting as proton acceptor.

2.2 Artificial Photosynthesis

2.2.1 State of the Art Ru Water Oxidation Catalysts (WOCs)

The first artificial water oxidation catalyst (**1**), called the blue dimer, has been reported by Meyer *et al.* already in 1982.[54] In this ruthenium polypyridyl complex, two Ru centers are connected with a μ-oxo bridge. Many studies have been conducted on this early example, so that up to now it is the best understood artificial water oxidizing system. The oxygen-oxygen bond formation was found to occur *via* the nucleophilic attack of a solvent water molecule (WNA) to a Ru-oxo moiety in the Ru^{V} state, whereas the oxidation of $Ru^{IV}ORu^{III}$ has been found to be rate-limiting.[129-131] This initial success, together with the multimetallic natural OEC as a blueprint, lead many scientists to the conclusion that a multinuclear complex is required to facilitate oxygen generation (**Figure 6**). Tanaka and co-workers pursued this approach by introducing non-innocent, redox-active ligands into a dimeric Ru water oxidation catalyst (**2**).[132, 133] The ruthenium centers have been connected *via* an anthracene or a xanthene bridge, and *o*-quinone derivatives served as redox-active ligands.[134-137] They were able to demonstrate that the ruthenium centers cycle only between the redox state +II and +III, whereas the rest of the redox chemistry is performed by the quinone ligands, which can adopt three different structures: quinone, semiquinone and catecholate.[138-140] The next substantial improvement regarding the catalytic performance, usually expressed in form of the catalyst's turnover number (TON) and turnover frequency (TOF), was again achieved with a dinuclear ruthenium complex. Llobet *et al.* developed catalyst **3** in which two Ru centers are connected with a Hbpp ligand (Hbpp = bis-(2-pyridyl)pyrazole).[141, 142] Interestingly, mechanistic studies revealed that for this complex both oxygen atoms of the released molecular oxygen originate from Ru bound oxygen species and from not the surrounding solvent molecules. Based on that information it was concluded that the O–O bond is formed *via* the intramolecular coupling of two metal oxyl radicals (I2M).[142] Furthermore, it has been shown that small structural changes can influence which mechanism is operable for this class of compounds.[143] A similar approach was followed by Thummel *et al.* who connected two Ru centers with an equatorial chelating ligand. However, the most interesting observation in this study was that the mononuclear reference compound **4** is also capable of oxidizing water.[144] Detailed kinetic studies for this complex revealed that the O–O bond is formed upon the nucleophilic attack of water to a $[Ru^{V}{=}O]^{3+}$ species and it has thus been proven that a single reaction site is sufficient for water oxidation.[145] This was the first example of a mononuclear water oxidation catalyst and since then a lot of other groups have followed this promising approach.[52, 146] Other successful examples following this strategy have been reported for instance by Meyer with the complex $[Ru(tpy)(bpm)OH_2]^{2+}$ **5** (bpm = 2,2'-bipyrimidine)[147-149] and Sakai with the closely related complex $[Ru(tpy)(bpy)OH_2]^{2+}$.[150] For the latter, detailed studies have been performed by the group of Berlinguette regarding the influence of electronic effects on the performance, the rate-determining step, and the reaction mechanism by introducing electron donating and withdrawing side chains.[151]

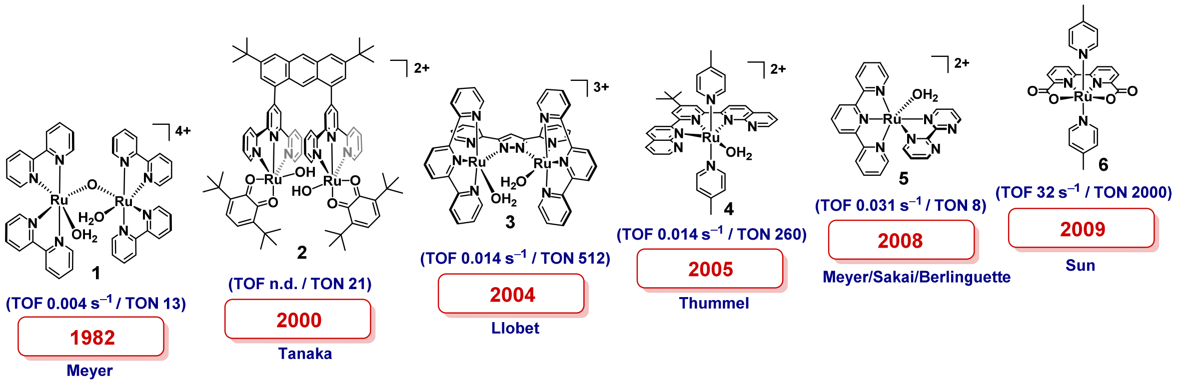

Figure 6: Important developments in the field of Ru water oxidation catalysts in chronological order.

A breakthrough was reported with the synthesis of the $[Ru(bda)(pic)_2]$ catalyst **6** by Sun *et al.* and the demonstration that this mononuclear complex catalyzes the oxygen-oxygen bond formation *via* the coupling of two metal oxyl radicals.[152] Its remarkable catalytic efficiency can be ascribed to the dianionic chelate bda ligand that reduces the oxidation potential of the ruthenium centers providing access to high oxidation states (bda = 2,2'-bipyridine-6,6'-dicarboxylate).[63] Furthermore, the octahedral geometry of $[Ru(bda)(pic)_2]$ is distorted in a favorable way by the equatorial chelate ligand with an obtuse O–Ru–O angle of ~124°. This deviation by 34° from a perfect rectangular arrangement opens up a seventh coordination site that is crucial for substrate water binding. The discovery of this catalyst and the easy manipulation of the axial ligands initiated the development of a whole class of catalysts based on the {Ru(bda)} fragment, which are among the best homogeneous water oxidation catalysts to date.[57]

2.2.2 Mechanisms for O–O Bond Formation

The basic mechanisms discussed for artificial water oxidation catalysts (WOCs) are the same as those previously discussed for the oxygen evolving complex of PSII. Sometimes subtle structural variations of the catalyst may lead to a complete change in the reaction mechanism as it has been shown by Sun and co-workers. The parent [Ru(bda)(pic)$_2$] complex **6** (pic = 4-picoline) oxidizes water following a bimolecular pathway (I2M) that involves radical coupling of two metal-oxo species before dioxygen release (**Figure 7**) with a turnover number (TON) of 1200 and a turnover frequency (TOF) of 4.5 s^{-1}.[70] Theoretical investigations revealed that the intermediate ruthenium(V) oxo species exhibits a distinct oxyl radical character facilitating radical coupling inevitable for O–O-bond formation. However, for the closely related [Ru(pda)(pic)$_2$] catalyst **7** a switch of the reaction mechanism from I2M to the water nucleophilic attack mechanism (WNA) occurs (pda = 1,10-phenanthroline-2,9-dicarboxylate).[70] Interestingly, rigidifying the dihedral angle of the bipyridine moiety by introducing a vinylene bridge seems to reduce the overall reorganization energy of forming the transition state, enabling a low activation barrier for the water nucleophilic attack. This WOC indeed catalyzes water oxidation by a nucleophilic attack of a substrate water molecule at the high-valent {Ru(V)=O}-intermediate that is initially generated by proton-coupled electron transfer processes (**Figure 7**), however with decreased catalytic activity (TON = 310; TOF 0.1 s^{-1}).[70]

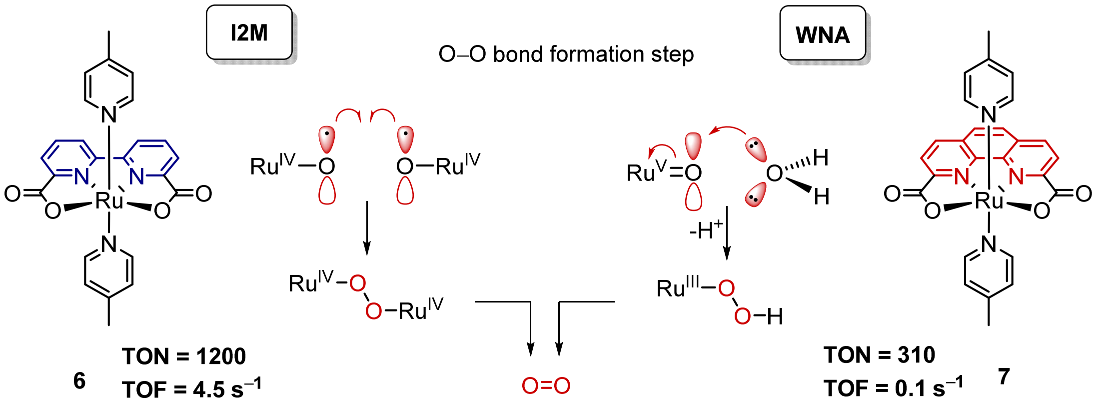

Figure 7: Two archetypical mononuclear Ru WOCs representing the two pathways for O–O bond formation [70] (Adapted with permission from ref. [74]); copyright (2017) Wiley-VCH).

Although WOCs proceeding *via* an I2M mechanism usually exhibit higher catalytic activities compared to systems following a WNA pathway, the bimolecular reaction mechanism prevents applications under highly diluted conditions or on heterogeneous surfaces on which diffusion-limited collision of two metal oxide subunits becomes unlikely.[153] The development of highly active WOCs operating under a unimolecular WNA mechanism is thus highly desirable although a specific manipulation is extremely challenging. Whereas the rate of water oxidation can readily be accelerated for I2M operating catalysts, *e.g.* by bringing the catalytic centers into spatial proximity, the optimization of WOCs with a WNA mechanistic pathway is rather ambitious since the reactivity of substrate water molecules has to be manipulated, *e.g.* by pre-organizing them appropriately in a hydrogen bonding network. Therefore, a series of complementary techniques is necessary to experimentally assess such weak supramolecular interactions that are best investigated by quantum mechanical studies on a high level of theory.

2.2.3 Techniques to Study the Water Oxidation Reaction

To study the performance and mechanism of water oxidation catalysts, the reductive half-reaction can be replaced using a sacrificial oxidant. Most commonly, the strong one-electron oxidant cerium(IV) ammonium nitrate (CAN) is used. With a reduction potential of 1.75 V vs. NHE at pH 0.9 (NHE = Normal Hydrogen Electrode), it provides enough overpotential to drive the water oxidation reaction which thermodynamically requires at least 1.23 V vs. NHE.[154] Compared with other oxidants, such as potassium peroxomonosulfate (oxone) and sodium periodate, the big advantage of CAN is that it is generally considered innocent, whereas for the other oxidants it was observed that some of their oxygen atoms can be found in the liberated molecular oxygen.[154] For photocatalytic experiments usually the photosensitizer $[Ru(bpy)_3]^{2+}$ is applied,[154-158] together with a sacrificial electron acceptor such as $[Co^{III}(NH_3)_5Cl]^{2+}$ or sodium peroxodisulfate ($Na_2S_2O_8$).[159-162] In any case, four equivalents of a one-electron oxidant are required to generate one oxygen molecule. Instead of using a sacrificial oxidant, the catalysts can also be tested under electrocatalytical conditions using foot of the wave analysis of cyclic voltammograms and bulk-electrolysis.[163-166]

2.2.3.1 Detection of Oxygen

The generation of oxygen can be monitored using different analytic techniques. With pressure transducers, the increase of pressure in a sealed reaction vessel can be determined which is the consequence of transforming liquid water into gaseous oxygen molecules.[167-169] Using the ideal gas law (eq. 4), the amount of evolved oxygen (Δn) can be calculated based on the pressure difference (Δp), the volume of the reaction vessel (V), the temperature (T), and the ideal gas constant (R).

$$\Delta n = \frac{\Delta p \cdot V}{R \cdot T} \tag{4}$$

This technique has the advantage that it is cheap, has a good time-resolution, and that it allows several experiments to be performed simultaneously. However, it provides no information on the composition of the released gas. For some catalysts oxidative degradation of the organic ligands to CO_2 is reported, which cannot be discriminated based on pressure data.[170, 171] Therefore, this technique is best combined with gas chromatographic analysis of the reaction head space after the oxygen evolution has ceased. The detection can either be performed by mass spectrometry or a thermal conductivity detector (TCD).[170, 172]

Furthermore, the sensitivity of the pressure sensors is limited, for what reason reactions with only little oxygen evolution, like for photocatalytic applications, become difficult to study. Therefore, a Clark electrode can be used, which is capable of measuring dissolved oxygen by the electrocatalytical reduction at a platinum cathode.[173] Since this method can only detect dissolved oxygen, it can be regarded as a complementary technique to the one described priorly.[174] Another method to study reactions with little amount of evolved oxygen is an indirect one. Using UV/Vis absorption spectroscopy, the consumption of the oxidant can be studied if it exhibits a characteristic UV/Vis absorption. By applying the Beer-Lambert law (eq. 5), the change of the oxidant concentration (Δc) can be calculated from the absorption changes (ΔA), the path length (d) and the extinction coefficient of the oxidant (ε). By correcting for the amount of electrons that can be accepted per oxidant molecule (*e.g.* 1 e^- for CAN), and that are required to oxidize two molecules of water to generate one molecule of oxygen (4 e^-), the amount of evolved oxygen can easily be calculated.[149, 175, 176]

$$\Delta c = \frac{\Delta A}{\varepsilon \cdot d} \tag{5}$$

2.2.3.2 Kinetic Analysis

To elucidate the mechanism of water oxidation, kinetic experiments are usually performed, which help to identify the rate-determining step (rds).[64, 70, 149, 177] If the O–O bond formation is rate-determining, both basic mechanisms can in principle be discriminated *via* concentration-dependent measurements regarding the catalyst. For the bimolecular I2M pathway a quadratic dependence is expected, whereas a linear relationship is observed for the monomolecular WNA mechanism. By variation of the oxidant concentration, it can furthermore be identified if an oxidation process is rate-determining. Moreover, H/D kinetic isotope effects (KIEs) reveal if a proton-release occurs during the rds.[131, 178, 179] However, if any of the reaction steps which occur before the O–O bond formation is rate-determining, kinetic experiments fail to distinguish between both pathways. In such cases the mass spectrometric analysis of the elemental oxygen that is evolved by catalysts bearing ^{18}O labeled aqua/hydroxo ligands is a powerful tool.[180-182] By the analysis of the isotopic composition of dioxygen, the two pathways can be differentiated by the source of the oxygen atoms of the evolved oxygen molecules. In case of a bimolecular I2M mechanism, monoisotopic oxygen is expected, whereas a mixture of isotopes is representative for a monomolecular WNA mechanism in which the O–O bond is formed between a metal-oxide and substrate water molecule.

2.2.3.3 Further Methods

Further information regarding the oxidation state of important intermediates and the resting state of the catalysis can be obtained by a wide range of spectroscopic techniques such as UV/Vis absorption spectroscopy and spectroelectrochemistry,[129, 183-185] nuclear magnetic resonance (NMR) and electron paramagnetic resonance (EPR) spectroscopy,[186-191] and near edge X-ray absorption fine structure (NEXAFS or XANES).[188-191] Additional information about changes that might occur in the ligand sphere can be derived from mass spectrometry.[70, 152, 176, 192] However, it is not possible by these conventional techniques to gain any insights into weak ligand interactions in the second coordination sphere that play an important role in natural [126-128] and artificial [192-197] water oxidation catalysis. Therefore, more sophisticated methods such as infrared predissociation spectroscopy have to be applied. Only recently, a hydrogen bonding water network could be substantiated in the first solvation shell of a $[Ru(tpy)(bpy)OH_2]^{2+}$ water oxidation catalyst using infrared pre-dissociation spectroscopy *in vacuo* on mass selected clusters with different amount of associated water molecules.[193] It was shown that strong hydrogen bonding is promoted by an electron transfer from the hydrogen atom of the aqua ligand to the Ru–OH_2 bond and the propagation through subsequent solvation shells highlights the role of the hydrogen-bonded water network for proton-coupled electron transfer processes. Similarly, Weber *et al.* managed to study the solvatochromism of the same mass selected catalyst-water clusters using photodissociation spectroscopy and it has been observed that four water molecules are sufficient to obtain spectra that closely resemble those of the bulk solution.[194]

2.2.3.4 Theoretical Chemistry[1]

Besides elaborate experimental techniques, theoretical studies are another option to further advance this field. Conventionally, intermediates and transitions states along a proposed reaction coordinate are calculated to determine crucial reaction barriers.[68, 198-201] However, the quantum chemical description of weak supramolecular interactions, such as hydrogen bonding, on a high level of theory is rather challenging. Here, advanced theoretical methods are required to accurately describe the interaction of catalysts with solvent water molecules to fully understand the different reaction mechanisms and the influence of weak non-covalent interactions that may result in conformational changes and cooperative effects. Density functional theory (DFT) calculations have generally been proven to be an adequate choice for the theoretical description of such complex systems.[202-205] However, these calculations are still based on an intuitive guess for the possible reaction coordinates that might be less feasible for unraveling the catalytic cycle in supramolecular structures. On the one hand, both experimental and theoretical studies have shown the importance of the distinct solvation shell surrounding the active center that has to be included in the calculations. On the other hand, cooperative effects between multiple reactive centers have to be taken into account, but are difficult to predict. A powerful tool for the description of large WOC assemblies is the QM/MM approach that allows for an explicit *ab initio* quantum chemical consideration of the molecular systems and solvation shells playing an active part in the catalytic cycle, while the “unreactive” water environment can be described more approximately using classical force fields. In combination with molecular dynamics (MD) simulations, all possible reaction pathways can in principle be revealed since the system freely explores the potential energy surface. However, since overcoming reaction barriers is

---

[1] This section has been written by M. I. S. Röhr and was part of the publication:
[74] V. Kunz, D. Schmidt, M. I. S. Röhr, R. Mitrić, F. Würthner, *Adv. Energy Mater.* **2017**, *7*, #1602939.

a rare event if the barriers are even only moderately high, quite long simulation times might be needed to identify the possible reaction steps and intermediates. Therefore, in order to sample reaction pathways in large supramolecular systems some sort of accelerated MD is needed. One possibility to enhance the sampling efficiency is the metadynamics approach developed by Parrinello and co-workers in which the system is forced to escape local minima that usually occur along the energetically most favorable reaction channel.[206] Fabris *et al.* have employed such simulations to reveal a novel catalytic cycle in the water splitting reaction of a Ru(II)-pincer complex that has considerably lower activation energies than pathways previously proposed by other approaches.[207] Furthermore, they point out the general importance of an explicit description of the solvent molecules for a predictive modeling of chemical reactions that involve its active participation.

2.3 Supramolecular Approaches in Artificial Photosynthesis[2]

2.3.1 Accelerating Bimolecular Catalytic Water Oxidation

In this part, supramolecular approaches are discussed which were applied to enhance the activity of {Ru(bda)}-based catalysts that follow a bimolecular I2M mechanism (**Figure 8**). Kinetic experiments for the parent [Ru(bda)(pic)$_2$] complex revealed that the rate-determining step is bimolecular regarding the catalytic ruthenium species and independent of the oxidant concentration.[152] Further support for the I2M mechanism was provided by the isolation and X-ray crystallographic characterization of the dimerized intermediate μ-(HOHOH)[Ru^{IV}(bda)(pic)$_2$]$_2$ (PF$_6$)$_3$, in which two molecules of **6** are bridged by hydrogen bonds between an aqua ligand at one catalytic center and a hydroxide ligand on the other (**Figure 8b**). Since the reaction rate for this type of catalysts is limited by the dimerization of two ruthenium centers, strategies that facilitate the interaction of two catalytic subunits were developed to improve the water oxidation performance.

One approach focuses on increasing the local catalyst concentration, for instance, by encapsulation of **6** into confined nano-cages such as mesoporous silica.[208] Therefore silica materials with varying pore sizes were investigated that can accommodate a different number of catalyst molecules. The catalyst loading was monitored by UV/Vis spectroscopy, and the catalytic units were trapped inside the voids by reducing the pore sizes through silylation of the inner walls. By increasing the average number of catalyst molecules per cage from one to seven, an enormous increase in catalytic activity was observed, which was not the case for the structurally related reference complex [Ru(pda)(pic)$_2$] **7** that follows the unimolecular WNA mechanism. Similarly, the direct linkage of two or more catalytic centers by metallosupramolecular coordination chemistry has been proven to be a promising approach to increase the water oxidation performance.[209] This concept should allow efficient catalysis under high dilution and conditions under which diffusion is limited, like for example as electro-catalysts on anode surfaces which otherwise are not compatible with

---

[2] This chapter was partly communicated in:
[74] V. Kunz, D. Schmidt, M. I. S. Röhr, R. Mitrić, F. Würthner, *Adv. Energy Mater.* **2017**, *7*, #1602939. (Reproduced with permission; copyright (2017) Wiley-VCH)

an I2M mechanism. Thus, several dinuclear WOCs have been reported and it was claimed by the authors that the right intramolecular distance between the ruthenium centers, together with a certain structural flexibility of the bridging ligand, are vital for promoting the crucial dimerization step resulting in highly active catalysts such as complex **8** (TON = 40,000; TOF = 40 s^{-1}).[209] And indeed, if a more rigid xanthene unit was used as the spacer for the construction of a Ru(bda) dimer, a complex was obtained that is not capable of following the radical coupling mechanism and thus shows only low performances.[210] To pursue this approach, the trinuclear complex **9** has further been synthesized that contains a third catalytic subunit as an additional backup and indeed a doubled TON of more than 86,000 turnovers has been measured in this case.[211] Generally, it has to be mentioned that benzyl pyridyl functionalities can become oxidized easily under harsh reaction conditions like they are applied in water oxidation catalysis. Hence, it has to be mentioned that the highest catalytic rate for **8** can only be observed after several minutes indicating that this catalyst might initially undergo structural changes. Oxidation of the organic ligand sphere can lead to catalytically active side-products or even highly active RuO_2 nanoparticles, like it has recently been observed under electro catalytic conditions.[171, 212] Therefore, for all complexes with organic ligand scaffolds that are prone to oxidative degradation, it has to be scrutinized if the initial structure represents the real catalytic species or just a pre-catalyst.[213, 214]

Alternatively, the interaction of two catalytic units can be enhanced by the use of ligands which direct aggregation in aqueous solutions. By exchanging the axial 4-picoline ligands by isoquinoline, complex **10** was synthesized which exhibits a drastically increased catalytic activity with a TOF of > 300 s^{-1}, making it able to compete with the activity of the natural oxygen evolving cluster.[64] Obviously, the larger π-surface of isoquinoline leads to a much stronger dimerization tendency in aqueous medium due to an increased hydrophobic effect, bringing two {Ru(V)=O} centers in spatial proximity. Therefore, the rate of bimolecular radical coupling is significantly accelerated as it has also been corroborated by density functional theory (DFT). The introduction of methoxy groups at the isoquinoline ligands leads to a slightly slipped aggregate geometry, giving rise to a dimeric transition state structure that makes the O–O bond formation even more favorable, resulting in an increased activity for catalyst **11** with a TOF around 900 cycles s^{-1}.[215] A very similar effect and performance is obtained by the introduction of fluorine substituents at the same position (**12**). The high turnover frequencies have been ascribed to the hydrophobic nature of the halogen substituent, since no strong impact on the electrochemistry of the complex has been observed.[216] If, on the other hand, positively charged substituents are introduced into the axial ligands, the catalytic activity drops dramatically to only 9 s^{-1} due to coulombic repulsion which hinders the formation of an encounter complex (**13**).[215] The replacement of the isoquinoline ligands with 6-bromophthalazine (**14**) leads to the most stable ruthenium WOC known so far with a TON > 100,000.[216] This was rationalized by the hydrophobic effect of the bromine substituent and decreased dissociative degradation of the catalyst. A correlation between the ruthenium-ligand binding strength and the HOMO of the dissociating ligand has been identified with DFT calculations, and due to the energetically high lying HOMO of the phthalazine (ptz) ligand those complexes are most stable.[168]

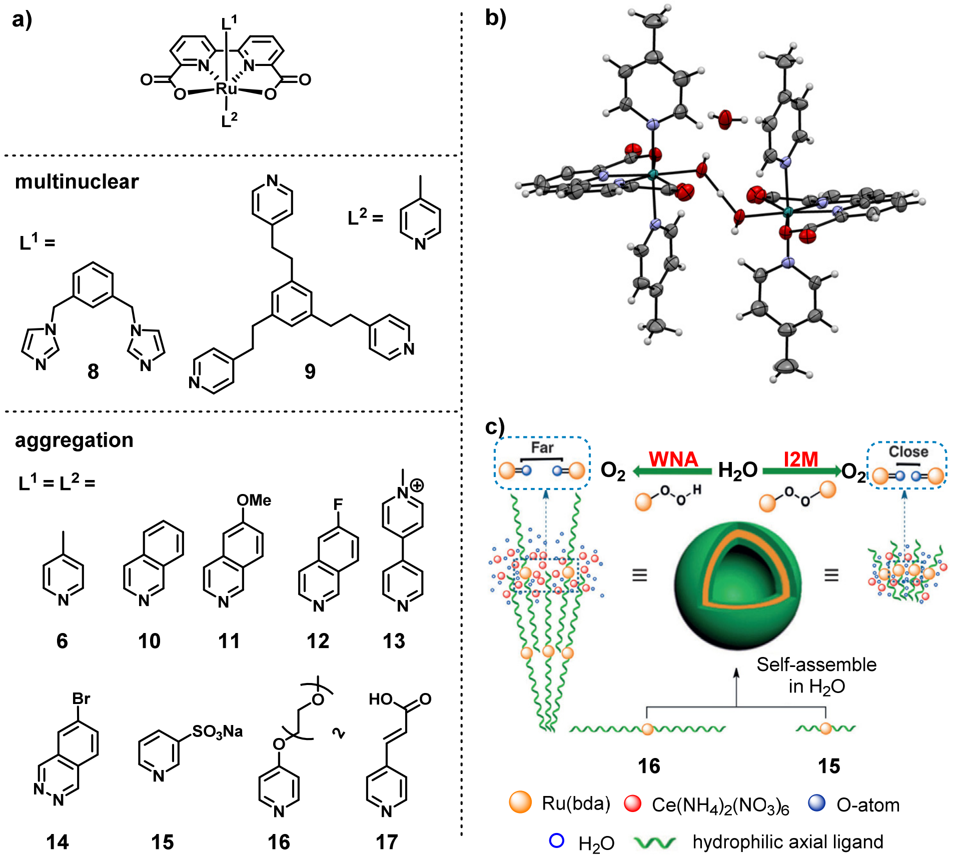

Figure 8: (a) Structures of homogeneous ruthenium water oxidation catalysts based on the {Ru(bda)} complex fragment. (b) X-ray crystallographic structure of the isolated μ-(HOHOH)[Ru^{IV}(bda)(pic)$_2$]$_2$ dimer of **6** (Adapted with permission from ref. [152]; copyright (2009) American Chemical Society). (c) Formation of vesicles by molecules **15** and **16** with different structures and reaction pathways (Adapted with permission from ref. [187]; copyright (2016) Wiley-VCH).

Self-assembly has also been utilized to manipulate the O–O bond formation step by exploiting the intrinsic structural information of the axial ligands (**Figure 8c**).[187] For instance, complexes **15** and **16** form vesicular structures in pure water once reaching the critical aggregation concentration of ~10^{-8} M, as it has been proven by monitoring the fluorescence enhancement of Nile Red upon encapsulation. Although the diameter of the individual vesicles of both complexes was estimated to approximately 100 nm by dynamic light scattering and electron microscopy, different supramolecular aggregation modes were assumed for both amphiphilic ligand systems giving rise to different supramolecular membrane structures. The hydrophilic parts of the sulfonated pyridines of complex **15** were expected to pile with each other, bringing the ruthenium centers into close spatial proximity that is ideal for an intramolecular I2M water oxidation pathway. In contrast, the pyridine ligands of complex **16** that are equipped with ethylene glycol side chains most likely aggregate in an alternating fashion, resulting in well separated ruthenium centers that are not accessible anymore for a bimolecular coupling reaction and thus, water oxidation proceeds *via* the WNA mechanism. Indeed, divergent electron paramagnetic resonance (EPR) spectroscopic behavior was elaborated for both vesicular WOCs indicative for different resting states and mechanistic pathways although both systems exhibit comparable catalytic activities in cerium(IV) ammonium nitrate (CAN) driven water oxidation catalysis. After addition of 20 equivalents of CAN to the catalyst solutions, **15** rests in a paramagnetic Ru(III) or Ru(V) state, whereas **16** does not exhibit any EPR signal under the same reaction conditions presumably due to a Ru(IV) resting state. Further evidence for the individual mechanisms proposed for **15** (I2M) and **16** (WNA) is provided by concentration dependent measurements of the oxygen evolution and by evaluating the respective rate laws. Accordingly, complex **16** exhibits a linear dependency on the catalyst concentration that is in line with a unimolecular WNA mechanism, whereas a quadratic dependency is observed for complex **15** as it is characteristic for the bimolecular I2M mechanism.

A further approach is the incorporation of WOCs into coordinatively linked materials *via* additional metal binding of functionalized ligands. Using this strategy, it was possible to create a good heterogeneous catalytic system connecting the {Ru(bda)} system with axial ligands bearing carboxylic acid groups **17** with Al(III) cations.[217] Another way to obtain a heterogeneous system based on homogeneous catalytic precursors is the immobilization of catalyst molecules on unmodified silica gel as shown by König.[218] By applying this strategy, it was possible to perform the water oxidation catalysis in pure water with the

[Ru(bda)(ptz)2] catalyst deposited onto silica particles, whereas for the application of this catalyst in homogeneous solution considerable amount of organic co-solvents is been required. However, the effect of the immobilization on the reaction mechanism has not been studied.

2.3.2 Accelerating Unimolecular Catalytic Water Oxidation

Accelerating the rate of water oxidation for catalysts that operate *via* the unimolecular WNA mechanism is particularly challenging since the nucleophilic attack of water is rate limiting in most cases and thus the interaction of the catalytic center with solvent water molecules has to be improved. This can principally be achieved by the introduction of pendant bases like carboxylates close to the reactive center (**Figure 9**).

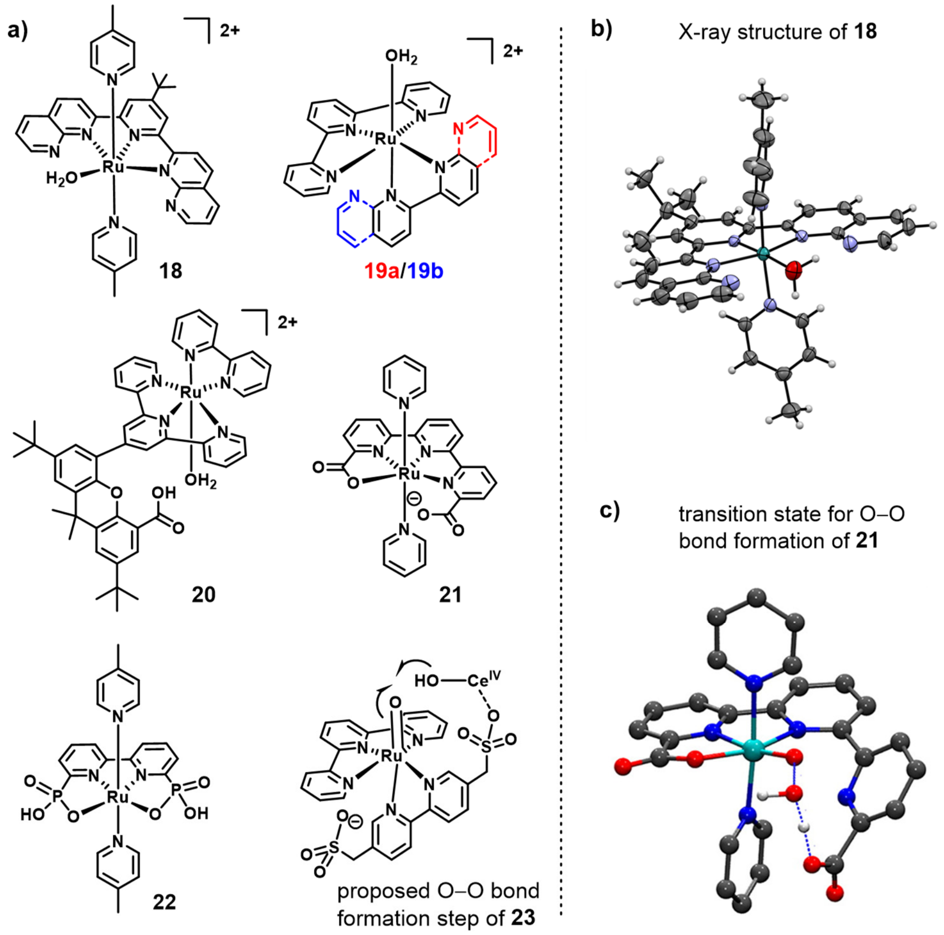

Figure 9: (a) Structures of homogeneous ruthenium water oxidation catalysts operating *via* an unimolecular reaction mechanism. (b) X-ray crystal structure of complex **18** (Adapted with permission from ref. [144]; copyright (2005) American Chemical Society). (c) Water nucleophilic attack transition state of complex **21** calculated with DFT (Adapted with permission from ref. [219]; copyright (2015) American Chemical Society).

Such bases may pre-coordinate water molecules for the nucleophilic attack at the high-valent {Ru(V)=O}-intermediate, thus lowering the activation barrier of the rate-determining step. Furthermore, they may assist as intermediate proton acceptors in proton-coupled reaction steps like PCET processes or water nucleophilic attack.[178] Both of these concepts are inspired by nature, where the oxygen evolving cluster of PSII is embedded into a proteinoic environment that manipulates the reactivity of solvent water molecules by forming an extensive hydrogen bonding network.

The first catalyst based on this strategy, that is also one of the first single site ruthenium WOCs, was reported by Thummel, Fujita and co-workers who introduced a polydentate ligand to give $[Ru(OH_2)(npm)(pic)_2]^{2+}$ **18** (npm = 4-*tert*-butyl-2,6-di-(10,80-naphthyrid-20-yl)-pyridine).[144] The single crystal X-ray structure of this mononuclear complex in the Ru(II) state revealed that the coordinated aqua ligand is additionally hydrogen-bonded to one of the free naphthyridine moieties promoting proton-coupled reaction steps (**Figure 9b**). The influence of pendant bases on the catalytic efficiency was further studied by the same groups synthesizing two coordination isomers **19a**/**19b** of $[Ru(tpy)(pynap)(OH_2)]^{2+}$ with different orientations of the asymmetric pynap ligand (tpy = 2,2';6',2''-terpyridine, pynap = 2-(pyrid-2'-yl)-1,8-naphthyridine).[220] The pKa value of the pynap ligand should principally be advantageous for the formation of hydrogen bonding interactions between the aqua ligand and the non-coordinating pyridyl moiety as it is assumed for isomer **19a** with its free base adjacent to the aqua ligand. Interestingly, this isomer has a significantly reduced activity in catalytic water oxidation compared to its isomer **19b** with the pendant base oriented opposite to the coordinated water molecule. The authors hypothesize that different stabilities may account for this behavior, since oxidative decomposition of the organic ligand system to CO_2 was observed for catalyst **19a** performing gas chromatography of the reaction head space. Furthermore, it seems to be very likely that the pendant base is constantly protonated under the applied reaction conditions (CAN in acidic aqueous solution) preventing an efficient proton relay.

That an appropriate balance between the pH value of the environment and the pKa of the adjacent base is of great importance for this supramolecular concept was demonstrated by the groups of Schwalbe and Llobet.[219, 221] Schwalbe *et al.* reported the hangman-type ruthenium complex **20** in which a dangling carboxylic acid group is closely located to the catalytic side of the Ru center. This complex exhibits only poor catalytic activity under acidic reaction conditions using CAN as the sacrificial electron acceptor.[222] However, electrochemical studies at pH 3–7 revealed that the carboxylic acid residue can indeed act as a proton shuttle accelerating catalytic water oxidation, if it readily can equilibrate between its protonated and deprotonated form.[221] Llobet *et al.* synthesized the closely related complex [Ru(tda)(py)$_2$] **21** (tda = 2,2':6',2"-terpyridine-6,6"-dicarboxylate) with the pendant carboxylate groups located at the equatorial position.[219] In the Ru(II) state of this complex, all three nitrogen atoms and one of the carboxylates of the tda ligand are coordinated to the ruthenium center with the second carboxylate moiety being accessible for proton transfer reactions. Under basic conditions at pH 10 this complex exhibits an impressive performance as electro-catalyst with a TOF of 50,000 s^{-1} and a Faradaic efficiency of 92% as it has been determined with foot-wave analysis of cyclic voltammograms and bulk electrolysis. Using DFT calculations it was shown that the activation barrier for the nucleophilic attack of water at the {Ru(V)=O} intermediate, that is accompanied by proton abstraction, can significantly be reduced by an intramolecular proton transfer and the pre-organization of the incoming water molecule (**Figure 9c**). Thereby, the intramolecular arrangement has a considerably greater influence than the threefold increase in catalytic activity that can be observed upon addition of external bases.

Very recently, Concepcion and co-workers reported a new phosphonate substituted WOC [Ru(bpaH$_2$)L$_2$] **22** that is equipped with an equatorial tetradentate bpaH$_2$ ligand (bpaH$_2$ = 2,2'-bipyridine-6,6'-diylbis(hydrogen phosphonate)).[223] This novel ligand system is a strong electron donor and capable of charge compensation upon oxidation of the ruthenium center by deprotonation of the phosphonic acid groups. Consequently, higher ruthenium oxidation states are more easily accessible since this complex is either neutrally or even negatively charged. Furthermore, the deprotonated phosphonic acid groups are able to assist as auxiliary bases in the proton-coupled electron transfer events (PCETs). Those steps include the primary binding of the first water molecule {Ru(IV)} → {Ru(IV)–OH}, that is assumed to be rate-determining, or the fast O–O bond formation step by nucleophilic attack of a water molecule {Ru(V)=O} → {Ru(III)–OOH}. For the latter process, DFT calculations suggest that the phosphonate groups are acting as initial proton acceptors, significantly lowering the activation barrier.

Masaoka *et al.* proposed that besides free water molecules also {Ce(IV)–OH} species may react with the ruthenium oxide intermediate in CAN driven water oxidation experiments. They introduced sulfonate groups into the ligand sphere of [Ru(tpy)(bpyms)(OH_2)] **23** (bpyms = 2,2'-bipyridine-5,5'-bis(methane sulfonate)) as potential binding sites for cerium(IV) ions to pre-organize the nucleophilic Ce(IV)-hydroxide species. Catalytic water oxidation experiments revealed a slightly accelerated reaction rate for **23** compared to a non-sulfonated analogue. Furthermore, the addition of free *p*-toluenesulfonic acid as a competitive binder for {Ce(IV)–OH} lead to decelerated catalytic water oxidation.[185, 224]

2.3.3 Metallosupramolecular Ru Macrocycles as Water Oxidation Catalysts

Another approach is based on metallosupramolecular macrocycles which are a favored class of supramolecular architectures.[225-227] The incorporation of catalytic ruthenium subunits into macrocyclic structures can be used to increase the stability of the catalyst itself with the potential side benefit of cooperative effects between the catalytic centers in such multi-nuclear structures. Axial ligand dissociation, that is a commonly accepted degradation pathway, can be suppressed in cyclic arrangements by the chelate effect of the bridging ligand and degradative ligand oxidation can be considerably reduced due to steric constrains that only allow small molecules like water to reach the catalytic centers.[63, 227]

The first example of a macrocyclic Ru WOC has been reported by Wei and co-workers (**Figure 10**).[228] However, this catalytic system (**24**) showed only a very low activity with a TOF of 0.027 h^{-1} and the mechanism was not studied in detail. The concept was furthermore used by the same group for the construction of an iridium analogue which had been applied in heterogeneous water oxidation catalysis due to its low solubility.[229] At about the same time, the incorporation of {Ru(bda)} fragments into a dinuclear macrocycle **25** has been published in a Chinese patent, and only the synthesis and X-ray crystallographic characterization but no catalytic studies have been reported.[230] However, the crystal structure itself is interesting since it shows that in this cyclic arrangement the {Ru(bda)} centers do not point towards each other and thus most likely cannot interact. Another example for a macrocyclic water oxidation catalyst has been published by Llobet and co-workers, who linked two Ru-Hbpp catalyst units using {Fe($tpy)_2$} coordination.[227]

Unfortunately, this approach failed because under the oxidative conditions Fe(II) is readily oxidized to Fe(III) which leads to a breaking of the {Fe(tpy)$_2$} connection and thereby to a disassembly of the cyclic system **26**.

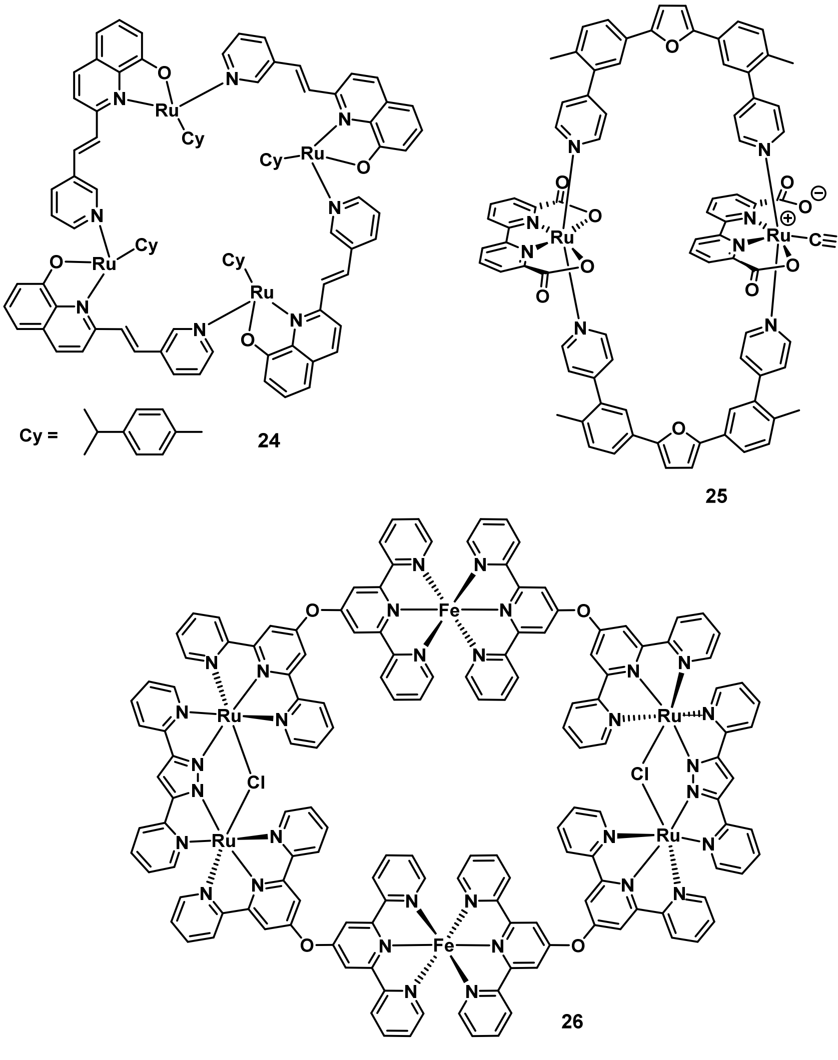

24

25

26

Figure 10: Overview about macrocyclic Ru water oxidation catalysts reported in the literature.

In 2016, our group has reported the incorporation of the catalytically active {Ru(bda)} complex fragment into a novel trinuclear metallosupramolecular macrocycle (**MC3**).[93] It was the first report in which the "macrocycle approach" has been proven to significantly increase the catalytic performance (TON = 7,400; TOF = 150 s^{-1}). The chelate effect of the bridging ligand and the reduced self-oxidation due to steric constraints that only allow small molecules to reach the catalytic center have been considered to be responsible for the improved stabilities. The O–O bond formation *via* an I2M mechanism, which is generally observed for other WOCs based on {Ru(bda)}, is prevented in such a cyclic structure due to the fixation of the catalytic sites within the macrocycle. With the help of kinetic studies, redox-titrations, and ^{18}O labelling experiments, the water nucleophilic attack (WNA) mechanism was found to be operating for this novel catalyst. The exceptionally high activity of this macrocyclic catalyst operating *via* the WNA mechanism has been explained with a hydrogen-bonded water network that exists inside the macrocyclic cavity according to DFT calculations. This should result in a lowered activation barrier for any reaction step that involves the abstraction of protons, and furthermore might help to direct the substrate water to the reaction center making the nucleophilic attack more favorable (**Figure 11**).

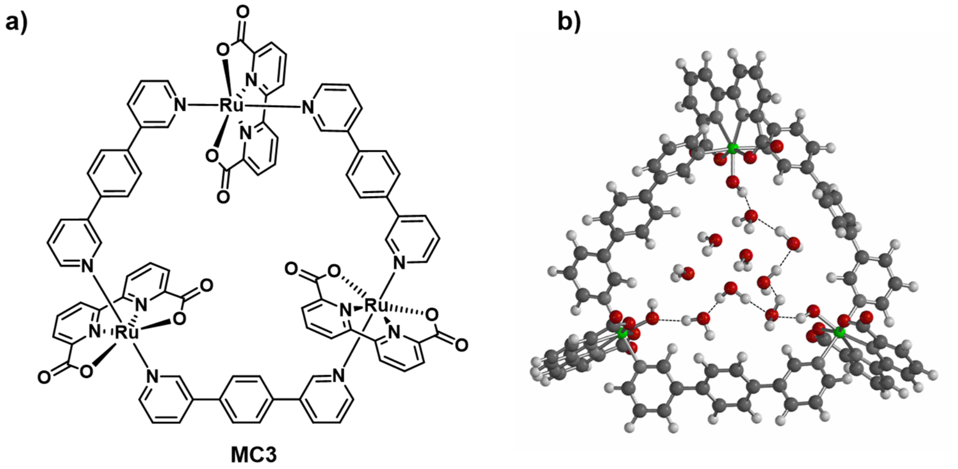

Figure 11: (a) Structure of the macrocyclic water oxidation catalyst **MC3**. (b) Hydrogen-bonded water network inside the cavity of $[Ru^{IV}–OH(bda)(bpb)]_3$ calculated with DFT (Reproduced with permission from ref. [93]; copyright (2016) Nature Publishing Group).

2.4 Supramolecular Catalyst-Photosensitizer Assemblies

2.4.1 Soluble Assemblies of Catalysts with Photosensitizers

Supramolecular approaches cannot only be used to manipulate the catalyst itself. Some effort has been spent to create efficient light-harvesting arrays that are capable of absorbing light over the whole visible spectrum using multichromophoric arrangements or dye-aggregates as it is also done by the natural light harvesting complexes.[24, 231-234] However, within this chapter only supramolecular strategies to improve the interplay between catalysts and photosensitizers are discussed in detail. The interaction of ruthenium catalysts with photosensitizers can be achieved in different ways.[161, 162, 235] The most simple approach is to add both components into a solution containing a sacrificial electron acceptor and let them interact in a diffusion controlled manner.[171, 192, 236-238] However, the electron transfer is much more efficient if those two units are fixed in close proximity. The most prominent strategy to achieve this, is connecting them using coordination chemistry (**Figure 12**).[24, 162, 239-241] There are some systems known in which the photosensitizer and the catalyst unit are connected to the same ligand or the ligands are highly conjugated.[242, 243] This leads to new molecular properties and the individual properties of the metal centers are not retained. Therefore, regarding the definition of supramolecular assemblies by Balzani, they are considered as one entirely new molecule rather than a supramolecular connection of two molecules, and are not discussed in detail here.[244]

Meyer and co-workers connected a $\{Ru(bpy)_3\}^{2+}$ photosensitizer moiety *via* an amide bond to a $[Ru(tpy)(bpy)OH_2]^{2+}$ water oxidation catalyst.[245] This presents an easy synthetic strategy to connect those two units while retaining the molecular properties of both components including the catalytic activity using Ce^{IV} as a sacrificial reagent. However, no photocatalytic water oxidation was demonstrated in solution for this assembly **27**. Another assembly **28** was developed in the same group in which a $\{Ru(bpy)_3\}^{2+}$ unit is connected to a ruthenium complex bearing an *N*-heterocyclic carbene ligand.[246] Again the properties of the individual components were retained. Although no photocatalytic oxidation has been shown for this assembly a distinct increase in catalytic activity was observed compared with the catalyst fragment alone under Ce^{IV} driven conditions, which was attributed to a redox mediator effect of the chromophore unit. A phosphonic acid derivative of this complex deposited onto a TiO_2 surface was capable to split water at an external bias of 600 mV and irradiation at 450 nm.[247] The first coordinatively linked system that was capable to split water under photocatalytic conditions in solution was developed by Sun and co-workers. Using an amide linkage, a $\{Ru(bpy)_3\}^{2+}$ unit was connected to a pyridine. Two of those functionalized pyridines can act as axial ligands for a $[Ru(bda)L_2]$ type catalyst to form the desired chromophore-catalyst assembly **29**.[248] Using sodium peroxodisulfate as a sacrificial electron acceptor, photocatalytic oxygen evolution could be demonstrated (TOF 4.7 min^{-1}, TON 38). The activity in the coordinatively linked system was five times higher than in a reference experiment using the unconnected components under the same conditions. By shortening the bridge between the catalyst and the chromophore in complex **30**, the activity was further increased up to a TON of 207 due to a more efficient electron transfer.[239]

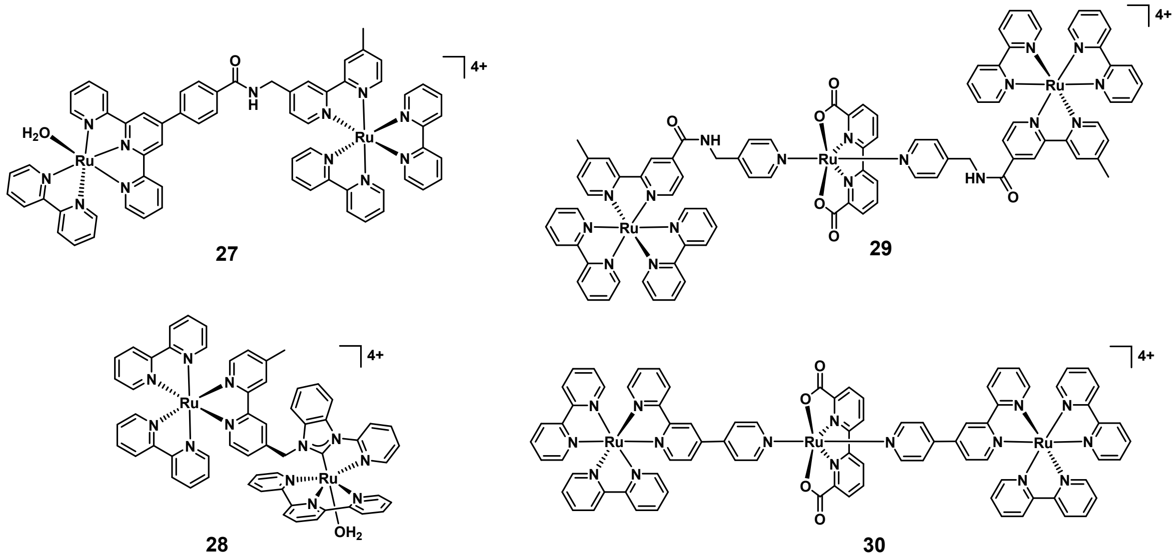

Figure 12: Different examples for catalysts-photosensitizer assemblies formed by coordination chemistry.

Moreover, detailed transient absorption spectroscopy studies have been performed for the triad **30** to gain insight into the photochemical processes (**Figure 13**). It has been shown that after excitation of the $\{Ru(bpy)_3\}^{2+}$ moieties and very fast relaxation into their ^{3}MLCT state, oxidative quenching by the connected {Ru(bda)} moiety can occur. After 150 ps an optical signature appeared that is characteristic of a reduced $\{Ru(bpy)_3\}^{+}$ species, which showed a lifetime of several microseconds but decayed much faster in the presence of the electron acceptor $S_2O_8^{2-}$. However, this electron transfer pathway, leading to the desired catalyst oxidation, was found to occur only with a yield of 5–10% due to an outcompeting pathway. The deactivation mainly proceeds *via* an energy transfer from the excited $*\{Ru(bpy)_3\}^{2+}$ photosensitizer to the {Ru(bda)} moiety and subsequent relaxation to the ground-state.

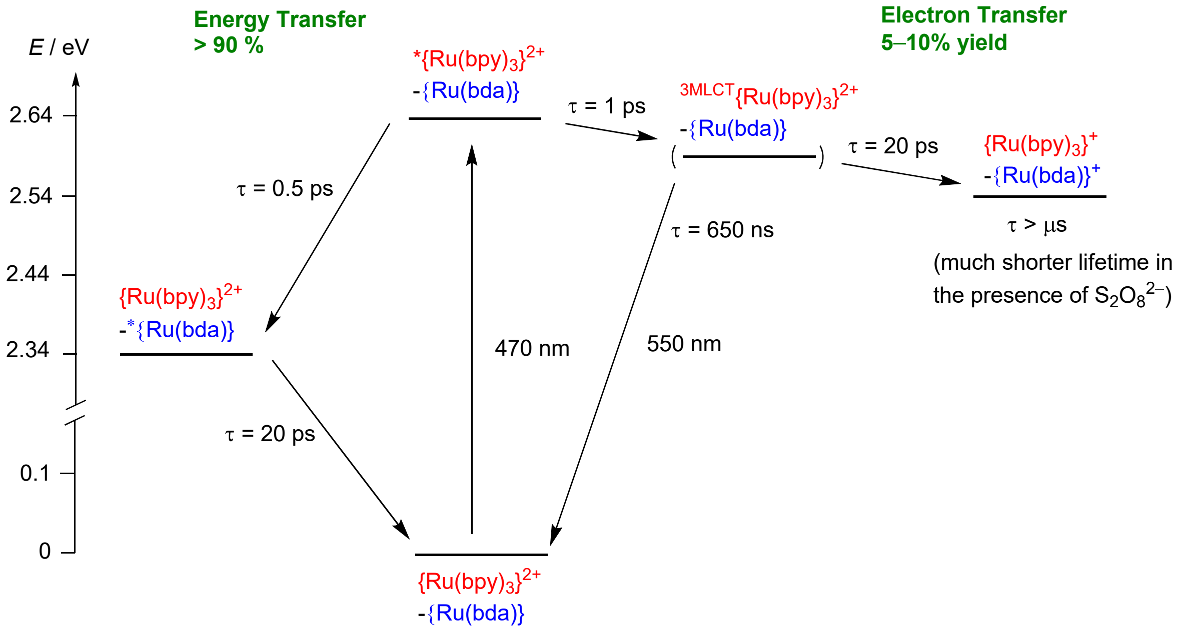

Figure 13: Energy level diagram and overview about processes (with related rate constants) occurring upon excitation of **30**.[239] For the sake of clarity only one of the two $\{Ru(bpy)_3\}^{2+}$ moieties is shown.

Another way to combine the photosensitizer and the catalyst is to use host-guest chemistry (**Figure 14a**). Sun and co-workers equipped a $[Ru(bpy)_3]^{2+}$ derivative with a cyclodextrin host that has a high binding affinity for a {Ru(bda)} catalyst with two axial 4-phenylpyridine ligands.[249] This supramolecularly assembled system **31** is highly efficient (TON = 267, TOF = 0.13 s^{-1}) with a photon-to-oxygen quantum efficiency of 84% (QE = 2 × moles of O_2 produced / moles of photons absorbed × 100%). This strategy can also be applied to bind the catalyst to dye sensitized electrodes.[250] Another approach is to co-embed both the catalyst and the photosensitizer into a membrane of a vesicle. This has been shown by the groups of König and Murata by using ligands that bear long hydrophobic alkyl chains (**Figure 14b**).[251, 252] König and co-workers found that the highest performance for the supramolecular system **32** was obtained working under the main transition temperature of the membrane, indicating that phase separation is a crucial factor for increasing the local concentration of the catalyst and the photosensitizer and thereby the performance of the light-driven water oxidation. This strategy allows catalysis under very high dilutions and TONs up to 394 were obtained.

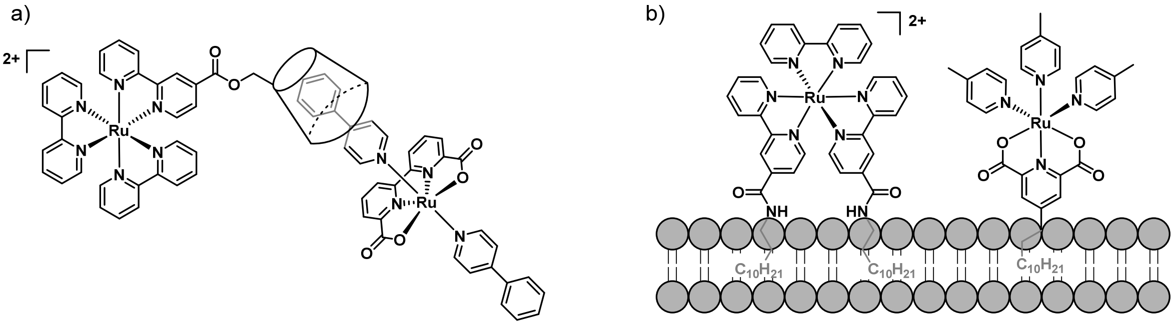

31

32

Figure 14: (a, b) Examples for **s**upramolecular strategies to improve the interplay between photosensitizers and water oxidation catalysts using host-guest chemistry (a), or co-embedding into membranes (b).

2.4.2 Assemblies of Catalysts with Photosensitizers on Surfaces

For the construction of functional devices, such as photo-electrochemical cells (PECs), the deposition of both the catalyst and the photosensitizer onto electrode surfaces with close spatial proximity is required. This can be achieved by the deposition of covalently linked catalyst-photosensitizer assemblies using the common anchoring groups like carboxylates or phosphonates.[247, 253-255] A remarkable example for this strategy stems from the groups of Sun and Imahori who were able to construct a PEC with an incident photon-to-current efficiency of 18% at a very low external bias of 0.2 V (**Figure 15a**).[255] The device was constructed by combining the TiO_2 photo-anode modified with a WOC-photosensitizer assembly (**33**), which consists of a {Ru(bda)} catalyst coordinatively linked to a porphyrin photosensitizer, and a platinum cathode for the reduction of protons. Another PEC that is capable of splitting water into its elements at an external bias of 0.6 V using a $[Ru(bpy)_3]^{2+}$ type photosensitizer was reported by Meyer *et al.*[247] Apart from depositing prefabricated assemblies on surfaces, the co-loading of the individual components,[253, 256-258] the co-polymerization,[259-262] the layer-by-layer approach,[253, 263-265] and host-guest chemistry [250] have also been proven successful for the construction of photo-anodes. An impressive result was achieved recently using the co-assembly strategy (**Figure 15b**). A ruthenium WOC (**35**) was co-assembled with a purely organic triarylamine photosensitizer (**34**) onto TiO_2 nanoparticles to construct the photo-anode. The other half reaction, was achieved on a photo-cathode consisting of NiO nanoparticles which were modified with another triarylamine photosensitizer (**36**) and a cobaloxime reduction catalyst (**37**). Together, both photo-electrodes allow the splitting of water into its elements without the application of any external bias, using entirely organic photosensitizers.[266]

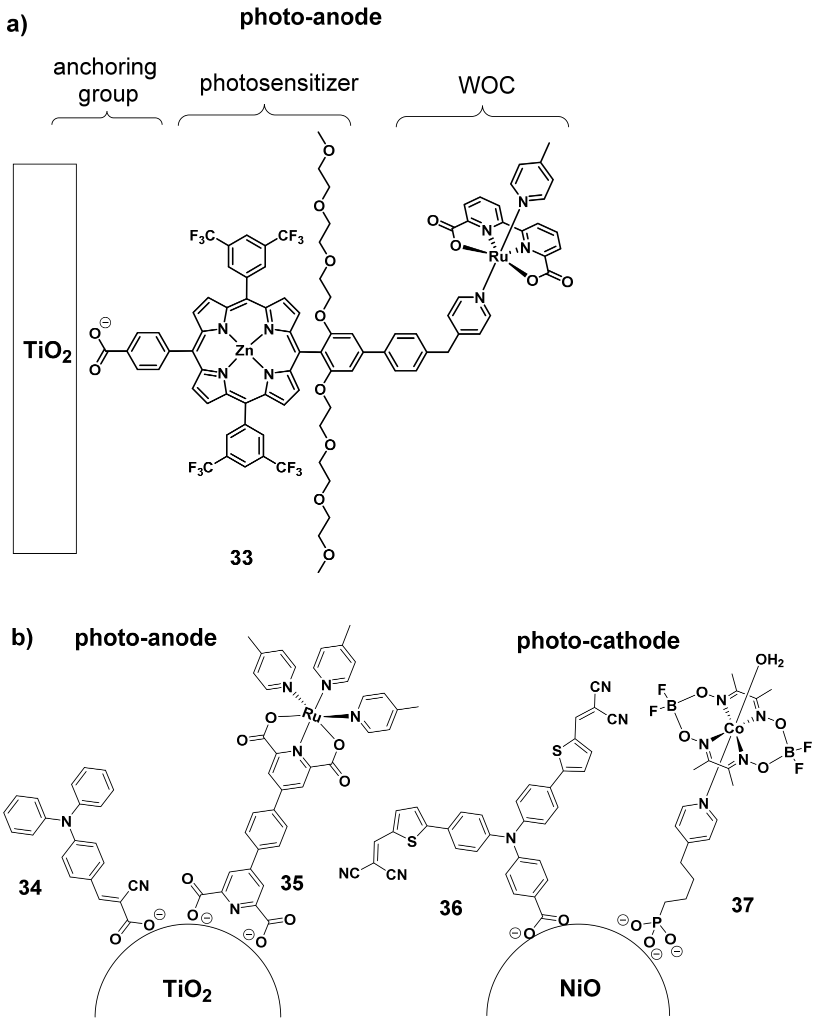

Figure 15: (a) Water oxidizing photo-anode by Sun and Imahori. (b) Photoelectrochemical cell consisting of a photo-anode and a photo-cathode using only organic photosensitizers.

CHAPTER 3 RESULTS AND DISCUSSION

3.1 Trinuclear Ruthenium Macrocycles: Cooperative Water Oxidation Catalysis[3]

3.1.1 Influence of the Second Coordination Sphere

In nature, the catalytic activity of enzymatic cofactors can be significantly improved by embedding the catalytic centers into complex supramolecular matrices in which weak non-covalent interactions lower the activation barrier or facilitate substrate transport. In many metallo-enzymes such proteinoic matrices are even crucial for the overall reactivity since the catalytic subunit alone would not catalyze a chemical transformation by itself, like it has been illustrated with the preparation of artificial mimics of the OEC that exhibit considerably high overpotentials.[75-77] Even more intriguing observations have been made for [FeFe] hydrogenases, which are responsible for biological proton reduction. Many groups reported synthetic mimics for the catalytically active di-iron center but failed to reproduce the high activity of the natural enzyme.[269] The groups of Happe and Fontecave, however, were able to show that this activity can be retained after the successful incorporation of such synthetic catalyst mimics into the natural apo-enzyme that does not contain any catalytic cofactor.[270, 271] Inspired by this concept, supramolecular catalysis aims to improve the catalytic performance by fine-tuning the second coordination sphere of the catalytic center by providing appropriate binding sites for the substrates [78-85] or by generating defined cavities that closely resemble enzymatic pockets.[86-90] Focusing on ruthenium based water oxidation catalysts, there are several examples on how intermolecular interactions have been exploited to improve the catalytic activity depending on the prevalent reaction mechanism.[74] Generally, efficient proton-coupled electron transfer (PCET) processes are vital to reduce the required overpotential and inevitable for the development of high performance water oxidation catalysts.[272-274] Both, quantum chemical calculations and infrared spectroscopy in the gas phase provide evidence that for ruthenium based water

---

[3] This chapter was partly communicated in:
[267] V. Kunz, J. O. Lindner, M. Schulze, M. I. S. Röhr, D. Schmidt, R. Mitrić, F. Würthner, *Energy. Environ. Sci.* **2017**, DOI: 10.1039/c7ee01557g. (Reproduced with permission; copyright (2017) The Royal Society of Chemistry)
[268] J. O. Lindner, Master Thesis, Julius-Maximilians-Universität Würzburg (Würzburg), **2016**.

oxidation catalysts a hydrogen-bonded water network in the first solvation shell has a strong influence on the activation barriers of proton-coupled reaction steps of the catalytic cycle.[192-197, 275] Similarly, an ordered hydrogen-bonded water network around the active center of the natural OEC is discussed to be essential for its remarkable efficiency.[126-128]

Very recently, our group has demonstrated that highly active water oxidation catalysts can be generated by incorporation of the catalytically active {Ru(bda)} complex fragment into metallosupramolecular macrocycles.[93, 276] The steric confinement and the reduced flexibility of the cyclic structure efficiently prevent O–O bond formation *via* an I2M mechanism like it is generally observed for other WOCs based on {Ru(bda)}. Instead, kinetic studies and ^{18}O labelling experiments suggested that these metallosupramolecular catalysts operate *via* the water nucleophilic attack (WNA) mechanism in which highly oxidized Ru^{V}=O species are nucleophilically attacked by water molecules, with the oxidation from Ru^{IV} to Ru^{V} being rate-determining. The improved stability of these macrocyclic catalysts has been attributed to the chelate effect of the bridging ligand and the reduced self-oxidation due to steric constraints that only allow small molecules to reach the catalytic center. To rationalize the exceptionally high activity of this new type of catalysts operating *via* the WNA mechanism, we hypothesized that a hydrogen-bonded water network exists inside the macrocyclic cavity resulting in a low activation barrier for the water nucleophilic attack and any reaction sequence involving the abstraction of protons. Based on this assumption, one has to anticipate that the size of the macrocyclic interior will have a substantial impact on the hydrogen bonding network and thus on the catalytic activity. Here, we present the synthesis of a series of differently sized trinuclear {Ru(bda)} macrocycles by simply manipulating the length of the bridging ligands. The metallosupramolecular macrocycles exhibit different activities in the catalytic water oxidation reaction and the origin of this phenomenon has been elucidated by molecular dynamics (MD) simulations in a water box with explicitly described water molecules in collaboration with the group of Prof. Roland Mitrić (Theoretical Chemistry, University of Würzburg).

3.1.2 Synthesis of Precursors and Kinetics of Ligand Exchange Processes

For the synthesis of the desired metallosupramolecular macrocycles, an appropriate ruthenium precursor is required. The complex [Ru(bda)(dmso)$_2$] **40** was chosen, since it already contains the essential {Ru(bda)} fragment with axial dmso ligands that should be easily exchangeable.[152] The synthesis of this precursor starts from commercially available RuCl$_3$ which is heated in DMSO to form the complex [RuCl$_2$(dmso)$_4$] **38**.[277] The 2,2'-bipyridine-6,6'-dicarboxyic acid **39** (H$_2$bda), was synthesized *via* Jones-Oxidation starting from commercially available 6,6'-dimethyl-2,2'-bipyridine.[278] The [Ru(bda)(dmso)$_2$] complex, in which the bda ligand binds to the ruthenium in a κ-N^{2}O^2 mode, can subsequently be obtained by heating [RuCl$_2$(dmso)$_4$] and 2,2'-bipyridine-6,6'-dicarboxyic acid in the presence of triethylamine as auxiliary base for the deprotonation of H$_2$bda (**Figure 16a**).[279] It is essential to use an equimolar stoichiometry of the ruthenium precursor and the bda ligand, since a deviation from this ratio leads to the formation of the novel by-product [Ru(bdaH)$_2$] **41**, in which the ruthenium atom is octahedrally coordinated by two bda ligands (each binds in κ-N^{2}O mode) as it has been confirmed by ^{1}H NMR spectroscopy and X-ray crystallography (**Figure 16b**). Such coordination complexes with the bda ligand have already been reported for Rh,[280] Co,[281] and Ni,[282] but are unknown for Ru. Product **40** and by-product **41** can easily be separated based on their different solubility. The complex [Ru(bda)(dmso)$_2$] precipitates from cold methanol, whereas the by-product is well soluble.

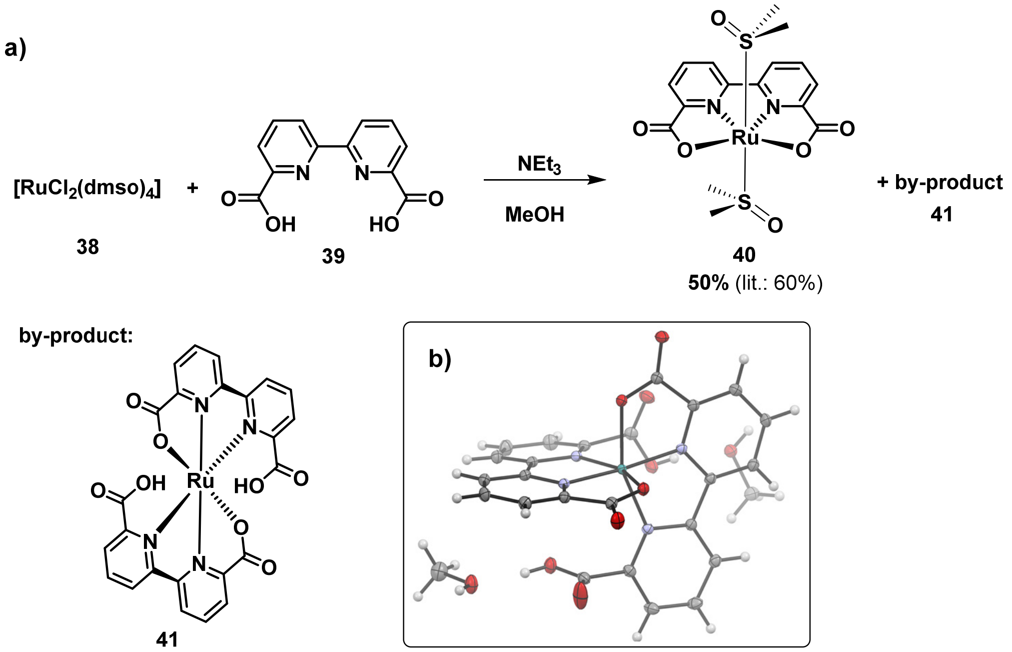

Figure 16: (a) Synthesis of the precursor [Ru(bda)(dmso)$_2$] and the by-product [Ru(bdaH)$_2$]. (b) X-ray crystal structure of [Ru(bdaH)$_2$] (ellipsoids set to 50% probability level).

In order to form the desired macrocycles, a series of ligand exchange reactions have to occur that can be classified into two individual processes. First the weak dmso ligands have to be exchanged with stronger coordinating pyridine type ligands. Second, those pyridine ligands could potentially undergo exchange reactions. To gain insight into the formation process of the metallosupramolecular macrocycles, those relevant ligand exchange reactions have been studied for a simple mononuclear model system using ^{1}H NMR spectroscopy. The results help to clarify whether the cyclic structures are formed under thermodynamic or kinetic control and to determine the optimal reaction conditions for their formation. Generally, the strength of coordinative bonds lies in the range of 60–210 kJ/mol, which is in between the strength of covalent single bonds (250–500 kJ/mol) and other classical non-covalent forces like *π-π,* or hydrogen bonding interactions (2–40 kJ/mol), making them potentially reversible.[283] There are three different substitution mechanisms described in literature how ligands can be exchanged in transition metal complexes.[284-286] The activation of the complex can either occur *via* the association of an incoming ligand (A), the dissociation of one of the ligands bound in the first solvation shell (D), or a concerted interchange mechanism (I) with no observable kinetic intermediate (**Figure 17**). If the rate of the reaction depends on the nature of the incoming ligand it is considered to be an associative interchange mechanism (I_a), if not, it is regarded to be a dissociative interchange mechanism (I_d). The change of the coordination number along the reaction coordinate leads to a concomitant change in geometry for the transition state. Under kinetic conditions the reaction pathway is determined by the relative energetic position of the respective transition states, which is governed by the ligand field stabilization energy (LFSE) for the specific geometries.[287] The discrimination of those mechanisms is usually based on the response of the reaction to the variation of parameters like pressure, temperature, and the nature of leaving and incoming ligand. In octahedral metal complexes, usually dissociative mechanisms (D and I_d) are favored.[285, 288] The solvent exchange reaction has been studied in detail for $[Ru(H_2O)_6]^{2+}$ and was found to proceed *via* a slow I_d type mechanism.[289-292] Usually octahedral metal complexes with d^6 electron configuration (Ru^{II}, Ir^{III}, Os^{II}) are found to be relatively inert due to their completely filled d-orbitals with 18 valence electrons (VEs).[288, 293]

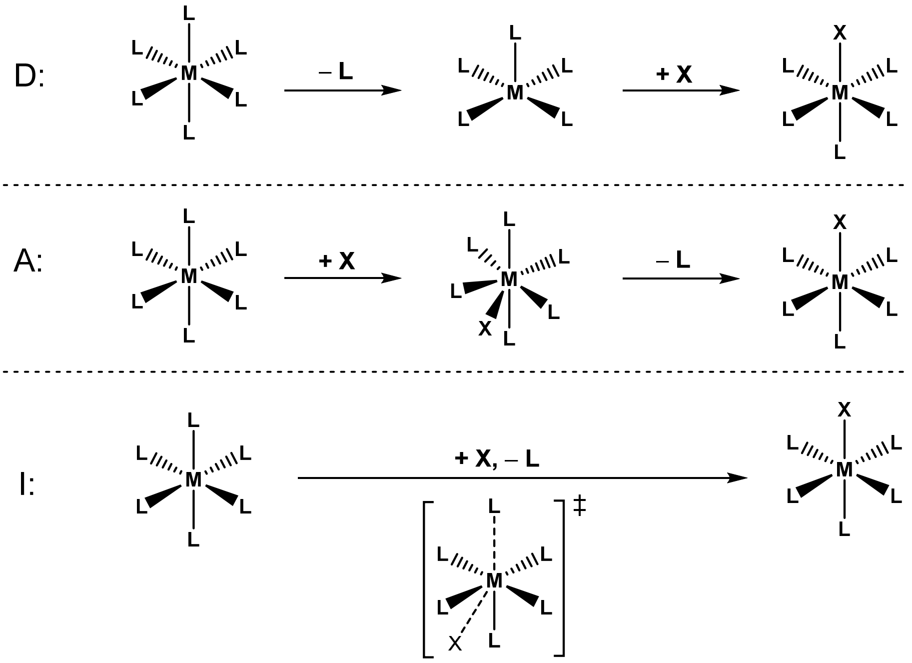

Figure 17: Dissociative (D), interchange (I), and associative (A) ligand exchange mechanisms for an octahedral metal complex (L = initial ligand, X = incoming ligand).

A way to determine the activation energy (E_a) for such a ligand exchange processes is to follow how the reaction rates (k) change with variation of temperature (T), as described by the Arrhenius equation (eq. 6) with R being the universal gas constant. By plotting ln(k) vs. 1/T, the activation barrier can be determined by the slope of the linear regression which represents E_a/R (eq. 7).

$$k = A \cdot \exp\left(\frac{-E_a}{R \cdot T}\right) \tag{6}$$

$$\ln(k) = \ln(A) - \frac{E_a}{R \cdot T} \tag{7}$$

An even simpler approach is the estimation of this energy by considering only the reaction rates (k_1 and k_2) at two distinct temperatures (T_1 and T_2) according to equations 8 and 9.

$$\ln\left(\frac{k_2}{k_1}\right) = -\frac{E_a}{R} \cdot \left(\frac{1}{T_2} - \frac{1}{T_1}\right) \tag{8}$$

$$E_a = R \cdot ln\left(\frac{k_2}{k_1}\right) \cdot \frac{T_1 \cdot T_2}{T_2 - T_1} \tag{9}$$

Thus, two different ligand exchange processes have been investigated for the mononuclear reference systems. First, the replacement of the dmso ligands of the precursor [Ru(bda)(dmso)$_2$] with deuterated pyridine (d_5-py) was studied. The driving force for the replacement by pyridine is the large gain in ligand field stabilization energy due to the good σ-bonding capacity of pyridine,[294] which is well reflected in the spectrochemical series.[295, 296] In a subsequent set of experiments, the interchange of coordinated undeuterated pyridines of the [Ru(bda)(py)$_2$] complex with deuterated pyridine has been examined, which is an energetically neutral reaction. In both cases deuterated pyridine was chosen as an incoming ligand, which was used in large excess as a solvent, facilitating the observation of the reactions with ^{1}H NMR spectroscopy.[297] For an octahedral complex with a d^6 electron configuration, a dissociative mechanism (D and I$_d$) is generally assumed, in which the reaction rate only depends on the leaving group and thus is invariant on the concentration of the incoming ligand. However, the special binding angles of the bda ligand make the coordination of a small seventh ligand possible to obtain a pentagonal bipyramidal geometry,[152] so that an associative mechanism cannot be fully excluded. Since the incoming ligand (d_5-py) is used as a solvent in the following experiments, both mechanisms should follow a (pseudo) first order rate law making a differentiation between both mechanisms based on the rate law impossible.

There are two dmso ligands that can be exchanged in the precursor complex [Ru(bda)(dmso)$_2$] (**40**). However, using ^{1}H NMR spectroscopy, only one transformation is observable as shown in **Figure 18**. This can most clearly be observed for the triplet belonging to the central proton of the bda ligand (y) and the protons of the dmso ligands. Both signals completely disappear within 15 hours at a temperature of 344.0 K (70.9 °C), whereas new signals for free DMSO and the product [Ru(bda)(d_5-py)$_2$] (**43**) can be observed.[298] This indicates, that the second substitution reaction is faster compared to the first, because no intermediate **42** is observable. Therefore, the binding of the first pyridine ligand most probably leads to a kinetic labilization of the dmso ligand in trans position to it due to the stronger trans effect of pyridine compared to dmso.[299]

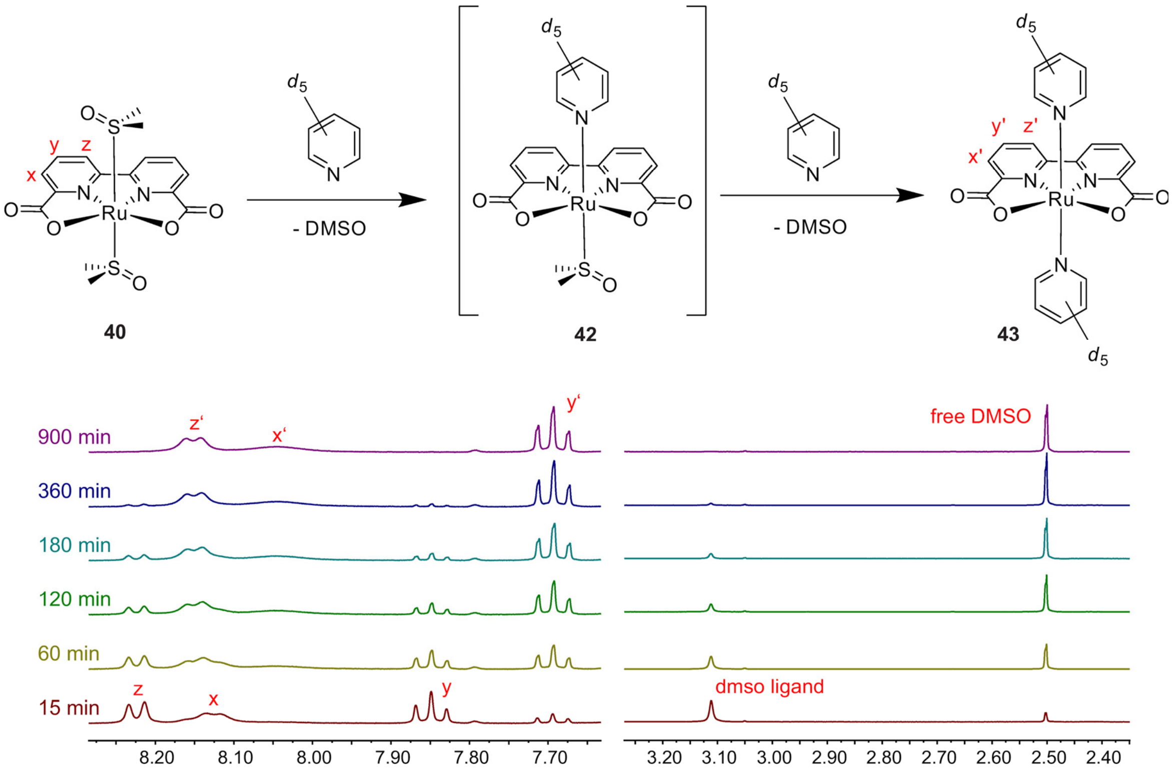

Figure 18: Time-dependent ^{1}H NMR spectra of [Ru(bda)(dmso)$_2$] in d_5-pyridine at a concentration of 6.41 mM and a temperature of 344.0 K (400 MHz, d_5-pyridine, ascorbic acid).

The reaction has been followed at two different temperatures (331.5 K and 344.0 K) to determine the respective activation barriers. The concentration of the initial complex **40** and of the product **43** have been determined by integration of the signals of bound and free DMSO. Very similar results can be obtained if the triplets (y and y') are analyzed. **Figure 19a** shows how the concentration of [Ru(bda)(dmso)$_2$] changes over time for the two different temperatures. Since those reactions follow a (pseudo) first order rate law, the concentration changes can be linearized by plotting the natural logarithm of the concentration against time (**Figure 19b**). The slope of such a linear regression represents the respective reaction rate. Using equation 9, the barrier for the ligand exchange process could thus be determined. Assuming a dissociative character of the reaction, this energy should represent the kinetic lability of the bound ligand. An activation energy of 81 ± 4 kJ/mol has been determined for the exchange of dmso with pyridine. This value is in a similar range as the activation energy of 95 ± 4 kJ/mol that has been determined for the *cis*/*trans* isomerization of the anticancer drug [RuCl$_4$(dmso)$_2$], which proceeds *via* an initial dmso ligand dissociation.[300]

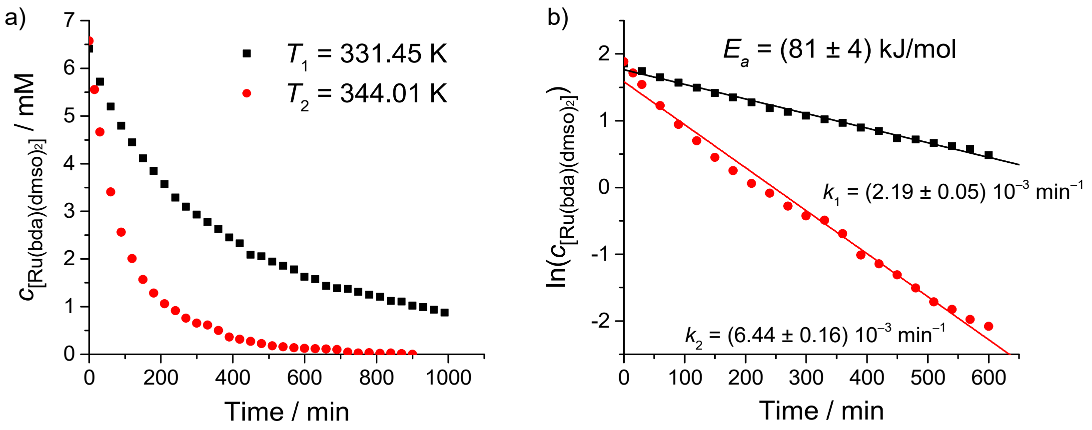

Figure 19: (a) Concentration changes of [Ru(bda)(dmso)$_2$] for the reaction with d_5-pyridine at two different temperatures (T_1, T_2). (b) Determination of the individual reaction rates (k_1, k_2) and of the corresponding activation energy (E_a).

The same experiment has been performed to study the interchange of pyridine ligands with their deuterated analogues. For that purpose, the [Ru(bda)(py)$_2$] (**44**) complex was used serving as a simple model compound for the more complex cyclic structures. As it can be seen from **Figure 20**, the ligand exchange is completed after heating the sample for 15 hours to a temperature of 377.6 K (104.5 °C). Within this period of time, the ^{1}H NMR signals of the pyridine ligands diminish due to the exchange with ^{1}H NMR-silent d_5-pyridine, whereas the signals of the bda ligand remain unchanged. Therefore, the ^{1}H NMR signals of the proton b (py) and y (bda) have been analyzed to determine the concentrations for [Ru(bda)(py)$_2$] and [Ru(bda)(d_5-py)$_2$] at each time interval (**Figure 21a**). Very similar results can, be obtained by analyzing the other NMR signals (a or c for pyridine and x or z for bda).

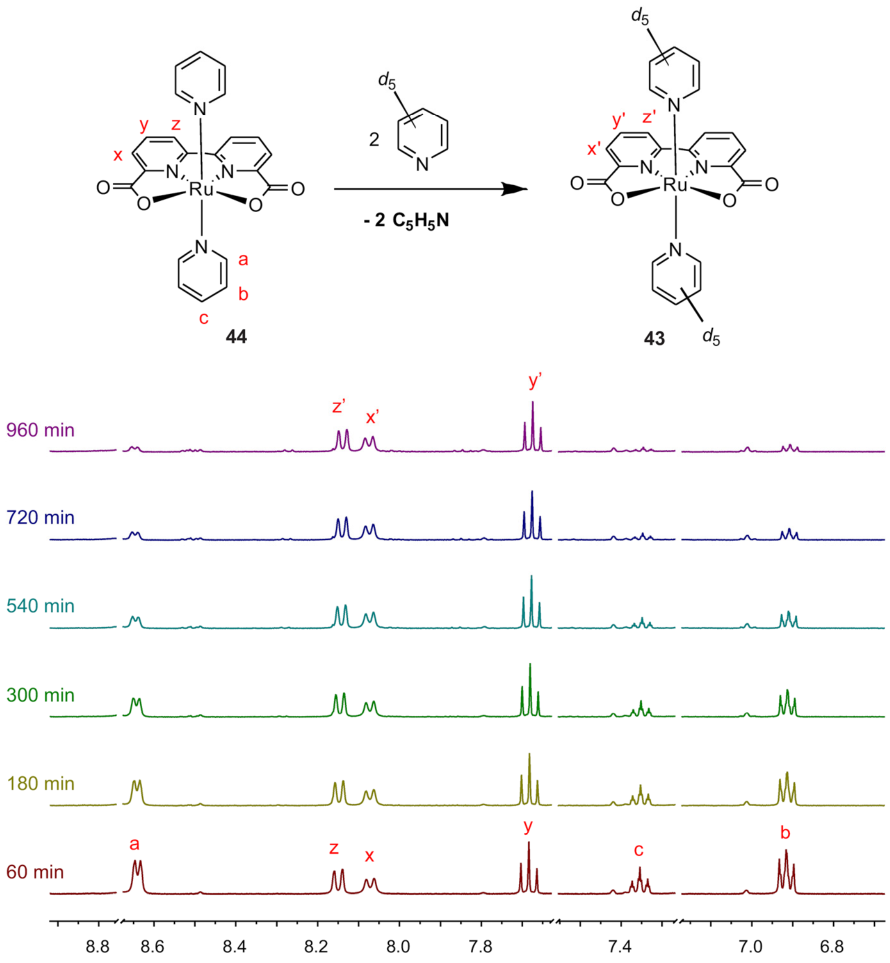

Figure 20: Time-dependent ^{1}H NMR spectra of [Ru(bda)(py)$_2$] in *d*$_5$-pyridine at a concentration of 6.85 mM and a temperature of 377.6 K (400 MHz, *d*$_5$-pyridine, ascorbic acid).

The kinetics can again be analyzed according to a first order rate law as described previously (**Figure 21b**). An activation energy of 124 ± 4 kJ/mol has been determined for the replacement of one pyridine ligand with its deuterated analogue. Similar barriers (100–112 kJ/mol) have been reported for the dissociation of pyridine and the subsequent exchange with *d*$_5$-pyridine in a series of dinuclear and trinuclear oxo-bridged ruthenium complexes.[301-303] The ligand exchange barrier for pyridine was thus found to be considerably higher by 43 ± 8 kJ/mol as the one determined for the replacement of a dmso ligand. The strong influence of the leaving ligand on the activation barrier indicates a dissociative nature of the ligand exchange mechanism. Based on the activation energies, it can be concluded that for the macrocyclization there are two different temperature regimes. At lower temperatures, sufficient to initiate the dmso dissociation from the {Ru(bda)} complex, the reaction proceeds under kinetic control and the binding of pyridine-type ligands is irreversible. At higher temperatures, however, this ligand coordination becomes reversible, so that the formation of the thermodynamically most stable product can occur.

The macrocycle synthesis, as it is already reported by our group, is usually performed in a refluxing mixture of chloroform and methanol at around 65 °C (338 K), and thus the reaction proceeds mainly under kinetic control due to the relatively high inertness of the ruthenium-pyridine bond.[288, 293] This is in line with the observation that higher temperatures and reaction times lead to increased amounts of polymeric material.

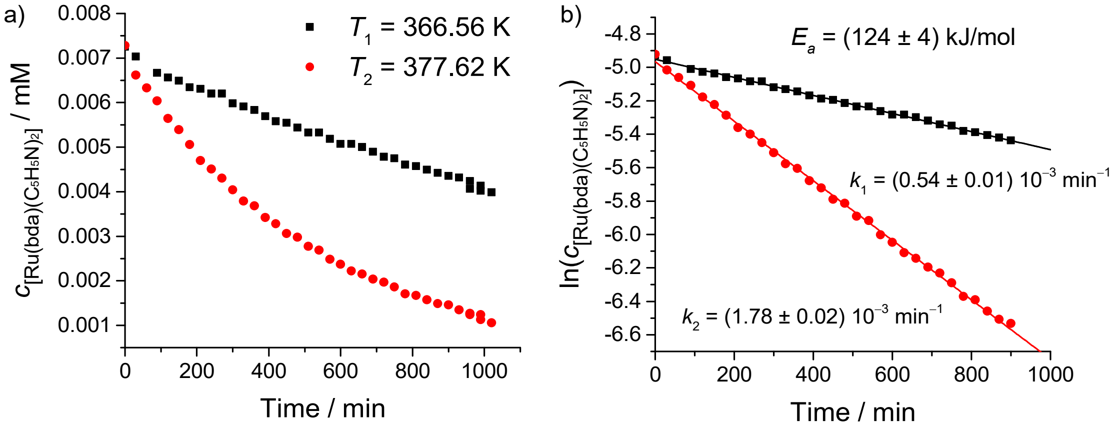

Figure 21: (a) Concentration changes of $[Ru(bda)(py)_2]$ for the reaction with d_5-pyridine at two temperatures (T_1, T_2). (b) Determination of the individual reaction rates (k_1, k_2) and of the activation energy (E_a).

3.1.3 Synthesis and Characterization of Differently Sized Macrocycles

To investigate the effect of the ring dimensions on the catalytic performance, a series of four differently sized macrocycles has been synthesized by self-assembly of equimolar amounts of the linear building block $[Ru(bda)(dmso)_2]$ (**40**) with ditopic *N*-heterocyclic bridging ligands, providing donor sites with angles of 60° (**Figure 22**).[225, 304-306] The length of the axial bridging ligands **45**–**48** (3,3'-bipyridine (bp), 1,2-bis(pyridin-3'-yl)ethyne (bpe), 1,4-bis(pyridin-3'-yl)benzene (bpb), and 4,4'-bis(pyridin-3''-yl)-1,1'-biphenyl (bpbp)) was adjusted by introducing different spacer groups in between the pyridyl binding sites, and all ligand systems were easily accessible through palladium-catalyzed cross-coupling reactions. Subsequently, the metallosupramolecular architectures **MC1**–**MC4** were isolated in moderate to high yields (16–55%), after heating the respective ligand together with the {Ru(bda)} precursor in a chloroform/methanol mixture under an atmosphere of nitrogen. Larger oligomeric by-products were removed by multiple filtrations over Al_2O_3 and the pure products could be obtained after crystallization out of dichloromethane/methanol solutions. Detailed synthetic procedures and the full characterization can be found in the Experimental Section in **chapter 5.2**.

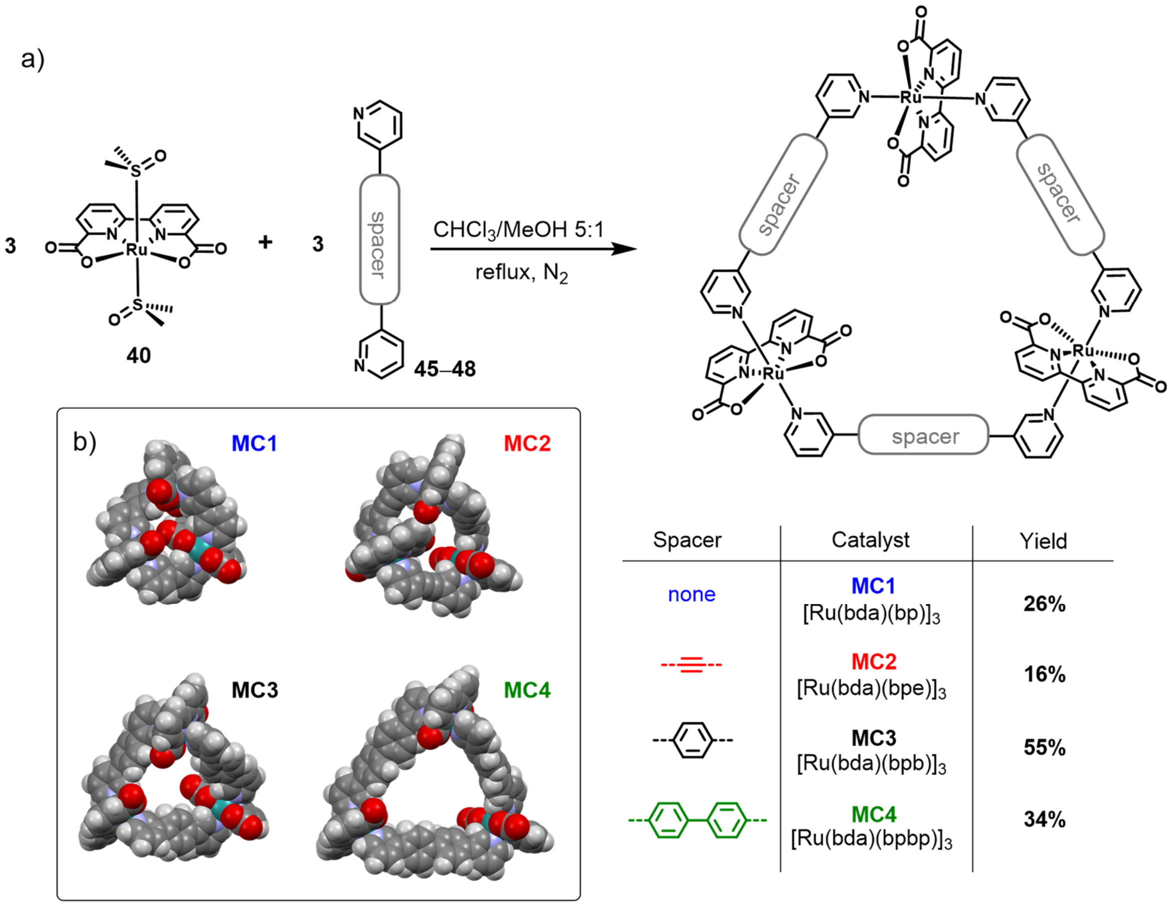

Spacer	Catalyst	Yield
none	**MC1** [Ru(bda)(bp)]$_3$	**26%**
--≡--	**MC2** [Ru(bda)(bpe)]$_3$	**16%**
--⬡--	**MC3** [Ru(bda)(bpb)]$_3$	**55%**
--⬡-⬡--	**MC4** [Ru(bda)(bpbp)]$_3$	**34%**

Figure 22: (a) Synthesis of the metallosupramolecular macrocycles **MC1**–**MC4** obtained by connecting {Ru(bda)} fragments with ditopic ligands of different length. (b) Space-filling models of **MC1**–**MC4** calculated for the [Ru^{II}|Ru^{II}|Ru^{II}] state using DFT (grey = carbon, white = hydrogen, red = oxygen, blue = nitrogen, turquoise = ruthenium).

The propensity of these macrocycles to crystallize adequately for X-ray diffraction experiments increases with their ring size. Whereas the smallest macrocycle **MC1** was exclusively obtained as an amorphous powder, the medium sized macrocycles **MC2** and **MC3** were isolated as microcrystalline materials for which a structure elucidation by X-ray diffraction was unfortunately not possible. However, for the largest cycle **MC4** suitable single crystals could be grown from a dichloromethane/methanol/2,2,2-trifluoroethanol mixture by slowly evaporating the solvent under an atmosphere of nitrogen to prevent partial oxidation of the ruthenium centers (**Figure 23**). The macrocycle **MC4** crystallizes in the trigonal space group *R*3*c* with a slipped stacked packing arrangement giving rise to one-dimensional pores, which are filled with 2,2,2-trifluoroethanol. Furthermore, several solvent accessible voids exist within the refined structure as evidenced by the squeezed electron density of highly disordered solvent molecules that could not be modeled satisfactorily.

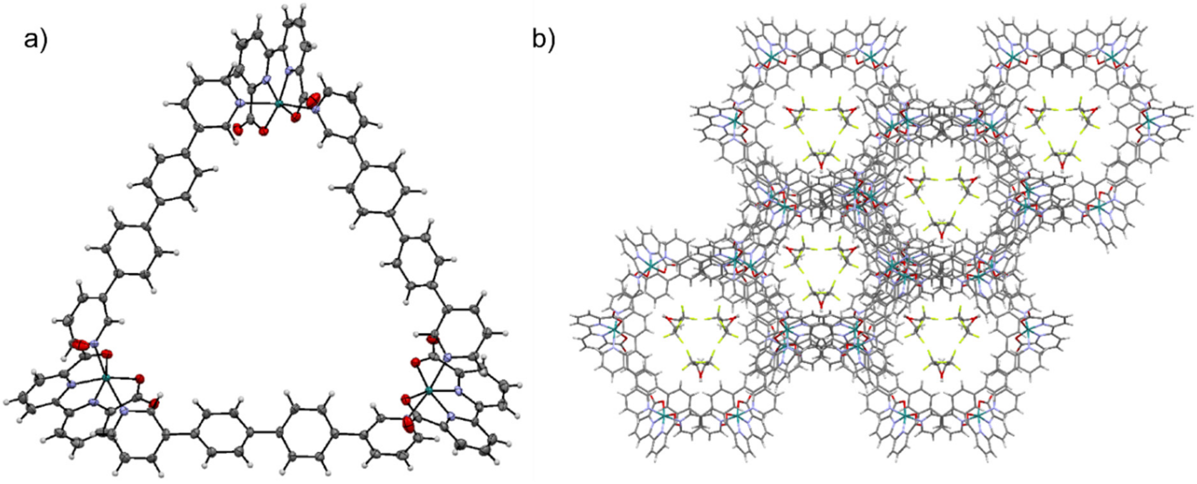

Figure 23: (a) Solid state molecular structure of **MC4** determined by single crystal X-ray diffraction. Solvent molecules were omitted for clarity (ORTEP diagram with thermal ellipsoids set at 50% probability). (b) Crystal packing of **MC4** viewed along the cell axis c with 2,2,2-trifluoroethanol molecules in the pores (capped stick model) (grey = carbon, white = hydrogen, red = oxygen, blue = nitrogen, turquoise = ruthenium, green = fluorine).

The distances between the ruthenium centers and the axially coordinated pyridyl ligands (2.066(5) and 2.078(7) Å) are comparable to those of the acyclic mononuclear reference compound [Ru(bda)(pic)$_2$] for which bond lengths of 2.070(6) and 2.084(6) Å have been reported.[152] Both complexes exhibit distorted octahedrally coordinated ruthenium centers with obtuse O–Ru–O angles of 123.0(2)°, providing an optimal seventh coordination site for small molecules like water. Minor differences are found for the N$_{ax}$–Ru–N$_{ax}$ bond angles with 173.0(2)° for [Ru(bda)(pic)$_2$] and 170.9(2)° for **MC4**. Due to the rigid cyclic structure, each one axial pyridyl ligand in **MC4** is considerably tilted towards the equatorial bda chelate, as it becomes obvious by the smaller Ru–N$_{ax}$–C$_{para}$ angles. Whereas [Ru(bda)(pic)$_2$] is characterized by almost perfectly linearly oriented picoline ligands (Ru–N$_{ax}$–C$_{para}$ = 178.2(3)° and 177.2(3)°), **MC4** exhibits Ru–N$_{ax}$–C$_{para}$ angles of 174.9(3)° and 159.9(3)°. This tilting in **MC4** causes the axial pyridyl ligands to be torsionally twisted by 46.1(2)° in contrast to 22.3(9)° in [Ru(bda)(pic)$_2$] which should be beneficial for substrate water binding (**Figure 24**). The intramolecular distance between two ruthenium centers is 16.274(1) Å, giving rise to an aperture size of approximately 115 Å^2. Most interestingly, the open coordination sites of all three ruthenium centers of **MC4** point into the interior of this cavity, giving support to the assumption that the catalytic subunits might cooperatively interact for the oxidation of water. Since the solid state molecular structures of the smaller macrocycles could not be determined experimentally, the geometries of **MC1**–**MC4** were optimized in their Ru(II) oxidation state in the gas phase using DFT calculations. Here, it turned out that in the smaller macrocycles some of the {Ru(bda)} centers are partially oriented to the outside, with the largest degree of torsion for **MC1**. The respective space filling models clearly show that the size of the cavities continuously decreases from **MC4** to **MC1**, with almost no water accessible void for the smallest macrocycle **MC1** (**Figure 22b**).

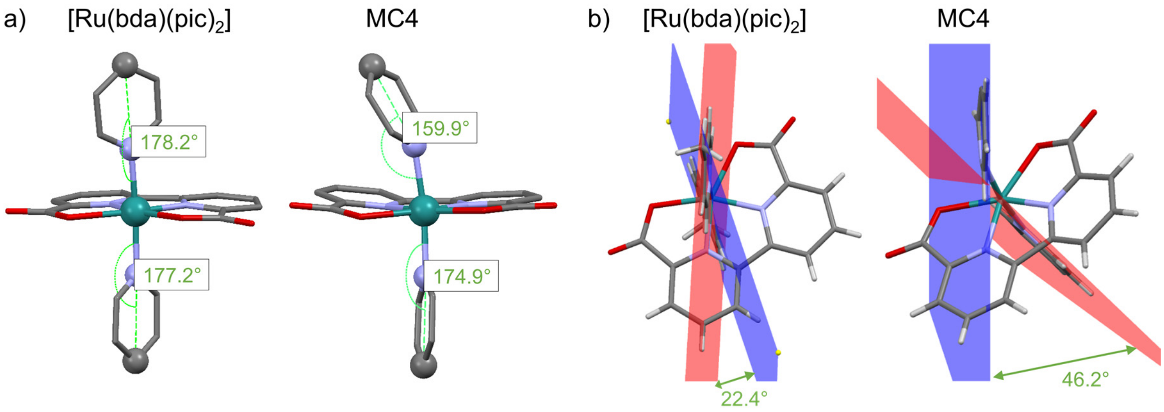

Figure 24: (a, b) Comparison of the X-ray crystal structures of [Ru(bda)(pic)$_2$] and **MC4:** Regarding the tilt angle of the axial ligands (a), and the torsion angle between the axial ligands (b). For **MC4** only one {Ru(bda)} center is displayed, and from the axial ligand only the coordinating pyridine moiety is shown for the sake of clarity (grey = carbon, white = hydrogen, red = oxygen, purple = nitrogen, turquoise = ruthenium).

3.1.4 Electrochemistry and UV/Vis Spectroscopy

The electrochemistry of the macrocycles **MC1**–**MC4** was investigated by differential pulse voltammetry (DPV) in acidic aqueous media using organic co-solvents exclusively for solubilization, since in a purely organic environment only the $Ru^{II/III}$ oxidation can be observed.[93] In aqueous solution, however, water can coordinate to the seventh coordination site of the ruthenium center, being a prerequisite to reach higher oxidation states. After substrate water binding, proton-coupled electron transfers (PCETs) become possible that contribute to prevent unfavorable charge accumulation.[178] For all macrocycles three subsequent oxidation events are thus observed that were assigned to the redox couples $Ru^{II/III}$, $Ru^{III/IV}$, and $Ru^{IV/V}$ in accordance to the electrochemistry reported for mononuclear [Ru(bda)L_2] complexes (**Figure A1**, see Appendix).[64, 163] However, it has to be noted that the existence of a Ru^{V} state is under debate for many water oxidation catalysts,[188, 190] and only few catalysts are known for which its existence has been proven experimentally. Thus, a Ru^{V} intermediate was substantiated by EPR spectroscopy for the complexes *cis*,*cis*-[(bpy)$_2$(H_2O)RuORu(OH_2)(bpy)$_2$]$^{4+}$ [189, 307, 308] and *cis*-[Ru(bpy)$_2$(OH_2)$_2$]$^{2+}$, [309, 310] whereas no clear evidence for a Ru^{V} species has been provided so far for the {Ru(bda)} catalyst family. The respective potentials of these oxidation events using non-coordinating 2,2,2-trifluoroethanol as co-solvent at pH 1 are very similar for all macrocycles and approximately

100 mV higher than those observed for the mononuclear reference complex [Ru(bda)(pic)$_2$],[64] presumably due to the close proximity of the three redox centers. In the presence of acetonitrile as co-solvent, the first oxidation from Ru^{II} to Ru^{III} is shifted to higher potentials by 250 mV, whereas the other oxidation events remain unaffected (**Figure A1**). This can be attributed to the fact that in the Ru^{II} state, the ruthenium centers are preferentially coordinated by acetonitrile, which has to be exchanged by water upon oxidation to Ru^{III} resulting in the observed overpotential.[163, 311]

Although in each oxidation event three electrons are removed simultaneously, different peak current intensities are found for the individual processes, which can be explained by the coupling of some oxidation events to proton transfer processes. In such cases, the oxidation is kinetically hindered giving rise to considerably decelerated reaction rates at the electrode and thus to lower peak current intensities.[312] This can nicely be illustrated at differential pulse voltammograms of **MC2** for different pH values **(Figure 25**). At pH 3.0, only the Ru$^{II/III}$ oxidation exhibits an intensive peak current, indicating that the subsequent oxidation steps from Ru^{III} to Ru^{IV} and Ru^{IV} to Ru^{V} are proton-coupled. However, by increasing the pH value, the ratio between the peak current intensities of all oxidation events changes dramatically. At pH 8.2, the Ru$^{IV/V}$ oxidation exhibits the strongest current, whereas at even higher pH values of > 9 a completely new oxidation event emerges that can be attributed to the oxidation of a Ru^{III}–OOH intermediate, which is formed by the nucleophilic attack of water at the Ru^{V}=O moiety.[149, 216, 313]

To further investigate the proton coupling of the individual oxidation events in detail, pH-dependent differential pulse voltammetry was performed and the corresponding Pourbaix diagrams were constructed for all complexes (**Figure A2**–**Figure A4**). Exemplarily for all macrocycles, the Pourbaix diagram of **MC2** is shown in **Figure 25b**, highlighting the stability regions of the different oxidation states. The changes of the potential with the pH value reflect the proton coupling of the individual processes with a Nernstian ideal of 59 mV/pH for a simple ne$^-$/nH$^+$ process.[57, 176] Under acidic and basic conditions, the slopes and the proton couplings are very similar for the macrocycles **MC1**–**MC3**. Merely at neutral pH values the situation is slightly more complicated, and minor differences can be observed. However, since the catalysis is usually driven by cerium(IV) ammonium nitrate (CAN) as sacrificial oxidant in highly acidic media (pH 1), only the oxidation events under those conditions are discussed in detail. The oxidations from Ru^{II} to Ru^{III} are independent of the pH values in all cases, and therefore proton-uncoupled. For the $Ru^{III/IV}$ redox couples, slopes of 42–49 mV/pH are found for the macrocycles **MC1**–**MC3** indicating $3e^-/2H^+$ processes. For **MC4** however, a slope of 62 mV/pH is observed which is in line with a $3e^-/3H^+$ PCET. This behavior is reversed for the subsequent oxidation from Ru^{IV} to Ru^{V}, for which **MC1**–**MC3** still exhibit slopes corresponding to a $3e^-/2H^+$ process, whereas **MC4** undergoes a $3e^-/1H^+$ oxidation. Thus, for all macrocycles the same oxidized species are formed before the current strongly increases due to water oxidation. In an acidic environment, partially protonated $[Ru^{V}{=}O|Ru^{V}–OH|Ru^{V}–OH]^{5+}$ species predominate, whereas in basic media completely deprotonated $[Ru^{V}{=}O|Ru^{V}{=}O|Ru^{V}{=}O]^{3+}$ intermediates are obtained. At these highly oxidized $Ru^{V}{=}O$ electrophiles, the nucleophilic attack of water takes place, generating the O–O bond. The resulting (hydro)peroxide species has to be oxidized once more to finally liberate elemental oxygen. However, this fourth oxidation can only be observed at basic pH values like it has already been reported by Sun and co-workers for mononuclear WOCs based on {Ru(bda)}.[216, 313]

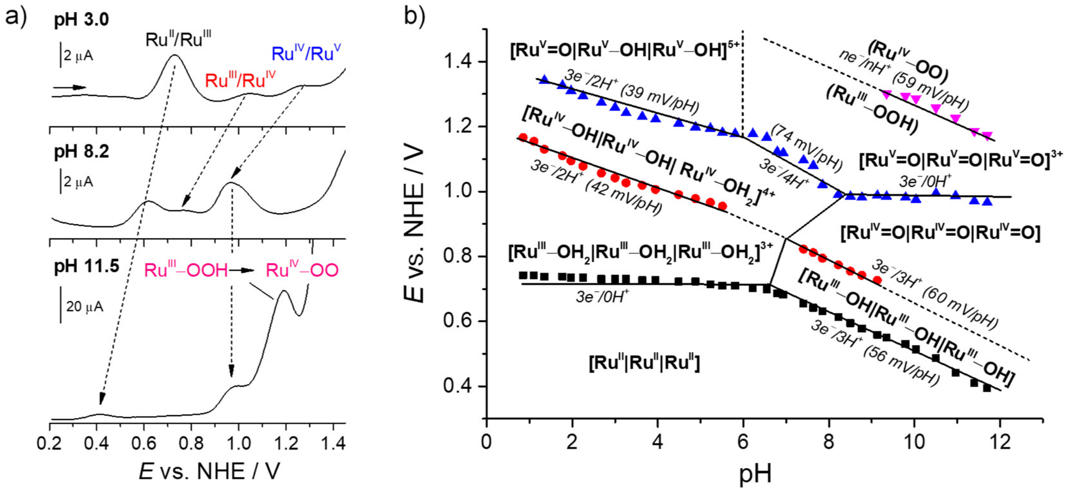

Figure 25: (a) Differential pulse voltammograms of **MC2** at three different pH values. (b) Pourbaix (*E*-pH) diagram of **MC2**. The experiment was performed in CH_3CN/H_2O 1:1 with an initial pH value of 1 (acid: CF_3SO_3H) and the successive addition of aq. NaOH for adjusting the higher pH values.

Since intriguing color changes were observed for the macrocycle **MC3** with proceeding oxidation,[93] spectroelectrochemistry and chemical titration experiments monitored by UV/Vis spectroscopy using cerium(IV) ammonium nitrate were performed for all macrocycles to gain further insights into the spectral changes that accompany the oxidation processes. The UV/Vis absorption spectra of all macrocycles in the $[Ru^{II}|Ru^{II}|Ru^{II}]$ oxidation state are very similar in CH_3CN/H_2O (pH 1) 1:1, and are characterized by L-π → L-π* transitions of the aromatic bridging ligands (L) around 300 nm together with several metal to ligand charge transfer (MLCT) bands between 350 and 500 nm.[183] With an increasing number of aromatic benzene rings within the π-system of the axial ligands (L), the extinction coefficient of the π–π* band continuously increases (**Figure A5** and **Figure A6**). According to our calculations and previous reports, the bands between 450 and 500 nm can be explained by Ru-d → bda-π* MLCTs, whereas the higher energetic ones at 350 nm are characteristic for Ru-d → L-π* MLCTs.[314] However, pronounced differences are observed in the UV/Vis absorption spectra for the oxidized macrocycles as it has been substantiated by spectroelectrochemistry in CH_3CN/H_2O 1:1 at pH 1 (**Figure 26**).

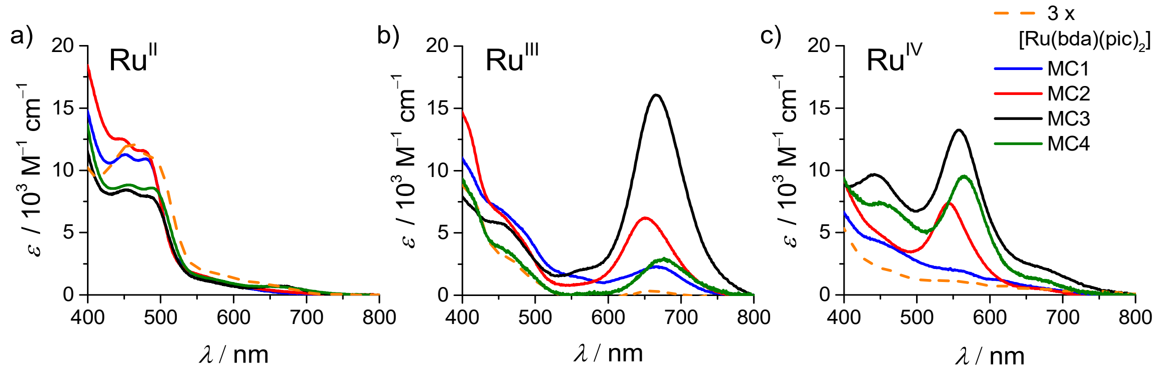

Figure 26: (a) UV/Vis absorption spectra of the $[Ru^{II}|Ru^{II}|Ru^{II}]$ state of **MC1**–**MC3** and $[Ru(bda)(pic)_2]$ in CH_3CN/H_2O 1:1 and of **MC4** in CH_3CN/H_2O 4:1 ($c = 10^{-5}$ M, pH 1, acid: CF_3SO_3H). (b, c) Spectra for the $[Ru^{IV}–OH|Ru^{IV}–OH|Ru^{IV}–OH_2]^{4+}$ (b) and $[Ru^{V}{=}O|Ru^{V}–OH|Ru^{V}–OH]^{5+}$ (c) oxidation states obtained by spectro-electrochemistry for **MC1**–**MC3** and $[Ru(bda)(pic)_2]$ in CH_3CN/H_2O 1:1 and for **MC4** in CH_3CN/H_2O 4:1 ($c = 0.6$–0.7 mM, pH 1, acid: CF_3SO_3H).

Upon increasing the potential from 600 mV to approximately 1000 mV vs. NHE, $[Ru^{II}|Ru^{II}|Ru^{II}]$ becomes gradually oxidized to $[Ru^{III}–OH_2|Ru^{III}–OH_2|Ru^{III}–OH_2]^{3+}$ which is accompanied by drastic spectral changes. The MLCT bands at 350 and 450–500 nm are bleached and new transitions around 670 nm appear, which are absent for the mononuclear reference complex $[Ru(bda)(pic)_2]$. From these measurements it becomes obvious that all Ru centers are oxidized at the same given potential, since the spectral features of Ru^{II} completely disappear. During this oxidation process precipitation occurs for **MC4** in the applied solvent mixture, so that higher contents of acetonitrile (80%) had to be used, making a direct comparison with **MC1**–**MC3** difficult, although the general trends are preserved (**Figure A11**). The extinction coefficients of the low-energy transitions around 670 nm strongly depend on the size of the macrocycle with the most intensive absorption for **MC3**. Further oxidation of **MC1**–**MC3** to $[Ru^{IV}–OH|Ru^{IV}–OH|Ru^{IV}–OH_2]^{4+}$ or **MC4** to $[Ru^{IV}–OH|Ru^{IV}–OH|Ru^{IV}–OH]^{3+}$, by applying potentials of 1200 mV vs. NHE, leads to a decrease of these low-energy absorption bands accompanied by an increase of new hypsochromically shifted transitions centered around 550 nm with the same intensity distribution. The spectral features of the $[Ru^{V}{=}O|Ru^{V}{-}OH|Ru^{V}{-}OH]^{5+}$ species could not be ascertained, since its formation immediately triggers the nucleophilic attack of water, which leads to strong catalytic currents. Detailed analyses of the absorption spectral changes in dependence of the applied potential is provided in the Supporting Information (**Figure A7**–**Figure A11**).

3.1.5 Simulation of UV/Vis Spectra[4]

Due to the strong intensity differences for the low-energy absorption bands of the Ru^{III} and Ru^{IV} states, theoretical simulations were performed within the hybrid QM/MM framework in order to identify the relevant transitions.[268] Similar absorption maxima at higher wavelengths have previously been reported for μ-oxo bridged multinuclear {Ru(bda)} species [183, 315-318] as well as the "blue dimer" *cis,cis*-$[(bpy)_2(H_2O)Ru^{III}ORu^{III}(OH_2)(bpy)_2]^{4+}$ (bpy = 2,2'-bipyridine).[319] For this well investigated catalyst, mixing of nonbonding Ru-d orbitals with p-π orbitals of the μ-oxo bridge was found to cause a significant bathochromic shift of the MLCT transition. DFT calculations further revealed a high solvent dependency due to hydrogen bonding and only under consideration of explicit water molecules a good agreement between experimental and calculated spectra could be obtained.[320] Moreover, Weber *et al.* have shown by photo-dissociation spectroscopy on mass selected catalyst-water clusters in the gas phase that an increasing number of water molecules induces a solvatochromic shift of MLCT bands in ruthenium polypyridine complexes.[194] According to their investigations, solvation of the ruthenium center by seven water molecules seems to be sufficient to approximate bulk solvent behavior.

Indeed, our initial attempts to reproduce the low-energy MLCT around 670 nm of **MC3** in the $[Ru^{III}|Ru^{III}|Ru^{III}]^{3+}$ state in a water box containing only three explicit water molecules failed. Accordingly, we optimized structures of **MC3** in the oxidation states Ru^{III} and Ru^{IV} by systematically increasing the amount of explicit water. Detailed analysis of all structures revealed that the amount of explicit water molecules strongly influences the Ru–OH and RuO–H bond lengths between the ruthenium center and the coordinated aqua or hydroxide ligands (**Figure 27a** and **Figure A12**). Natural transition orbital (NTO) analysis of each

---

[4] These calculations were carried out by Joachim O. Lindner under the supervision of Prof. Roland Mitrić and Dr. Merle I. S. Röhr, Theoretical Chemistry, University of Würzburg

structure provided evidence that the changes of these bond lengths significantly influence the energetic position of the individual MLCT transitions (**Figure 27b**).

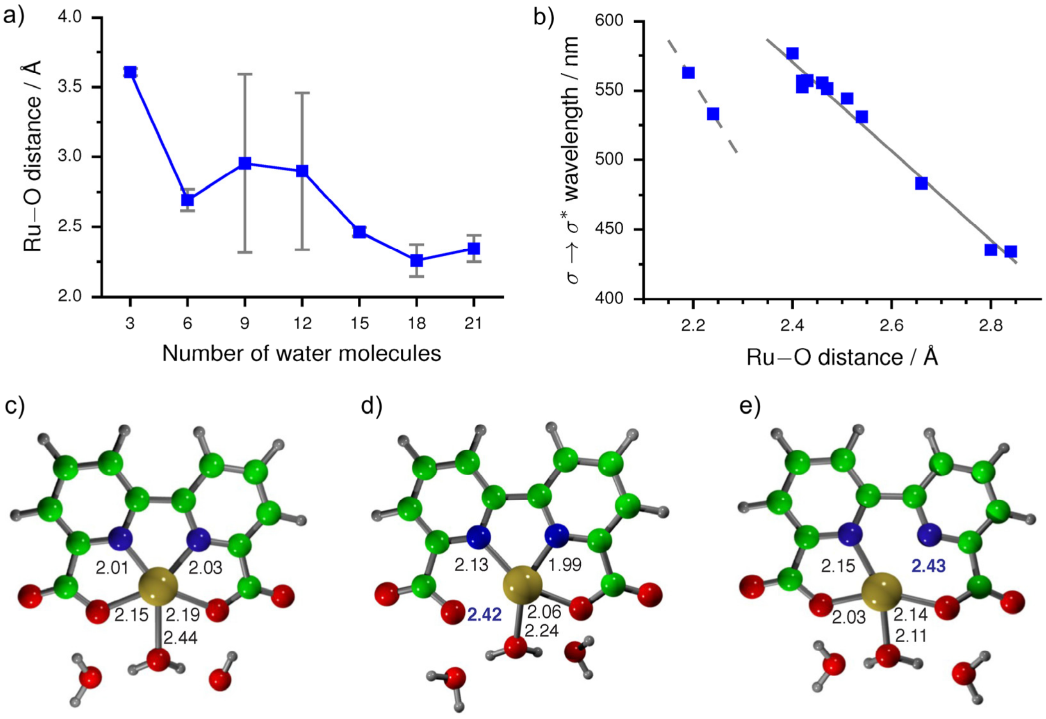

Figure 27: Influence of the amount of explicit water molecules on important properties of **MC3** in the Ru^{III} state. (a) Mean Ru–O distances (blue squares) and standard deviations (error bars) for all Ru centers against the number of explicit water molecules. (b) Wavelength of the {Ru(bda)}-$\sigma \rightarrow$ {Ru(bda)}-σ^* transition against the Ru–O distance (blue squares) and linear regressions for distances > 2.3 Å (solid line) and < 2.3 Å (dashed line). Note that excitations at Ru^{III} centers with Ru–O bond lengths below 2.3 Å occur at unexpected low wavelengths in the spectra due to an induced change in the geometry in the near environment of the Ru atom resulting in an asymmetric bda-ligand. (c–e) Comparison of the symmetric Ru(bda) structure (c) with the asymmetric structures (d and e).

Obviously, the calculated excited state energies are very sensitive towards structural changes and a sufficient number of explicit water molecules has to be taken into account to properly describe important structural rearrangements and fluctuations within the QM/MM framework. Due to the shallow potential energy surfaces of solvated compounds, many geometries are expected to coexist in solution and one single geometry optimized structure might not be sufficient to explain the differences in the experimental spectra. In order to scan the potential energy surface taking structural fluctuations into account, molecular dynamics (MD) has proven to be a valuable tool. Examples from literature have shown that theoretically predicted absorption spectra, even of small molecules like nitrobenzene, are considerably improved by considering a whole ensemble of structures sampled from a molecular dynamics (MD) trajectory.[321] Therefore, QM/MM MD simulations have been performed for complexes [Ru(bda)(pic)$_2$], **MC1**, and **MC3** to correlate structural features with the experimentally observed spectra. Calculations were performed in the oxidation states Ru^{II}, Ru^{III}, and Ru^{IV} with well solvated Ru centers, and 30 structures were sampled from the molecular dynamics trajectories in steps of 50 fs. The averaged ensemble UV/Vis spectra are in good agreement with the experimentally observed absorption maxima and the most relevant transitions that contribute to the low-energy absorption bands, have been identified for each oxidation state (**Figure 28**).

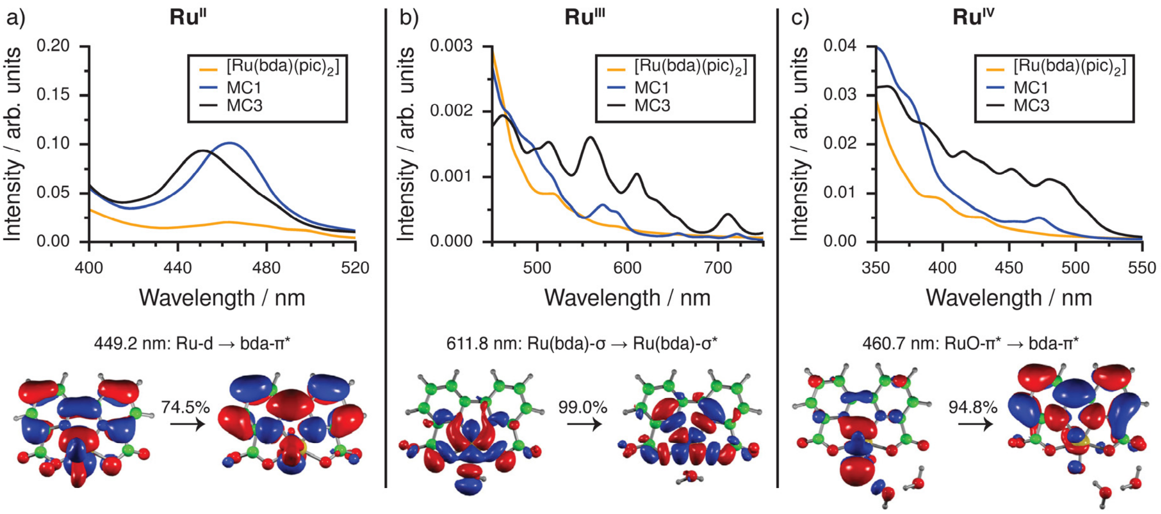

Figure 28: Top: Calculated ensemble spectra in the Ru^{II} (a), Ru^{III} (b), and Ru^{IV} (c) oxidation states of [Ru(bda)(pic)$_2$], **MC1**, and **MC3** obtained from 30 geometries sampled along the MD trajectories. Bottom: NTOs of the low-energy transitions of **MC3** in the respective oxidation states. Only the relevant parts of the molecule are displayed for the sake of clarity (green = carbon, grey = hydrogen, red = oxygen, blue = nitrogen, yellow = ruthenium).

In the Ru^{II} oxidation state, Ru-d → bda-π^* transitions are located at wavelengths around 449 nm whereas the bathochromically shifted absorption maxima at 612 nm in the Ru^{III} state could be attributed to {Ru(bda)}-σ → {Ru(bda)}-σ^* transitions. In the Ru^{IV} oxidation state RuO-π → bda-π^* MLCTs give rise to the low-energy bands at 461 nm. The deviation of less than 0.4 eV of the calculated low-energy transitions from the experimental values is a reasonable accuracy for the applied CAM-B3LYP functional.[322] Thus, the origin of the new absorption bands at longer wavelengths of the higher oxidation states has been ascertained and it has been shown that the solvation of the catalytic center strongly influences the structural parameters as well as the energetic position of the MLCT transitions.

In the Ru^{III} oxidation state, the low-energy absorption at 612 nm is mainly dependent on the Ru–OH bond length which has been sampled for all structures along the MD trajectories and its distribution is depicted in **Figure 29a**. None of the 30 structures of [Ru(bda)(pic)$_2$] exhibits water molecules within a distance of less than 2.5 Å to the Ru center and could thus be considered as strongly coordinated. On the other hand, for the structures of **MC1**, one Ru center is found on the average to be coordinated by a water molecule, whereas in **MC3** even two Ru centers are bound by water molecules in most of the structures. Recent EPR studies on a fully water soluble derivative of [Ru(bda)(pic)$_2$] revealed that in aqueous solution an equilibrium exists between a six-coordinated [Ru^{III}]$^+$ and a seven-coordinated [Ru^{III}–OH$_2$]$^+$ species.[186] In our simulations, we note that the position of this equilibrium is different for each complex. In its most favorable conformation, the 4-picoline ligands of [Ru(bda)(pic)$_2$] with nearly perfectly eclipsed π-surfaces efficiently block the seventh coordination site of the ruthenium center allowing water to coordinate only very weakly. In contrast, the axial bridging ligands of the macrocyclic catalysts are rotationally restricted, readily providing access to the seventh coordination site and thus to a beneficial coordination of water. Since the appearance of {Ru(bda)}-$\sigma \rightarrow$ {Ru(bda)}-σ^* transitions at longer wavelengths is strongly dependent on the Ru–OH bond lengths between the ruthenium centers and the coordinated aqua or hydroxide ligands, these findings rationalize the absence of such low-energy MLCTs for [Ru(bda)(pic)$_2$] in its Ru^{III} state. Likewise, in the Ru^{IV} oxidation state, the positions of the energetically low MLCT bands mainly depend on the Ru–OH and the RuO–H bond lengths.

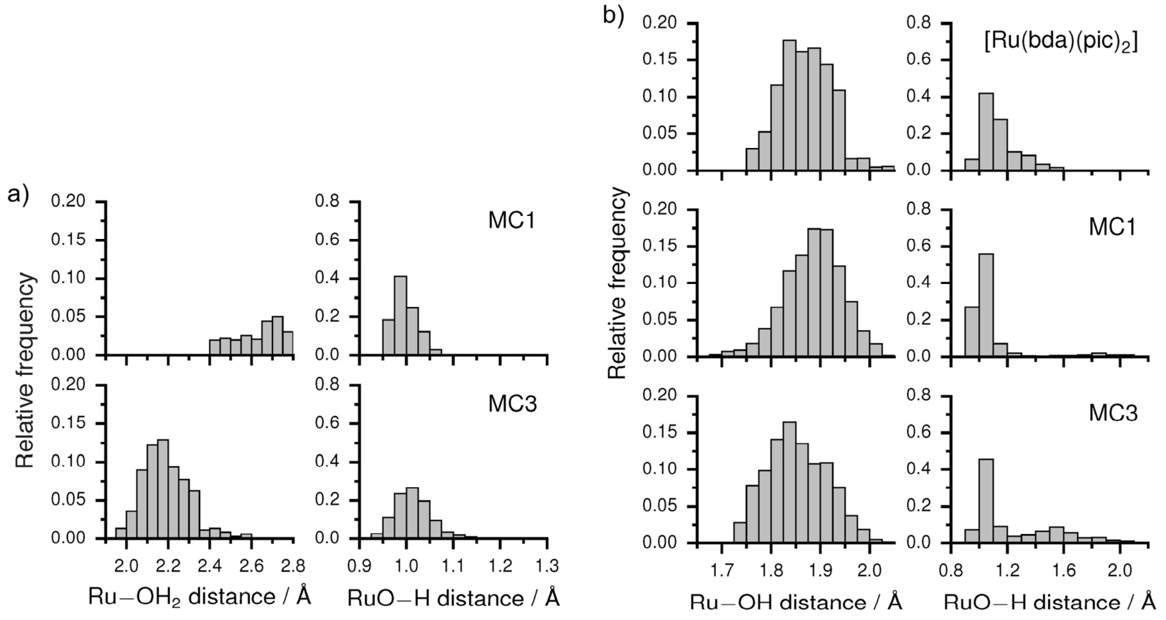

Figure 29: (a, b) Normalized distributions of the Ru–OH and the RuO–H bond lengths of [Ru(bda)(pic)$_2$], **MC1**, and **MC3** obtained by each 30 structures sampled along the MD simulation trajectories: In the Ru^{III} oxidation state (a), and in the Ru^{IV} oxidation state (b). Note that for [Ru(bda)(pic)$_2$] no water molecule was found in a distance < 2.8 Å to the ruthenium in all of the 30 structures for the Ru^{III} state.

During our MD simulations, the Ru^{IV} centers of all complexes are permanently coordinated by hydroxide ligands and the distributions of the bond lengths are displayed in **Figure 29b**. In [Ru(bda)(pic)$_2$], Ru–OH bond lengths are most frequently found between 1.8 and 1.9 Å, while the RuO–H bond length is usually shorter than 1.4 Å. In the smallest macrocycle **MC1**, the distribution of the Ru–OH distances exhibits a maximum at 1.9 Å with a minor amount of shorter bond lengths near 1.7 Å, while the RuO–H distances exceed 1.4 Å only in rare cases. On the other hand, the maximum of the Ru–OH bond lengths distribution of **MC3** is shifted near 1.8 Å, accompanied with a considerable elongation of the RuO–H bonds up to 2.0 Å. These stretched RuO–H bonds account for the appearance of RuO-π → bda-π^* transitions in the Ru^{IV} oxidation state and rationalize the experimentally observed absorption maxima at 550 nm.

Altogether, our MD simulations reveal significant structural differences between the investigated complexes and elucidate the different intensities of the experimentally observed low-energy transitions. The structural diversity is caused by the solvation of the Ru centers which is different for each catalyst and each macrocyclic cavity. For **MC3**, a network of hydrogen-bonded water molecules has been identified inside its cavity resulting in an enhanced hydrogen bonding between the substrate water molecules and the coordinated aqua or hydroxide ligands and therefore in elongated RuO–H as well as shortened Ru–OH bonds. This effect is considerably reduced for **MC1**, since its cavity is not large enough to accommodate the required amount of water molecules. For **MC1**, two Ru centers are oriented towards the catalysts' exterior, being well solvated by water molecules from outside. These two subunits more closely resemble the isolated monomeric reference system without any hydrogen bonding between adjacent reaction centers. The different solvation behavior of the reactive Ru centers is expected to have a major influence on the catalytic activity.

3.1.6 Water Oxidation Catalysis by Differently Sized Macrocycles

In our recent report on the catalytic behavior of **MC3**, we have demonstrated by ^{18}O labelling experiments that this catalyst oxidizes water *via* the "water nucleophilic attack" (WNA) mechanism with the oxidation from a Ru^{IV} to a Ru^{V} species being rate-determining.[93] A simplified mechanistic picture considering only one single Ru center is depicted in equations

10–15, using the strong one-electron oxidant cerium(IV) ammonium nitrate (CAN) as sacrificial electron acceptor to drive the catalysis.[154] Upon oxidation of the initial Ru^{II} state to Ru^{III}, water binds to the seventh coordination site (eq. 10). In a sequence of proton-coupled electron transfer processes, this $Ru^{III}–OH_2$ intermediate is transformed into a $Ru^{V}=O$ species (eq. 11–12), which is nucleophilically attacked by water to form $Ru^{III}–OOH$ (eq. 13). Subsequent oxidation to $Ru^{IV}–O_2$ (eq. 14), and reductive elimination of molecular oxygen (eq. 15) eventually closes the catalytic cycle.

$$Ru^{II} + Ce^{IV} + H_2O \rightarrow Ru^{III}–OH_2 + Ce^{III} \quad (10)$$

$$Ru^{III}–OH_2 + Ce^{IV} \rightarrow Ru^{IV}–OH + Ce^{III} + H^+ \quad (11)$$

$$Ru^{IV}–OH + Ce^{IV} \rightarrow Ru^{V}=O + Ce^{III} + H^+ \quad (12)$$

$$Ru^{V}=O + H_2O \rightarrow Ru^{III}–OOH + H^+ \quad (13)$$

$$Ru^{III}–OOH + Ce^{IV} \rightarrow Ru^{IV}– O_2 + Ce^{III} + H^+ \quad (14)$$

$$Ru^{IV}–O_2 \rightarrow Ru^{II} + O_2 \quad (15)$$

To study the catalytic performance of the new series of trinuclear WOCs (**MC1**–**MC4**), the chemical oxidant CAN has initially been added in large excess to ensure a pseudo-zeroth order for all reaction steps with respect to the CAN concentration. Thus, the catalytic rate should solely depend on the catalyst concentration.[175] After injection of the respective catalyst solution into an acidic CAN solution, immediate formation of gas bubbles could be observed and the pressure increase was measured with pressure transducers (for experimental details and reaction conditions see **chapter 5.1**). Gas chromatographic head space analysis was performed after each run to prove that elemental oxygen is the only gaseous product formed during catalysis, and to confirm the determined turnover numbers (TONs). From the linear part of the first few seconds in pressure increase, the initial reaction rates have been determined. By plotting these rates vs. the amount of catalyst, the rate laws regarding the catalyst concentration as well as the turnover frequencies (TOFs) were obtained. For all experiments acetonitrile was chosen as organic co-solvent because of its strong oxidative resistance and its good miscibility with water. However, it is well known that with increasing amount of acetonitrile the catalytic reaction severely slows down due to competitive binding of acetonitrile to the seventh coordination site of the ruthenium center.[311, 323] Thus, for an optimal catalytic performance the content of acetonitrile should not be higher than absolutely necessary to keep the macrocyclic catalysts and their intermediates in solution.[276] Since the solubility of **MC1**–**MC4** in water strongly deviates from each other due to their different sizes, the catalytic experiments have been performed both under optimized and under comparable solvent compositions (**Table 1**). Whereas the smallest macrocycle **MC1** is soluble in nearly pure water, containing only 2% (*v*/*v*) of acetonitrile as co-solvent, the amount of organic additive required to achieve sufficient solubility rises significantly with increasing ring size. To reach their best performances, 50% and 60% of acetonitrile, respectively, have to be added to the intermediate sized macrocycles **MC2** and **MC3**. The largest macrocycle **MC4** already requires at least 80% of organic co-solvent, and even then concentrations cannot be obtained as high as for the smaller analogues. To still properly compare all catalysts, concentration-dependent water oxidation experiments have been performed for **MC1**–**MC4** with a constant 80% acetonitrile content (**Figure 30** and **Figure A14**–**Figure A17**).

Table 1: Catalytic activity and kinetic isotope effects of the macrocyclic WOCs **MC1**–**MC4**.

Method	**CH_3CN content**	**MC1**		**MC2**		**MC3**		**MC4**	
		TOF / s^{-1}	TON	TOF / s^{-1}	TON	TOF / s^{-1}	TON	TOF / s^{-1}	TON
Ce(IV)-driven Catalysis [a]	2%	38	2500	–	–	–	–	–	–
	50%	–	–	70	3240	–	–	–	–
	60%	–	–	–	–	150	7400	–	–
	80%	0.3	660	1.6	680	7.9	3590	3.8	1810
Light-driven [b]	50%	0.56	61 [d]	3.1	130 [d]	5.3	440 [d]	5.3	350 [d]
H/D KIE [c]	50%	1.2		1.5		2.8		1.8	

a) (CH_3CN/H_2O mixtures, pH 1, acid: CF_3SO_3H, [CAN] = 0.53 M, [cat] = 10–240 μM), measured with pressure transducers; **b)** (CH_3CN/H_2O 1:1 mixture, pH 7.2, buffer: phosphate, $[[Ru(bpy)_3]Cl_2]$ = 1.5 mM, $[Na_2S_2O_8]$ = 37 mM, [cat] = 0.5–5 μM) measured with a Clark-electrode; **c)** (CH_3CN/H_2O 1:1 and CH_3CN/D_2O 1:1 mixtures, pH 1, acid: CF_3SO_3H, [CAN] = 0.53 M, [cat] = 10–20 μM), measured with a Clark-electrode; **d)** Note that the TONs are limited by the stability of $[Ru(bpy)_3]^{2+}$.

A linear dependency of the reaction rate on the amount of catalyst is obtained for all macrocycles within the first 50 s of the catalytic reaction. In such linear cases, the slope of the linear regression represents the turnover frequency of the individual catalyst. On the other hand, a quadratic dependency on the catalyst concentration is observed for the mononuclear reference $[Ru(bda)(pic)_2]$, which is in line with its well-established bimolecular reaction mechanism (**Figure A18**).[64] The best performance is obtained for the catalyst **MC3** (TOF = 7.9 s^{-1}, TON = 3590) with TONs and TOFs being one order of magnitude higher compared to the smallest macrocycle **MC1** (TOF = 0.3 s^{-1}, TON = 660). The other two catalysts **MC2** (TOF = 1.6 s^{-1}, TON = 680) and **MC4** (TOF = 3.8 s^{-1}, TON = 1810) are intermediate representatives. The activity of the mononuclear complex $[Ru(bda)(pic)_2]$ is in the same range (TOF = 0.09–1.17 s^{-1}, TON = 450) as the slowest macrocyclic catalyst, however, operating *via* a different mechanism. Apparently, the size of the metallosupramolecular macrocycles **MC1**–**MC4** has an enormous influence on their activity in catalytic water oxidation (*vide infra*). The catalytic performance of the more soluble macrocycles **MC1**–**MC3** was further investigated under the respectively optimized solvent compositions mentioned above. Maximal TOFs of 38 s^{-1}, 70 s^{-1}, and 150 s^{-1} as well as TONs of 2500, 3240, and 7400 have been measured for the catalysts **MC1**–**MC3**, respectively (**Figure A19**–**Figure A21**). All catalysts are active for more than one hour, and gas chromatographic analysis of the head space at the end of each catalytic reaction confirms that the measured pressure increase is solely due to the formation of oxygen. Interestingly, macrocycle **MC3** exhibits also the best performance under the optimized solvent composition, although higher amounts of acetonitrile as co-solvent are required compared to its smaller analogues.

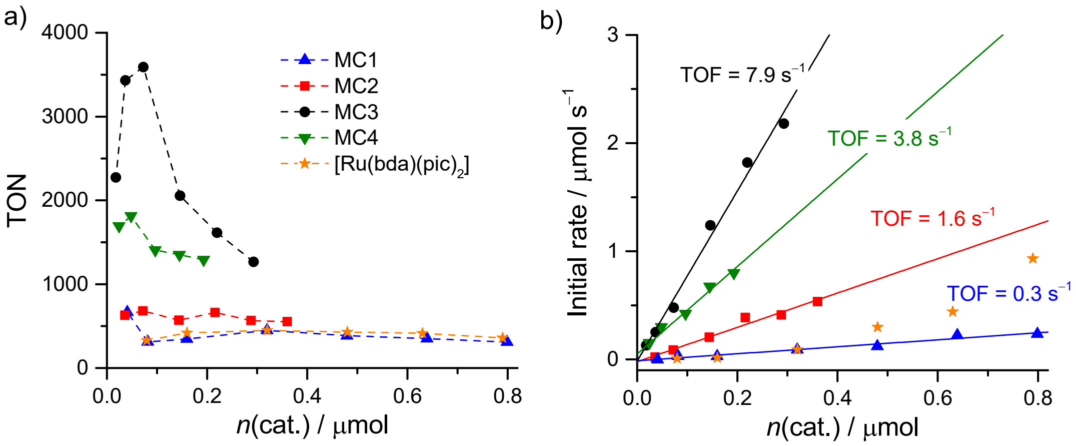

Figure 30: (a, b) Water oxidation experiments using the catalysts **MC1**–**MC4** and [Ru(bda)(pic)$_2$] at various concentrations for the determination of the respective TONs (a) and TOFs (b). The measurements were performed using cerium(IV) ammonium nitrate as sacrificial oxidant and pressure transducers for the oxygen detection (1.0 g CAN was dissolved in 3.0 mL CH_3CN/H_2O (pH 1, CF_3SO_3H) 4:1, 400 µL of the catalyst solution in the same solvent mixture were injected).

Additional kinetic experiments have been performed using stoichiometric amounts of CAN to gain further insights into the mechanism of water oxidation. Under those conditions, the concentration of the oxidant cannot be neglected anymore and all oxidative steps in the reaction sequence should exhibit a first order dependence on its concentration. Furthermore, far less oxygen should be evolved which is why the previously described setup reaches its detection limit. Therefore, UV/Vis spectroscopy has been used to study the consumption of CAN during the water oxidation reaction. Cerium(IV) ammonium nitrate was dissolved in a CH_3CN/H_2O (pH 1) 1:1 mixture, and after addition of the catalysts, the decay of the characteristic CAN absorption band at 360 nm was monitored over time. By applying Lambert-Beer's law the corresponding concentration changes have been calculated. The dependence of the reaction rates on the concentrations of both, catalysts and oxidant, was studied with two different types of experiments. First, the CAN concentration was kept constant and only the respective catalyst concentration has been varied (**Figure 31a** and **Figure A22–Figure A26**). In a reversed series of measurements, the concentrations of the catalysts were kept constant, while the CAN concentration has been varied (**Figure 31b** and **Figure A27–Figure A31**). For all macrocyclic catalysts **MC1–MC4** a linear dependence of the initial reaction rate on the catalyst concentration was observed. In contrast, the reference complex [Ru(bda)pic$_2$] exhibits a quadratic dependence (**Figure A22**), as it has already been shown in previously described experiments using CAN in large excess. For this mononuclear catalyst, the O–O bond formation is known to proceed *via* the coupling of two ruthenium oxyl radicals in the rate-determining step.[152] Since this process does not involve any further oxidation, the reaction rate of [Ru(bda)pic$_2$] does not depend on the oxidant concentration as it has been proven by varying the amount of CAN (**Figure A27**). All macrocycles, however, exhibit a linear dependence of the reaction rate on the CAN concentration. Consequently, an oxidation step has to be rate-determining for those metallosupramolecular catalysts, as it has previously been investigated in great detail for **MC3**.[93]

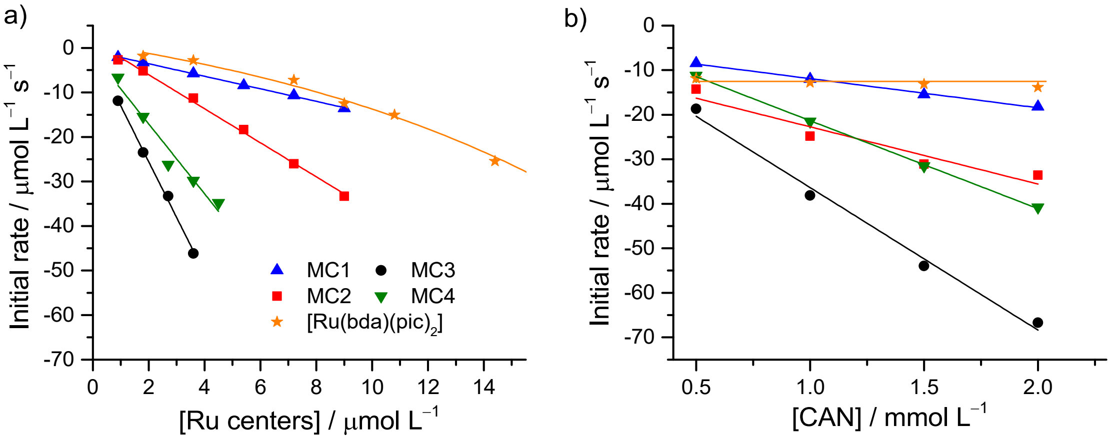

Figure 31: (a, b) Water oxidation experiments at stoichiometric CAN conditions investigated by the consumption of CAN by monitoring the corresponding UV/Vis absorption at 360 nm (measured in CH_3CN/HNO_3 1:1 (pH 1, acid: HNO_3). (a) Variation of the catalyst concentration with fixed CAN concentration (2.0 mM). (b) Variation of the CAN concentration with fixed catalyst concentration (3 µM for **MC1**–**MC4** and 9 µM for [Ru(bda)(pic)$_2$]).

Based on this information, redox titration experiments using the one-electron oxidant CAN have been performed and the absorption spectral changes were monitored by UV/Vis spectroscopy (**Figure A32–Figure A36**). Upon the successive addition of oxidant in portions of one equivalent per macrocycle, a stepwise oxidation of all ruthenium centers from Ru^{II} to Ru^{III} occurs. After addition of three CAN equivalents, the oxidation processes are completed and the respective low-energy transitions at approximately 670 nm reach their maxima. Subsequent addition of another three CAN equivalents leads to spectra that are characteristic for the Ru^{IV} state, without Ru^{III} absorptions present anymore. Any further addition of oxidant does not result in significant spectral changes, indicating that for all macrocycles the resting state is a Ru^{IV} species, with the Ru^{IV}/Ru^{V} oxidation being rate-determining. Altogether, we have proven that **MC1**–**MC4** catalyze water oxidation following the WNA mechanism, in which the O–O-bond formation proceeds *via* the nucleophilic attack of water at a Ru^{V}=O species.

To verify that the metallosupramolecular macrocycles are the actual catalysts, post-catalytic analysis has been performed on reaction mixtures using MALDI-ToF mass spectrometry (**Figure A37**–**Figure A40**). Therefore, 128 equivalents of CAN (corresponding to 32 catalytic cycles) were added to the respective catalyst solutions in CH_3CN/H_2O (pH 1) 4:1, and all samples were reduced with ascorbic acid after the gas evolution had ceased. In all cases, the macrocycles are still present and give rise to the most prominent peaks in most of the mass spectra. Furthermore, minor fragmentation can be observed by the loss of one bridging ligand, which is known to be the main degradation pathway.[168] However, it seems to be most likely that fragmentation occurs within the mass spectrometer because only coordinatively unsaturated ruthenium centers could be detected. If the fragmentation would already occur during catalysis, coordination of acetonitrile should take place, which would result in appropriate mass signals. The macrocycle **MC4** itself is hardly ionizable, for what reason high laser intensities had to be applied, resulting in a pronounced fragmentation behavior and a noisy baseline (**Figure A40**).

3.1.7 Photocatalysis

To use water as a feedstock for a sustainable economy, it is inevitable to replace the sacrificial chemical oxidant CAN by other environmentally friendly energy sources, most preferentially sunlight. Therefore, a good interaction of the catalyst with the respective photosensitizer has to be guaranteed. To address this requirement, we performed light-driven water oxidation experiments replacing CAN by the much milder oxidant $[Ru(bpy)_3]^{3+}$,[154-156] which is photo-generated in situ from the photosensitizer $[Ru(bpy)_3]^{2+}$ in the presence of $Na_2S_2O_8$ as sacrificial electron acceptor (**Figure 32**).[159]

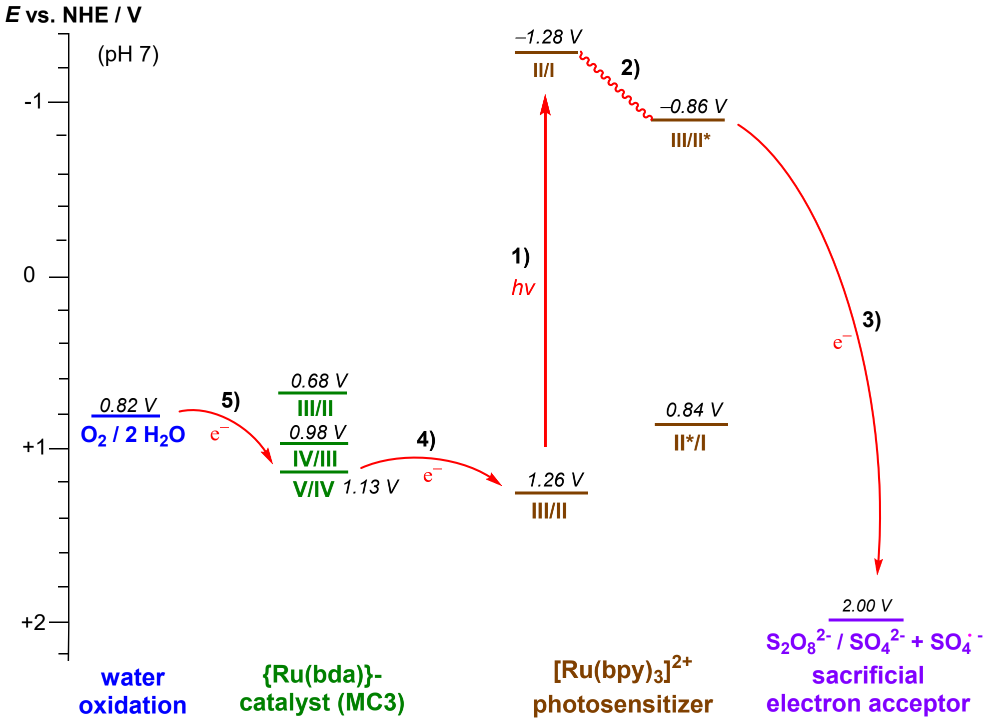

Figure 32: Schematic representation of the major processes (1–5) involved in the light-driven water oxidation using a three component system based on **MC3** as water oxidation catalyst,[93] $[Ru(bpy)_3]^{2+}$ as photosensitizer,[156, 324] and NaS_2O_8 as sacrificial electron acceptor.[154]

All processes involved in the light-driven water oxidation using this three component system (1–5) are schematically represented in **Figure 32**, and the important redox potentials under neutral conditions (pH 7) have been included. The required potential to oxidize water is pH-dependent and can be calculated using the Nernst equation.[325] For the construction of this scheme, **MC3** was chosen as the catalyst. The potentials for its redox couples have been extracted from the respective Pourbaix diagram (**Figure A3**). After excitation of $[Ru(bpy)_3]^{2+}$ (1), a quick relaxation to the ^{3}MLCT state occurs (2).[156, 324] From this excited state an electron is transferred to the sacrificial electron acceptor $S_2O_8^{2-}$ (3), leading to the generation of $[Ru(bpy)]^{3+}$.[154] This oxidized photosensitizer is now capable to subsequently oxidize the catalyst (4). The sequence has to proceed repeatedly before the catalyst reaches the Ru^V oxidation state, which is responsible for water oxidation (5).

The experiments were performed concentration-dependent for each catalyst, whereas all other factors such as the solvent composition or the concentrations of $Na_2S_2O_8$ and $[Ru(bpy)_3]Cl_2$ were kept constant (**Figure A41–Figure A44**). Irradiation was performed with a Xenon lamp and a Clark electrode was used for oxygen detection. All components were dissolved in the dark in a CH_3CN/H_2O (pH 7.2, buffer: phosphate) 1:1 mixture. No oxygen evolution is detected in the dark, but immediately after light exposure, generation of molecular oxygen is observed (**Figure 33a**). Likewise, these photocatalytic experiments exhibit first order reaction rates with respect to the catalyst concentrations (**Figure 33b**). However, this behavior is only valid for low catalyst concentrations with oxygen evolution rates below 4–5 nmol s^{-1}, as the photo-generation of the oxidant $[Ru(bpy)_3]^{3+}$ becomes rate-determining above this limit (**Figure A44**).[72, 326]

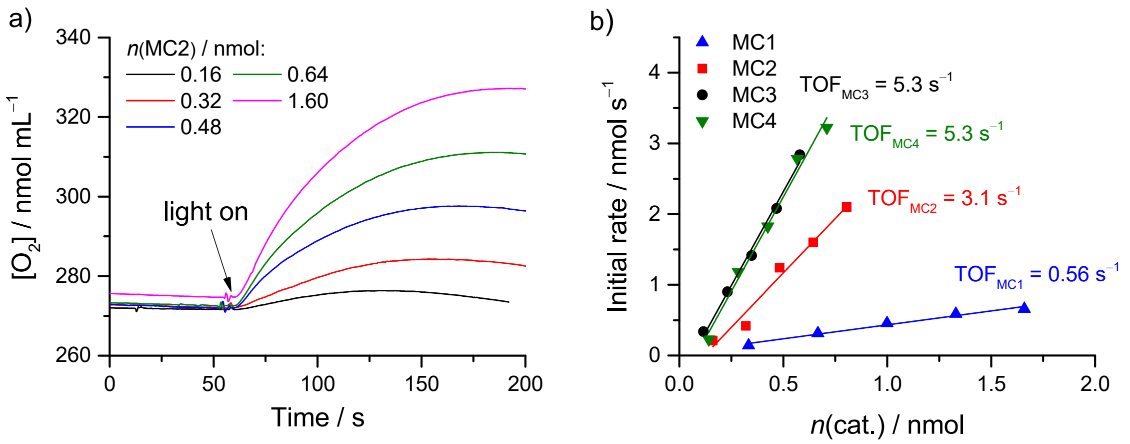

Figure 33: (a) Photocatalytic oxygen evolution using **MC2** as catalyst at various concentrations. (b) Plot of the initial reaction rates vs. the amount of catalysts for **MC1**–**MC4** and the linear regressions for the determination of TOFs. (2.0 mL CH_3CN/H_2O (pH 7.2, buffer: phosphate) 1:1, $[Na_2S_2O_8]$ = 37 mM, $[[Ru(bpy)_3]Cl_2]$ = 1.5 mM; $\lambda_{irr} > 380$ nm, 230 mW/cm^2).

Therefore, the turnover frequencies were determined for concentrations with catalytic rates below this threshold, for which a linear regression can be realized. Under these conditions, similar trends are observed for the catalytic activities of **MC1**–**MC4** like in the CAN driven experiments described before. The highest activities have been measured for the larger macrocycles **MC3** and **MC4**, which both exhibit TOFs of 5.3 s^{-1}, with **MC1** being again one order of magnitude slower (**Table 1**).[5] Although the tendency of the respective TONs is in principle the same, the absolute values are significantly lower compared to the chemical water oxidation using CAN, which can be explained by the limited stability of the photosensitizer.[327] Despite that, all catalysts are highly active under these photocatalytic conditions, since TOFs below 1 cycle s^{-1} are usually found for most homogenous metalorganic photo-catalysts.[161]

---

[5] In our previous publication (ref. [93]) a TOF of 13.1 s^{-1} was reported for **MC3**. This discrepancy is presumably due to contamination of the Clark electrode or intensity fluctuations of the light source.

3.1.8 H/D Kinetic Isotope Effects

The observed rate laws for water oxidation, in combination with the oxidative UV/Vis titration experiments, revealed that for all macrocycles **MC1**–**MC4** the oxidation from Ru^{IV} to Ru^{V} is rate-determining, as it has been described for previously reported polypyridine water oxidation catalysts.[131, 147, 312] Using electro-chemistry at different pH values, this step was found to be proton-coupled for all macrocycles under acidic conditions. Chemical reactions in which an element-hydrogen bond breaking is involved in the rate-determining step are characterized by different reaction rates regarding their protonated and deuterated isotopes, respectively. If the ratio of this H/D kinetic isotope effect exceeds the value of two, a direct covalent bond breaking or forming is usually involved.[65, 73, 131]

Therefore, we performed the catalytic water oxidation experiments in both normal and heavy water to get insights into the rate-determining step and its proton coupling (**Figure A45**–**Figure A48**). All catalysts were tested under the same reaction conditions in a CH_3CN/H_2O 1:1 mixture (pH 1, acid: CF_3SO_3H) using cerium(IV) ammonium nitrate (CAN) as sacrificial oxidant and a Clark-electrode for O_2 detection. From the slopes of the oxygen evolution curves, the initial rates of the catalysis have been determined. Plotting these rates against the catalyst concentrations allows the determination of the corresponding reaction rates (k_{H_2O} and k_{D_2O}). Similar tendencies are obtained for their activities like in the water oxidation experiments described above, with a clear optimum for **MC3** and the lowest activity for **MC1**. Accordingly, strong differences are also found in the kinetic isotope effects, which were calculated from the different reaction rates using H_2O and D_2O as the solvent. The most active catalyst **MC3** exhibits the highest KIE with a value of 2.8, whereas only a very low KIE of 1.2 is obtained for the least efficient catalyst **MC1**, with **MC2** and **MC4** being in between (**Figure 34** and **Table 1**). Such different values indicate that the degree of proton coupling is different for each macrocycle in the rate-determining step, and that the overall catalytic rate depends on the proton abstraction during the oxidation from Ru^{IV}–OH to Ru^{V}=O. It is well established that even small structural changes in relatively simple systems can result in substantial changes of the proton coupling and thus in the KIE, since the proton transfer efficiency strongly depends on the right structural orientation and distance between the donor and acceptor side.[328, 329]

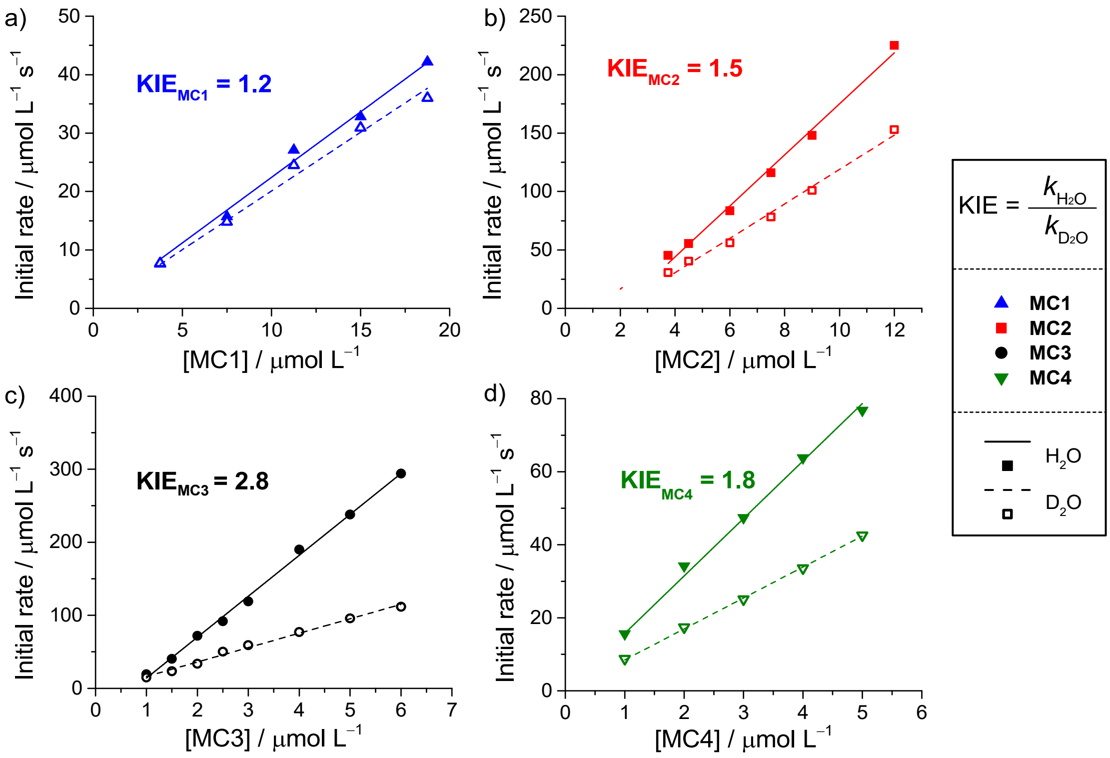

Figure 34: (a–d) Kinetic isotope experiments for the catalysts **MC1**–**MC4**. Plot of the initial catalytic rates vs. the catalyst concentration with the corresponding linear regression fits to determine the reaction rates k_{H2O} and k_{D2O} (Measured with a Clark electrode in 2.0 mL aqueous pH 1 solutions (H_2O or D_2O) with 50% acetonitrile as co-solvent using CAN (0.525 M) as a sacrificial oxidant).

In principle, there are three extreme cases how the Ru^{IV}–OH species can be converted into Ru^{V}=O intermediates (**Figure 35**).[273, 274, 330, 331] Under the applied acidic reaction conditions pathway **A** should not be of relevance since substrate water deprotonation is less favored. The other two extrema are characterized by an initial oxidation followed by subsequent deprotonation (**B**), or a simultaneous proton-coupled electron transfer process (**C**). The relatively small KIEs of **MC1**–**MC4** suggest that the investigated PCETs are not fully concerted, but somewhere in between the extreme cases **B** and **C**.[332, 333] Apparently, the proton-coupled oxidation of **MC3** from Ru^{IV}–OH to Ru^{V}=O is rather concerted with the highest KIE value of 2.8, whereas those of the other macrocycles proceed more stepwise.

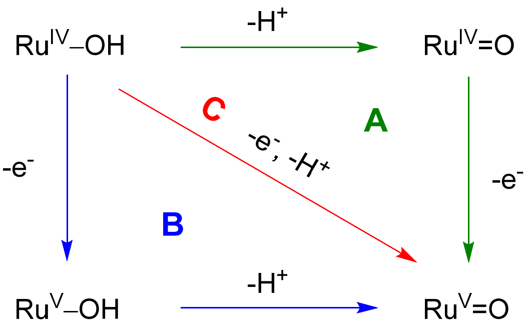

Figure 35: The three extreme pathways for the conversion from Ru^{IV}–OH to a Ru^{V}=O species.

3.1.9 Mechanistic Investigations by Molecular Dynamics Simulations[6]

To fully understand the different activities of the macrocyclic catalysts, all proton-coupled oxidation processes of **MC3** and the mononuclear reference complex [Ru(bda)(pic)$_2$] have been investigated by QM/MM molecular dynamics simulations.[202, 204, 205] Therefore, the complexes were integrated into a box of water which is described by molecular mechanics (MM) containing a certain number of explicit water molecules. These water molecules were placed in close proximity to the catalytically active ruthenium centers and were fully described quantum-mechanically (QM). First, we have calculated the oxidation potential of Ce^{IV} and the ionization potentials of the different ruthenium oxidation states to verify that cerium(IV) has a sufficient oxidation strength. Next, starting geometries have been optimized for every oxidation state of the catalytic cycle and one electron for [Ru(bda)(pic)$_2$] and three electrons for **MC3** have been removed from each of those structures. The subsequent proton release from the catalysts to the explicit water molecules has finally been monitored by MD simulations. The experimentally established PCETs of **MC3** are well reproduced by our calculations. After oxidation from [Ru^{II}|Ru^{II}|Ru^{II}] to [Ru^{III}|Ru^{III}|Ru^{III}]$^{3+}$, water coordinates to the ruthenium centers without any proton transfer to adjacent water molecules (**Figure A49**). After removal of another three electrons, a reduction of the Ru–OH bond lengths can be observed in the MD simulations which is accompanied by the release of two protons after 1100 fs and 1600 fs (**Figure A50**). Likewise, the abstraction of only two protons could be observed after removal of further three electrons from a predefined [Ru^{IV}–OH|Ru^{IV}–OH|Ru^{IV}–OH]$^{3+}$ species, giving rise to the same odd 3e^{-}/2H^{+} PCET experimentally determined by pH-dependent differential pulse voltammetry (**Figure 36**). Within this process, two of the RuO–H bonds become elongated after very short time, whereas the third one remains unaffected during the whole simulation, although several neighboring water molecules are present to further transfer the released proton.

---

[6] These calculations were carried out by Joachim O. Lindner under the supervision of Prof. Roland Mitrić and Dr. Merle I. S. Röhr, Theoretical Chemistry, University of Würzburg

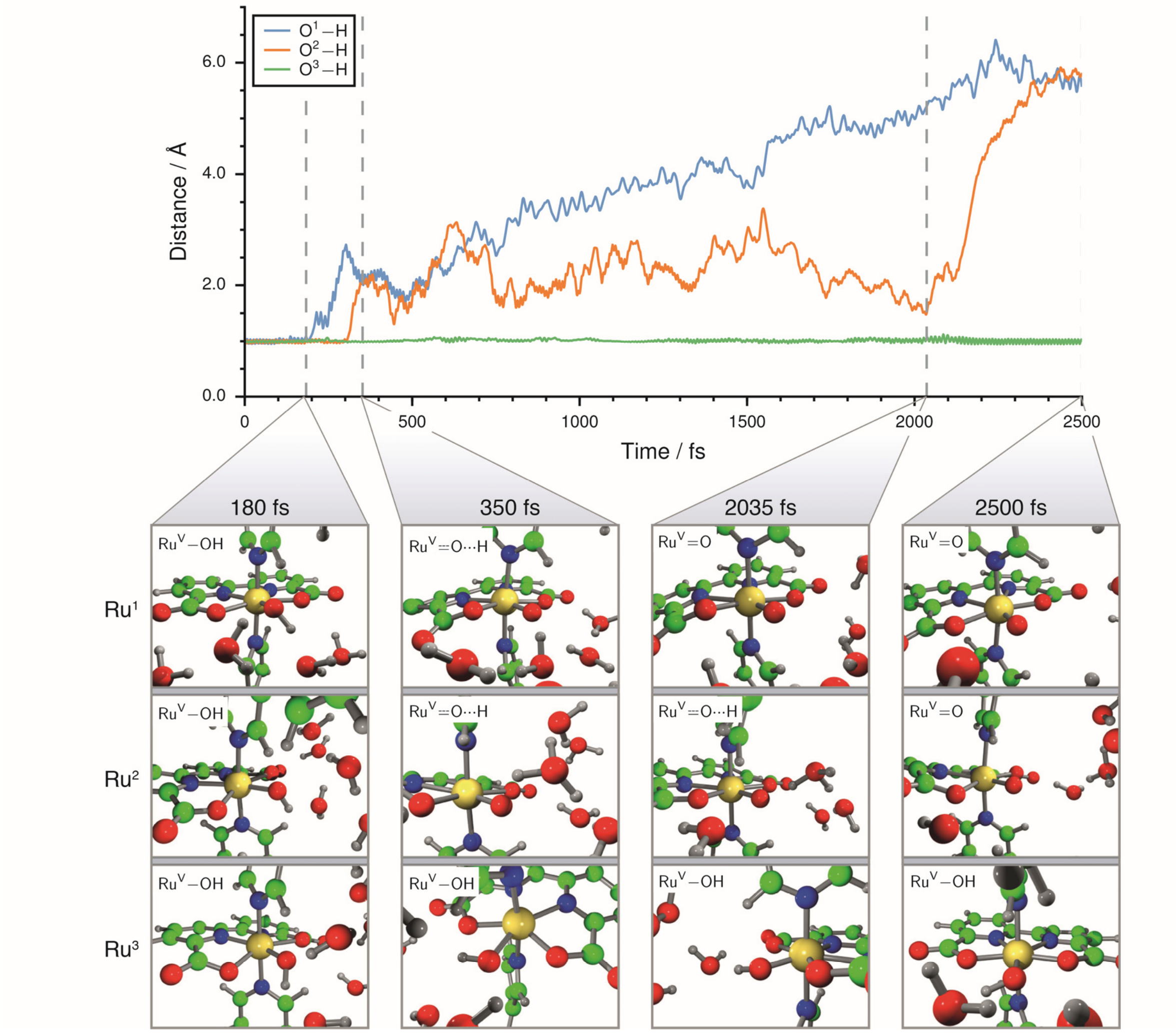

Figure 36: Evolution of the RuO–H bond lengths in the MD simulation after the oxidation from Ru^{IV} to Ru^{V} of **MC3**. For several key time steps, snapshots of the three ruthenium centers (Ru^1, Ru^2, Ru^3) are given below. Hydrogen atoms are denoted as bonded with distances < 1.4 Å, weakly coordinated with distances > 1.4 Å and < 2.5 Å, and non-bonded with distances > 2.5 Å (green = carbon, grey = hydrogen, red = oxygen, blue = nitrogen, yellow = ruthenium).

In the case of the monomeric [Ru(bda)(pic)$_2$], the first oxidation to $[Ru^{III}]^+$ also leads to the coordination of water (**Figure A52**). However, the coordination is much weaker compared to **MC3** due to the sterical crowding of the axial 4-picoline ligands which partially block the seventh coordination site in their preferential orientation (*vide infra*). The subsequent two oxidation events exhibit $1e^-/H^+$ PCETs generating $[Ru^{IV}–OH]^+$ and $[Ru^{V}=O]^+$, respectively (**Figure A53–Figure A54**). After removing three electrons from the default $[Ru^{V}=O|Ru^{V}=O|Ru^{V}=O]^{3+}$ species of **MC3** and one electron from the $[Ru^{V}=O]^+$ species of the reference complex, O–O bond formation takes place in both cases by the nucleophilic attack of water, which is accompanied by the release of one proton. Ultimately, a change from singlet to triplet state enables the second proton transfer and liberation of elemental dioxygen (**Figure A51** and **Figure A55**).[70, 196] Note that the bimolecular coupling pathway is not possible in our simulations for [Ru(bda)(pic)$_2$], because only one single catalyst molecule has been included in the calculations. Most interestingly, our simulations reveal that the released protons are cooperatively stabilized by a well-defined hydrogen bonding water network bridging the Ru centers inside the macrocyclic cavity of **MC3** (**Figure 37**). This cooperative effect is characteristic for the different catalytic activities of **MC1**–**MC4**, because the dimension and the geometry of the macrocycle interior should crucially affect the hydrogen-bonded water network.

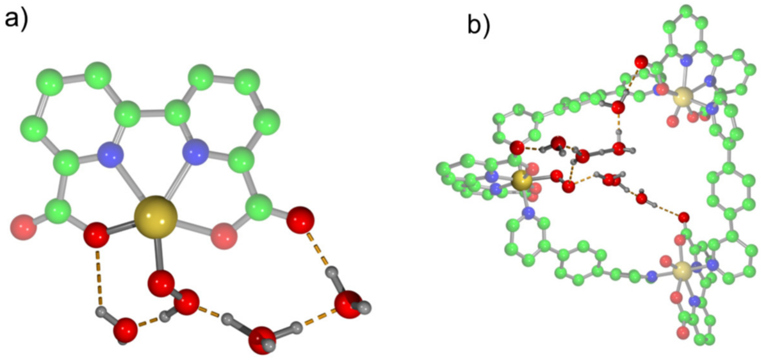

Figure 37: (a, b) Depiction of hydrogen bonding networks in the O–O bond formation step after the first proton abstraction for [Ru(bda)(pic)$_2$] (a) and **MC3** (b). C-bound hydrogen atoms and pic-ligands are omitted for clarity. Only relevant water molecules are displayed (green = carbon, grey = hydrogen, red = oxygen, blue = nitrogen, yellow = ruthenium).

Therefore, the critical oxidation from Ru^{IV} to Ru^{V} was investigated in an analogous way for the macrocyclic catalysts **MC1** and **MC2**. In all three macrocycles, proton abstraction is observed at only two Ru–OH subunits. Unfortunately, in a system with multiple reaction centers and a large number of explicit water molecules, proton transfer cannot simply be traced by considering the solvent in close proximity to the ruthenium centers.[334] Instead, we defined dynamic proton delocalization cavities as a new dimension to measure the capability of specific protons to move between the individual reaction centers during our MD simulations. The number of bonded hydrogen atoms was determined for each oxygen atom in time steps of 5 fs, applying a threshold of 1.25 Å. If the final number adds up to at least three for water molecules and one for carboxylic substituents, a defined volume element has been added to the cavity at the position of the respective oxygen atom to visualize proton movement during the simulation. In **Figure 38**, the dynamic proton delocalization cavities of **MC1** and **MC3** are depicted. The protons that are released at both Ru–OH subunits of **MC1** are well separated from the other reaction centers and remain localized at solvent molecules in vicinity to the oxygen atom from which they have initially been released. Apparently, two ruthenium binding sites of the small macrocycle are oriented to the exterior which efficiently prevents a cooperative stabilization of the released protons inside the macrocyclic cavity. The third Ru–OH group does not get into contact with solvent water molecules because it is trapped in between the carboxylic groups of the other two {Ru(bda)} subunits. In contrast, all three catalytic centers of **MC3** are pointing into its cavity and the proton transfer appears to be completely different. The two released protons are attracted by the carboxylic groups from the third {Ru(bda)} moiety, resulting in a dynamic proton delocalization cavity that is located inside the void of the macrocycle. Thus, the third {Ru(bda)} subunit cooperatively facilitates the proton abstraction from the reactive centers by involving its carboxylate substituents, which are known to act as proton acceptors.[199]

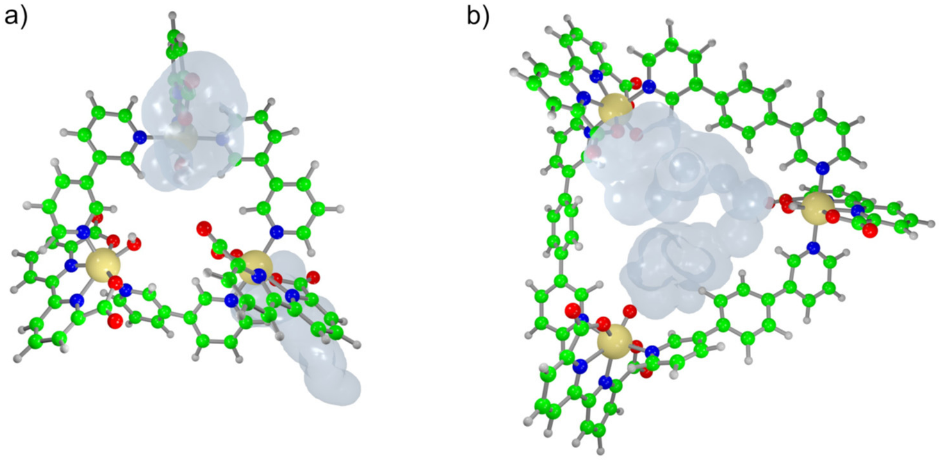

Figure 38: (a, b) Dynamic proton delocalization cavities of **MC1** (a) and **MC3** (b) calculated based on the reaction MD from $\mathrm{Ru^{IV}}$ to $\mathrm{Ru^{V}}$ in the time interval from 0 to 1715 fs. The given structures are taken from the last simulation step. The solvent is not displayed for clarity.

Recent DFT calculations on the "blue dimer" revealed that proton relays are highly important for the operation of multinuclear WOCs, and that the activation barriers of PCETs are mainly dependent on the structural reorganization of the hydrogen-bonded water network. Therefore, similar to the situation in many enzymes an appropriate preorganization of water molecules as proton relays in **MC3** lowers crucial activation barriers and accelerates water oxidation.[195-197] In the case of **MC2**, the dynamic proton delocalization cavity exhibits characteristics of both extreme cases, more closely resembling **MC1** than **MC3** (**Figure A56**), which is in good agreement with its intermediate catalytic activity. Our MD simulations demonstrate that cooperative effects facilitate proton abstraction in the rate-determining step and explain the enhanced catalytic activity of **MC3.**

3.1.10 Conclusion

A series of trinuclear {Ru(bda)} macrocycles with varying ring sizes has successfully been synthesized using ditopic bridging ligands of different lengths. A distinct size dependence was observed for their catalytic activities in chemical water oxidation, and all our experiments revealed the smallest macrocycle **MC1** to be least catalytically active, whereas the medium-sized macrocycle **MC3** exhibits the best performance (**Table 1**). For all supramolecular WOCs, the catalytic rate of water oxidation depends linearly on the catalyst and oxidant concentration. The resting states of the catalysis are Ru^{IV}–OH species with the oxidation from Ru^{IV} to Ru^{V} being rate-determining. Consequently, the O–O bond formation steps presumably proceed *via* the WNA mechanism like it has previously been proven for **MC3** by ^{18}O labelling experiments.[93] Most interestingly, the catalytic activities are reflected in the magnitude of the H/D kinetic isotope effects (KIE), with a KIE of 2.8 for **MC3** and a negligible KIE of 1.2 for **MC1**. The KIE values are related to the quality of the hydrogen-bonded water network inside the macrocyclic cavities and a high degree of proton coupling in the rate-determining Ru^{IV}–OH to Ru^{V}=O oxidation is beneficial for the catalytic activity.

Molecular dynamics simulations revealed that the rigid cyclic structures of **MC1**–**MC4** provide better access to the seventh coordination site of the {Ru(bda)} fragment than the flexible mononuclear complex $[Ru(bda)(pic)_2]$, facilitating substrate water binding. Theoretical examination of relevant proton-coupled oxidation processes of **MC1** and **MC3** provided evidence that each {Ru(bda)} center in **MC1** catalyzes water oxidation solitary due to steric constraints that force the {Ru(bda)} centers to be partially oriented to the exterior. For the larger compound **MC3**, cooperative effects between the individual ruthenium centers have been substantiated with an extended hydrogen-bonded water network inside the macrocyclic cavity, acting as efficient proton relay between the catalytic subunits. The abstracted protons are therefore stabilized and can be quickly removed from the reactive centers giving rise to more concerted proton-coupled electron transfer processes with a high experimental KIE value. Interestingly, the intensities of the low-energy absorption bands of the Ru^{III} and Ru^{IV} states of the macrocyclic WOCs mirror the catalytic activity and the KIE and can thus be used to estimate the catalytic performance. DFT calculations disclosed the nature of these transitions and molecular dynamics simulations revealed that the energetic positions of these bands are highly dependent on the Ru–OH and the RuO–H bond lengths. These bonds are mainly influenced by the degree of hydrogen bonding between the aqua or hydroxide ligands and the water molecules inside the macrocyclic cavity, and thus strongly depend on the size of the macrocycle itself. Accordingly, we have shown that the incorporation of catalytically active {Ru(bda)} fragments into trinuclear metallosupramolecular macrocycles may result in new and beneficial cooperative effects similar as found in many natural catalysts (enzymes, natural oxygen evolving cluster, etc.) that rely on specific networks of water molecules in the vicinity of catalytic sites. By tuning the size of the macrocyclic cavity, the inner hydrogen bonding water network bridging the reactive {Ru(bda)} centers could be manipulated specifically to increase the catalytic activity. Based on these results we assume that the modification of the macrocyclic interior by endo-functionalization of the bridging ligands is a promising approach to further improve such metallosupramolecular water oxidation catalysts.

3.2 Trinuclear Ruthenium Macrocycles: Towards Supramolecular Water Oxidation Catalysis in Pure Water [7]

3.2.1 Water Solubility of Trinuclear Macrocycles

Incorporating the {Ru(bda)} fragment into large metallosupramolecular structures significantly decreases the solubility in water. Thus, acetonitrile is required as organic co-solvent to perform catalytic water oxidation studies. From a green chemistry perspective this is highly undesired, since acetonitrile is regarded to be a non-eco-friendly solvent, especially compared to water.[335] Therefore, we intended to develop fully water soluble derivatives of the macrocyclic system, which showed the best catalytic performance (**MC3**), to facilitate the oxidative splitting of water completely without any co-solvents. Furthermore, it is known that acetonitrile acts as a competitive binder to the seventh coordination site of the {Ru(bda)} fragment, competing with the coordination of water and thereby creating an off-pathway which slows down the overall catalytic rate.[216] By avoiding the use of acetonitrile, an increase in the catalytic activity can hence be anticipated. Here, a comprehensive study on two analogues of the parent macrocycle $[Ru(bda)(bpb)]_3$ (**MC3**) bearing additional water solubilizing groups such as triethylene glycol chains (**MC3b**) or protonable tertiary amines (**MC3c**) is reported. Those solubilizing groups were incorporated into the bridging ligands to minimize the alteration of electrochemical and catalytic properties of the parent system.

3.2.2 Synthesis and Characterization of the Functionalized Macrocycles

The bridging ligands **52**–**54** required for the macrocyclization have been obtained *via* Suzuki couplings between benzene-1,4-diboronic acid and adequately functionalized bromo-pyridines **49**–**51** that were synthesized according to literature known methods.[336-338] By heating the divalent ligands together with $[Ru(bda)(dmso)_2]$ in a 1:1 ratio, it was possible to synthesize the desired trinuclear metallosupramolecular macrocycles as shown in **Figure 39**.

---

[7] This chapter was communicated in:
[276] V. Kunz, M. Schulze, D. Schmidt, F. Würthner, *ACS Energy Lett.* **2017**, *2*, 288-293. (Reproduced with permission; copyright (2017) American Chemical Society)

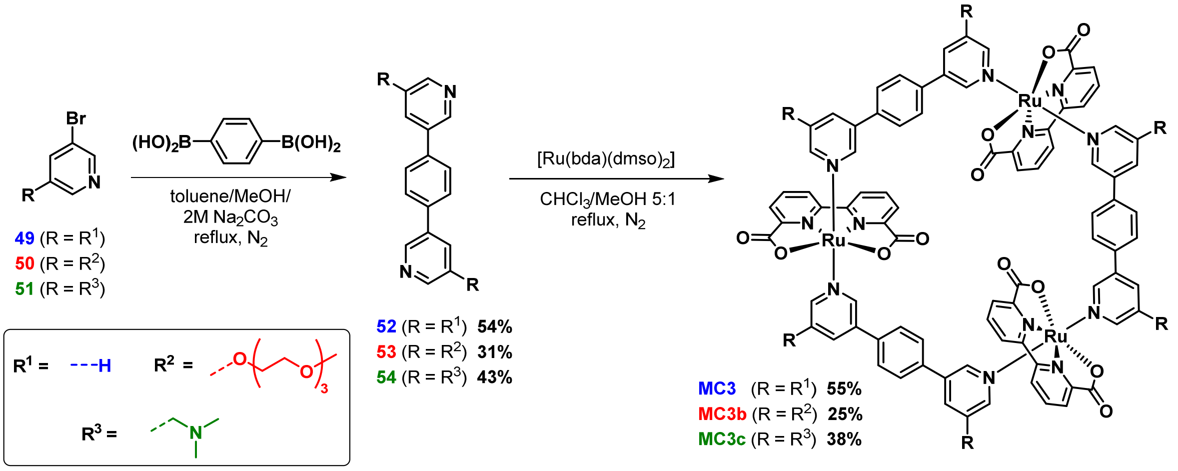

Figure 39: Synthesis of the bridging ligands **52**–**54** and trinuclear macrocycles **MC3**, **MC3b**, and **MC3c**.

To confirm the macrocyclic arrangement and to prove the stability of the new catalysts, we performed temperature dependent ^{1}H NMR experiments in different solvents. **Figure 40a** shows exemplarily the aromatic region of the ^{1}H NMR spectrum of **MC3c** in CD_2Cl_2/MeOD 5:1. Only three signals for the bda ligand (blue) and four signals for the bridging ligand **54** (red) can be observed, proving the D_{3h} symmetry of the cyclic system. Although the macrocycle **MC3c** is not fully soluble in neutral water the addition of few equivalents of ascorbic acid, commonly added to NMR samples to reduce traces of paramagnetic Ru^{III} to diamagnetic Ru^{II}, is sufficient to bring the macrocycle into solution due to concomitant protonation of the amine groups. Most ^{1}H NMR signals in the aromatic region are significantly shifted to lower fields due to the different solvent environment but the amount, multiplicity and sharpness of the signals is not affected (**Figure 40b**).

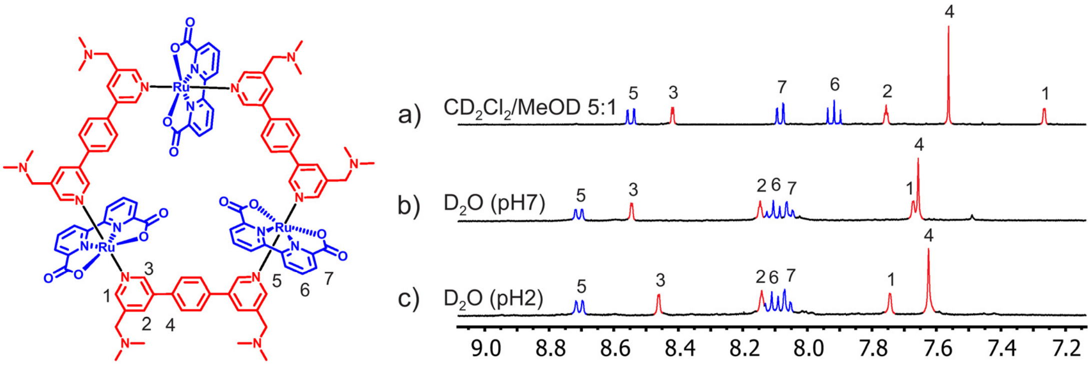

Figure 40: (a–c) Aromatic region of the ^{1}H NMR (400 MHz, ascorbic acid) spectra of **MC3c** in different solvents: CD_2Cl_2/MeOD 5:1 (a), D_2O (pH 7) (b), and D_2O (pH 2, acid: CF_3SO_3H) (c).

Even after acidification with trifluoromethane sulfonic acid to a pH of 2, no decomposition was observed over 1 week (**Figure 40c**). However, when the pH is further lowered to a value of 1, a severe signal broadening is observed. This broadening can be overcome by heating the sample up to 355 K (**Figure 41**) and can be explained by the reduced symmetry upon protonation of one of the carboxylate arms and the resulting dynamic coordinating /decoordinating equilibrium between the two carboxylates of one bda ligand, which is a known phenomenon for {Ru(bda)} complexes under highly acidic conditions.[163, 216]

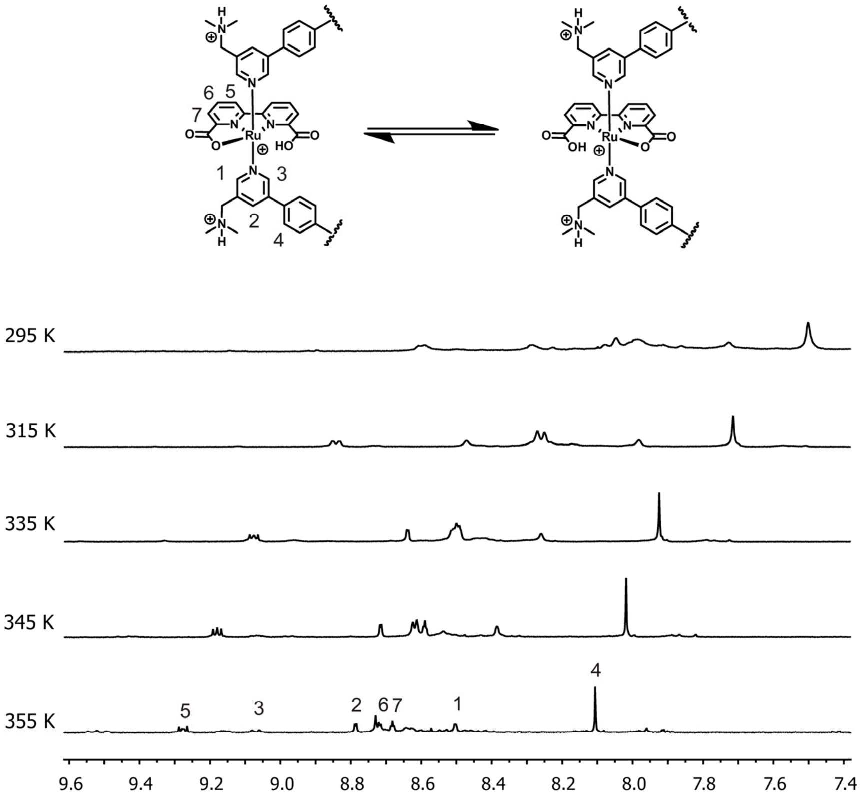

Figure 41: ^{1}H NMR spectra (400 MHz, D_2O, ascorbic acid) of **MC3c** under acidic conditions (pH 1, acid: CF_3SO_3H) at various temperatures.

In the Ru^{II} state, with an 18 valence electron configuration, always one of the carboxylate functionalities has first to dissociate for the accommodation of a new incoming ligand. Although electrochemical measurements performed on related {Ru(bda)} based WOCs in aqueous solutions suggest the coordination of water in the Ru^{II} state,[11] this cannot be seen by NMR spectroscopy, because the ligand exchange between the water molecule and the carboxylate group is very fast.[311] In contrast, for the stronger σ-donor acetonitrile, which exchanges only slowly with the carboxylate ligands, strongly broadened resonances can be observed for related mononuclear complexes.[163, 216, 311] Therefore, no sharp ^{1}H NMR spectrum for the triethylene glycol macrocycle **MC3b** could be obtained, because always some acetonitrile is required for solubility. Accordingly, also the spectrum of **MC3c** broadens upon addition of acetonitrile into the solvent mixture. The broadening is stronger than for the mononuclear reference systems due to the formation of many isomers upon desymmetrization. All in all, these NMR experiments clearly prove the high stability of the cyclic arrangement in water, even under strongly acidic conditions and elevated temperatures.

3.2.3 UV/Vis Spectroscopy and Electrochemistry

The UV/Vis absorption spectra of all [Ru(bda)L]$_3$ macrocycles in the Ru^{II} state show a strong absorption band around 300 nm for the ligand centered L-π → L-π^* transitions and bands at 360, 450 and 490 nm which can be attributed to metal-to-ligand charge transfer (MLCT) transitions. The band around 360 nm can be attributed to the Ru-d → L-π^* transition, whereas the 450 to 490 nm absorption can be assigned to the Ru-d → bda-π^* transitions.[339] For **MC3c**, those low-energy MLCT bands are slightly blue shifted, whereas the high-energy MLCT band at 360 nm is bathochromically shifted, meaning that the axial ligand **54** is slightly less electron donating compared to **52** and **53** (**Figure 42**).[314]

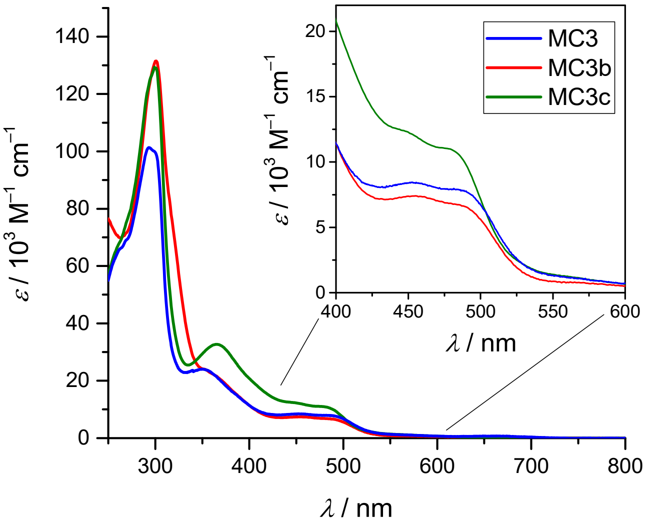

Figure 42: UV/Vis spectra of **MC3**, **MC3b** and **MC3c** at a concentration of 8 × 10^{-6} M in CH_3CN/H_2O (pH 1, acid: CF_3SO_3H) 1:1 (inset: amplified region between 400 and 600 nm).

Differential pulse voltammetry was used to verify that the electronic features of the ruthenium centers are not strongly perturbed by the exchange of the bridging ligand. The macrocycle **MC3c** was measured in pure water at pH 1, whereas the macrocycles **MC3** and **MC3b** were investigated in the presence of the non-coordinating CF_3CH_2OH as co-solvent, which is known to have no influence on the redox potentials (in contrast to the coordinating solvent acetonitrile).[93, 163] At pH 1, all voltammograms exhibit three oxidation events at potentials around 0.75 V, 1.1 V and 1.4 V vs. NHE (NHE = normal hydrogen electrode), that can be assigned to the $Ru^{II/III}$, $Ru^{III/IV}$ and $Ru^{IV/V}$ redox couples, respectively. After the last oxidation, a strong increase in current is observed due to the catalytic oxidation of water. For all macrocyclic WOCs this onset potential is centered around 1.5 V vs. NHE, meaning that all catalysts are capable of oxidizing water with an overpotential of ca. 270 mV. Additionally, the very similar oxidation potentials of all macrocycles prove that the redox properties of the new WOCs are not very different compared to the parent system **MC3**.[93] For the macrocycle **MC3c**, pH-dependent measurements were performed under acidic conditions (pH 1 to pH 3), to ensure full protonation of the amino groups over the whole pH range. From those measurements, a Pourbaix (*E* vs. pH) diagram can be constructed which provides information about the proton coupling of the individual redox events (**Figure 43**).[220] The first oxidation from Ru^{II} to Ru^{III} is found to be proton uncoupled, whereas the other two oxidation events are characterized by a slope of −44 mV/pH. According to the Nernst equation this correlates with a $3e^{-}/2H^{+}$ proton-coupled electron transfer process, which is in line with the results previously reported for **MC3**.[93]

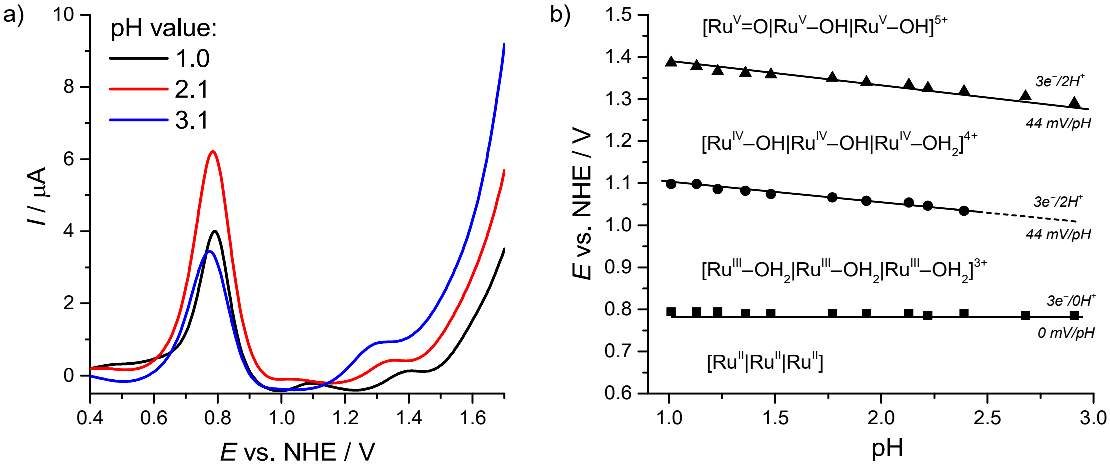

Figure 43: (a) Differential pulse voltammograms for **MC3c** in H_2O at selected pH values, and (b) a corresponding Pourbaix diagram for **MC3c**. The initial pH was 1 (acid: CF_3SO_3H), which was then increased by the addition of aq. NaOH. The Pourbaix diagram was constructed by the redox potentials determined at different pH values.

3.2.4 Water Oxidation Catalysis by Highly Water Soluble Macrocycles

Since some amount of acetonitrile is required for the solubility of the catalysts but it also acts as a competitive binder to the catalytic site, the optimal solvent composition had to be identified for each catalyst. To determine the optimal reaction conditions, the catalytic activity was screened in different solvent compositions for all catalysts under otherwise fixed conditions. Cerium(IV) ammonium nitrate (CAN) was used as the sacrificial oxidant dissolved in CH_3CN/H_2O (pH 1, acid: CF_3SO_3H) mixtures (*v*/*v*) with different mixing ratios.[154] After the injection of the catalyst solution, the evolution of molecular oxygen was monitored using pressure transducers and the gas composition was analyzed with gas chromatography (GC) at the end of the reaction. All three catalysts show different optimal solvent compositions as it has been determined by the initial rate of catalysis for the first three seconds. For the optimal performance **MC3** requires approximately 60% acetonitrile, whereas the amount of co-solvent can be lowered to 30% for **MC3b** and to 20% for **MC3c** (**Figure 44** and **Figure A58–Figure A60**, see Appendix).

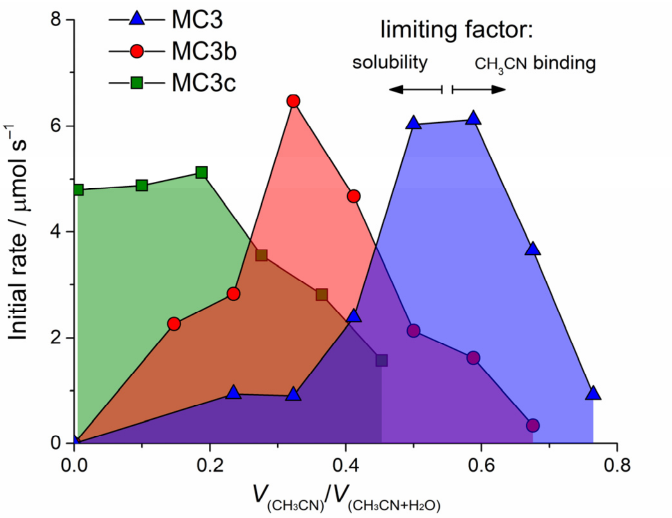

Figure 44: Variation of the solvent composition for the catalytic water oxidation reaction using the catalysts **MC3**–**MC3c** at otherwise fixed conditions ([CAN] = 536 mM, [**MC3**–**MC3c**] = 24.3 µM, *V* = 3.4 mL, pH 1, acid: CF_3SO_3H).

If the amount of co-solvent is too low, precipitation occurs during the reaction leading to slower catalysis and thus lower turnover numbers. At higher acetonitrile contents than required for optimal solubility, the catalytic performance decreases due to the inhibiting role of acetonitrile as a competitive binder, which has also been demonstrated for [Ru(bda)(pic)$_2$] as a reference.[216] Interestingly, the initial rates of **MC3c** reach a plateau for low acetonitrile contents and only after some time partial precipitation of apparently less soluble intermediates occurs which leads to a slower catalysis. However, in contrast to the other two catalysts the water oxidation reaction never ceases completely, even under completely acetonitrile-free conditions. Therefore, catalyst **MC3c** was studied both, in pure aqueous trifluoromethane sulfonic acid at pH 1 as well as under the conditions showing the optimal performance using 20% acetonitrile as a co-solvent.

Concentration-dependent measurements under the optimized reaction conditions were used to determine the turnover frequency (**Figure 45a**) and the turnover number (**Figure 45b**) and to get further information about the kinetics of the reaction (**Figure A61**–**Figure A63**). In pure water (pH 1), a high TOF of 72 ± 6 s^{-1} and a maximal TON of 2.2×10^3 can be achieved for **MC3c** (**Figure A64**). Analysis of the reaction head space composition using gas chromatography confirmed that the increase in pressure is solely due to the formation of oxygen as the only gaseous product (**Figure A65**). The addition of 20% (*v*/*v*) acetonitrile leads to an increased TOF of 98 ± 9 s^{-1} and a TON of 2.8×10^3, which can be attributed to the improved solubility and thus a faster reaction. The catalytic activity is significantly higher for **MC3b** with a TOF of 147 ± 9 s^{-1} and a TON of 5.2×10^3 using 30% acetonitrile. The comparison of the catalytic activities of these new derivatives with the already reported parent compound **MC3** (TOF = 150 s^{-1} and TON = 7.4×10^3), shows similar catalytic activities for all macrocycles.[93]

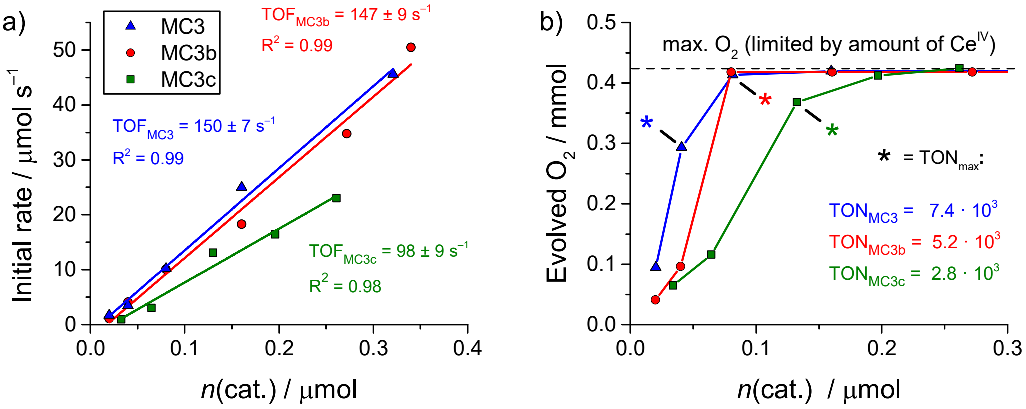

Figure 45: (a, b) Concentration-dependent oxygen evolution at individually optimized conditions for **MC3**–**MC3c**. (a) Initial rates and the corresponding TOFs. (b) Amount of evolved oxygen and the corresponding TONs. (CH_3CN/H_2O (pH 1) 6:4 for **MC3**, 3:7 for **MC3b** and 2:8 for **MC3c**; *V* = 3.4 mL, [CAN] = 536 mM).

The slightly lower TONs of the new supramolecular WOCs might be due to a somehow decreased stability caused by the newly introduced side chains which make the compounds more prone to oxidative decomposition (*e.g.* benzylic position).[171] Indeed, ligand oxidation could only be demonstrated for **53** and **54** by differential pulse- and cyclic voltammetry with an obviously irreversible oxidation process for **54** (**Figure 46**).

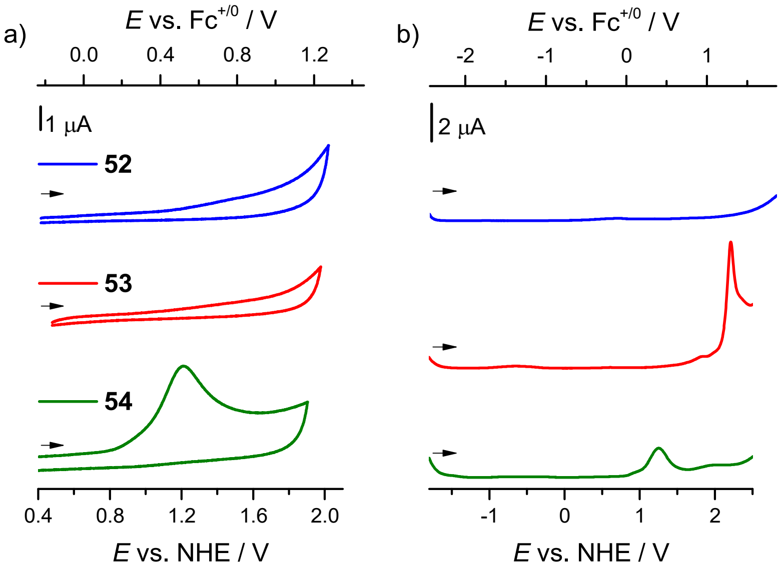

Figure 46: (a) Cyclic-, and (b) differential pulse (right) voltammograms of **52**, **53**, and **54** (0.25 mM) in dichloromethane using (n-$C_4H_9)_4NPF_6$ (0.1 M) as electrolyte and ferrocene (Fc) as internal standard (0.25 mM) at the end of each measurement (scan rate: 100 mV/s).

Under comparable conditions, **MC3b** reaches the same TOF as **MC3**, however in a different solvent composition. Although **MC3c** exhibits a lower activity compared to the other two catalysts, the TOF of 98 s^{-1} (33 s^{-1} per ruthenium center) is still in the same range compared to the monomeric reference complex [Ru(bda)(pic)₂] (TOF = 33 s^{-1}).[64] However, it has to be noted that the high performance of [Ru(bda)(pic)₂] is achieved with only 1% (*v*/*v*) of acetonitrile as co-solvent and by the usually much faster I2M mechanism, whereas the macrocycles reported here work *via* the nucleophilic attack of a water molecule to a ruthenium oxide species. Thus, all macrocyclic catalysts show the expected linear dependency of the reaction rate on the catalyst concentration, meaning that the reaction is pseudo first-order in catalyst concentration with a monomolecular rate-determining step (the CAN concentration can be neglected due to the large excess). This also explains the high activity of **MC3c** considering its highly charged nature under the reaction conditions noting that for a mononuclear [Ru(bda)L₂] catalyst operating *via* the I2M mechanism only negligible catalytic activity was observed when equipped with cationic axial ligands.[215] To finally prove the macrocyclic integrity of the newly synthesized WOCs during catalysis, **MC3c** was exemplarily analyzed by MALDI-ToF mass spectrometry after 30 catalytic cycles. The mass spectrum of **MC3c** thus obtained is nearly identical with the high resolution ESI-ToF mass spectrum of the analytical pure sample exhibiting the same mass spectrometric fragmentation behavior (**Figure A66**).

3.2.5 Kinetic Oxidation Experiments

The difference in catalytic activity between the highly active **MC3** and **MC3b** and the somewhat slower **MC3c** can be rationalized by the fact that the rate-determining step was previously found to be the oxidation from Ru^{IV} to Ru^{V}, presumably proceeding *via* an inner-sphere electron transfer.[93, 185] Although the oxidation potentials of this processes are almost the same for all compounds (**Figure A57**), this oxidation event should be slowed down considerably for **MC3c** using cerium(IV) ammonium nitrate as the oxidant due to coulombic repulsion between the highly charged catalyst and the Ce^{IV} cation. To demonstrate that the charge of the catalyst really influences the rate of oxidation, a UV/Vis experiment was performed monitoring the bleach of the MLCT band upon the oxidation of Ru^{II} to Ru^{III} by adding one equivalent CAN per ruthenium center to a 0.1 mM solution of the catalyst. This was done for both catalysts under the same reaction conditions and under priorly optimized solvent compositions, namely 30% acetonitrile for **MC3b** and 20% for **MC3c**. This one-electron oxidation is a second order reaction with the reaction rate depending on the concentration of both, the reductant (Ru^{II} centers) and the oxidant (Ce^{IV}). In the special case that the concentration of the oxidant and reductant are the same, the rate equation 16 can be simplified to:

$$-\frac{\mathrm{d}\,[\mathrm{Ru^{II}}]}{\mathrm{d}t} = \mathrm{k} \cdot [\mathrm{Ru^{II}}] \cdot \left[\mathrm{Ce^{IV}}\right] = \mathrm{k} \cdot [\mathrm{Ru^{II}}]^2 \qquad (16)$$

This rate law can be used to determine the second order rate constant k of the oxidation process by fitting absorption spectral changes at a specific wavelength according to the following equation 17 (with A_0 being the initial and A_∞ the final absorption, t the time and $[\mathrm{Ru^{II}}]_0$ the initial ruthenium concentration):[175, 340]

$$A = \frac{A_0 + A_\infty \cdot [\mathrm{Ru^{II}}]_0 \cdot k \cdot t}{[\mathrm{Ru^{II}}]_0 \cdot k \cdot t + 1} \qquad (17)$$

By fitting the decay of the MLCT absorption band at 450 nm, which is characteristic for the Ru^{II} state,[183] the average rate constant for the oxidation of all ruthenium centers from the oxidation state +II to the oxidation state +III can readily be estimated. This oxidation process is roughly three times faster for **MC3b** (k = 1687 $M^{-1}\ s^{-1}$) compared to **MC3c** (504 $M^{-1}\ s^{-1}$) under the particularly optimized reaction conditions (**Figure 47**). The difference becomes even more evident, if the oxidation is performed under exactly the same reaction conditions

(30% acetonitrile each). The rate of the Ru$^{II/III}$ oxidation of **MC3c** decreases to 221 M^{-1} s^{-1} becoming almost 8 times slower than for **MC3b** (**Figure A67**). This clearly demonstrates, that the oxidation processes of **MC3c** are dramatically slowed down by introducing charged side chains. Obviously, a coulombic repulsion accounts for this effect, since the oxidation potentials were not affected by the side chains as it has been proven with differential pulse voltammetry. Although the other oxidation processes could not be further analyzed due to a lack of significant changes in the UV/Vis spectra, it is a valid assumption that this behavior also strongly influences them. Since the oxidation from Ru^{IV} to Ru^{V} is assumed to be rate-determining, the coulombic repulsion between the positively charged side chains of **MC3c** and the Ce^{IV} cation seems to be accountable for slowing down the water oxidation catalysis in comparison to **MC3** and **MC3b**. For **MC3b** also a beneficial effect of the triethylene glycol chains cannot fully be excluded, which are known to bind metal ions and thus can bring the cerium(IV) into close contact to the ruthenium center, possibly leading to faster oxidation processes.[224] However, this effect would not explain almost identical TOF values that were observed for the two catalysts **MC3** and **MC3b**.

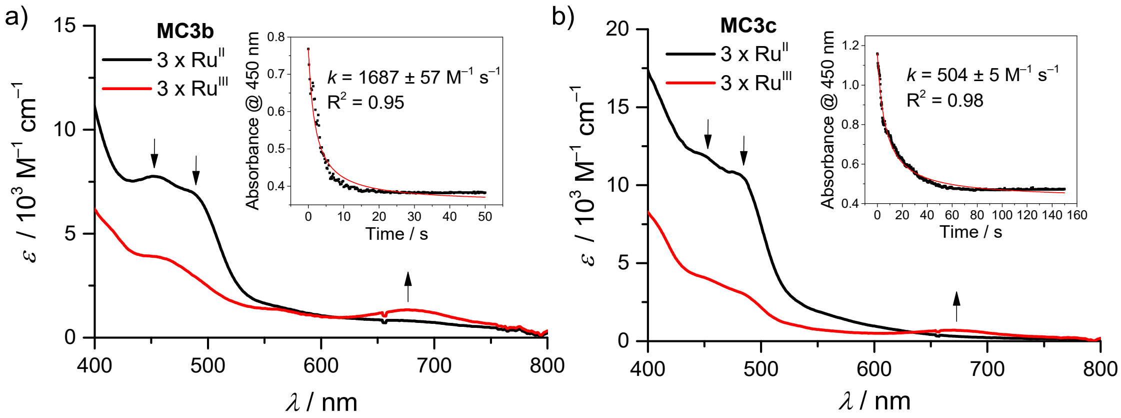

Figure 47: (a, b) UV/Vis absorption spectra of **MC3b** in CH_3CN/H_2O (pH 1) 3:7 (a), and **MC3c** in 2:8 (b) before (black) and after (red) the addition of 1 equivalent CAN (V = 2.0 mL, [cat] = 0.1 mM, [Ru-centers] = 0.3 mM, [CAN] = 0.3 mM) and the time resolved decay of the absorption at 450 nm as insets.

3.2.6 Conclusion

In conclusion, the parent trinuclear macrocyclic $[Ru(bda)L]_3$ water oxidation catalyst was equipped with triethylene glycol and protonable tertiary amine side chains to improve the water solubility of such supramolecular systems. Accordingly, it was possible to perform the water oxidation catalysis under much eco-friendlier reaction conditions in pure water. By the introduction of triethylene glycol side-chains the required amount of acetonitrile was halved. Complete water solubility under acidic conditions could be achieved by the introduction of charged ammonium side chains, however, at the expense of reduced catalytic activity in chemically driven water oxidation experiments presumably due to coulombic repulsions with the oxidant cerium(IV). Because **MC3c** is soluble in pure water, the typical line broadening in NMR experiments originating from acetonitrile coordination could be avoided. Thus, it was possible to prove the high stability of the cyclic arrangement in aqueous solutions with ^{1}H NMR studies under highly acidic conditions at pH 1 and at elevated temperatures up to 355 K.

3.3 Embedding of {Ru(bda)} Catalysts in Supramolecular Aggregates[8]

3.3.1 Perylene Bisimides as Ligands for the Self-Assembly of Catalysts

For the technical application of water oxidation catalysts, the incorporation into an appropriate matrix can be of great importance.[90, 341-343] The major advantages of this approach are the better protection of the catalytically active species as well as the compartmentalization, which helps to organize reactive modules into multifunctional structures.[75] The matrix concept is inspired by nature, where the catalytically active Mn_4CaO_5 cluster of the chloroplasts is embedded into the protein environment of the photosystem II, creating a surrounding that facilitates redox levelling to reduce the overpotential for water oxidation.[110] Examples for the realization of this concept are the deposition of water oxidation catalysts onto surfaces,[344] inside nano-cages [208] and nanotubes,[343] or the incorporation into metal organic frameworks,[345, 346] as well as the embedding into soft matter structures such as membranes,[347] vesicles,[187, 251] polymers[348] and polymer gels.[349]

In this chapter, the successful incorporation of the {Ru(bda)} water oxidation catalyst into perylene dye aggregates is presented. This has been achieved by equipping the {Ru(bda)} fragment with axial ligands containing perylene bisimide (PBI) moieties that facilitate self-assembly in a polar environment due to strong π-π interactions.[350-352] The optical and electronic properties, as well as the aggregation tendency of PBI molecules, can easily be tuned by adequate functionalization at the bay positions.[94, 353-355] Furthermore, perylene bisimides are among the most robust π-systems. Their electron-poor π-scaffold is very resistant against photo-oxidation and other chemical or thermal decomposition pathways,[354] which is a prerequisite for the design of matrices for water oxidation catalysis. Accordingly, two different PBIs have been prepared and used as ligands for the formation of complexes with the {Ru(bda)} fragment. The aggregation behavior of these complexes in aqueous solution has been studied, and the influence of the aggregate morphology on the water oxidation performance has been investigated.

---

[8] This section was partially communicated in:
[323] V. Kunz, V. Stepanenko, F. Würthner, *Chem. Commun.* **2015**, *51*, 290-293.
(Reproduced with permission; copyright (2015) The Royal Society of Chemistry)

3.3.2 Synthesis of Perylene Bisimide (PBI) Ligands

Unsymmetrically substituted perylene bisimide molecules have been designed to provide both, sufficient solubility, and the ability to coordinate metals (**Figure 48**). One of the two imide positions was thus functionalized with a pyridyl group for metal coordination, whereas the second imide position was derivatized with a solubilizing group. For this purpose, a triethylene glycol swallowtail was introduced as it is known to provide good solubility in aqueous media.[356, 357] The respective amine **55** was prepared in a four-step synthesis according to literature known procedures.[356, 358, 359] The pyridyl group was connected to the PBI *via* a short alkyl spacer, using 2-(4-pyridyl)ethylamine (**56**), to introduce some flexibility for more efficient metal binding.[360] Moreover, two different perylene core structures have been used to control the electronic properties and the aggregation behavior. The introduction of chloride substituents at the bay positions of the perylene core (1,6,7,12), should result in a higher oxidative stability and a lower aggregation tendency compared to bay-unsubstituted PBI analogues. A sterically less demanding pyridine derivative bearing a glycol chain (**PyO**) has been synthesized as an additional water-solubilizing ligand according to a literature known procedure.[361]

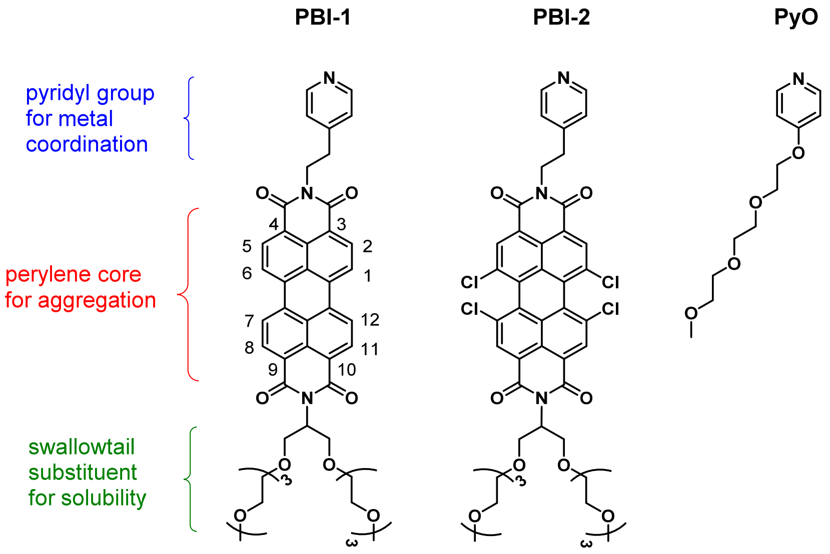

Figure 48: Overview of the synthesized ligands based on perylene bisimide (PBI) or pyridine scaffolds.

Generally, there are different strategies to synthesize such unsymmetrical PBIs (**Scheme 1**), depending on when the individual imide substituents are introduced. For the bay-unsubstituted derivative, the pyridyl substituent has primarily been introduced starting from bisanhydride **57**, and the second anhydride functionality was simultaneously converted into a diester to obtain the well soluble intermediate **58**.[362] Under strongly acidic and dehydrating conditions, the diester has been cleaved and condensed to prepare the respective anhydride **59** as nearly insoluble solid, which can only be purified by filtration and washing. The more valuable swallowtail imide substituent (**55**) was then introduced applying standard imidization reaction conditions to yield **PBI-1** in the last step of the reaction sequence.

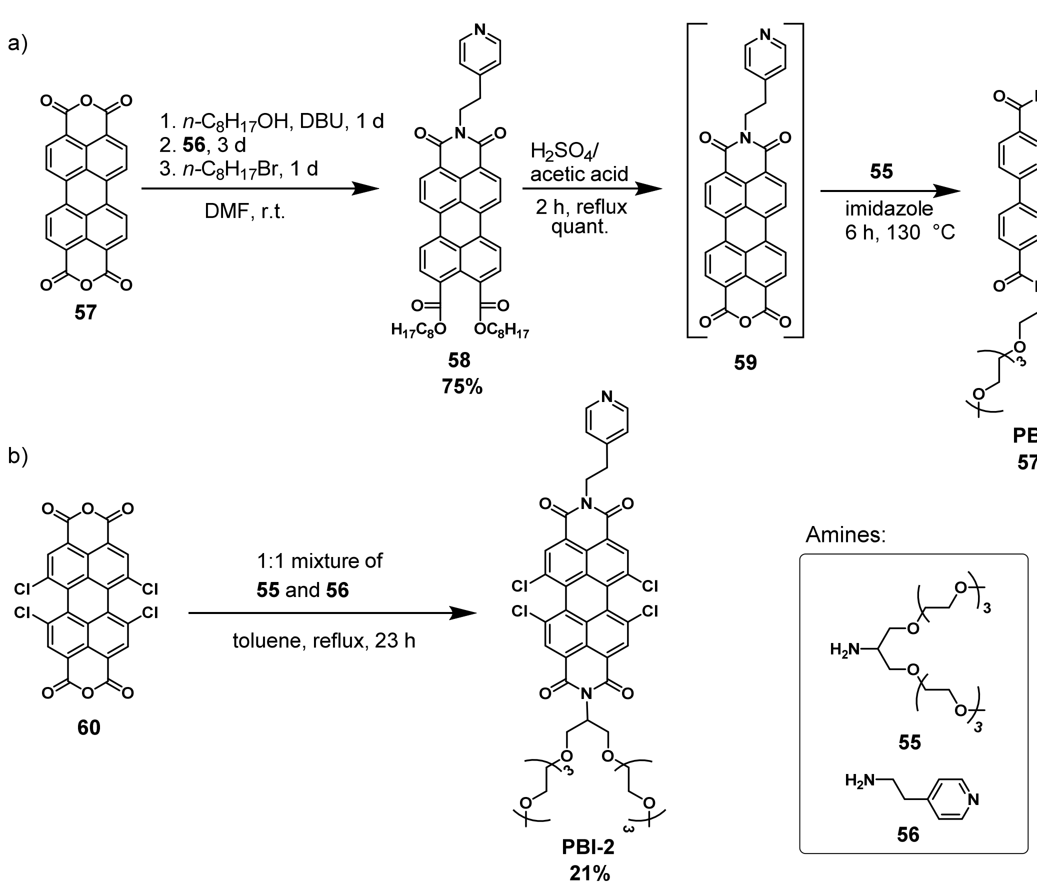

Scheme 1: (a, b) Synthesis of the PBI-ligands. Multi-step synthesis of the bay-unsubstituted ligand **PBI-1** (a), and one-pot reaction for the synthesis of the 1,6,7,12-tetrachloro-substituted ligand **PBI-2** (b).

Due to the intrinsically higher solubility of 1,6,7,12-tetrachloro-perylene derivatives, an alternative synthetic strategy has been applied for the preparation of **PBI-2**.[363, 364] In a one-pot imidization reaction, starting from the tetrachlorinated perylene bisanhydride **60** and the equimolar mixture of amines **55** and **56**, the unsymmetrical perylene bisimide could be obtained besides the symmetrically substituted by-products. Due to its high solubility, **PBI-2** could easily be separated by column chromatography from this mixture.

3.3.3 Synthesis and Characterization of Ru-PBI Complexes

With the novel PBI ligands in hand, coordination complexes with the {Ru(bda)} water oxidation catalyst fragment have been synthesized (**Scheme 2**). Therefore, the ligands **PBI-1** and **PBI-2** have been reacted with [Ru(bda)(dmso)$_2$] (**40**) to obtain the desired symmetric complexes [Ru(bda)(PBI-1)$_2$] (**C1**) and [Ru(bda)(PBI-2)$_2$] (**C2**). Additionally, an asymmetric complex [Ru(bda)(PyO)(PBI-1)] (**C3**) has been synthesized in a one-pot reaction bearing only one axial **PBI-1** ligand and **PyO** as the second ligand to further enhance the water solubility and reduce the aggregation tendency.

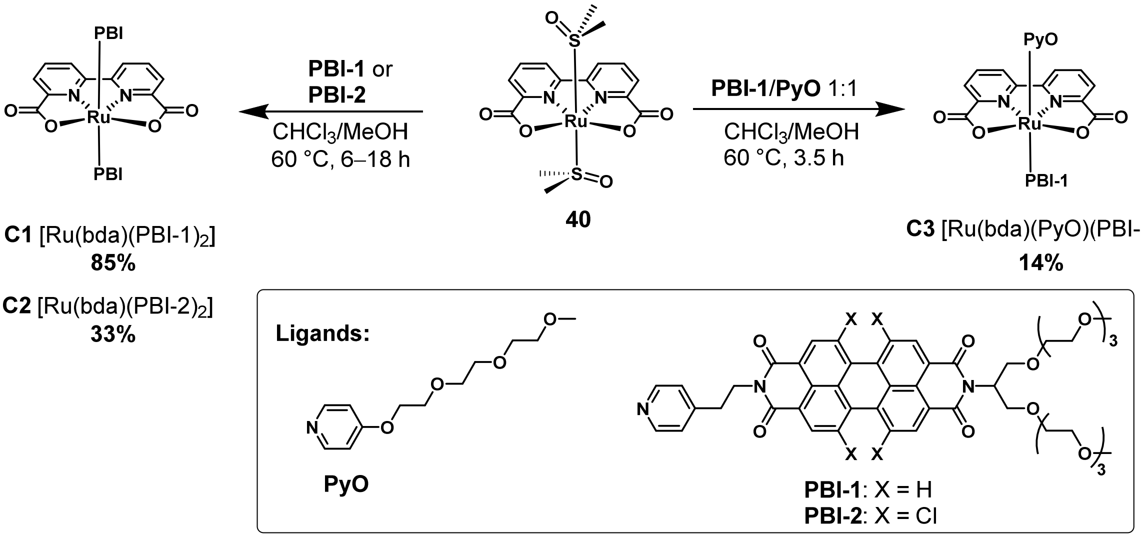

Scheme 2: Synthesis of symmetrical (**C1** and **C2**) and unsymmetrical (**C3**) {Ru(bda)} complexes with PyO and/or PBI ligands.

In the following section, the optical and electrochemical properties of the PBI ligands and the changes upon complex formation with {Ru(bda)} are discussed. **Figure 49** shows cyclic- and differential pulse voltammograms of the ligands **PBI-1** and **PBI-2**, as well as of the complexes **C1**, **C2**, and **C3** in dichloromethane solutions. For both ligands, two reversible reductions and one oxidation can be observed, as it is characteristic for perylene bisimides.[353] For the bay-unsubstituted **PBI-1**, the PBI^-/PBI^{2-}, PBI/PBI^-, and PBI^+/PBI redox couples are detected at −1.25 V, −1.05 V and +1.28 V vs. $Fc^{+/0}$, respectively (**Table 2**). In contrast, the chlorinated molecule **PBI-2** shows two reductions at −1.01 V and −0.80 and one oxidation at +1.53 V vs. $Fc^{+/0}$. Accordingly, **PBI-2** is easier to reduce and more difficult to oxidize by ca. 250 mV due to the electronic withdrawing character of the chloro-substituents.[94] This higher oxidative stability should be advantageous for the harsh oxidative reaction conditions applied in chemical water oxidation. For the corresponding complexes [Ru(bda)(PBI-1)$_2$] (**C1**), [Ru(bda)(PBI-2)$_2$] (**C2**), and [Ru(bda)(PyO)(PBI-1)]

(**C3**) those PBI-related potentials remain essentially unchanged, confirming that the ruthenium fragment and the PBI ligands are electronically not coupled as it is expected due to the node in the HOMO and LUMO located at the imide nitrogen atom of the PBIs.[353, 354] However, coordination to the {Ru(bda)} fragment leads to one additional redox event.[152] For all complexes, the Ru^{III}/Ru^{II} redox couple can be observed at nearly identical potentials. As it has already been discussed in **chapter 3.1**, higher ruthenium oxidation states can only be reached in the presence of water that enables proton-coupled electron transfers upon coordination, and are thus not observed under the applied conditions.

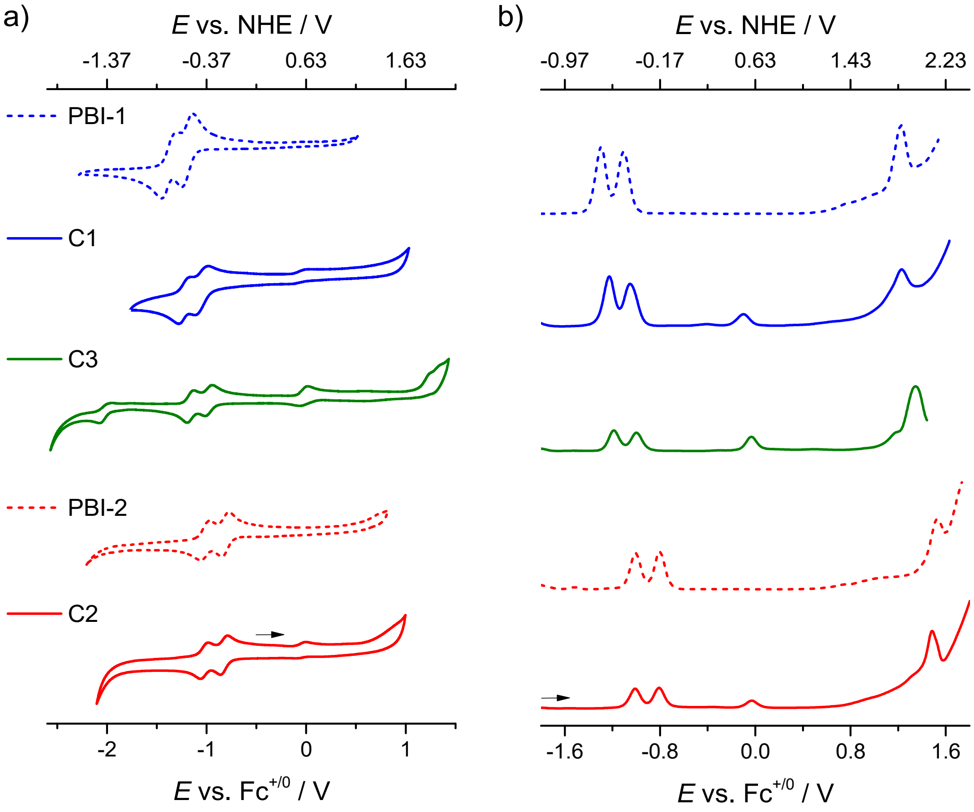

Figure 49: (a) Cyclic-, and (b) differential pulse voltammograms of the PBI ligands **PBI-1** and **PBI-2**, and the corresponding complexes [Ru(bda)(PBI-1)$_2$] (**C1**), [Ru(bda)(PBI-2)$_2$] (**C2**), and [Ru(bda)(PBI-1)(PyO)] (**C3**) in dichloromethane measured against the Fc^+/Fc^0 redox couple (c = 0.2 mM, 100 mV s^{-1} scan rate, 0.1 M $(n\text{-}Bu)_4NPF_6$ as electrolyte).

The electrochemical potentials of **C3** are very similar compared to those of **C1** (**Table 2**). However, different current ratios for the PBI and the {Ru(bda)} centered redox events are observed for both complexes bearing axial **PBI-1** ligands, which is well in line with the stoichiometry of the respective subunits of **C1** (2:1) and **C3** (1:1).

Table 2: Comparison of the redox potentials for the PBI ligands and Ru-PBI complexes.

	***E* vs. Fc$^{+/0}$ / V**				
Compound	Ru$^{II/I}$	PBI^{-}/PBI^{2-}	PBI/PBI^{-}	Ru$^{III/II}$	PBI^{+}/PBI
PBI-1	–	−1.25	−1.05	–	+1.28
PBI-2	–	−1.01	−0.80	–	+1.53
C1	n.d.	−1.23	−1.05	−0.09	+1.23
C2	n.d.	−1.02	−0.82	−0.04	+1.49
C3	−2.02	−1.25	−1.06	−0.09	+1.29

The UV/Vis spectra of the PBI ligands **PBI-1** and **PBI-2** and of the respective ruthenium complexes **C1**, **C2**, and **C3** in dichloromethane are compared in **Figure 50**. The PBI absorption spectra are dominated mainly by absorption bands between 450 and 550 nm resulting from the S_0–S_1 transition (polarized along the long molecular axis) with well-resolved vibronic progressions. Tetrachloro-substitution results in an additional absorption band around 420 nm, which can be attributed to the now partially symmetry allowed S_0–S_2 transition (polarized along the short molecular axis).[363] Furthermore, **PBI-2** exhibits a significantly lower extinction coefficient compared to **PBI-1** as a consequence of the less planar and more flexible π-scaffold, and slightly hypsochromically shifted absorption maxima due to the electron withdrawing effect of the chloro-substituents that results in a larger HOMO-LUMO gap (**Figure 50a**).[94, 363] The UV/Vis absorption spectra of the coordination complexes are basically a superposition of the respective ligand spectra and the {Ru(bda)}-MLCT transitions around 300 nm (**Figure 50b**). The extinction coefficient of the PBI S_0–S_1 transition in the range between 450 and 550 nm is twice as high for complex **C1**, equipped with two bay-unsubstituted **PBI-1** ligands, compared to **C3** that only contains one **PBI-1** ligand. For complex **C2**, which bears two tetrachloro-substituted **PBI-2** ligands, comparably low extinction coefficients and less defined vibronic progressions are observed, together with an additional band for the S_0–S_2 transition at around 420 nm (like for **PBI-2**). These spectra show once again that there is little electronic interaction between the ruthenium complex fragment and the axial PBI ligands in the ground state. However, the strong fluorescence of the PBI ligands becomes quenched upon transition metal coordination, either due to an electron transfer from the perylene to the ruthenium center and non-radiative recombination, or due to triplet population induced by enhanced intersystem crossing as a consequence of the heavy-atom effect (**Figure A69**, see Appendix).[365-367]

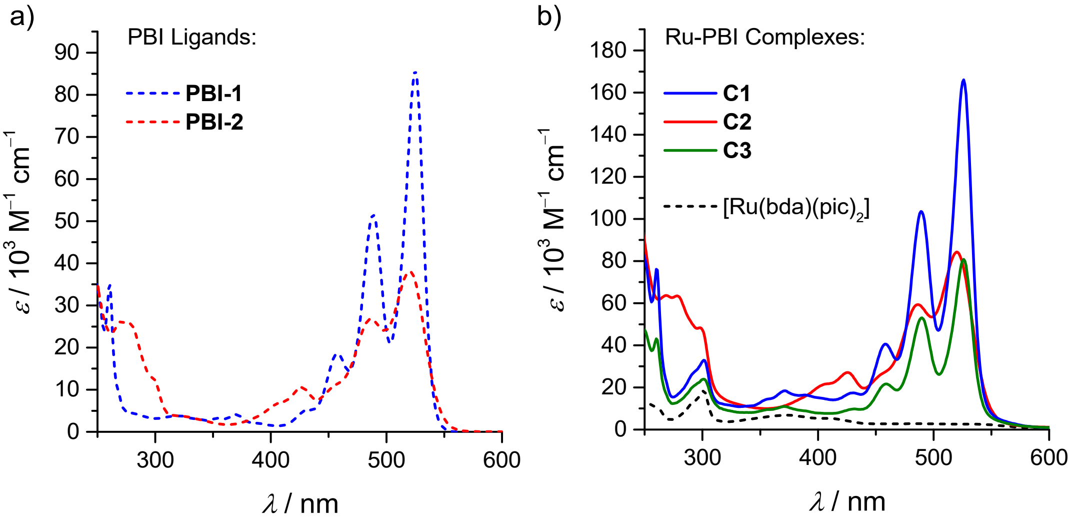

Figure 50: (a) UV/Vis absorption spectra of PBI ligands **PBI-1** and **PBI-2**, and (b) of coordination complexes [Ru(bda)(PBI-1)$_2$] (**C1**), [Ru(bda)(PBI-2)$_2$] (**C2**), [Ru(bda)(PyO)(PBI-1)] (**C3**), and [Ru(bda)(pic)$_2$] in dichloromethane at a concentration of 10^{-5} M.

3.3.4 Characterization of Aggregates

The aggregation behavior of the Ru-PBI complexes **C1**–**C3** in polar solvents has been investigated by solvent-dependent UV/Vis absorption spectroscopy (**Figure 51**). The spectra in dichloromethane, which already have been described in the previous section, represent the monomeric state of the molecules since no aggregation is observed in this solvent. Conversely, in acetonitrile, spectral changes are observed for all complexes, whereas the absorption spectra of the pure ligands remain basically unchanged (**Figure A70**). Pronounced aggregation can be observed for **C1**, which results in a strongly broadened spectrum with a loss of the vibronic fine structure and reduced extinction coefficients. Furthermore, the absorption maximum is hypsochromically shifted from 526 nm to 495 nm with an arising shoulder at 553 nm, indicating that H-type aggregation takes place.[368] In contrast, minor spectral changes are observed for complex **C2**, which bears two chlorinated **PBI-2** ligands. The ratio between the 0–0 and 0–1 vibronic absorption bands (A_{0-0}/A_{0-1}) decreases from 1.42 for the non-aggregated molecule in dichloromethane to 1.28 in acetonitrile, indicating weak interchromophoric inter-actions.[94, 369] As expected, the introduction of bulky bay-substituents significantly lowers the aggregation tendency of the PBI π-scaffold and the respective complex. The same observation is made for complex **C3**, which is equipped with only one bay-unsubstituted **PBI-1** ligand, and accordingly shows a lower tendency to aggregate than **C1** with two PBI ligands. Here the A_{0-0}/A_{0-1} ratio decreases from 1.52 for the monomer in dichloromethane to 1.32 in acetonitrile. Upon addition of water (pH 7) to the acetonitrile solutions only minor changes can be observed in all cases. Likewise, the addition of aqueous trifluoromethane sulfonic acid (pH 1) does not result in significant changes of the spectrum of the aggregated complex **C1**, demonstrating the stability of the aggregates under acidic conditions, like they are applied for catalytic water splitting reactions (*vide infra*). In the case of **C2** and **C3**, acidification slightly increases the chromophoric interactions, as the A_{0-0}/A_{0-1} ratio decreases further to 1.17 for **C2** and to 1.19 for **C3** (**Figure A71**).

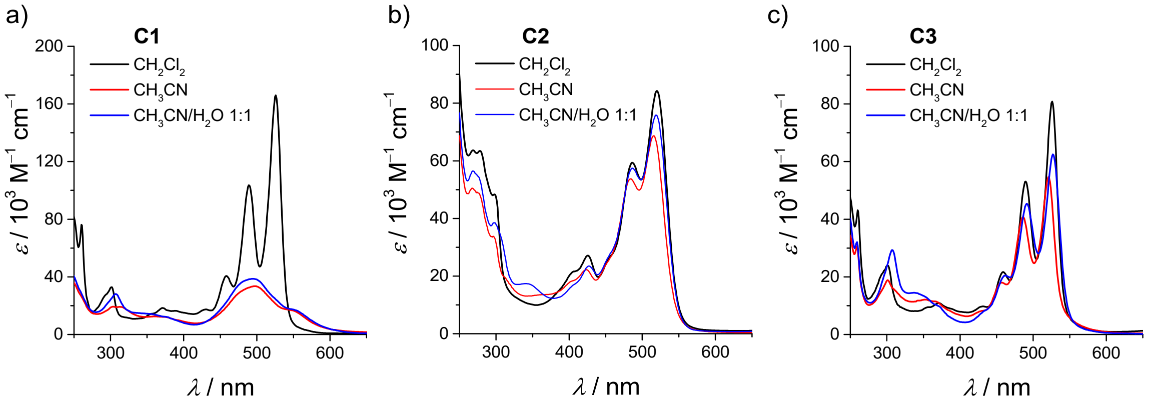

Figure 51: (a–c) UV/Vis absorption spectra of the ruthenium-PBI complexes: **C1** (a), **C2** (b), and **C3** (c) in various solvents at a concentration of 10^{-5} M.

Besides UV/Vis spectroscopy, atomic force microscopy (AFM) and cryogenic scanning electron microscopy (cryo-SEM) have further been used to study the aggregation of the complexes **C1**–**C3**, and to gain information on the morphology of the different aggregates. Solutions of the complexes in acetonitrile and acetonitrile/water 1:1 have been spin-coated onto mica to analyze the aggregates by AFM (**Figure 52**). Extended fibrous aggregates with a height of 2.5 ± 0.3 nm and various lengths between 15 and 200 nm have been observed for **C1** even in pure acetonitrile. In accordance with the UV/Vis spectroscopic studies, the aggregated fibers remain intact after the addition of water and solely a stronger entanglement can be observed. This becomes even more obvious for the same experiment performed on a less polar HOPG surface, where the individual fibers exhibit a lower tendency to bundle (**Figure A72** and **Figure A73**). In contrast, spin coating of an acetonitrile solution of **C2** yields a totally different aggregate morphology. Uniform nanoparticles with a diameter of 6.2 ± 0.5 nm are observed, which likewise do not change upon the addition of water. A completely different behavior is observed for **C3**, where spin coating of the acetonitrile solution leads to a film of inhomogeneous particles, and only after the addition of water, relatively uniform fibrous aggregates can be obtained with a diameter of 4.9 ± 0.3 nm and lengths up to 130 nm. Altogether, these experiments support the observations made by UV/Vis spectroscopy that **C1** is aggregating most strongly. The changes regarding the aggregate morphology can be ascribed to the stronger core twist of **PBI-2** induced by the bulky chloro substituents or the exchange of one axial **PBI-1** ligand by **PyO**, which hampers the extended aggregate formation.[370]

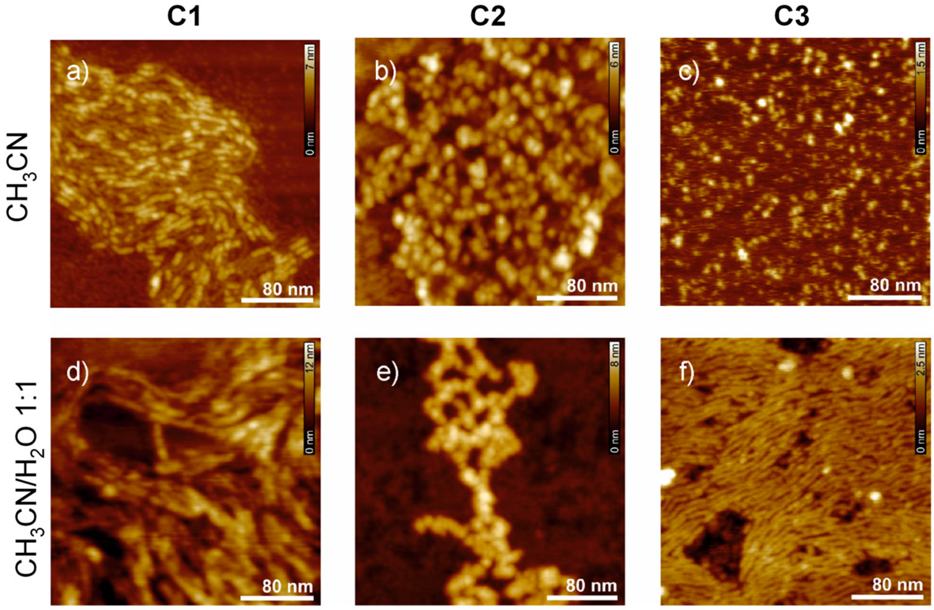

Figure 52: AFM height images of samples obtained by spin-coating of solutions of **C1** (a and f), **C2** (b and e), and **C3** (c and f) in acetonitrile (a–c) and a acetonitrile/water (pH 7) 1:1 mixture (d–f) onto mica ($c = 10^{-5}$ M).

To prove that the observed aggregates are not only formed upon drying of the sample during the spin-coating process, cryogenic scanning electron microscopy (cryo-SEM) has further been performed. For this technique, a droplet of the solution is frozen in liquid nitrogen, cut, and the cutting edges are subsequently investigated by electron microscopy, providing information about the frozen solvated structures present at the interface. Due to the relatively high volatility of acetonitrile, this technique is not applicable for pure acetonitrile solutions and was only used to study the 1:1 acetonitrile/water (pH 7) mixtures (**Figure 53**). For the complex **C1**, networks of entangled nanofibers can be observed, which is in line with the observations made by AFM. However, in contrast to the dried fibers studied by AFM (width: 2.5 ± 0.3 nm), the solvated fibers investigated by cryo-SEM exhibit an increased width of 5–6 nm. This can be attributed to more stretched oligoethylene glycol chains due to interactions with solvent molecules, and the dimensions are in good agreement with the length of fully stretched molecules of **C2**. The cryo-SEM images of **C3** also show extended aggregates, similar to those observed by AFM. Compared to the fibers obtained for **C1**, the fibers of **C3** seem to be shorter and less entangled, confirming that reducing the amount of aggregating PBI ligands lowers the aggregation tendency. In contrast, for **C2** no extended structures are observed by cryo-SEM, which is well in line with the nanoparticles observed by AFM that are too small to be resolved by this technique.

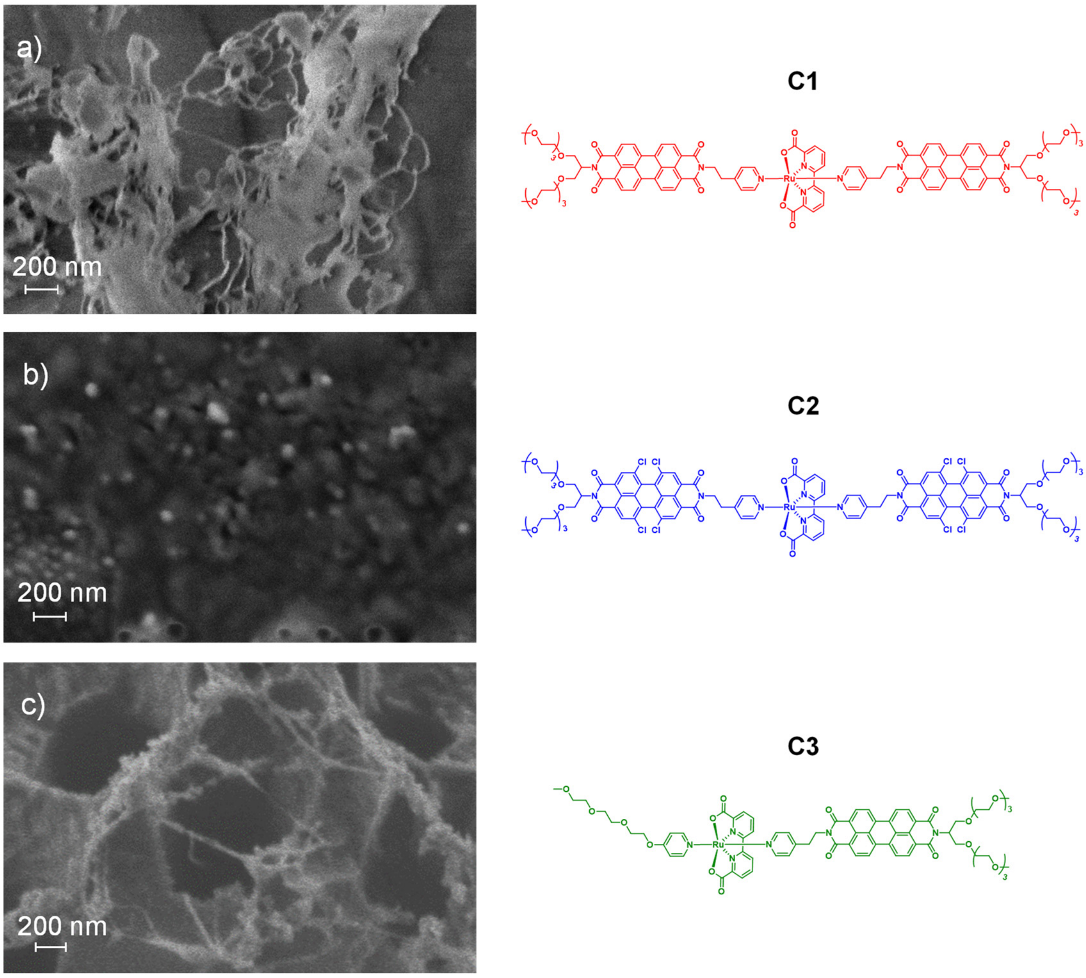

Figure 53: (a–c) Cryo-SEM images of solutions of **C1** (a), **C2** (b), and **C3** (c) in acetonitrile/water (pH 7) 1:1 at a concentration of 10^{-5} M and the respective molecular structures of **C1**–**C3**.

In conclusion, it could be shown that by tuning the axial PBI ligands, the aggregate morphologies of the {Ru(bda)}-PBI complexes in aqueous solutions can specifically be manipulated. By reducing the amount of PBI ligands from two to one, the aggregation tendency becomes reduced and shorter fibrous aggregates can be obtained. If a large core-twist is induced in the PBI ligand, the formation of extended aggregates is completely prevented and smaller nanoparticles are obtained instead.

3.3.5 Water Oxidation Catalysis by Supramolecular Aggregates

The aggregated {Ru(bda)}-PBI complexes **C1**–**C3** have been studied regarding their water oxidation performance. Those experiments have been performed for different catalyst concentrations in acidic solutions (acetonitrile/water (pH 1) 1:1) by adding cerium(IV) ammonium nitrate (CAN) as a sacrificial oxidant and applying pressure transducers for the oxygen detection. As a comparison, the non-aggregating reference catalyst [Ru(bda)(pic)$_2$] (**6**) has also been tested under the same reaction conditions. Under optimized conditions, catalyst **6** exhibits a TON of 2010,[64] but with higher acetonitrile contents, as used in these studies for solubility reasons, a considerably lower performance is observed. Obviously, this can be explained by the competitive binding of acetonitrile to the seventh coordination site of the ruthenium center (*vide supra*, **Figure A13**).[216, 311]

For complex **C1**, which forms large networks of extended nanofibers in aqueous solutions, an incubation time of 1–5 minutes is observed before the oxygen evolution starts. This indicates that a structural change has to occur before catalysis begins, and that the initial system only represents a pre-catalyst that needs to be activated first. This finding can be explained by the fact that the catalytically active {Ru(bda)} centers are shielded inside the aggregates, and are therefore not easily accessible for the oxidant and substrate water molecules. Therefore, loosening of the aggregate structure might be necessary to provide enough catalytically active sites exposed to the surrounding. In contrast, if **C3** is used as the catalyst, an incubation time is still observed, which is not so much dependent on the catalyst concentration, however. The catalytic activity of these both systems is very similar, with maximal turnover numbers (TONs) of 830 (**C1**) and 840 (**C3**), whereas the reference complex [Ru(bda)(pic)$_2$] only reaches a TON of 610 under the same reaction conditions (**Figure 54**). Accordingly, the stability of the complexes **C1** and **C3** is slightly increased compared to the non-aggregated reference catalyst **6** by embedding the catalytic centers into fibrous aggregates. However, the kinetics of the reaction are drastically changed, since for both aggregated complexes an incubation time is observed, indicating initial structural changes, which is not the case for [Ru(bda)(pic)$_2$] (**6**). Altogether, both complexes **C1** and **C3** with the planar **PBI-1** as a ligand show very similar aggregate morphologies with comparable catalytic performances.

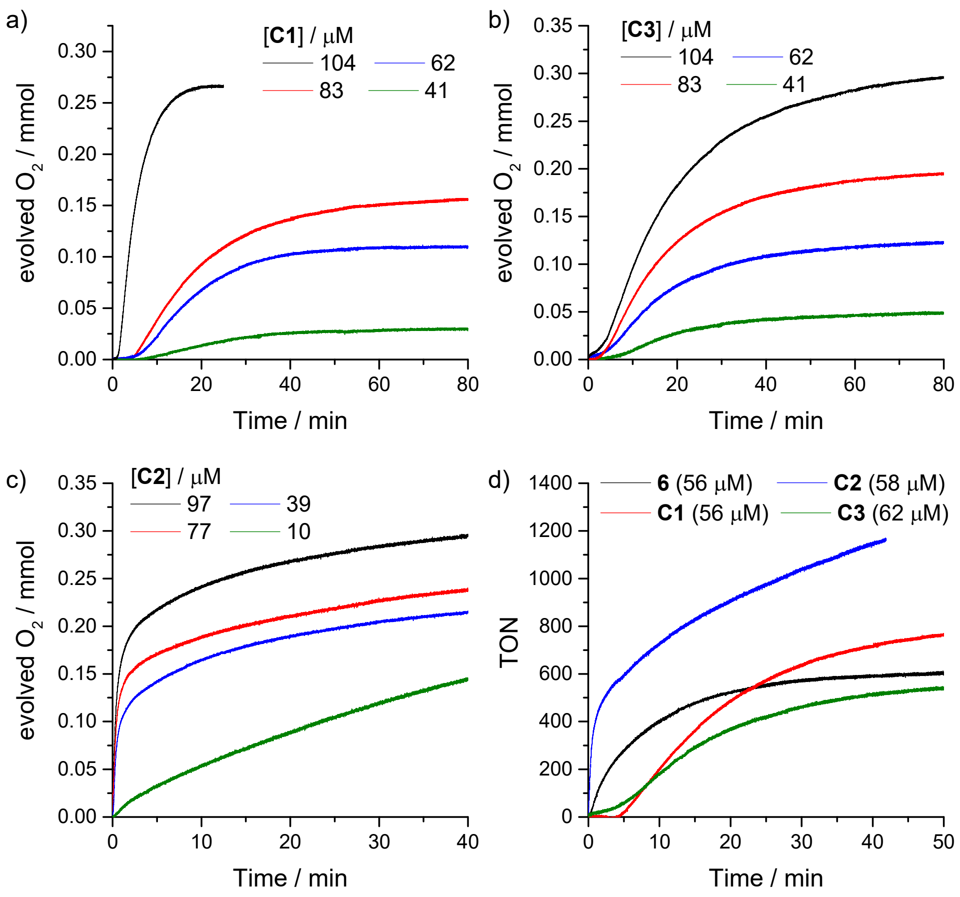

Figure 54: (a–c) Oxygen evolution as a function of reaction time in 3.4 mL acetonitrile/water (pH 1) 1:1 using CAN (1.0 g, 1.82 mmol) as sacrificial oxidant for the different Ru-PBI catalysts: **C1** (a), **C3** (b), and **C2** (c). (d) Comparison of turnover numbers achieved by catalysts **C1**–**C3** and the reference catalyst [Ru(bda)(pic)$_2$] (**6**) at comparable catalyst concentrations.

A different picture is obtained when **C2** with the core-twisted tetrachloro **PBI-2** ligand is used as the catalyst, which forms nanoparticles instead of extended nanofibers upon aggregation. Then, the oxygen evolution immediately starts without any incubation period, and significantly higher TONs of more than 4800 can be achieved. This leads to the conclusion that for **C2**-aggregates no structural rearrangement to activate the catalyst is required because the catalytic {Ru(bda)} sites are already better accessible in such small aggregated structures. The increased stability of the system can furthermore be explained by the higher oxidative stability of the 1,6,7,12-tetrachlorinated PBI ligands, which are more difficult to oxidize by ca. 250 mV compared to the bay-unsubstitued PBI ligands as it has been corroborated with cyclic voltammetry.

3.3.6 Conclusion

For the first time, we have equipped the {Ru(bda)} water oxidation catalyst with perylene bisimide containing axial ligands. Within this project, two different PBI ligands have been synthesized, with different optical, electrochemical, and aggregation properties, that can coordinate to transition metals *via* the pyridyl groups. These PBI derivatives have been used as axial ligands to coordinate the {Ru(bda)} fragment, and thus to construct complexes containing strongly aggregating subunits. Investigations with UV/Vis spectroscopy, AFM and cryo-SEM demonstrated that the aggregation behavior of those complexes can be controlled by the PBI ligand structure and the amount of PBI containing ligands. Whereas for bay-unsubstituted **PBI-1** ligands extended nanofibers are formed, much smaller nanoparticles are obtained using the 1,6,7,12-tetrachloro-substituted **PBI-2** ligand. Interestingly, these complexes with different aggregate morphologies also exhibit very different catalytic performances for the water oxidation reaction. On the one hand, the nanofibers of **C1** and **C3** act as pre-catalysts with an incubation period of a few minutes. Slightly increased turnover numbers compared to the non-aggregated reference have been achieved for these fibrous systems. On the other hand, the smaller nanoparticles of **C2** are immediately catalytically active and exhibit a much higher turnover number. Obviously, the smaller aggregate size is beneficial, presumably because it provides a better accessibility to the catalytic sites. The present study shows that the longevity of catalysts can generally be increased by incorporation into supramolecular aggregates that serve as stabilizing matrices. An explanation for the improved stability might be that one of the major decomposition pathways, namely the dissociation of the axial ligands,[63, 64] becomes partially suppressed in such aggregates.

CHAPTER 4 SUMMARY

4.1 Summary

Within the 21st century, our society's thirst for energy will lead to the total consumption of fossil fuels. This makes the development of alternative energy carriers and efficient processes for their generation inevitable. In this regard, hydrogen is a promising fuel, which facilitates long-term energy storage and clean combustion. Most importantly, it can be generated by the splitting of water, one of the most abundant resources on earth. The oxidation of water to generate oxygen and protons is the critical step of this process, and thus the development of highly efficient water oxidation catalysts (WOCs) is required. Up to now, relatively few attempts have been undertaken to improve the catalytic performance by modifying the chemical environment in close proximity to the active site. Accordingly, in this dissertation, different supramolecular approaches are established to manipulate the activity of "state of the art" WOCs based on the {Ru(bda)} catalytic fragment (bda = 2,2'-bipyridine-6,6'-dicarboxylate). The first part of the thesis focusses on the incorporation of WOCs into metallosupramolecular macrocycles, in which the metal centers possess a catalytic function in addition to their structural role. The second part addresses the embedding of catalytic fragments into self-assembled aggregates by using {Ru(bda)} complexes bearing perylene bisimde (PBI) containing ligand systems (**Figure 55**).

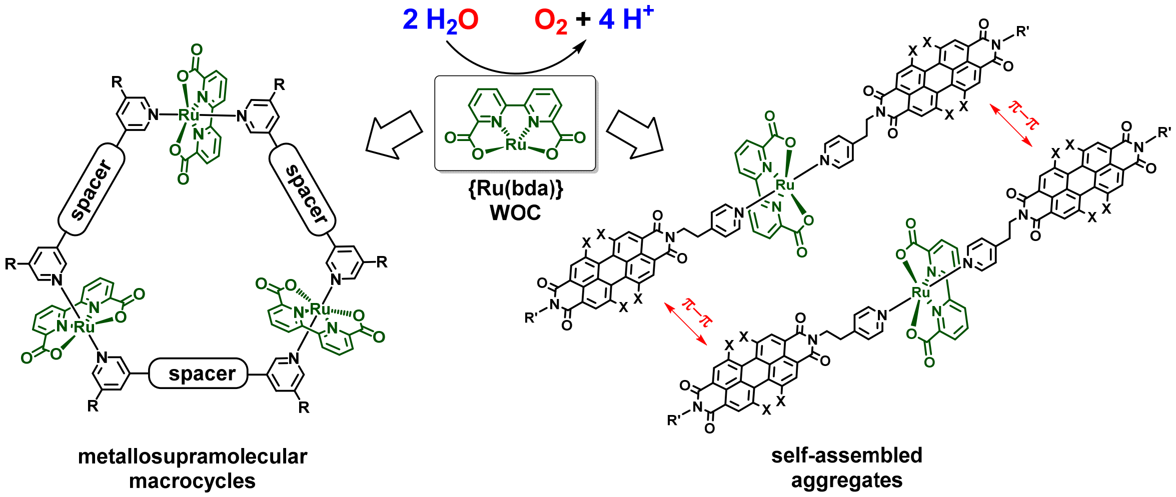

Figure 55: Supramolecular strategies investigated within this thesis: Incorporation of the {Ru(bda)} WOC fragment into metallosupramolecular macrocycles (left), and embedding into aggregates formed by the self-assembly of {Ru(bda)} complexes equipped with perylene bisimide (PBI) containing axial ligands (right).

In **chapter 3.1**, metallosupramolecular macrocycles are presented that gather three {Ru(bda)} catalytic centers by connecting them with ditopic bridging ligands. It is of particular interest to investigate how the cavity size and the ruthenium-ruthenium distances of such trinuclear assemblies influence the catalytic performance. Accordingly, the synthesis and characterization of a series of four differently sized trinuclear macrocycles is described (**Figure 56**), and a crystal structure for the largest macrocycle (**MC4**) is compared to a non-cyclic reference complex to identify important structural features that are affected by the incorporation into a cyclic assembly. In order to gain a better understanding of the cyclization process, ligand exchange reactions are discussed for a simple mononuclear reference system.

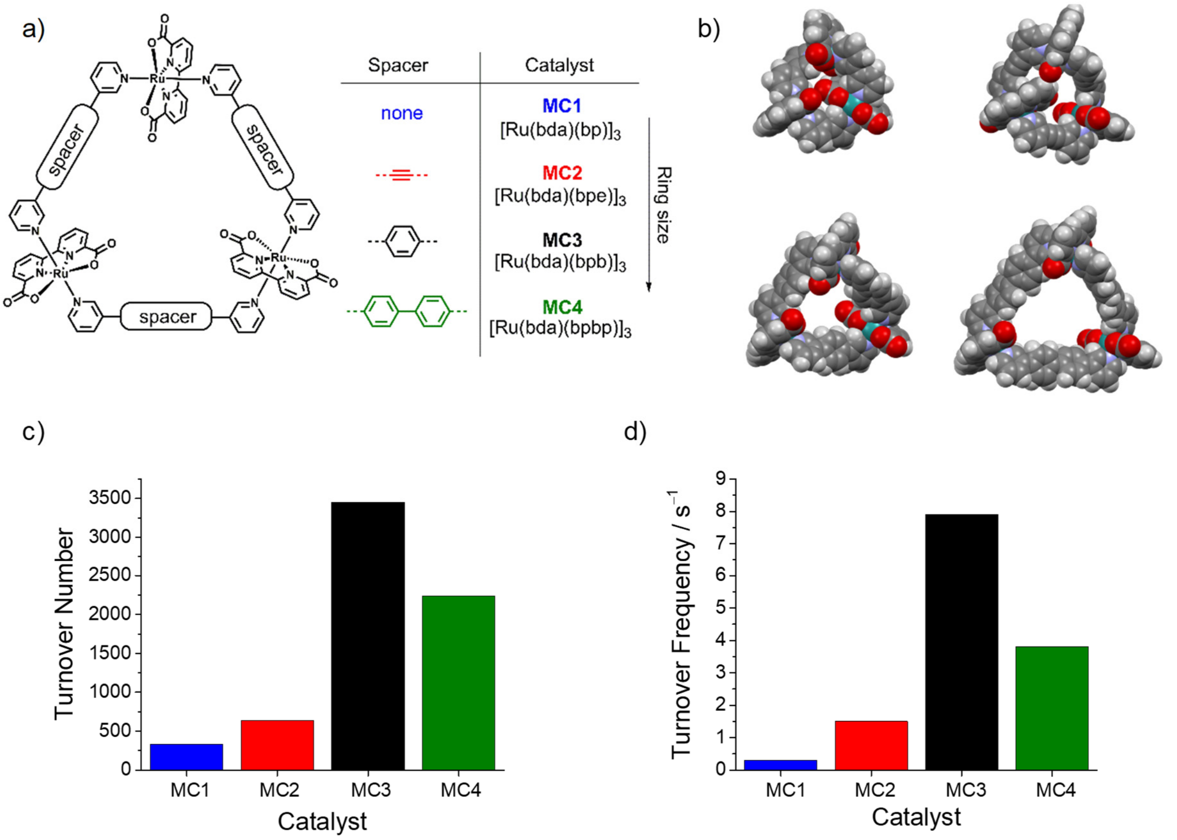

Figure 56: (a) A series of differently sized trinuclear macrocycles for water oxidation synthesized using various bridging ligands. (b) Space-filling models for the series of macrocycles reveal very different accessible cavity sizes. (c, d) Comparison of the catalysts with respect to their catalytic performance under the same reaction conditions in terms of the turnover number (c), and the turnover frequency (d).

Before the focus is laid on water oxidation catalysis, the optical and electrochemical properties of the trinuclear complexes are discussed. This is done for the different oxidation states that the ruthenium centers have to pass (+II, +III, +IV) before the O–O bond formation takes place at a Ru(V)-oxo species. Interesting spectral differences concerning new low-energetic UV/Vis absorption bands in those oxidation states are observed for the macrocycles. To identify the responsible transitions, density functional theory (DFT) calculations were performed in collaboration with the group of Prof. Mitrić (Theoretical Chemistry, University of Würzburg). The calculations reveal that the energy of those transitions heavily depends on the coordination bond lengths between aqua- or hydroxo-ligands and the ruthenium centers. The crucial bond lengths are strongly affected by the hydrogen bonding situation of the water molecules inside the macrocyclic cavity, which differs depending on the ring-size. Those water molecules can form proton-relay chains connecting the individual catalytic sites (**Figure 57a**), which facilitates cooperative effects between them during important proton-coupled electron transfer steps. If the macrocycles are large enough, all catalytic centers, with their additional coordination site for water, point towards the interior of the cavity allowing for such cooperative interactions (**Figure 57b**). However, if the macrocycles are too small, those centers are oriented to the exterior due to steric crowding and no interaction between them can take place (**Figure 57c**). Consequently, the catalytic activity and the H/D kinetic isotope effect follow a clear trend that correlates with the macrocyclic ring-size, with an intermediate size (**MC3**) being optimal (**Figure 56c** and **56d**). Furthermore, detailed mechanistic studies were performed revealing that the oxygen-oxygen bond formation is achieved by the nucleophilic attack of a substrate water molecule on a highly oxidized Ru^{V}=O species, and that the Ru^{IV}–OH/Ru^{V}=O oxidation is rate-determining. Altogether, it is demonstrated that the incorporation of {Ru(bda)} fragments into metallosupramolecular assemblies gives access to catalytic systems with increased stabilities and activities and that a fine-tuning of the catalytic system is possible by a careful manipulation of the ring size.

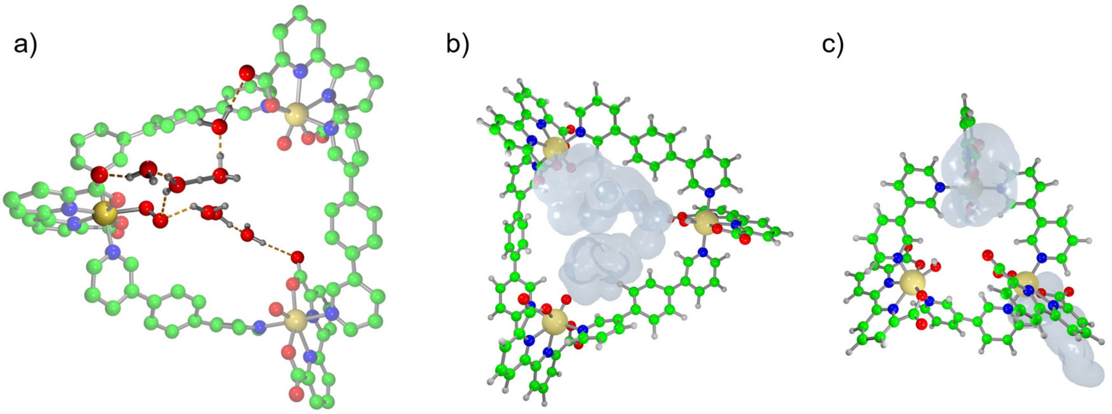

Figure 57: (a) Visualization of the water network acting as proton relay chain during the O–O bond formation of **MC3**, which occurs *via* the nucleophilic attack of a substrate water molecule on a Ru^{V}=O center. (b, c) Comparison of different pathways for the proton removal from the catalytic center during the rate-determining Ru^{IV}–OH/Ru^{V}=O oxidation *via* water networks for two macrocyclic catalysts of different size: **MC3** (b) and **MC1** (c).

As described above, a well-chosen intermediate ring-size of metallosupramolecular macrocycles is beneficial for the correct organization of the water network inside the cavity, and thus for efficient water oxidation catalysis. However, the water solubility of those assemblies decreases drastically with increasing molecular size, necessitating the addition of large amounts of acetonitrile as organic co-solvent. The use of organic co-solvents is highly undesired from an ecological point of view. Furthermore, acetonitrile is known to act as a ligand to transition metal WOCs and thus could adversely affect catalytic activity. This solubility problem is consequently addressed in **chapter 3.2** by an appropriate functionalization of the optimally sized macrocycle (**MC3**) with solubilizing side-chains at the bridging ligands. The introduction of triethylene glycol chains makes it possible to halve the required amount of co-solvent, whereas positively charged ammonium side-groups enable water oxidation catalysis in pure water (**Figure 58**). The solubility in pure water also allows ^{1}H NMR spectroscopic studies of the macrocyclic system that otherwise suffer from spectrum broadening related to acetonitrile coordination. Thereby, unequivocal proof for the high stability of the cyclic assemblies in acidic aqueous environment was obtained.

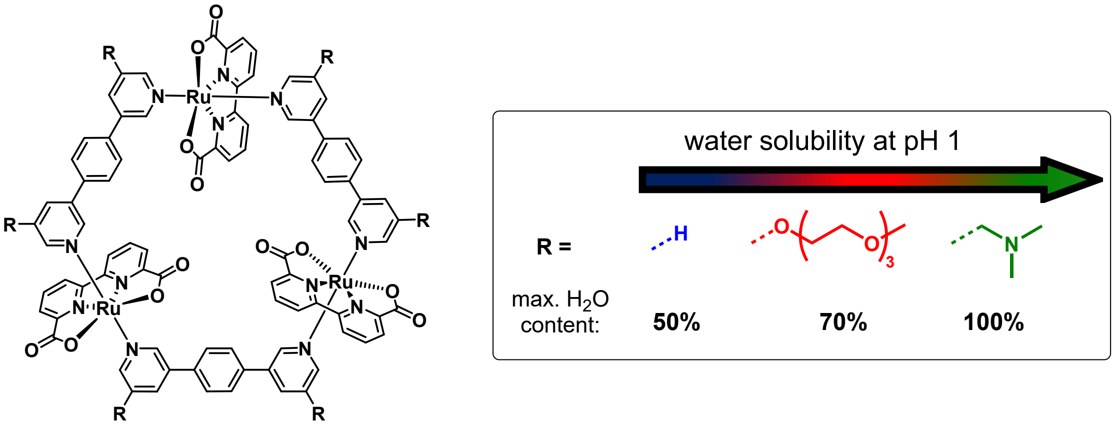

Figure 58: Functionalization of optimally sized trinuclear macrocycle with solubilizing side-chains at the bridging ligands to improve water solubility.

An entirely different approach has been pursued in **chapter 3.3**, in which the embedding of water oxidation catalysts into supramolecular aggregates is described. For that purpose, the {Ru(bda)} catalyst was equipped with perylene bisimide containing ligands that tend to self-assemble in polar solvents. Two novel PBI ligands have been synthesized for the construction of the respective complexes bearing triethylene glycol swallowtail groups as solubilizing imide substituents (**Figure 59**). The bay-substitution pattern was varied to control the aggregation behavior and the oxidative stability of the π-system. Exchanging the protons with chloro-substituents at all four bay-positions leads to a stronger core-twist of the perylene and a decreased tendency towards aggregation. Moreover, their electron withdrawing effects make the PBI molecule more difficult to oxidize, as it was corroborated with cyclic voltammetry.

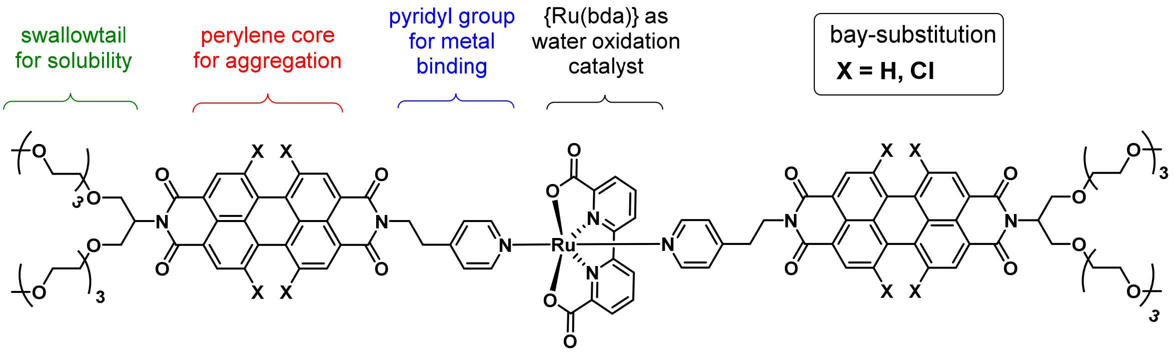

Figure 59: Coordination complex of the {Ru(bda)} WOC fragment with novel axial perylene bisimide ligands.

The novel PBI derivatives were used as axial ligands for the construction of the respective {Ru(bda)} coordination complexes. In aqueous medium those complexes form aggregated structures due to the hydrophobic effect and strong π-π interactions between the perylene bisimide moieties. This aggregation was studied with UV/Vis spectroscopy, atomic force microscopy (AFM) and cryogenic scanning electron microscopy (cryo-SEM). By manipulating the PBI structure, different aggregate morphologies can be generated. For complexes equipped with bay-unsubstituted PBIs, extended nanofibers are obtained, whereas the complexes with tetrachloro-substituted PBI ligands form smaller nanoparticular aggregates (**Figure 60a**). Catalytic studies reveal that all aggregated systems show higher turnover numbers compared to a non-aggregated {Ru(bda)} catalyst. However, strong differences for the stability of the catalytic system and the reaction kinetics are observed among the different complexes. The extended nanofibers show an incubation time before the oxygen evolution begins, indicating structural changes in the initial phase of catalysis. On the other hand, the nanoparticles show no incubation period and a higher catalytic activity and stability (**Figure 60b**). Thus, the discrete PBI ligands provide access to different aggregate morphologies with distinct catalytic behavior that all show an increased stability compared to a non-aggregated reference catalyst. Important factors controlling the catalytic performance are the accessibility of the catalytic site, which is connected to the aggregate size, and the stability of the organic PBI ligand scaffold towards oxidation under the harsh reaction conditions.

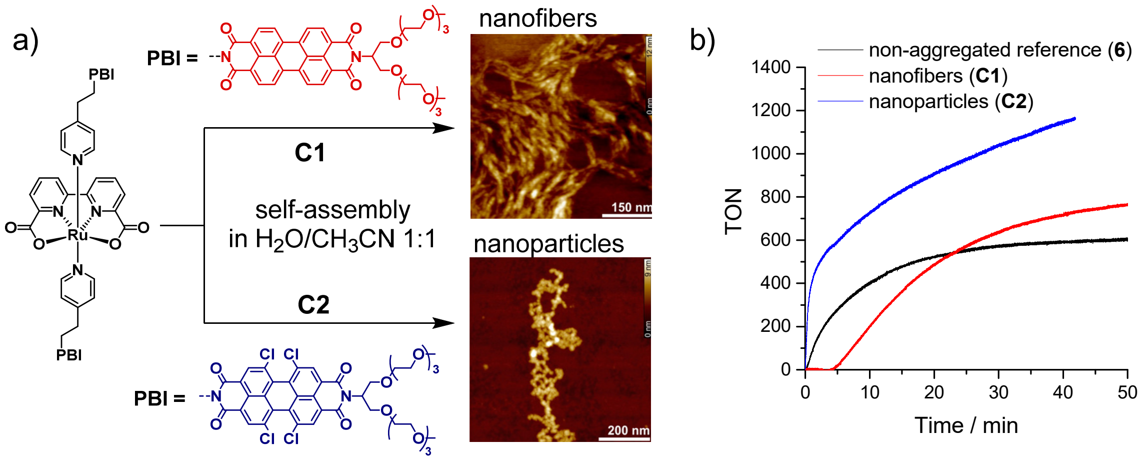

Figure 60: (a, b) The self-assembly of {Ru(bda)} catalysts **C1** and **C2** equipped with perylene bisimide (PBI) ligands in aqueous environment leads to the formation distinct aggregate morphologies (a), with different catalytic activities under same reaction conditions (b).

Altogether, two supramolecular concepts have successfully been established in the scope of this thesis that both lead to more stable catalytic systems for water oxidation. Both approaches are based on the well-established {Ru(bda)} WOC fragment and its incorporation into larger structures by axial ligand manipulation. Using ditopic bridging ligands, a series of differently sized metallosupramolecular macrocycles was synthesized, and the optimal ring-size has been determined. Additionally, the water solubility of the optimized structure could be improved substantially. On the other hand, the coordination of the {Ru(bda)} fragment with ligands containing perylene bimide (PBI) moieties yielded complexes that form aggregated structures in aqueous environment. These aggregates show an increased stability compared to non-aggregated systems and can be tuned regarding their aggregate morphologies and catalytic performance by the choice of different PBI ligands.

4.2 Zusammenfassung

Der stetig steigende Hunger unserer Gesellschaft nach Energie wird noch im 21. Jahrhundert zum vollständigen Verbrauch der fossilen Brennstoffe führen und macht daher die Entwicklung alternativer Energieträger und effizienter Verfahren für ihre Erzeugung notwendig. In dieser Hinsicht ist Wasserstoff ein äußerst vielversprechender Brennstoff, der eine langfristige Energiespeicherung und eine saubere Verbrennung ermöglicht. Darüber hinaus lässt er sich durch die Spaltung von Wasser gewinnen, einer nahezu unerschöpflichen Ressource. Die Wasseroxidation zur Erzeugung von Sauerstoff und Protonen gilt als der kritische Schritt dieses Prozesses und erfordert daher die Entwicklung effizienter Wasseroxidationskatalysatoren (WOK). Da supramolekulare Konzepte bisher eher selten Anwendung zur Steigerung der katalytischen Aktivität fanden, wurden im Rahmen dieser Dissertation verschiedene metallosupramolekulare Ansätze dahingehend erprobt. Aufgrund seiner hohen katalytischen Aktivität in mit axialen Pyridinliganden versehenen Komplexen wurde das {Ru(bda)}-Fragment als Katalysator-Leitmotiv gewählt (bda = 2,2'-Bipyridin-6,6'-dicarboxylat).

Der erste Teil dieser Arbeit beschäftigt sich mit der Synthese und Untersuchung von metallosupramolekularen Makrozyklen, in denen das Metallzentrum neben einer strukturellen auch über eine katalytische Funktion verfügt. Im zweiten Teil wird hingegen die Synthese von {Ru(bda)}-Komplexen mit Perylenbisimid (PBI)-Ligandensystemen diskutiert, welche die Einbettung der katalytischen Zentren in selbstassemblierte Aggregate ermöglichen (**Abbildung 55**).

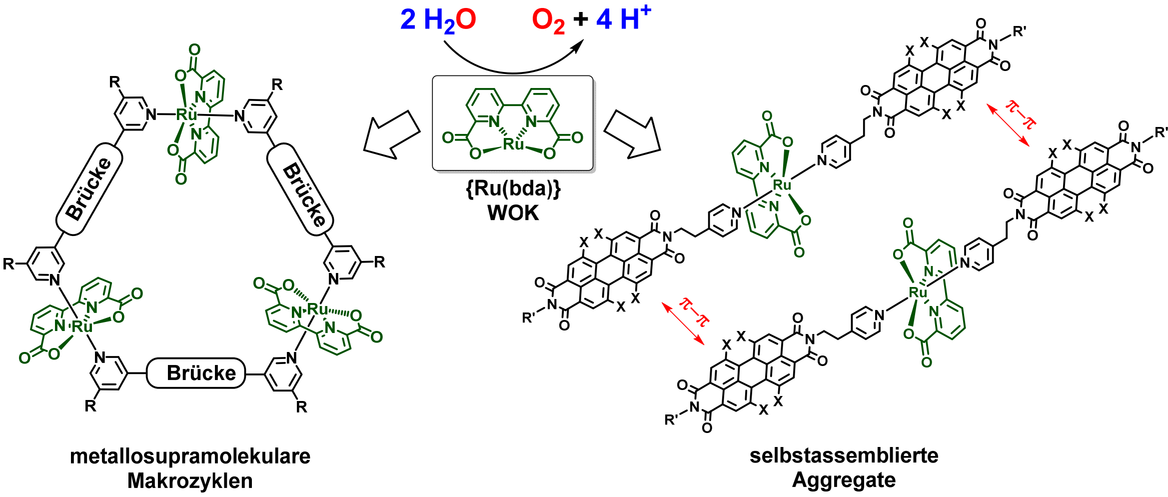

Abbildung 55: In dieser Arbeit vorgestellte supramolekulare Konzepte: Einbau von {Ru(bda)} Wasseroxidationskatalysatoren (WOKs) in metallosupramolekulare Makrozyklen (links) und deren Einbettung in selbstassemblierte Aggregate von Komplexen mit axialen Perylenbisimid Liganden (rechts).

In **Kapitel 3.1** werden metallosupramolekulare Makrozyklen vorgestellt, welche durch die Verknüpfung dreier {Ru(bda)}-Zentren mit verbrückenden Liganden aufgebaut sind. Das Ziel war es insbesondere, den Einfluss der Ringgröße auf die katalytische Aktivität zu untersuchen. Deshalb wurde eine Serie aus vier unterschiedlich großen Makrozyklen durch die Variation des verbrückenden Liganden erstellt (**Abbildung 56a** und **56b**). Die Kristallstruktur für den größten Makrozyklus (**MC4**) wurde mit der eines azyklischen, mononuklearen Referenzkomplexes verglichen, um den Einfluss der Zyklisierung auf wichtige strukturelle Parameter zu ermitteln. Zum besseren Verständnis der Makrozyklus-Bildung wurden darüber hinaus Ligandenaustauschreaktionen anhand eines einfachen mononuklearen Modellsystems untersucht.

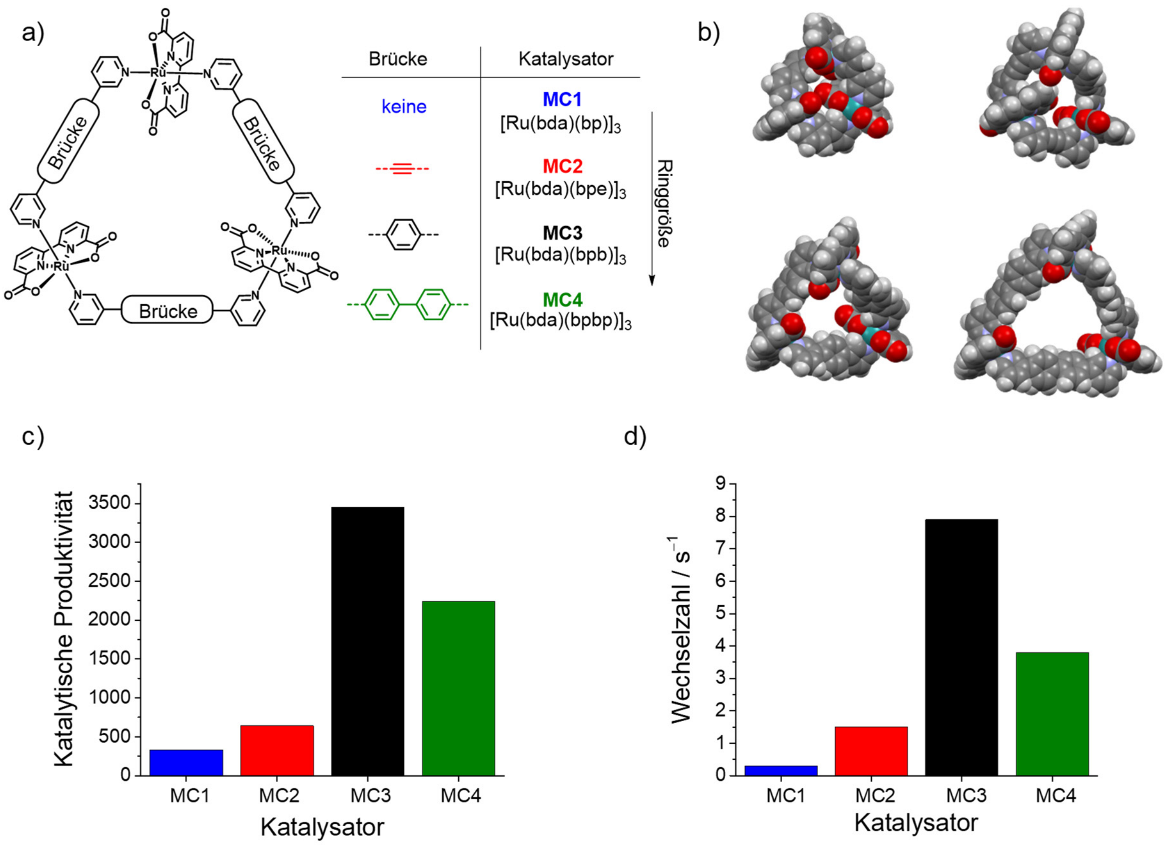

Abbildung 56: (a) Eine Serie verschieden großer trinuklearer {Ru(bda)}-Makrozyklen wurde durch die Variation des verbrückenden Liganden hergestellt. (b) Die Kalotten-Modelle für diese Serie verdeutlichen die unterschiedlich große Kavität. (c, d) Vergleich der Katalysatoren unter denselben Reaktionsbedingungen in Bezug auf ihre katalytische Produktivität (c) und ihre katalytische Wechselzahl (d).

Den Experimenten zur Wasseroxidationskatalyse vorausgestellt war die Untersuchung der Makrozyklen hinsichtlich ihrer optischen und elektrochemischen Eigenschaften. Betrachtet wurden alle Oxidationsstufen (+II, +III, +IV), welche die Ruthenium Zentren durchlaufen müssen bevor die Ausbildung der O–O Bindung an einer Ru(V)-Oxo Spezies stattfinden kann. Interessante niederenergetische Absorptionsbanden wurden beobachtet, welche in ihrer Intensität eine starke Abhängigkeit bezüglich der Ringgröße aufweisen. In einer Kooperation mit Prof. Mitrić (Theoretische Chemie, Universität Würzburg) konnten die verantwortlichen Übergänge mittels Dichtefunktionaltheorie-Rechnungen (DFT) identifiziert werden. Darüber hinaus wurde gezeigt, dass die energetische Lage der entsprechenden Absorptionsbanden stark von der Bindungslänge zwischen Ruthenium-Zentren und koordinierten Aqua- bzw. Hydroxo-Liganden beeinflusst wird. Diese Abhängigkeit beruht auf der unterschiedlichen Ausprägung von Wassernetzwerken in den verschieden großen Makrozyklus-Kavitäten. Die Wassermoleküle können zudem als Protonenrelais zwischen zwei Ruthenium-Zentren mit ihrer Koordinationsstelle für Wasser fungieren und somit kooperative Effekte für wichtige protonengekoppelte Reaktionsschritte ermöglichen (**Abbildung 57a**). Sind die Zyklen groß genug, orientieren sich alle Ruthenium-Zentren ins Innere der Kavität, sodass derartige kooperative Wechselwirkungen auftreten können (**Abbildung 57b**). Sind die Makrozyklen hingegen zu klein, ist die optimale Ausrichtung der {Ru(bda)}-Zentren und somit deren Interaktion nicht möglich. (**Abbildung 57c**).

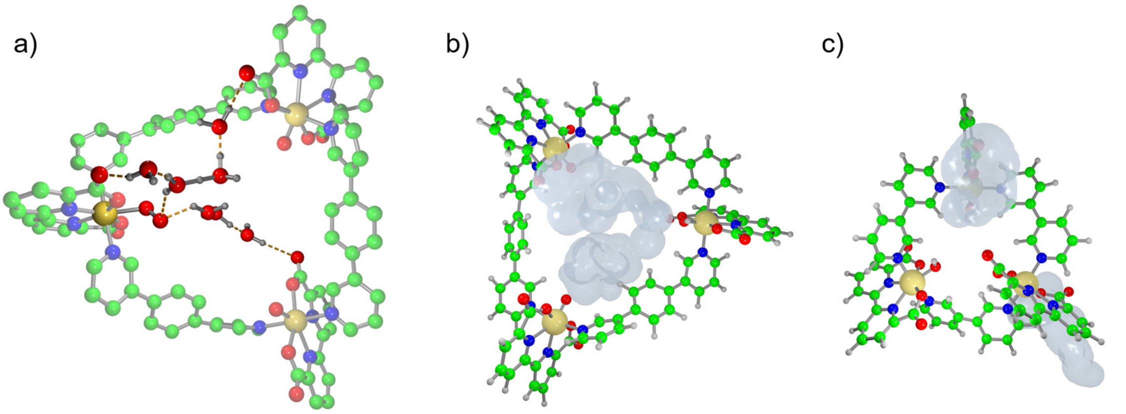

Abbildung 57: (a) Veranschaulichung des Wassernetzwerks, welches als Protonenrelais zwischen zwei {Ru(bda)}-Zentren während des O–O Bindungsschrittes fungiert. Dieser erfolgt durch den nukleophilen Angriff eines Substrat-Wassermoleküls an einer Ru^{V}=O Spezies. (b, c) Vergleich der unterschiedlichen Möglichkeiten für **MC3** (b) und **MC1** (c), das abgespaltene Proton nach der geschwindigkeitsbestimmenden Ru^{IV}–OH/Ru^{V}=O Oxidation über Wassernetzwerke vom reaktiven Zentrum abzuführen.

Demzufolge sind auch die katalytische Aktivität und der zu beobachtende H/D kinetische Isotopeneffekt von der Ringgröße der Makrozyklen abhängig und eine mittlere Ringgröße (**MC3**) erweist sich als optimal (**Abbildung 56c** und **56d)**. Anhand detaillierter mechanistischer Untersuchungen wurde des Weiteren festgestellt, dass die O–O Bindung durch den nukleophilen Angriff eines Wassermoleküls an einer Ru^{V}=O Spezies geknüpft wird, und dass die Ru^{IV}–OH/Ru^{V}=O Oxidation geschwindigkeits-bestimmend ist.

Insgesamt hat diese Studie ergeben, dass die Aktivität und Stabilität von {Ru(bda)}-Katalysatoren durch den Einbau in zyklische metallosupramolekulare Strukturen prinzipiell gesteigert und dass der Wasseroxidationsmechanismus beeinflusst werden kann. Außerdem wurde gezeigt, dass kooperative Effekte auftreten können, welche stark von der Ausrichtung und dem Abstand zwischen den Ruthenium Zentren abhängen.

Wie zuvor beschrieben, weisen die größeren Makrozyklen der Serie eine höhere katalytische Aktivität für die Wasseroxidationsreaktion auf, da eine ausreichende Ringgröße Voraussetzung für kooperative Wechselwirkungen zwischen den katalytischen Zentren ist. Jedoch führt die zunehmende Größe dieser metallosupramolekularen Strukturen zu einer deutlichen Abnahme der Wasserlöslichkeit, was die Zugabe größerer Mengen von Acetonitril als organischem Co-Solvens notwendig macht. Im Hinblick auf eine umweltfreundliche Anwendung gilt es jedoch die Verwendung organischer Lösungsmittel weitestgehend zu minimieren. Überdies kann Acetonitril an das Ruthenium-Zentrum koordinieren und somit die katalytische Aktivität beeinträchtigen. In **Kapitel 3.2** wird daher dem Löslichkeitsproblem durch die entsprechende Funktionalisierung der Makrozyklen begegnet. Von dem katalytisch aktivsten Makrozyklus (**MC3**) wurden Derivate synthetisiert, welche an den verbrückenden Liganden mit löslichkeitsfördernden Gruppen ausgestattet sind. Das Einbringen von Triethylenglycol-Ketten erlaubt eine Verringerung des benötigten Acetonitril-Anteils auf die Hälfte, während positiv geladene Ammoniumgruppen die Wasseroxidation in reinem Wasser ermöglichen (**Abbildung 58**). Die Löslichkeit in reinem Wasser erlaubt zudem ^{1}H-NMR spektroskopische Untersuchungen, ohne die durch Acetonitril-Koordination ausgelösten Signalverbreiterungen. Dadurch war es möglich, die hohe Stabilität der Makrozyklen unter wässrig-sauren Bedingungen zweifelsfrei nachzuweisen.

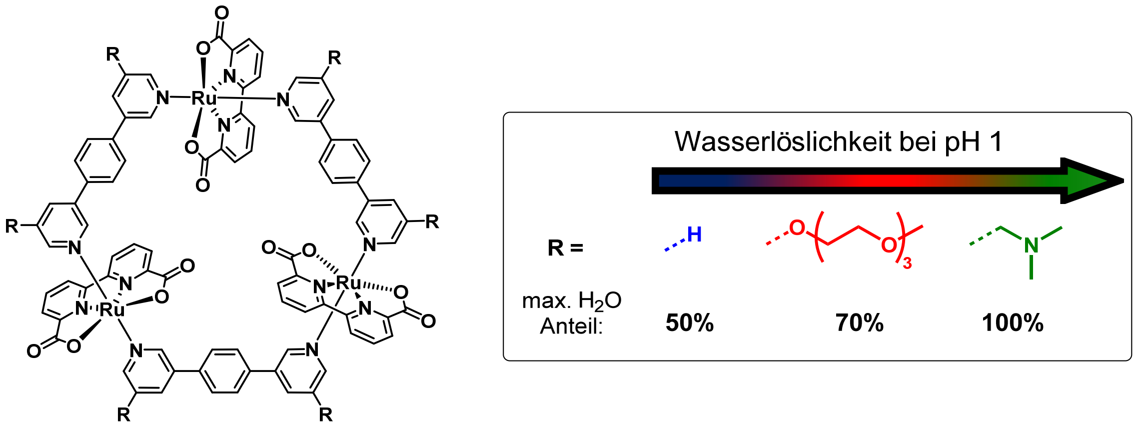

Abbildung 58: Makrozyklen mit optimaler Ringgröße und gesteigerter Wasserlöslichkeit durch adäquate Funktionalisierung der verbrückenden Liganden mit löslichkeitsfördernden Seitenketten.

Ein gänzlich anderer Ansatz wird in **Kapitel 3.3** vorgestellt. Hier wird die Einbettung von Wasseroxidationskatalysatoren in selbstassemblierte Aggregate beschrieben. Zu diesem Zweck wurde das {Ru(bda)}-Fragment mit axialen Perylenbisimid (PBI)-Liganden ausgestattet, welche zur Aggregation in polaren Lösungsmitteln neigen (**Abbildung 59**). Ein Triethylenglycol-Schwalbenschwanz als Imidsubstituent garantiert die gewünschte Wasserlöslichkeit. Die Buchtsubstituenten wurden variiert, um die Aggregationseigenschaften und die oxidative Stabilität der Liganden und somit der Komplexe zu beeinflussen. Der Austausch aller vier Protonen gegen Chlor-Substituenten induziert eine stärkere Verdrehung der Naphthyl-Untereinheiten des Perylengrundkörpers und verringert somit die Tendenz zur Ausbildung größerer Aggregate. Darüber hinaus führt deren elektronenziehender Effekt zu einer Erhöhung des PBI-Oxidationspotentials und somit zu einer höheren Stabilität unter oxidativen Bedingungen.

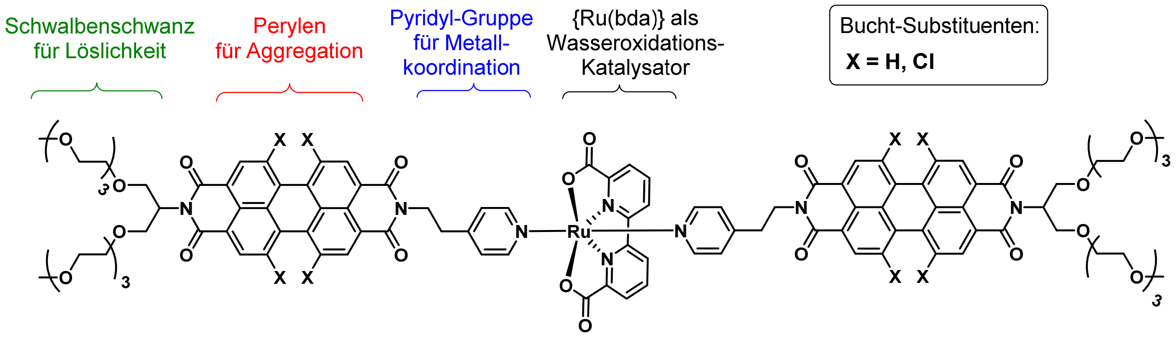

Abbildung 59: Komplex des {Ru(bda)} WOK Fragments mit neuen axialen Perylenbisimid-Liganden.

Durch Koordination der PBI-Liganden an das {Ru(bda)}-Fragment wurden die entsprechenden Rutheniumkomplexe hergestellt. In wässrigem Medium kommt es zur Aggregation dieser Komplexe aufgrund des hydrophoben Effekts und starker π-π

Wechselwirkungen zwischen den Perylenbisimid-Einheiten. Die Aggregation wurde mit Hilfe von UV/Vis Spektroskopie, Rasterkraftmikroskopie und cryo-Rasterelektronenmikroskopie untersucht. In Abhängigkeit von den PBI-Liganden werden verschiedene Aggregatstrukturen erhalten. Komplexe mit buchtunsubstituierten PBI Liganden erzeugen lange Nanofasern, während die Verwendung von Tetrachloro-PBI Liganden zur Bildung von deutlich kleineren Nanopartikeln führt. (**Abbildung 60a**) Alle aggregierten Systeme zeigen eine erhöhte katalytische Stabilität und somit höhere Umsatzzahlen als ein nichtaggregiertes {Ru(bda)}-Referenzsystem. Jedoch zeigen sich deutliche Unterschiede für die verschiedenen Ru-PBI-Komplexe bezüglich der Aktivität sowie der Reaktionskinetik. (**Abbildung 60b**) Die zu Nanofasern aggregierenden Komplexe weisen eine Inkubationszeit vor der Sauerstofffreisetzung aus. Dies deutet darauf hin, dass ein katalytisch aktives System erst nach einer anfänglichen strukturellen Veränderung erhalten wird. Diese Aktivierungsphase entfällt bei der Verwendung des Komplexes mit Tetrachloro-PBI-Liganden. Die dadurch erhaltenen Nanopartikel zeichnen sich zudem durch eine deutlich höhere katalytische Stabilität auf. Einen großen Einfluss auf die katalytischen Eigenschaften haben die Zugänglichkeit des katalytisch aktiven {Ru(bda)}-Zentrums und die Stabilität der organischen Liganden gegenüber oxidativem Abbau.

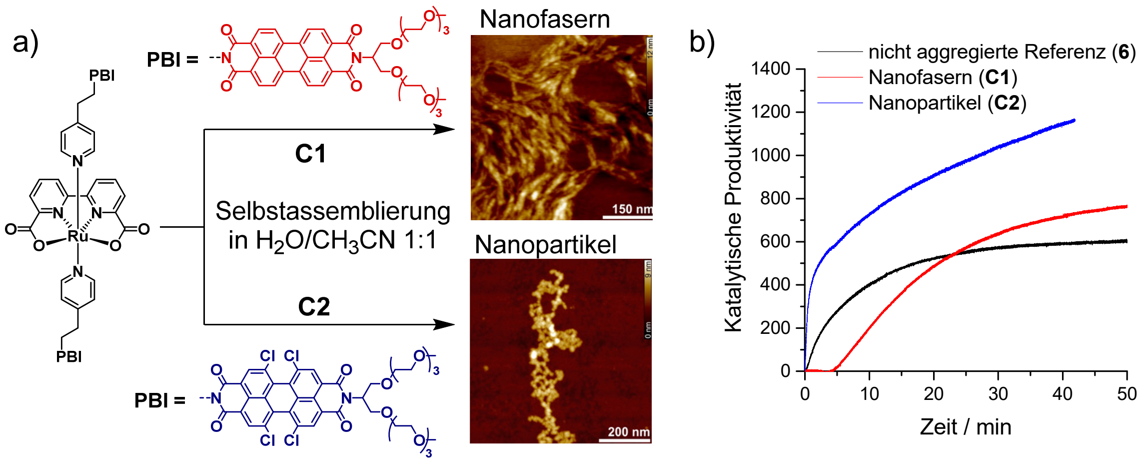

Abbildung 60: (a, b) Die Selbstassemblierung von mit axialen Perylenbisimid (PBI)-Liganden ausgestatteten {Ru(bda)}-Katalysatoren **C1** und **C2** erzeugt katalytisch aktive Aggregate für die Wasseroxidationsreaktion mit unterschiedlicher Morphologie (a) und katalytischer Aktivität (b).

Zusammengefasst wurden im Rahmen dieser Dissertation zwei supramolekulare Konzepte für die Verbesserung der Stabilität von Wasseroxidationskatalysatoren erfolgreich etabliert. Beide Ansätze basieren auf dem literaturbekannten {Ru(bda)}-Fragment und seiner Einbettung in größere supramolekulare Strukturen. Durch die Verwendung verbrückender axialer Liganden wurde eine Serie trinuklearer metallosupramolekularer Makrozyklen hergestellt und die optimale Ringgröße in Bezug auf die katalytische Aktivität ermittelt. Darüber hinaus gelang es, die Wasserlöslichkeit dieser großen Strukturen durch Funktionalisierung mit Ammonium- oder Triethylenglycolsubstituenten erheblich zu steigern. Im zweiten Ansatz wurden Ligandensysteme mit oxidationsstabilen Perylenbisimid-Untereinheiten axial an das {Ru(bda)}-Fragment koordiniert. Dadurch wurden Komplexe erzeugt, welche in wässrigem Medium aggregieren und eine höhere Stabilität aufweisen als ein vergleichbarer nicht aggregierter Katalysator. Durch die Wahl verschiedener PBI-Strukturen ließen sich darüber hinaus die Aggregationseigenschaften und die Stabilität des Systems beeinflussen.

CHAPTER 5 EXPERIMENTAL SECTION

5.1 Materials and Methods

5.1.1 Materials

All chemicals and solvents, if not stated otherwise, were purchased from commercial sources and used without further purification. $RuCl_3 \cdot 3\ H_2O$ (ABCR, 98%) was used as ruthenium source for all ruthenium complexes. $[RuCl_2(dmso)_4]$ (**38**),[277, 300] 2,2'-bipyridine-6,6'-dicarboxylic acid (**39**, H_2bda),[278] $[Ru(bda)(dmso)_2]$ (**40**),[279] $[Ru(bda)(pic)_2]$ (**6**),[162] 5-bromo-*N*,*N*-dimethyl-3-pyridinemethanamine (**50**),[337, 338] 3-bromo-5-[2-[2-(2-methoxyethoxy)ethoxy]ethoxy]-pyridine (**51**),[336] and the ditopic pyridine ligands 1,2-bis(pyridin-3'-yl)ethyne (**46**, bpe),[371] 1,4-bis(pyridin-3'-yl)benzene (**47**, bpb),[304] and 4,4'-bis(pyridin-3''-yl)-1,1'-biphenyl (**48**, bpbp)[304] were synthesized according to literature known methods. The synthesis and characterization of **MC3** has previously been described by our group.[93] Synthetic routes for the ditopic ligands 1,4-bis(5-(2-(2-(2-methoxyethoxy)-ethoxy)ethoxy)-pyridin-3-yl)benzene (**53**) and 1,1'-(5,5'-(1,4-phenylene)bis(pyridine-5,3-diyl))bis(*N*,*N*-dimethylmethanamine) (**54**) as well as for the trinuclear macrocycles **MC1**, **MC2**, **MC3b**, **MC3c**, and **MC4** can be found in the **chapters 5.2.1** and **5.2.2**.

The starting compounds for the pyridine ligands, perylene-3,4:9,10-tetracarboxylic-bisanhydride (**57**) and 1,6,7,12-tetrachloroperylene-3,4:9,10-tetracarboxylic-bisanhydride (**60**), were obtained from BASF SE.[372] The compound 2-(pyridin-4-yl)ethan-1-amine (**56**) was purchased from TCI in 97% purity. The swallowtail amine 2,5,8,11,15,18,21,24-octaoxapentacosan-13-amine (**55**) [356, 358] and the additional ligand 4-(2-(2-(2-methoxyethoxy)ethoxy)ethoxy)pyridine (**PyO**) were synthesized according to literature known methods.[361] The synthesis of the novel PBI ligands and {Ru(bda)}-PBI complexes is described in the **chapters 5.2.3** and **5.2.4**, respectively.

The experiments in aqueous solutions were performed in deionized water obtained from an ELGA Purelab Classic water purification system. As co-solvents, acetonitrile (Sigma-Aldrich, HPLC grade, >99.9%) and 2,2,2-trifluoroethanol (Alfa Aesar, 99+%) were used. Trifluoromethanesulfonic acid (TCI, >98%) was used for the preparation of acidic aqueous solutions and the pH value was determined using a pH-meter. The photocatalysis experiments were performed in a phosphate buffer (Fluka/Honeywell, pH 7.2). For the kinetic isotope experiment, deuterium oxide with a purity of 99.9% was used (Deutero GmbH). As sacrificial reagents, the oxidants cerium(IV) ammonium nitrate (Sigma-Aldrich, >98%) and sodium peroxidisulfate (Merck KGaA, >99.0%) and the photosensitizer $[Ru(bpy)_3]Cl_2 \cdot 6\ H_2O$ (Sigma-Aldrich, 99.95%) were applied.

5.1.2 Methods

Purification. Column chromatographic separations were performed on silica gel 60M (0.04–0.063 mm) and neutral aluminium oxide (MP Alumina N, Act. V). For thin-layer chromatography (TLC), plastic sheets precoated with silica gel (Polygram SIL G/UV_{254}, Macherey-Nagel) and aluminium oxide (Polygram ALOX N/UV_{254}, Macherey-Nagel) were used. Further separations were performed with size exclusion chromatography on Bio-Beads S-X3 (M.W. exclusion limit: 2000, Bio-Rad) or with a Shimadzu Recycling GPC system (LC-20AD prominence pump, SPD-M20A prominence diode array detector, 3 preparative columns from Japan Analytical Industries: JAIGEL-1H, JAIGEL 2-H and JAIGEL-2.5H, eluent: $CHCl_3$ stabilized with ethanol).

NMR Spectroscopy. NMR spectra were recorded on a 400 MHz NMR spectrometer (Bruker Avance III HD 400) in deuterated solvents at 25 °C if not noted otherwise. ^{13}C NMR spectra are broadband proton decoupled. Chemical shifts are reported in parts per million (ppm, δ scale) relative to residual solvent signals. The following abbreviations were used to describe peak patterns: s = singlet, d = doublet, t = triplet, and m = multiplet.

Kinetic NMR Experiments. To study the ligand exchange reactions, two different experiments have been performed. To investigate the exchange of dmso ligands, the starting complex $[Ru(bda)(dmso)_2]$ (**40**) (2.0 mg, 4.0 μmol, 6.7 mM) was dissolved in 0.6 mL of d_5-pyridine together with some ascorbic acid (0.78 mg, 4.4 μmol, 7.7 mM). The sample was heated to two different temperatures (331.45 K and 344.01 K) and ^1H NMR spectra with 64 scans have been acquired in time intervals of 30 minutes. Analogously, to study the interchange of pyridine ligands, $[Ru(bda)(py)_2]$ (**44**) (2.2 mg, 4.4 μmol, 7.3 mM) was dissolved in 0.6 mL of d_5-pyridine together with some ascorbic acid (0.40 mg, 2.3 μmol, 3.8 mM). The sample was heated to two different temperatures (370.00 K and 377.62 K) and ^1H

NMR spectra with 64 scans have been acquired in time intervals of 30 minutes. The temperature has been calibrated with a sample of 80% glycol in dimethylsulfoxide.

Mass Spectrometry. MALDI-ToF mass spectra have been measured on an Autoflex II spectrometer (Bruker). The spectra were measured in the positive reflector mode using DCTB (*trans*-2-[3-(4-*tert*-butylphenyl)-2-methyl-2-propenylidene]malononitrile) as matrix. High resolution mass spectra (ESI) were recorded on an ESI micrOTOF focus mass spectrometer (Bruker).

X-ray Crystallography. Single crystals of **MC4** were obtained out of a dichloromethane/ methanol/2,2,2-trifluoroethanol solution by slowly letting the solvent evaporate under a nitrogen atmosphere. Single crystal X-ray diffraction data for **MC4** was collected at 100 K on a Bruker X8APEX-II diffractometer with a CCD area detector and multi-layer mirror monochromated MoK_α radiation. The structure was solved using direct methods, expanded with Fourier techniques and refined with the Shelx software package.[373] All non-hydrogen atoms were refined anisotropically with exception of those of the disordered 2,2,2-trifluoroethanol molecules. Hydrogen atoms were included in the structure factor calculation on geometrically idealized positions. The refinement contained residual electron density resulting from solvent molecules that could not be modeled satisfactorily. Therefore, the PLATON squeeze routine was applied to remove the respective electron density.[374] The remaining structure could be refined nicely. Crystallographic data have been deposited with the Cambridge Crystallographic Data Centre as supplementary publication no. CCDC 1554426. These data can be obtained from The Cambridge Crystallographic Data Centre *via* www.ccdc.ac.uk/data.request/cif.

Electrochemistry. For cyclic- and differential pulse voltammetry measurements, a BAS Cell Stand C3 (BAS Epsilon) with a three electrode single-compartment cell was used. The measurements were carried out in dichloromethane at a concentration of about 0.2 mM with ferrocene (Fc) as an internal standard for the calibration of the potential (Fc^+/Fc^0 = 0.63 V vs. NHE)[375]. Dichloromethane (HPLC grade) was dried over calcium hydride under an atmosphere of argon before use. The supporting electrolyte tetrabutylammonium hexafluorophosphate ($(n\text{-}Bu)_4NPF_6$) was prepared according to the literature and recrystallized from ethanol/water.[376] A Pt disc and a Pt wire were applied as working and auxiliary electrodes, respectively, and Ag/AgCl was used as reference electrode. For measurements in aqueous medium, glassy carbon was used as working electrode and a platinum wire as counter electrode. As a reference an Ag/AgCl electrode in 3 M KCl was used, and the potentials were referenced to NHE by the addition of +0.209 V.[377] The aqueous solutions were either measured in acetonitrile/water (pH 1, acid: trifluoromethane sulfonic acid (CF_3SO_3H)) or 2,2,2-trifluoroethanol/water (pH 1) mixtures. The measurements for the Pourbaix diagrams initially started in a 1:1 acetonitrile/water mixture at a pH value of 1. The further pH values were adjusted by the addition of NaOH solutions and measured with a pH-meter.

UV/Vis Spectroscopy. UV/Vis absorption spectra were measured on a JASCO V-770 spectrophotometer at 25 °C in 1 cm quartz cuvettes with spectroscopic grade solvents.

Spectroelectrochemistry. Spectroelectrochemical experiments in reflexion mode were performed in an Agilent Cary 5000 Spectrometer in combination with a home-built sample compartment consisting of a cylindrical PTFE cell with a sapphire window and an adjustable three in one electrode (6 mm platinum disc working electrode, 1 mm platinum counter and pseudo reference electrode) with a layer thickness of ~100 µm in a 1:1 acetonitrile/water mixture (pH 1, acid: CF_3SO_3H) at concentrations in the range of 0.6–0.7 mM. The potential was always referenced to the first oxidation event that was measured with differential pulse voltammetry against a Ag/AgCl reference electrode (3 M KCl) and the extinction coefficient was determined for the $[Ru^{II}|Ru^{II}|Ru^{II}]$ state using conventional UV/Vis spectroscopy at a concentration of 10^{-5} M in the same solvent mixture due to the inaccuracy of the layer thickness of the spectroelectrochemical cell.

Time-resolved stoichiometric redox titration. The experiment was performed using a diode array spectrometer (Ocean Optics Maya200Pro) at 20 °C. The catalyst solution (2.0 mL, 0.1 mM) was loaded into a 1 cm cuvette equipped with a magnetic stirrer (300 rpm) and a freshly prepared cerium(IV) ammonium nitrate (CAN) solution was injected in increments of one equivalent per macrocycle (10 µL, $c = 60$ mM) using an Eppendorf pipette. Spectra were acquired with a rate of 5 spectra per second (integration time: 10 ms, scans taken for average: 20, boxcar width: 3). The oxidation was monitored by the bleach of the MLCT band at 450 nm.

UV/Vis Redox Titration. The catalyst solutions in acetonitrile/water 1:1 (2.0 mL, $c =$ 0.1 mM, pH 1, acid: CF_3SO_3H) were loaded into a 1 cm quartz cuvette and freshly dissolved cerium(IV) ammonium nitrate in the same solvent mixture was titrated to it in increments of one equivalent per {Ru(bda)} center (10 µL, c = 20 mM, per addition) using an Eppendorf pipette. After each addition the mixture was stirred for ~5 min at 20 °C before the spectrum was acquired using a diode array spectrometer (Ocean Optics Maya200Pro).

Water Oxidation Catalysis with large excess of Ce(IV). The chemically driven water oxidation reactions were performed at 20 °C in reaction vessels which were connected to pressure transducers from Honeywell (SSCDANN030PAAA5, absolute pressure, 0 to 30 psi). For each measurement 1.0 g (1.82 mmol) of cerium(IV) ammonium nitrate was dissolved in 3.0 mL of an acetonitrile/water mixture (pH 1, acid: CF_3SO_3H, ratios varying) in the reaction vessel (V = 20.6 mL) and the catalyst solution (400 µL in acetonitrile/water mixtures) was injected through a septum using a Hamilton syringe. After the gas-evolution had ceased, 500 µL of the gas head space were taken with a gas tight Hamilton syringe and injected into a gas chromatograph GC-2010 Plus from Shimadzu, equipped with a thermal conductivity detector (detector current 30 mA, argon as carrier gas), to determine the gas composition at the end of the reaction. The turnover numbers (TONs) have been calculated based on the total amount of evolved oxygen during catalysis divided by the amount of used catalyst. The amount of evolved oxygen has been determined by using pressure transducers to measure the pressure increase in the reaction vessel. Using the ideal gas law $\Delta p \times V = \Delta n \times R \times T$ (T = 293.15 K, V = 20.6 mL, R = 8.314 J/Kmol) this pressure difference (Δp) can be converted into the amount of molecular oxygen in moles that is generated during the reaction (Δn). The TONs have been calculated for each concentration in the concentration-dependent measurements and the highest TONs are reported. The turnover frequencies (TOFs) have been determined from the same concentration-dependent measurements. For each concentration the initial rate of catalysis has been determined by a linear regression through the first linear part of the oxygen evolution curve. The TOF has then been determined by the slope of a linear regression of these initial rates vs. the respective catalyst amounts.

Water Oxidation Catalysis with Stoichiometric Ce(IV) Amounts. The catalysis in the presence of stoichiometric amounts of cerium(IV) ammonium nitrate was investigated by monitoring the decrease of the CAN absorption at 360 nm using a JASCO V-770 UV/Vis spectrometer at 25 °C. The studies were performed in 1:1 acetonitrile/water solution (pH 1, acid: nitric acid (HNO_3)) as followed: 1.99 mL of a freshly prepared CAN solution were mixed with 10 µL of the catalyst solution in the same solvent mixture. Afterwards the cuvette was shaken and placed inside the spectrometer (~4 s) and the Ce(IV) absorption decay (360 nm, $\varepsilon_{360} = 760\ M^{-1}\ cm^{-1}$) was monitored for 300 s. Using the Beer-Lambert law, the absorption change was converted into the change in CAN concentration.

Stability Test Using Mass Spectrometry. The following procedure was applied to test the stability of the macrocyclic structures during water oxidation catalysis: Each catalyst was dissolved in 1.0 mL 4:1 acetonitrile/water (c = 0.7 mM, pH 1, acid: CF_3SO_3H). After the addition of 130 equivalents cerium(IV) ammonium nitrate (~33 catalytic cycles) vigorous oxygen evolution occurred. After the oxygen evolution had ceased, the sample was reduced using ascorbic acid and analyzed by MALDI-ToF mass spectrometry (matrix = DCTB).

Photocatalysis. The photocatalytic water oxidation reactions were carried out using a Clark-type electrode for electrochemical oxygen detection (Oxygraph Plus System of Hansatech Instruments Ltd). Irradiation of the sample was performed with a 150 W xenon lamp by Newport equipped with a 380 nm cutoff filter and a water jacket to remove UV and IR radiation, respectively. The intensity with which the sample was irradiated was ~230 mW/cm^2. Before the measurement, all components (catalyst, $[Ru(bpy)_3]Cl_2 \cdot 6\ H_2O$ and $Na_2S_2O_8$ were dissolved in 2.0 mL 1:1 acetonitrile/phosphate buffer (pH 7.2) solution in the dark ($[Na_2S_2O_8]$ = 50 mM, $[[Ru(bpy)_3]Cl_2 \cdot 6\ H_2O]$ = 2.0 mM, [catalyst] = varying). Afterwards the sample was transferred to the reaction chamber and kept in the dark. When the baseline of the measurement was constant, the sample was irradiated. During the measurement the reaction temperature was kept constant at 20 °C. The initial rates were determined from the steepest linear part.

Kinetic Isotope Experiments. The reactions were performed in 2.0 mL of a 1:1 acetonitrile/water mixture (H_2O or D_2O, pH 1, acid: CF_3SO_3H), using CAN (c = 0.525 M) as a sacrificial oxidant, and the dissolved oxygen concentration was measured with a Clark-type electrode setup (Oxygraph Plus System of Hansatech Instruments Ltd.) at a constant temperature of 20 °C. For each measurement 1.5 mL of a freshly prepared CAN solution in 1:1 acetonitrile/water (c = 0.7 M, pH 1 solution (H_2O or D_2O)) were placed in the Clark electrode reaction chamber. When the baseline was constant, 0.5 mL of the catalyst solution in the same solvent mixture (varying concentrations) were added. The D_2O used for this experiment had a purity of 99.9 %.

DFT Calculations.[9] In order to generate initial structures for the exploration of the catalytic steps in the framework of QM/MM MD simulations, the catalyst structures were first optimized in the presence of explicit water molecules at the PBE/def2-SVP level of theory [378, 379] employing 28-electron Stuttgart-Dresden effective core potentials [380] for the ruthenium atoms. The ensemble of catalyst structures in solution used for the calculation of UV/Vis spectra has been generated by embedding pre-optimized structures into a water sphere and propagating for 2.5 ps utilizing classical MD with time steps of 0.5 fs at a constant temperature of 300 K. A QM/MM approach was applied with electrostatic embedding in which the catalyst and the nearest 10 ([Ru(bda)(pic)$_2$]), 13 (**MC1**) and 25 (**MC3**) water molecules were included into the QM model. The respective number of quantum-mechanically treated water molecules was chosen so that spheres of 5 Å around the binding sites of all ruthenium atoms were filled with water, including the important carboxy ligands. Additional water molecules were added for the bigger macrocycles to fill the cavity between the three centers and therefore ensure the proper description of cooperativity effects. The applied QM/MM interface accounts for non-covalent interactions, whereas proton diffusion to the surrounding solvent is not possible in our model, but also not expected on the time scale of our simulations. QM calculations were performed at the PBE/def2-SVP level in Turbomole.[381] The TIP-3P force field [382] was applied to the surrounding classical water utilizing Tinker package [383] and including water molecules with a maximum distance of 2.0 nm (for [Ru(bda)(pic)$_2$]) and 1.2 nm (for **MC1**–**MC3**) to the catalyst. Van der Waals parameters for the QM system were taken from the OPLS-aa force field [384] (organic ligands) and the UFF force field [385] (ruthenium atoms, explicit water), respectively. After 1.0 ps of equilibration, 30 structures were sampled along the trajectory in equal time steps of 50 fs. Vertical excitation energies were then calculated for each structure using the long-range corrected CAM-B3LYP functional [386] with the def2-SVP basis set as implemented in Gaussian09.[387] Ensemble absorption spectra were obtained by convolution of each set of oscillator strengths with Lorentzian functions of 20 nm width.

For the dynamic exploration of reaction pathways, starting structures generated as described above were propagated within the same QM/MM approach. In order to model the oxidation steps, one electron per ruthenium center was removed in every simulated reaction step and the relaxation of the solvated catalyst in the respective oxidation state was observed

---

[9] These calculations were carried out by Joachim O. Lindner under the supervision of Prof. Roland Mitrić and Dr. Merle I. S. Röhr, Theoretical Chemistry, University of Würzburg

using MD. Reactive trajectories were propagated with time steps of 0.25 fs at a constant temperature of 500 K in order to speed up the reaction. Oxygen liberation has been observed after removing three electrons from the default $[Ru^{V}=O|Ru^{V}=O|Ru^{V}=O]^{3+}$ species of **MC3** and one electron from the $[Ru^{V}=O]^{+}$ species of $[Ru(bda)(pic)_2]$. The nucleophilic attack of water is accompanied by the release of one proton and the change from singlet to triplet state enables the second proton transfer and liberation of elemental dioxygen. The MD simulations for all oxidation steps and the oxygen liberation of **MC3** have been combined to a video, which is added as additional supplementary material.

Atomic Force Microscopy (AFM). The AFM measurements were performed under ambient conditions using a Bruker AXS Nanoscope IV system operating in tapping mode in air. Silica cantilevers (OMCL AC160TS, Olympus) with a resonance frequency of ~300 kHz and a spring constant of ~ 40 Nm^{-1} were used. The samples were prepared by spin-coating a solution of a Ru-PBI complex in acetonitrile or acetonitrile/water 1:1 mixture ($c = 10^{-5}$ M) onto mica or highly oriented pyrolytic graphite (HOPG) at 2000 rpm.

Cryogenic Scanning Electron Microscopy (cryo-SEM). The sample preparation consisted of placing a small drop of the complex solution in 1:1 acetonitrile/water ($c = 10^{-5}$ M) onto a copper stub sample holder. Prior to measurement, the specimen was plunged into liquid nitrogen slush at −210 °C. The sample was transferred under vacuum using the loading transfer rod into the high vacuum cryo preparation chamber (Quorum PP2000T) at −150 °C and fractured. The specimen was then transferred into a SEM sample chamber maintained at about −150 °C. Images of the sample were taken using a Zeiss Ultra plus field emission scanning electron microscope operated at 1.7 kV with an aperture size set to 30 μm to avoid excessive charging and radiation damage of the areas imaged.

5.2 Synthesis and Characterization

5.2.1 Trinuclear {Ru(bda)} Macrocycles with Different Ring Size

[Ru(bdaH)$_2$]

(41)

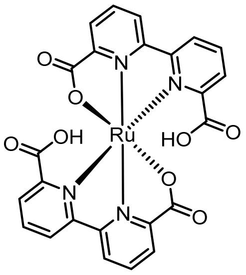

The compound [Ru(bdaH)$_2$] (**41**) was obtained during the synthesis of [Ru(bda)(dmso)$_2$] (**40**) as a by-product. Under an argon atmosphere, [RuCl$_2$(dmso)$_4$] (**38**) (1.00 g, 2.06 mmol) and 2,2'-bipyridine-6,6'dicarboxylic acid (**39**, H$_2$bda) (0.55 g, 2.27 mmol) were dissolved in degassed methanol (60 mL) and triethylamine (2.5 mL) was added. The mixture was heated under reflux for 20 hours. The precipitate was filtered off and washed with methanol. From the precipitate 510 mg of [Ru(bda)(dmso)$_2$] were obtained as a brown powder (1.02 mmol, 50%). From the dark red filtrate, crystals of [Ru(bdaH)$_2$] (**41**) were isolated as a by-product by slow evaporation of the solvent after letting the filtrate stand overnight.

^{1}H NMR (400 MHz, MeOD, 272.1 K, ascorbic acid): δ = 8.93 (br s, 2H), 8.63 (s, 2H), 8.36 (d, J = 6.3 Hz, 2H), 7.94 (m, 4H), 7.68 (t, J = 6.8 Hz, 2H), 6.91 (d, J = 5.7 Hz, 2H) ppm. **^{13}C NMR** (101 MHz, MeOD, 272.1 K, ascorbic acid): δ = 181.2, 173.7, 170.5, 166.4, 164.0, 159.3, 142.5, 139.3, 130.5, 130.2, 128.3, 127.3 ppm. **HR-MS** (ESI, negative, MeOH, *m*/*z*): Calculated for $[M-H]^-$ ($C_{24}H_{13}N_4O_8Ru$): 586.9782, found: 586.9774; (error = 1.4 ppm). **Melting point**: > 300 °C.

$[Ru(bda)(bp)]_3$

(MC1)

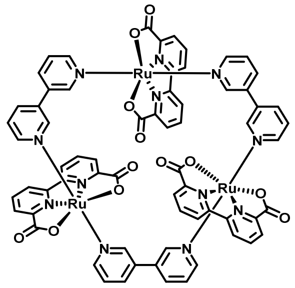

The starting materials $[Ru(bda)(dmso)_2]$ (**40**) (280 mg, 560 µmol) and 3,3'-bipyridine (**45**, bp) (79 mg, 506 µmol) were dissolved in a degassed 5:1 chloroform/methanol mixture (150 mL) and stirred at 60 °C for 23 hours under a nitrogen atmosphere. The solvent was then removed under reduced pressure. The crude was redissolved in dichloromethane/ methanol and purified by column chromatography (neutral Al_2O_3 deactivated with 15% H_2O *w*/*w*, CH_2Cl_2/MeOH 6:1) several times. The product was obtained as a red-brown solid (65 mg, 43.3 µmol, **26%**).

^{1}H NMR (400 MHz, CD_2Cl_2/MeOD 5:1, ascorbic acid): δ = 8.85 (br s, 6H), 8.66 (d, J = 7.9 Hz, 6H), 8.14 (d, J = 7.7 Hz, 6H), 7.92 (t, J = 7.9 Hz, 6H), 7.65 (d, J = 7.9 Hz, 6H), 7.16–7.05 (m, 12H) ppm. **^{13}C NMR** (101 MHz, CD_2Cl_2/MeOD 5:1, ascorbic acid): δ = 174.1, 160.2, 157.4, 152.5, 150.4, 136.2, 134.1, 133.0, 127.0, 125.8, 125.7 ppm. **HR-MS** (ESI, positive, $CHCl_3$/MeOH 3:1, *m*/*z*): Calculated for $[M]^+$ ($C_{66}H_{42}N_{12}O_{12}Ru_3$): 1499.0217, found: 1499.0400; (error = 12 ppm). **Melting point**: > 300 °C.

$[Ru(bda)(bpe)]_3$

(**MC2**)

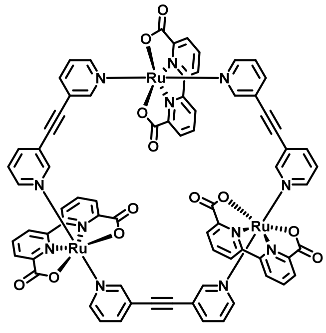

The starting materials $[Ru(bda)(dmso)_2]$ (**40**) (554 mg, 1.11 mmol) and 1,2-di(pyridin-3'-yl)-ethyne (**46**, bpe) (200 mg, 1.11 mmol) were dissolved in a degassed 1:1 chloroform/ methanol mixture (150 mL) and stirred at 60 °C for 20 hours under a nitrogen atmosphere. After the solvent was removed under reduced pressure, the crude was redissolved in dichloromethane/methanol and purified by column chromatography (neutral Al_2O_3 deactivated with 15% H_2O *w*/*w*, CH_2Cl_2/MeOH 9:1) several times. After slow evaporation of the solvent, the product was obtained as dark crystals, which were filtered off, washed with diethyl ether and dried under high vacuum (90 mg, 57.3 µmol, **16%**).

^{1}H NMR (400 MHz, CD_2Cl_2/MeOD 5:1, ascorbic acid): δ = 8.73 (d, J = 7.1 Hz, 6H), 8.33 (s, 6H), 8.12 (dd, J = 7.8, 1.1 Hz, 6H), 7.99 (t, J = 7.9 Hz, 6H), 7.67–7.63 (m, 6H), 7.52 (d, J = 5.5 Hz, 6H), 7.07 (dd, J = 7.6, 6.1 Hz, 6H) ppm. **^{13}C NMR** (101 MHz, CD_2Cl_2/MeOD 5:1, ascorbic acid): δ = 174.2, 160.4, 157.6, 156.3, 151.3, 139.8, 133.4, 127.1, 125.8, 125.4, 121.2, 89.2 ppm. **HR-MS** (ESI, positive, $CHCl_3$/MeOH 3:1, *m*/*z*): Calculated for $[M+Na]^+$ ($C_{72}H_{42}N_{12}O_{12}Ru_3Na$): 1594.0108, found: 1594.0150; (error = 2.6 ppm). **Melting point**: > 300 °C.

[Ru(bda)(bpbp)]$_3$

(**MC4**)

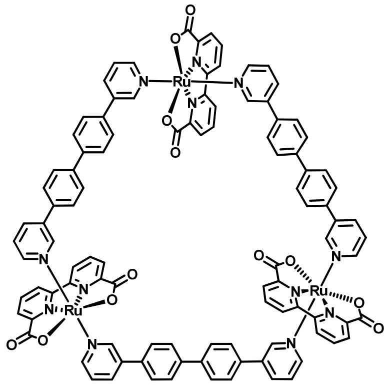

The starting materials [Ru(bda)(dmso)$_2$] (**40**) (303 mg, 607 µmol) and 4,4'-bis(pyridin-3''-yl)-1,1'-biphenyl (**48**, bpbp) (178 mg, 579 µmol) were dissolved in a degassed 5:1 chloroform/methanol mixture (200 mL) and stirred at 60 °C for 14 hours under a nitrogen atmosphere. The solvent was removed under reduced pressure and purification by column chromatography (neutral Al_2O_3 deactivated with 15% H_2O *w*/*w*, CH_2Cl_2/MeOH 5:1) and subsequent crystallization from the same solution afforded the product as dark brown crystals (128 mg, 65.5 µmol, **34%**).

^{1}H NMR (400 MHz, CD_2Cl_2/MeOD/CF_3CH_2OH 5:1:0.2, ascorbic acid): δ = 8.50 (d, J = 2.0 Hz, 6H), 8.47 (dd, J = 8.2, 1.0 Hz, 6H), 8.11 (dd, J = 7.8, 1.0 Hz, 6H), 7.90 (t, J = 8.1 Hz, 6H), 7.9–7.82 (m, 6H), 7.78 (d, J = 8.5 Hz, 12H), 7.56 (d, J = 8.5 Hz, 12H), 7.38 (dd, J = 5.8, 0.7 Hz, 6H), 7.15 (dd, J = 8.1, 5.7 Hz, 6H) ppm. **^{13}C NMR** (101 MHz, CD_2Cl_2/MeOD/ CF_3CH_2OH 5:1:0.2, ascorbic acid): δ = 173.9, 159.8, 156.7, 151.0, 149.2, 140.6, 137.8, 135.0, 134.9, 132.0, 127.7, 127.4, 126.3, 124.9, 124.6 ppm. **HR-MS** (ESI, positive, $CHCl_3$/MeOH 1:1, *m*/*z*): Calculated for $[M]^+$ ($C_{102}H_{66}N_{12}O_{12}Ru_3$): 1955.2107, found: 1955.2116; (error = 0.5 ppm). **Melting point**: > 300 °C.

5.2.2 Water Soluble Ligands and {Ru(bda)} Macrocycles

1,4-bis(5-(2-(2-(2-methoxyethoxy)ethoxy)ethoxy)pyridin-3-yl)benzene

(53)

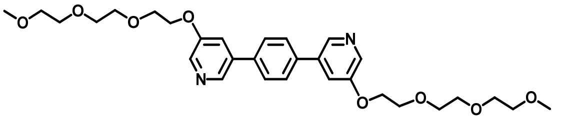

The starting materials 1,4-benzenediboronic acid (696 mg, 4.20 mmol), 3-bromo-5-[2-[2-(2-methoxyethoxy)ethoxy]ethoxy]-pyridine (**50**) (2.96 g, 9.23 mmol), [$Pd_2(dba)_3$] (270 mg, 0.294 mmol, dba = dibenzylideneacetone), and triphenylphosphine (308 mg, 1.17 mmol) were loaded into a Schlenk flask under a nitrogen atmosphere. The compounds were dissolved in a degassed mixture of toluene (160 mL), methanol (20 mL) and 2M aq. Na_2CO_3 (20 mL). The mixture was stirred at 70 °C for 15 hours. Then the organic phase was separated and washed twice with water. The combined aqueous phases were extracted with dichloromethane three times. The solvent of the organic phase was removed under reduced pressure and the product isolated by column chromatography several times (SiO_2, ethyl acetate/methanol 9:1). The product was obtained as waxy white solid (720 mg, 1.26 mmol, **31%**).

^{1}H NMR (400 MHz, $CDCl_3$): δ = 8.50 (d, J = 1.6 Hz, 2H), 8.33 (d, J = 2.6 Hz, 2H), 7.68 (s, 4H), 7.48–7.46 (m, 2H), 4.29–4.24 (m, 4H), 3.91 (dd, J = 5.3, 4.1 Hz, 4H), 3.77–3.73 (m, 4H), 3.71–3.67 (m, 4H), 3.66–3.62 (m, 4H), 3.56–3.52 (m, 4H), 3.36 (s, 6H) ppm. **^{13}C NMR** (101 MHz, $CDCl_3$): δ = 155.4, 140.6, 137.6, 136.7, 136.6, 128.0, 120.3, 72.1, 71.1, 70.8, 70.7, 69.8, 68.2, 59.2 ppm. **HR-MS** (ESI, positive, $CHCl_3$/MeOH 1:1, *m/z*): Calculated for $[M+H]^+$ ($C_{30}H_{41}N_2O_8$): 557.2857, found: 557.2846; (error = 2.0 ppm). **Elemental Analysis** (%): Calculated for $C_{30}H_{40}N_2O_8$: C, 64.73; H, 7.24; N, 5.03; found: C, 64.72; H, 7.04; N, 5.00. **Melting point**: 64–65 °C.

1,1'-(5,5'-(1,4-phenylene)bis(pyridine-5,3-diyl))bis(*N*,*N*-dimethylmethanamine)

(55)

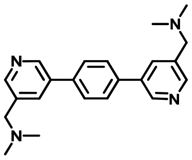

The starting materials 1,4-benzenediboronic acid (325 mg, 1.96 mmol), 5-bromo-*N*,*N*-dimethyl-3-pyridinemethanamine (**51**) (930 mg, 4.32 mmol) and [Pd(PPh$_3$)$_4$] (147 mg, 0.127 mmol) were loaded into a Schlenk flask under a nitrogen atmosphere. The compounds were dissolved in a degassed mixture of toluene (20 mL), methanol (10 mL) and 2M aq. Na$_2$CO$_3$ (10 mL). The mixture was stirred at 80 °C for 24 hours. Afterwards, water was added (50 mL) and the mixture was extracted with dichloromethane three times. The product was isolated using column chromatography (SiO$_2$, CH$_2$Cl$_2$/MeOH 20:1, 10:1). The product was obtained as a white solid (188 mg, 0.832 mmol, **43%**).

^{1}H NMR (400 MHz, CD$_2$Cl$_2$): δ = 8.70 (d, J = 2.3 Hz, 2H), 8.41 (d, J = 2.0 Hz, 2H), 7.85 (s, 2H), 7.68 (s, 4H), 3.43 (s, 4H), 2.18 (s, 12H) ppm. **^{13}C NMR** (101 MHz, CD$_2$Cl$_2$): δ = 149.4, 147.3, 137.6, 135.8, 135.1, 134.4, 127.9, 61.6, 45.6 ppm. **HR-MS** (ESI, positive, CHCl$_3$/MeOH 1:1, *m*/*z*): Calculated for [M+H]$^+$ (C$_{22}$H$_{27}$N$_4$): 347.2230, found: 347.2231; (error = 0.3 ppm). **Elemental Analysis** (%): Calculated for (C$_{22}$H$_{26}$N$_4$ • 0.66 H$_2$O): C, 73.71; H, 7.69; N, 15.63; found: C, 73.30; H, 7.53; N, 15.37. **Melting point**: 122–124 °C.

[Ru(bda)(53)]$_3$

(MC3b)

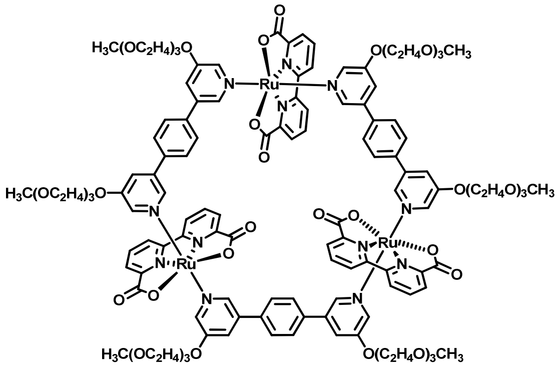

The starting materials [Ru(bda)(dmso)$_2$] (**40**) (415 mg, 0.832 mmol) and **53** (441 mg, 0.792 mmol) were loaded into a Schlenk flask under a nitrogen atmosphere. Then a degassed 1:1 mixture of chloroform and methanol (210 mL) was added and the mixture was stirred at 60 °C for 14 hours. The solvent was removed under reduced pressure and the crude was filtered several times (neutral Al_2O_3 deactivated with 15% H_2O *w/w*, CH_2Cl_2/MeOH 9:1), further purified by size exclusion chromatography (BioBeads SX3, CH_2Cl_2/MeOH 9:1) and finally purified by recycling GPC with chloroform as eluent to obtain the pure product as a brown powder (180 mg, 66.6 µmol, **25%**).

^{1}H NMR (400 MHz, CD_2Cl_2/MeOD 5:1, ascorbic acid): δ = 8.52 (dd, J = 8.1, 0.9 Hz, 6H), 8.04 (dd, J = 7.8, 1.0 Hz, 6H), 7.99 (d, J = 1.5 Hz, 6H), 7.88 (t, J = 8.0 Hz, 6H), 7.44 (s, 12H), 7.29 (dd, J = 2.4, 1.7 Hz, 6H), 7.05 (d, J = 2.4 Hz, 6H), 3.99–3.97 (m, 12H), 3.67–3.65 (m, 12H), 3.55–3.47 (m, 36H), 3.42–3.39 (m, 12H), 3.24 (s, 18H) ppm. **^{13}C NMR** (101 MHz, CD_2Cl_2/MeOD 5:1, ascorbic acid): δ = 173.4, 159.7, 157.1, 155.6, 143.7, 138.6, 137.5, 136.3, 131.9, 127.9, 126.1, 124.8, 120.1, 71.7, 70.5, 70.3, 70.2, 69.1, 68.2, 58.4 ppm. **HR-MS** (ESI, positive, $CHCl_3$/MeOH 1:1, *m/z*): Calculated for $[M]^+$ ($C_{126}H_{138}N_{12}O_{36}Ru_3$): 2700.6533, found: 2700.6596; (error = 2.3 ppm). **Melting point**: 187–190 °C.

[Ru(bda)(54)]$_3$

(MC3c)

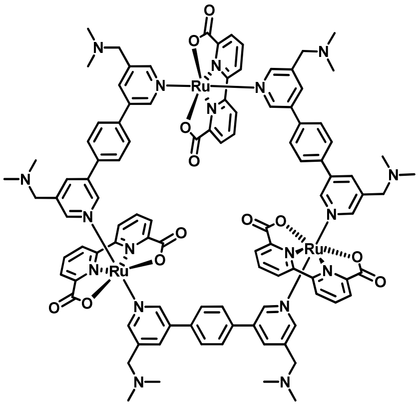

The starting materials [Ru(bda)(dmso)$_2$] (**40**) (166 mg, 0.333 mmol) and **54** (105 mg, 0.303 mmol) were loaded into a Schlenk flask under a nitrogen atmosphere. Then a degassed 4:1 mixture of chloroform and methanol (100 mL) was added and the mixture was stirred at 60 °C for 8 hours. After several column chromatographic filtrations (neutral Al_2O_3 deactivated with 15% H_2O *w*/*w*, CH_2Cl_2/MeOH 7:1), the product was isolated by size exclusion chromatography (BioBeads SX3, CH_2Cl_2/MeOH 9:1) and finally purified by recycling GPC with chloroform as eluent to obtain the pure product as a brown powder (80 mg, 38.5 µmol, **38%**).

^{1}H NMR (400 MHz, CD_2Cl_2/MeOD 5:1, ascorbic acid): δ = 8.58 (d, J = 7.5 Hz, 6H), 8.34 (s, 6H), 8.09 (dd, J = 7.7, 0.8 Hz, 6H), 7.93 (t, J = 7.9 Hz, 6H), 7.78 (s, 6H), 7.55 (s, 12H), 7.38 (s, 6H), 3.32 (s, 12H), 2.09 (s, 36H) ppm. **^{13}C NMR** (101 MHz, CD_2Cl_2/MeOD 5:1, ascorbic acid): δ = 173.6, 160.0, 157.3, 150.5, 150.3, 137.0, 136.4, 135.6, 135.3, 132.1, 128.1, 126.3, 124.9, 60.3, 44.6 ppm. **HR-MS** (ESI, positive, $CHCl_3$/MeOH 1:1, *m*/*z*): Calculated for $[M]^+$ ($C_{102}H_{96}N_{18}O_{12}Ru_3$): 2070.4639, found: 2070.4603; (error = 1.7 ppm). **Melting point**: > 300 °C.

5.2.3 Perylene Bisimide (PBI) Ligands

9,10-bis(octyloxycarbonyl)-*N*-(2-(pyridin-4-yl)ethyl)-perylene-3,4-dicarboxylic imide (58)

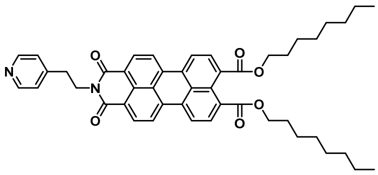

Perylene-3,4:9,10-tetracarboxylic acid bisanhydride (**57**) (2.0 g, 5.10 mmol) was suspended in DMF (20 mL) and 1,8-diazabicycloundec-7-ene (3.0 mL, 3.09 g, 20.3 mmol) and 1-octanol (6.4 mL, 5.31 g, 40.8 mmol) were added. After stirring for one hour at room temperature a homogeneous red solution was obtained. After 24 hours 4-(2-amino-ethyl)pyridine (**56**) (312 mg, ρ = 1.03 g/mL, 0.151 mL, 2.56 mmol) was added and the solution was stirred for 3 days. Then 1-octyl bromide (3.34 g, ρ = 1.05 g/mL, 3.2 mL, 20.3 mmol) was added and the mixture was stirred for further 24 hours. The mixture was poured into deionized water (100 mL) and neutralized with 2N hydrochloric acid, and subsequently extracted four times with dichloromethane (250 mL each). The combined organic phases were dried over anhydrous sodium sulfate. The product was isolated by column chromatography (SiO_2, CH_2Cl_2/MeOH 40:1, 32:1) as a red solid (1.44 g, 1.93 mmol, **75%**).

^{1}H NMR (400 MHz, $CDCl_3$): δ = 8.55 (dd, J = 4.4, 1.6 Hz, 2H), 8.47 (d, J = 8.0 Hz, 2H), 8.28 (dd, J = 8.2, 3.9 Hz, 4H), 8.05 – 8.01 (m, 2H), 7.31 (dd, J = 4.4, 1.6 Hz, 2H), 4.47–4.41 (m, 2H), 4.35 (t, J = 6.9 Hz, 4H), 3.08 (dd, J = 9.0, 6.8 Hz, 2H), 1.87–1.77 (m, 4H), 1.52–1.25 (m, 20H), 0.92–0.86 (t, J = 6.9 Hz, 6H) ppm. **^{13}C NMR** (101 MHz, $CDCl_3$): δ = 168.3, 163.5, 150.1, 147.8, 135.8, 132.2, 132.0, 131.5, 130.4, 129.3, 129.2, 129.1, 126.0, 124.5, 122.8, 121.9, 121.8, 66.1, 40.8, 33.7, 32.0, 29.5, 29.4, 28.8, 26.2, 22.8, 14.2 ppm. **HR-MS** (ESI, positive, $CH_3CN/CHCl_3$ 1:1, *m*/*z*): Calculated for $[M+H]^+$ ($C_{47}H_{51}N_2O_6$): 739.3742, found: 739.3736; (error = 0.8 ppm). **Elemental analysis** (%): Calculated for $C_{47}H_{50}N_2O_6$: C, 76.40; H, 6.82; N, 3.79; found: C, 76.54; H, 6.93; N, 3.91. **UV/Vis** (CH_2Cl_2, 10^{-5} M: λ_{max} (ε, 10^3 L mol^{-1} cm^{-1})): 263 (37), 446 (19), 475 (40), 505 (53) nm. **Melting point**: 180–182 °C.

N-(2,5,8,11,15,18,21,24-octaoxapentacosan-13-yl)-*N*'-(2-(pyridin-4-yl)ethyl)-perylene-3,4:9,10-tetracarboxylic acid bisimide

(PBI-1)

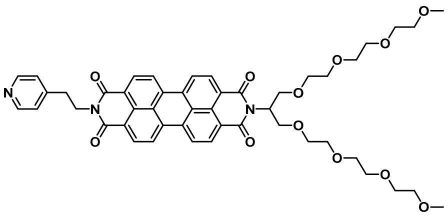

The diester **58** (1.28 g, 1.73 mmol) was suspended in a mixture of glacial acetic acid (30 g) and concentrated sulfuric acid (1.5 g) and refluxed for two hours. The mixture was cooled to room temperature and then poured into deionized water (100 mL). The precipitate was filtered off and washed with water until the filtrate was neutral. After drying the red-brown solid at 80 °C for 12 hours under high vacuum the monoanhydride **59** was obtained (890 mg, 1.79 mmol, 100%). This intermediate was used without further purification and characterization due to insolubility in all common organic solvents. Monoanhydride **59** (500 mg, 1.01 mmol) and the swallowtail amine **55** (630 mg, 1.64 mmol) were stirred together in molten imidazole (4 g) for 6 hours at 130 °C under a nitrogen atmosphere. Then the reaction mixture was poured into deionized water (100 mL) and neutralized with 2N hydrochloric acid (30 mL). The mixture was extracted three times with dichloromethane (15 mL each). The organic phase was washed with a saturated potassium carbonate solution (200 mL) and dried over anhydrous sodium sulfate. The crude product was purified by column chromatography (SiO_2, CH_2Cl_2/MeOH 30:1, 20:1, 16:1) as a greasy red solid (500 mg, 0.580 mmol, **57%**).

^{1}H NMR (400 MHz, $CDCl_3$): δ = 8.62 (d, J = 8.0 Hz, 2H), 8.59–8.53 (m, 4H), 8.53–8.48 (m, 4H), 7.31 (dd, J = 4.4, 1.6 Hz, 2H), 5.74–5.66 (m, 1H), 4.50–4.43 (m, 2H), 4.20 (dd, J = 10.6, 7.8 Hz, 2H), 3.98 (dd, J = 10.6, 5.9 Hz, 2H), 3.76–3.69 (m, 2H), 3.67–3.50 (m, 18H), 3.49–3.45 (m, 4H), 3.32 (s, 6H), 3.13–3.06 (m, 2H) ppm. **^{13}C NMR** (101 MHz, $CDCl_3$): δ = 163.9, 163.3, 150.1, 147.6, 135.0, 134.4, 131.6, 131.5, 129.6, 129.4, 126.6, 126.3, 124.5, 123.7, 123.3, 123.2, 123.0, 72.0, 70.7, 70.7, 70.6, 70.6, 70.5, 69.5, 59.1, 52.3, 40.9, 33.7 ppm. **HR-MS** (ESI, positive, CH_2Cl_2/CH_3CN 1:1, *m*/*z*): Calculated for $[M+H]^+$ ($C_{48}H_{52}N_3O_{12}$): 862.3546, found: 862.3520; (error = 3.0 ppm). **Elemental analysis** (%): Calculated for $C_{48}H_{51}N_3O_{12}$: C, 66.89; H, 5.96; N, 4.88; found: C, 66.72; H, 6.12; N, 5.04. **UV/Vis** (CH_2Cl_2, 10^{-5} M, λ_{max} (ε, 10^3 L mol^{-1} cm^{-1})): 260 (35), 429 (5), 457 (19), 489 (52), 525 (86) nm. **Melting point**: 163–165 °C.

N-(2,5,8,11,15,18,21,24-octaoxapentacosan-13-yl)-*N*'-(2-(pyridin-4-yl)ethyl)-1,6,7,12-tetrachloroperylene-3,4:9,10-tetracarboxylic acid bisimide

(PBI-2)

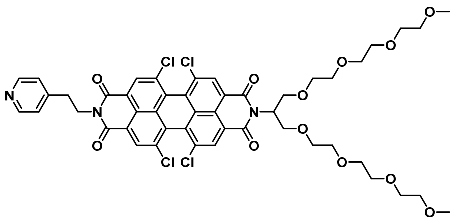

A mixture of 1,6,7,12-tetrachloroperylene-3,4:9,10-tetracarboxylic acid bisanhydride (**60**) (400 mg, 0.755 mmol), the triethylene glycol swallowtail amine **55** (390 mg, 1.02 mmol) and 4-(2-aminoethyl)pyridine (**56**) (123 mg, 1.00 mmol) were refluxed in toluene (8 mL) for 23 hours. The solvent was removed under reduced pressure and the product was isolated by column chromatography (SiO_2, CH_2Cl_2/THF 2:1) and size exclusion chromatography (Biobeads SX3, CH_2Cl_2/CH_3OH 9:1) to yield a greasy red solid (161 mg, 0.161 mmol, **21%**).

^{1}H NMR (400 MHz, CD_2Cl_2): δ = 8.58 (s, 4H), 8.41 (dd, J = 4.4, 1.6 Hz, 2H), 7.19 (dd, J = 4.4, 1.6 Hz, 2H), 5.56 (tt, J = 8.2, 5.7 Hz, 1H), 4.40–4.34 (m, 2H), 4.07 (ddd, J = 10.1, 8.2, 1.7 Hz, 2H), 3.83 (ddd, J = 10.4, 5.7, 1.9 Hz, 2H), 3.61–3.55 (m, 2H), 3.53–3.32 (m, 22H), 3.19 (m, 6H), 2.99 (dd, J = 12.6, 4.7 Hz, 2H) ppm. **^{13}C NMR** (101 MHz, CD_2Cl_2): δ = 163.3, 162.7, 150.4, 148.0, 135.9, 135.8, 133.4 (2C), 132.1, 131.9, 129.5, 129.1, 126.0, 124.9, 124.1, 123.9, 123.5, 72.4, 71.0, 71.0, 70.9, 70.8, 69.4, 69.3, 59.1, 53.3, 41.4, 33.9 ppm. **HR-MS** (ESI, positive, $CHCl_3/CH_3CN$ 1:1, *m*/*z*): Calculated for $[M+H]^+$ ($C_{48}H_{48}Cl_4N_3O_{12}$): 998.1987, found: 998.1983; (error = 0.4 ppm). **Elemental analysis** (%): Calculated for $C_{48}H_{47}Cl_4N_3O_{12}$: C, 57.67; H, 4.74; N, 4.20; found: C, 57.82; H, 4.96; N, 3.88. **UV/Vis** (CH_2Cl_2, 10^{-5} M, λ_{max} (ε, 10^3 L mol^{-1} cm^{-1})): 270 (26), 280 (25), 427 (11), 455 (11), 487 (27), 520 (38) nm. **Melting point**: 118–119 °C.

5.2.4 {Ru(bda)}-PBI Complexes

[Ru(bda)(PBI-1)₂]

(C1)

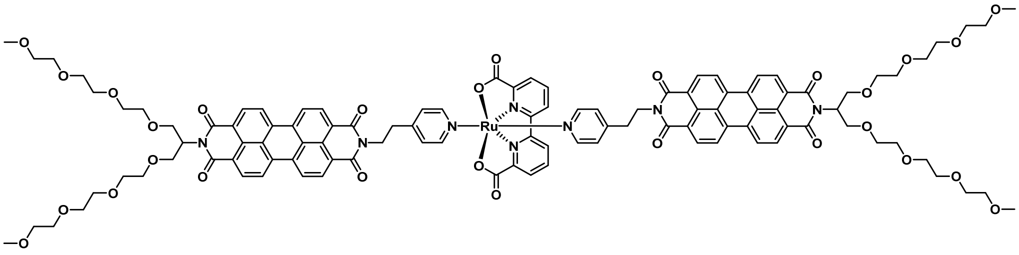

The ligand **PBI-1** (130 mg, 0.151mmol) and the ruthenium precursor [Ru(bda)(dmso)$_2$] (**40**) (30.2 mg, 60.4 µmol) were dissolved in a degassed 1:1 chloroform/methanol mixture (30 mL) and stirred at 60 °C for 6 hours under a nitrogen atmosphere. Then the solvent was removed under reduced pressure and the product was isolated by column chromatography (neutral Al_2O_3 deactivated with 15% H_2O *w*/*w*, CH_2Cl_2/MeOH 100:1, 50:1, 30:1) as a dark red solid (106 mg, 51.3 µmol, **85%**).

^{1}H NMR (400 MHz, δ, ppm, CD_2Cl_2/MeOD 5:1, ascorbic acid): δ = 8.49 (d, *J* = 8.0 Hz, 2H), 8.33–8.06 (m, 18H), 7.85 (t, *J* = 8.0 Hz, 2H), 7.76, (d, *J* = 4.9 Hz, 4H), 7.20 (d, *J* = 5.4 Hz, 4H), 5.58 (m, 2H), 4.25 (m, 4H), 4.17 (m, 4H), 3.96 (m, 4H), 3.76–3.39 (m, 48H), 3.25 (s,12H), 2.99 (m, 4H) ppm. **^{13}C NMR** (400 MHz, δ, ppm, CD_2Cl_2/MeOD 5:1, ascorbic acid): δ = 174.2, 164.2, 163.5, 160.7, 157.7, 152.3, 150.1, 134.7, 134.2, 132.1, 131.5, 131.4, 129.3, 129.1, 126.7, 126.4, 126.0, 125.9, 125.1, 123.7, 123.6, 123.5, 122.8, 72.4, 71.0, 71.0, 71.0, 71.0, 70.9, 70.0, 59.1, 53.0, 40.7, 33.7 ppm. **HR-MS** (ESI, positive, $CHCl_3$/MeOH 1:1, *m*/*z*): Calculated for $[M+H]^+$ ($C_{108}H_{109}N_8O_{28}Ru$): 2067.6389, found: 2067.6402; (error = 0.6 ppm). **UV/Vis** (CH_2Cl_2, 10^{-5} M): λ_{max} (ε, 10^3 L mol^{-1} cm^{-1}): 260 (76), 301 (33), 429 (17), 458 (41), 526 nm (166) nm. **Melting point**: 245–247 °C.

[Ru(bda)(PBI-2)$_2$]

(C2)

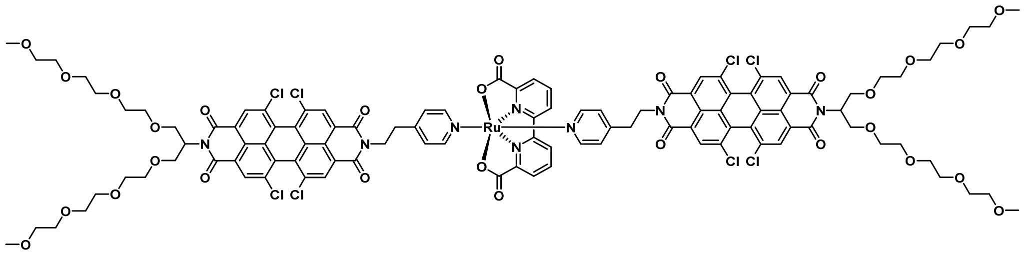

The ligand **PBI-2** (121 mg, 0.121 mmol) and the ruthenium precursor [Ru(bda)(dmso)$_2$] (**40**) (27 mg, 0.054 mmol) were dissolved in a degassed 1:1 chloroform/methanol mixture (30 mL) which was then stirred at 60 °C for 18 hours under an argon atmosphere. The product was isolated by column chromatography (neutral Al_2O_3 deactivated with 15% H_2O *w*/*w*, CH_2Cl_2/CH_3OH 49:1) and size exclusion chromatography (Biobeads SX3, CH_2Cl_2/MeOH 9:1). The solvent was removed under reduced pressure and the product precipitated from diethyl ether to yield a red-black solid (42 mg, 17.9 µmol, **33%**).

^{1}H NMR (400 MHz, CD_2Cl_2/MeOD 5:1, ascorbic acid): δ = 8.57 (s, 4H), 8.55 (s, 4H), 8.30 (d, J = 7.3 Hz, 2H), 7.98 (dd, J = 7.7, 0.9 Hz, 2H), 7.74 (td, J = 8.0, 1.3 Hz, 2H), 7.66 (d, J = 6.6 Hz, 4H), 7.08 (d, J = 6.7 Hz, 4H), 5.60–5.52 (m, 2H), 4.25–4.18 (m, 4H), 4.07 (ddd, J = 12.5, 6.9, 2.8 Hz, 4H), 3.84 (ddd, J = 10.4, 5.6, 1.3 Hz, 4H), 3.59 (ddd, J = 9.9, 4.6, 2.3 Hz, 4H), 3.53–3.35 (m, 44H), 3.22–3.19 (m, 12H), 2.92–2.85 (m, 4H) ppm. **^{13}C NMR** (101 MHz, CD_2Cl_2/MeOD 5:1, ascorbic acid): δ = 173.4, 171.6, 162.9, 162.2, 159.7, 157.0, 152.6, 151.7, 148.9, 135.3, 135.2, 132.8, 131.5, 131.3, 131.2, 128.9, 128.5, 126.0, 125.4, 124.1, 123.5, 123.3, 122.8, 71.7, 70.3, 70.3, 70.2, 70.2, 68.8, 68.7, 62.7, 58.4, 40.3, 32.9 ppm. **HR-MS** (ESI, positive, $CHCl_3$/MeOH 1:1, *m*/*z*): Calculated for $[M]^+$ ($C_{108}H_{100}Cl_8N_8O_{28}Ru$): 2342.3188, found: 2342.3126; (error = 2.6 ppm). **UV/Vis** (CH_2Cl_2, 10^{-5}M): λ_{max} (ε, 10^3 L mol^{-1} cm^{-1}): 279 (63), 299 (48), 426 (27), 454 (26), 486 (59), 520 (84) nm. **Melting point**: 180–182 °C.

[Ru(bda) (PyO) (PBI-1)]

(C3)

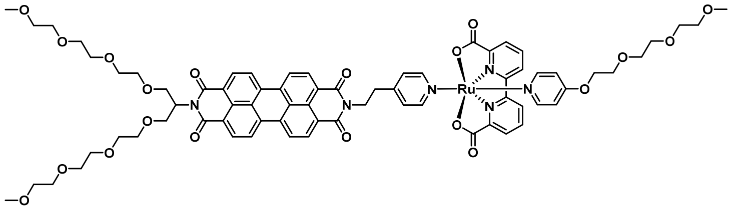

The ligands **PBI-1** (453 mg, 0.526 mmol), and 4-(2-(2-(2-methoxyethoxy)ethoxy)ethoxy)-pyridine (**PyO**) (126 mg, 0.526 mmol), and the ruthenium precursor [Ru(bda)(dmso)$_2$] (**40**) (263 mg, 0.526 mmol) were dissolved in a degassed 5:1 chloroform/methanol mixture (60 mL) and stirred at 60 °C for 3.5 hours under a nitrogen atmosphere. The solvent was then removed under reduced pressure and the crude was purified by column chromatography (neutral Al_2O_3 deactivated with 15% H_2O *w*/*w*, CH_2Cl_2/MeOH 9:1), and size exclusion chromatography (Biobeads SX3, CH_2Cl_2/MeOH 9:1). The final purification was performed using recycling GPC ($CHCl_3$, three columns) to yield a dark red solid (107 mg, 74.0 µmol, **14%**).

^{1}H NMR (400 MHz, CD_2Cl_2/MeOD 5:1, ascorbic acid): δ = 8.42 (dd, J = 8.1, 1.0 Hz, 2H), 8.19 (d, J = 7.9 Hz, 4H), 8.10–8.01 (m, 6H), 7.80 (t, J = 7.9 Hz, 2H), 7.69 (dd, J = 5.3, 1.3 Hz, 2H), 7.55 (dd, J = 5.8, 1.3 Hz, 2H), 7.15 (d, J = 6.7 Hz, 2H), 6.67 (dd, J = 5.8, 1.3 Hz, 2H), 5.64–5.55 (m, 1H), 4.07–4.03 (m, 2H), 3.96 (dd, J = 10.5, 5.9 Hz, 2H), 3.76–3.38 (m, 38H), 3.28 (s, 3H), 3.24 (s, 6H), 3.00–2.94 (m, 2H) ppm. **^{13}C NMR** (101 MHz, CD_2Cl_2/MeOD 5:1, ascorbic acid): δ = 174.2, 166.1, 164.2, 163.4 (2 C), 160.6, 157.6, 153.0, 152.3, 149.9, 134.7, 134.2, 131.7, 131.5 (2C), 129.4, 129.1, 126.6, 126.2, 126.0, 125.9, 124.9, 123.6 (2C), 122.8, 112.5, 72.3, 71.2 (2C), 71.0, 71.0, 70.9 (2C), 70.8, 70.8, 69.9 (2C), 69.4, 68.7, 59.0 (2C), 52.9, 40.7, 33.6 ppm. **HR-MS** (ESI, positive, $CHCl_3$/MeOH 1:1, *m*/*z*): Calculated for $[M]^+$ ($C_{72}H_{76}N_6O_{20}Ru$): 1446.4152, measured: 1446.4187; (error = 2.4 ppm). **UV/Vis** (CH_2Cl_2, 10^{-5} M): λ_{max} (ε, 10^3 L mol^{-1} cm^{-1}): 260 (43), 301 (24), 458 (22), 490 (53), 526 (81) nm. **Melting point**: 220–221 °C.

CHAPTER 6 REFERENCES

[1] M. F. Hohmann-Marriott, R. E. Blankenship, *Annu. Rev. Plant Biol.* **2011**, *62*, 515-548.

[2] F. A. Armstrong, *Philos. Trans. R. Soc., B* **2008**, *363*, 1263-1270.

[3] J. Barber, P. D. Tran, *J. R. Soc., Interface* **2013**, *10*, #2012.0984.

[4] N. Armaroli, V. Balzani, *Chem. – Eur. J.* **2016**, *22*, 32-57.

[5] S. Shafiee, E. Topal, *Energy Policy* **2009**, *37*, 181-189.

[6] N. Armaroli, V. Balzani, *Angew. Chem., Int. Ed.* **2007**, *46*, 52-66.

[7] A. K. Ringsmuth, M. J. Landsberg, B. Hankamer, *Renewable Sustainable Energy Rev.* **2016**, *62*, 134-163.

[8] M. Beller, G. Centi, L. Sun, *ChemSusChem* **2017**, *10*, 6-13.

[9] M. P. R. Perez, *A Fundamental Look At Supply Side Energy Reserves For The Planet, Vol. 62*, The International Energy Agency SHCP Solar Update, **2015**.

[10] N. S. Lewis, D. G. Nocera, *Proc. Natl. Acad. Sci. U.S.A.* **2006**, *103*, 15729-15735.

[11] M. A. Green, K. Emery, Y. Hishikawa, W. Warta, E. D. Dunlop, D. H. Levi, A. W. Y. Ho-Baillie, *Prog. Photovoltaics* **2017**, *25*, 3-13.

[12] M. C. Beard, J. L. Blackburn, J. C. Johnson, G. Rumbles, *ACS Energy Lett.* **2016**, *1*, 344-347.

[13] N. S. Lewis, *Science* **2016**, *351*, aad1920-1926.

[14] C. Kost, J. N. Mayer, J. Thomsen, N. Hartmann, C. Senkpiel, S. Philipps, S. Nold, S. Lude, N. Saad, T. Schlegl, *Levelized cost of electricity renewable energy technologies*, Fraunhofer Institute for Solar Energy Systems ISE, **2013**.

[15] International Energy Agency, Nuclear Energy Agency, France, *Projected Costs of Generating Electricity – 2015 Edition*, **2015**.

[16] Bundesministerium für Wirtschaft und Technologie, Bundesministerium für Umwelt Naturschutz und Reaktorsicherheit, *Energiekonzept für eine umweltschonende, zuverlässige und bezahlbare Energieversorgung*, **2010**.

[17] S. Schemme, R. C. Samsun, R. Peters, D. Stolten, *Fuel* **2017**, *205*, 198-221.

[18] R. Schlögl, *Angew. Chem., Int. Ed.* **2015**, *54*, 4436-4439.

[19] H.-M. Henning, A. Palzer, C. Pape, F. Borggrefe, H. Jachmann, M. Fischedick, *Phasen der Transformation des Energiesystems*, Wuppertal Institut für Klima, Umwelt, Energie, **2015**.

[20] N. Nitta, F. Wu, J. T. Lee, G. Yushin, *Mater. Today* **2015**, *18*, 252-264.

[21] G. E. Blomgren, *J. Electrochem. Soc.* **2017**, *164*, A5019-A5025.

[22] O. Gröger, H. A. Gasteiger, J.-P. Suchsland, *J. Electrochem. Soc.* **2015**, *162*, A2605-A2622.

[23] P. P. Edwards, V. L. Kuznetsov, W. I. F. David, N. P. Brandon, *Energy Policy* **2008**, *36*, 4356-4362.

[24] P. D. Frischmann, K. Mahata, F. Würthner, *Chem. Soc. Rev.* **2013**, *42*, 1847-1870.

[25] J. J. Concepcion, R. L. House, J. M. Papanikolas, T. J. Meyer, *Proc. Natl. Acad. Sci. U.S.A.* **2012**, *109*, 15560-15564.

[26] M. Natali, F. Scandola, in *Applied Photochemistry: When Light Meets Molecules*, 1st ed. (Eds.: G. Bergamini, S. Silvi), Springer International Publishing, Cham (Switzerland), **2016**, pp. 1-66.

[27] D. G. Nocera, *Acc. Chem. Res.* **2012**, *45*, 767-776.

[28] S. Berardi, S. Drouet, L. Francàs, C. Gimbert-Suriñach, M. Guttentag, C. Richmond, T. Stoll, A. Llobet, *Chem. Soc. Rev.* **2014**, *43*, 7501-7519.

[29] K. J. Young, L. A. Martini, R. L. Milot, R. C. Snoeberger III, V. S. Batista, C. A. Schmuttenmaer, R. H. Crabtree, G. W. Brudvig, *Coord. Chem. Rev.* **2012**, *256*, 2503-2520.

[30] M. D. Kärkäs, E. V. Johnston, O. Verho, B. Åkermark, *Acc. Chem. Res.* **2014**, *47*, 100-111.

[31] G. Bottari, O. Trukhina, M. Ince, T. Torres, *Coord. Chem. Rev.* **2012**, *256*, 2453-2477.

[32] M. R. Wasielewski, *Acc. Chem. Res.* **2009**, *42*, 1910-1921.

[33] R. J. Detz, K. Sakai, L. Spiccia, G. W. Brudvig, L. Sun, J. N. H. Reek, *ChemPlusChem* **2016**, *81*, 1024-1027.

[34] R. E. Blankenship, D. M. Tiede, J. Barber, G. W. Brudvig, G. Fleming, M. Ghirardi, M. R. Gunner, W. Junge, D. M. Kramer, A. Melis, T. A. Moore, C. C. Moser, D. G. Nocera, A. J. Nozik, D. R. Ort, W. W. Parson, R. C. Prince, R. T. Sayre, *Science* **2011**, *332*, 805-809.

[35] V. R. Stamenkovic, D. Strmcnik, P. P. Lopes, N. M. Markovic, *Nat. Mater.* **2017**, *16*, 57-69.

[36] L. Carrette, K. A. Friedrich, U. Stimming, *Fuel Cells* **2001**, *1*, 5-39.

[37] I. Ganesh, *Renewable Sustainable Energy Rev.* **2014**, *31*, 221-257.

[38] B. A. Johnson, S. Maji, H. Agarwala, T. A. White, E. Mijangos, S. Ott, *Angew. Chem., Int. Ed.* **2016**, *55*, 1825-1829.

[39] G. A. Olah, *Angew. Chem., Int. Ed.* **2013**, *52*, 104-107.

[40] J. Qiao, Y. Liu, F. Hong, J. Zhang, *Chem. Soc. Rev.* **2014**, *43*, 631-675.

[41] J. L. White, M. F. Baruch, J. E. Pander, Y. Hu, I. C. Fortmeyer, J. E. Park, T. Zhang, K. Liao, J. Gu, Y. Yan, T. W. Shaw, E. Abelev, A. B. Bocarsly, *Chem. Rev.* **2015**, *115*, 12888-12935.

[42] W.-H. Wang, Y. Himeda, J. T. Muckerman, G. F. Manbeck, E. Fujita, *Chem. Rev.* **2015**, *115*, 12936-12973.

[43] J. P. Torella, C. J. Gagliardi, J. S. Chen, D. K. Bediako, B. Colón, J. C. Way, P. A. Silver, D. G. Nocera, *Proc. Natl. Acad. Sci. U.S.A.* **2015**, *112*, 2337-2342.

[44] C. Liu, B. C. Colón, M. Ziesack, P. A. Silver, D. G. Nocera, *Science* **2016**, *352*, 1210-1213.

[45] J. L. Inglis, B. J. MacLean, M. T. Pryce, J. G. Vos, *Coord. Chem. Rev.* **2012**, *256*, 2571-2600.

[46] D. Gust, T. A. Moore, A. L. Moore, *Acc. Chem. Res.* **2009**, *42*, 1890-1898.

[47] L. Hammarström, *Acc. Chem. Res.* **2015**, *48*, 840-850.

[48] R. L. House, N. Y. M. Iha, R. L. Coppo, L. Alibabaei, B. D. Sherman, P. Kang, M. K. Brennaman, P. G. Hoertz, T. J. Meyer, *J. Photochem. Photobiol., C* **2015**, *25*, 32-45.

[49] T. Shinagawa, K. Takanabe, *ChemSusChem* **2017**, *10*, 1318-1336.

[50] A. J. Bard, M. A. Fox, *Acc. Chem. Res.* **1995**, *28*, 141-145.

[51] H. Dau, C. Limberg, T. Reier, M. Risch, S. Roggan, P. Strasser, *ChemCatChem* **2010**, *2*, 724-761.

[52] D. G. H. Hetterscheid, J. N. H. Reek, *Angew. Chem., Int. Ed.* **2012**, *51*, 9740-9747.

[53] M. Okamura, S. Masaoka, *Chem. – Asian J.* **2015**, *10*, 306-315.

[54] S. W. Gersten, G. J. Samuels, T. J. Meyer, *J. Am. Chem. Soc.* **1982**, *104*, 4029-4030.

[55] M. D. Kärkäs, O. Verho, E. V. Johnston, B. Åkermark, *Chem. Rev.* **2014**, *114*, 11863-12001.

[56] L. Francàs, R. Bofill, J. García-Antón, L. Escriche, X. Sala, A. Llobet, in *Molecular Water Oxidation Catalysis*, 1st ed. (Ed.: A. Llobet), John Wiley & Sons, Ltd, Chichester (U.K.), **2014**, pp. 29-50.

[57] L. Duan, L. Wang, F. Li, F. Li, L. Sun, *Acc. Chem. Res.* **2015**, *48*, 2084-2096.

[58] A. Singh, L. Spiccia, *Coord. Chem. Rev.* **2013**, *257*, 2607-2622.

[59] J. D. Blakemore, R. H. Crabtree, G. W. Brudvig, *Chem. Rev.* **2015**, *115*, 12974-13005.

[60] M. D. Kärkäs, B. Åkermark, *Dalton Trans.* **2016**, *45*, 14421-14461.

[61] J. L. Fillol, Z. Codolà, I. Garcia-Bosch, L. Gómez, J. J. Pla, M. Costas, *Nat. Chem.* **2011**, *3*, 807-813.

[62] M. Okamura, M. Kondo, R. Kuga, Y. Kurashige, T. Yanai, S. Hayami, V. K. K. Praneeth, M. Yoshida, K. Yoneda, S. Kawata, S. Masaoka, *Nature* **2016**, *530*, 465-468.

[63] P. Garrido-Barros, C. Gimbert-Suriñach, R. Matheu, X. Sala, A. Llobet, *Chem. Soc. Rev.* **2017**, 10.1039/C7CS00248C.

[64] L. Duan, F. Bozoglian, S. Mandal, B. Stewart, T. Privalov, A. Llobet, L. Sun, *Nat. Chem.* **2012**, *4*, 418-423.

[65] X. Sala, S. Maji, R. Bofill, J. García-Antón, L. Escriche, A. Llobet, *Acc. Chem. Res.* **2014**, *47*, 504-516.

[66] R. Cao, W. Lai, P. Du, *Energy Environ. Sci.* **2012**, *5*, 8134-8157.

[67] T. Kikuchi, K. Tanaka, *Eur. J. Inorg. Chem.* **2014**, *2014*, 607-618.

[68] R.-Z. Liao, M. D. Kärkäs, T. M. Laine, B. Åkermark, P. E. M. Siegbahn, *Catal. Sci. Tech.* **2016**, *6*, 5031-5041.

[69] S. Maji, L. Vigara, F. Cottone, F. Bozoglian, J. Benet-Buchholz, A. Llobet, *Angew. Chem., Int. Ed.* **2012**, *51*, 5967-5970.

[70] L. Tong, L. Duan, Y. Xu, T. Privalov, L. Sun, *Angew. Chem., Int. Ed.* **2011**, *50*, 445-449.

[71] D. W. Shaffer, Y. Xie, D. J. Szalda, J. J. Concepcion, *Inorg. Chem.* **2016**, *55*, 12024-12035.

[72] D. Scherrer, M. Schilling, S. Luber, T. Fox, B. Spingler, R. Alberto, C. J. Richmond, *Dalton Trans.* **2016**, *45*, 19361-19367.

[73] F. Li, K. Fan, L. Wang, Q. Daniel, L. Duan, L. Sun, *ACS Catal.* **2015**, *5*, 3786-3790.

[74] V. Kunz, D. Schmidt, M. I. S. Röhr, R. Mitrić, F. Würthner, *Adv. Energy Mater.* **2017**, *7*, #1602939.

[75] W. Lubitz, E. J. Reijerse, J. Messinger, *Energy Environ. Sci.* **2008**, *1*, 15-31.

[76] C. Zhang, C. Chen, H. Dong, J.-R. Shen, H. Dau, J. Zhao, *Science* **2015**, *348*, 690-693.

[77] J. Barber, *Biochemistry* **2016**, *55*, 5901-5906.

[78] M. Raynal, P. Ballester, A. Vidal-Ferran, P. W. N. M. van Leeuwen, *Chem. Soc. Rev.* **2014**, *43*, 1660-1733.

[79] M. Raynal, P. Ballester, A. Vidal-Ferran, P. W. N. M. van Leeuwen, *Chem. Soc. Rev.* **2014**, *43*, 1734-1787.

[80] P. Dydio, J. N. H. Reek, *Chem. Sci.* **2014**, *5*, 2135-2145.

[81] J. Meeuwissen, J. N. H. Reek, *Nat. Chem.* **2010**, *2*, 615-621.

[82] M. L. Helm, M. P. Stewart, R. M. Bullock, M. R. DuBois, D. L. DuBois, *Science* **2011**, *333*, 863-866.

[83] W.-H. Wang, J. F. Hull, J. T. Muckerman, E. Fujita, Y. Himeda, *Energy Environ. Sci.* **2012**, *5*, 7923-7926.

[84] T. B. Rauchfuss, *Acc. Chem. Res.* **2015**, *48*, 2107-2116.

[85] C. J. Chang, L. L. Chng, D. G. Nocera, *J. Am. Chem. Soc.* **2003**, *125*, 1866-1876.

[86] S. Zarra, D. M. Wood, D. A. Roberts, J. R. Nitschke, *Chem. Soc. Rev.* **2015**, *44*, 419-432.
[87] M. Yoshizawa, M. Tamura, M. Fujita, *Science* **2006**, *312*, 251-254.
[88] S. H. A. M. Leenders, R. Gramage-Doria, B. de Bruin, J. N. H. Reek, *Chem. Soc. Rev.* **2015**, *44*, 433-448.
[89] C. García-Simón, R. Gramage-Doria, S. Raoufmoghaddam, T. Parella, M. Costas, X. Ribas, J. N. H. Reek, *J. Am. Chem. Soc.* **2015**, *137*, 2680-2687.
[90] Z. Dong, Q. Luo, J. Liu, *Chem. Soc. Rev.* **2012**, *41*, 7890-7908.
[91] P. D. Frischmann, V. Kunz, F. Würthner, *Angew. Chem., Int. Ed.* **2015**, *54*, 7285-7289.
[92] M. Schulze, Dissertation, Julius-Maximilians-Universität Würzburg (Würzburg), **2016**.
[93] M. Schulze, V. Kunz, P. D. Frischmann, F. Würthner, *Nat. Chem.* **2016**, *8*, 576-583.
[94] F. Würthner, C. R. Saha-Möller, B. Fimmel, S. Ogi, P. Leowanawat, D. Schmidt, *Chem. Rev.* **2016**, *116*, 962-1052.
[95] J. D. J. Olmos, J. Kargul, *Acta Soc. Bot. Pol.* **2014**, *83*, 423-440.
[96] M. Şener, J. Strümpfer, J. Hsin, D. Chandler, S. Scheuring, C. N. Hunter, K. Schulten, *ChemPhysChem* **2011**, *12*, 518-531.
[97] T. Pullerits, V. Sundström, *Acc. Chem. Res.* **1996**, *29*, 381-389.
[98] X. Qin, M. Suga, T. Kuang, J.-R. Shen, *Science* **2015**, *348*, 989-995.
[99] X. Wei, X. Su, P. Cao, X. Liu, W. Chang, M. Li, X. Zhang, Z. Liu, *Nature* **2016**, *534*, 69-74.
[100] J. A. Bassham, M. Calvin, *The Path of Carbon in Photosynthesis*, **1960**.
[101] N. Cox, D. A. Pantazis, F. Neese, W. Lubitz, *Acc. Chem. Res.* **2013**, *46*, 1588-1596.
[102] M. M. Najafpour, G. Renger, M. Hołyńska, A. N. Moghaddam, E.-M. Aro, R. Carpentier, H. Nishihara, J. J. Eaton-Rye, J.-R. Shen, S. I. Allakhverdiev, *Chem. Rev.* **2016**, *116*, 2886-2936.
[103] J. Limburg, J. S. Vrettos, L. M. Liable-Sands, A. L. Rheingold, R. H. Crabtree, G. W. Brudvig, *Science* **1999**, *283*, 1524-1527.
[104] I. Rivalta, G. W. Brudvig, V. S. Batista, in *Molecular Water Oxidation Catalysis*, 1st ed. (Ed.: A. Llobet), John Wiley & Sons, Ltd, Chichester (U.K.), **2014**, pp. 1-14.
[105] J. Barber, B. Andersson, *Trends Biochem. Sci.* **1992**, *17*, 61-66.
[106] P. Joliot, G. Barbieri, R. Chabaud, *Photochem. Photobiol.* **1969**, *10*, 309-329.
[107] B. Kok, B. Forbush, M. McGloin, *Photochem. Photobiol.* **1970**, *11*, 457-475.
[108] N. Cox, M. Retegan, F. Neese, D. A. Pantazis, A. Boussac, W. Lubitz, *Science* **2014**, *345*, 804-808.
[109] A. Zouni, H.-T. Witt, J. Kern, P. Fromme, N. Krauss, W. Saenger, P. Orth, *Nature* **2001**, *409*, 739-743.
[110] Y. Umena, K. Kawakami, J.-R. Shen, N. Kamiya, *Nature* **2011**, *473*, 55-60.
[111] M. Suga, F. Akita, K. Hirata, G. Ueno, H. Murakami, Y. Nakajima, T. Shimizu, K. Yamashita, M. Yamamoto, H. Ago, J.-R. Shen, *Nature* **2015**, *517*, 99-103.
[112] L. Rapatskiy, N. Cox, A. Savitsky, W. M. Ames, J. Sander, M. M. Nowaczyk, M. Rögner, A. Boussac, F. Neese, J. Messinger, W. Lubitz, *J. Am. Chem. Soc.* **2012**, *134*, 16619-16634.
[113] M. Pérez Navarro, W. M. Ames, H. Nilsson, T. Lohmiller, D. A. Pantazis, L. Rapatskiy, M. M. Nowaczyk, F. Neese, A. Boussac, J. Messinger, W. Lubitz, N. Cox, *Proc. Natl. Acad. Sci. U.S.A.* **2013**, *110*, 15561-15566.
[114] H. Nilsson, F. Rappaport, A. Boussac, J. Messinger, *Nat. Commun.* **2014**, *5*, 4305-4311.
[115] J. Barber, *Nat. Plants* **2017**, *3*, #17041.
[116] J. Messinger, *Phys. Chem. Chem. Phys.* **2004**, *6*, 4764-4771.

[117] R. Gupta, T. Taguchi, B. Lassalle-Kaiser, E. L. Bominaar, J. Yano, M. P. Hendrich, A. S. Borovik, *Proc. Natl. Acad. Sci. U.S.A.* **2015**, *112*, 5319-5324.

[118] R. D. Britt, D. L. M. Suess, T. A. Stich, *Proc. Natl. Acad. Sci. U.S.A.* **2015**, *112*, 5265-5266.

[119] K. N. Ferreira, T. M. Iverson, K. Maghlaoui, J. Barber, S. Iwata, *Science* **2004**, *303*, 1831-1838.

[120] P. E. M. Siegbahn, *Chem. – Eur. J.* **2006**, *12*, 9217-9227.

[121] P. E. M. Siegbahn, *Philos. Trans. R. Soc., B* **2008**, *363*, 1221-1228.

[122] P. E. M. Siegbahn, *Acc. Chem. Res.* **2009**, *42*, 1871-1880.

[123] I. D. Young, M. Ibrahim, R. Chatterjee, S. Gul, F. D. Fuller, S. Koroidov, A. S. Brewster, R. Tran, R. Alonso-Mori, T. Kroll, T. Michels-Clark, H. Laksmono, R. G. Sierra, C. A. Stan, R. Hussein, M. Zhang, L. Douthit, M. Kubin, C. de Lichtenberg, L. Vo Pham, H. Nilsson, M. H. Cheah, D. Shevela, C. Saracini, M. A. Bean, I. Seuffert, D. Sokaras, T.-C. Weng, E. Pastor, C. Weninger, T. Fransson, L. Lassalle, P. Bräuer, P. Aller, P. T. Docker, B. Andi, A. M. Orville, J. M. Glownia, S. Nelson, M. Sikorski, D. Zhu, M. S. Hunter, T. J. Lane, A. Aquila, J. E. Koglin, J. Robinson, M. Liang, S. Boutet, A. Y. Lyubimov, M. Uervirojnangkoorn, N. W. Moriarty, D. Liebschner, P. V. Afonine, D. G. Waterman, G. Evans, P. Wernet, H. Dobbek, W. I. Weis, A. T. Brunger, P. H. Zwart, P. D. Adams, A. Zouni, J. Messinger, U. Bergmann, N. K. Sauter, J. Kern, V. K. Yachandra, J. Yano, *Nature* **2016**, *540*, 453-457.

[124] M. Suga, F. Akita, M. Sugahara, M. Kubo, Y. Nakajima, T. Nakane, K. Yamashita, Y. Umena, M. Nakabayashi, T. Yamane, T. Nakano, M. Suzuki, T. Masuda, S. Inoue, T. Kimura, T. Nomura, S. Yonekura, L.-J. Yu, T. Sakamoto, T. Motomura, J.-H. Chen, Y. Kato, T. Noguchi, K. Tono, Y. Joti, T. Kameshima, T. Hatsui, E. Nango, R. Tanaka, H. Naitow, Y. Matsuura, A. Yamashita, M. Yamamoto, O. Nureki, M. Yabashi, T. Ishikawa, S. Iwata, J.-R. Shen, *Nature* **2017**, *543*, 131-135.

[125] C. Zhang, C. Chen, H. Dong, J.-R. Shen, H. Dau, J. Zhao, *Science* **2015**, *348*, 690-693.

[126] B. C. Polander, B. A. Barry, *J. Phys. Chem. Lett.* **2013**, *4*, 786-791.

[127] B. C. Polander, B. A. Barry, *Proc. Natl. Acad. Sci. U.S.A.* **2013**, *110*, 10634-10639.

[128] A. Sartorel, M. Bonchio, S. Campagna, F. Scandola, *Chem. Soc. Rev.* **2013**, *42*, 2262-2280.

[129] R. A. Binstead, C. W. Chronister, J. Ni, C. M. Hartshorn, T. J. Meyer, *J. Am. Chem. Soc.* **2000**, *122*, 8464-8473.

[130] F. Liu, J. J. Concepcion, J. W. Jurss, T. Cardolaccia, J. L. Templeton, T. J. Meyer, *Inorg. Chem.* **2008**, *47*, 1727-1752.

[131] D. Moonshiram, V. Purohit, J. J. Concepcion, T. J. Meyer, Y. Pushkar, *Materials* **2013**, *6*, 392-409.

[132] V. K. K. Praneeth, M. R. Ringenberg, T. R. Ward, *Angew. Chem., Int. Ed.* **2012**, *51*, 10228-10234.

[133] T. Wada, K. Tanaka, J. T. Muckerman, E. Fujita, in *Molecular Water Oxidation Catalysis*, 1st ed. (Ed.: A. Llobet), John Wiley & Sons, Ltd, Chichester (U.K.), **2014**, pp. 77-111.

[134] T. Wada, K. Tsuge, K. Tanaka, *Angew. Chem., Int. Ed.* **2000**, *39*, 1479-1482.

[135] T. Wada, K. Tsuge, K. Tanaka, *Inorg. Chem.* **2001**, *40*, 329-337.

[136] T. Wada, K. Tanaka, *Eur. J. Inorg. Chem.* **2005**, *2005*, 3832-3839.

[137] M.-K. Tsai, J. Rochford, D. E. Polyansky, T. Wada, K. Tanaka, E. Fujita, J. T. Muckerman, *Inorg. Chem.* **2009**, *48*, 4372-4383.

[138] J. T. Muckerman, D. E. Polyansky, T. Wada, K. Tanaka, E. Fujita, *Inorg. Chem.* **2008**, *47*, 1787-1802.

[139] S. Ghosh, M.-H. Baik, *Angew. Chem., Int. Ed.* **2012**, *51*, 1221-1224.
[140] H. Isobe, K. Tanaka, J.-R. Shen, K. Yamaguchi, *Inorg. Chem.* **2014**, *53*, 3973-3984.
[141] C. Sens, I. Romero, M. Rodríguez, A. Llobet, T. Parella, J. Benet-Buchholz, *J. Am. Chem. Soc.* **2004**, *126*, 7798-7799.
[142] F. Bozoglian, S. Romain, M. Z. Ertem, T. K. Todorova, C. Sens, J. Mola, M. Rodríguez, I. Romero, J. Benet-Buchholz, X. Fontrodona, C. J. Cramer, L. Gagliardi, A. Llobet, *J. Am. Chem. Soc.* **2009**, *131*, 15176-15187.
[143] N. Kaveevivitchai, R. Zong, H.-W. Tseng, R. Chitta, R. P. Thummel, *Inorg. Chem.* **2012**, *51*, 2930-2939.
[144] R. Zong, R. P. Thummel, *J. Am. Chem. Soc.* **2005**, *127*, 12802-12803.
[145] D. E. Polyansky, J. T. Muckerman, J. Rochford, R. Zong, R. P. Thummel, E. Fujita, *J. Am. Chem. Soc.* **2011**, *133*, 14649-14665.
[146] D. J. Wasylenko, R. D. Palmer, C. P. Berlinguette, *Chem. Commun.* **2013**, *49*, 218-227.
[147] J. J. Concepcion, J. W. Jurss, J. L. Templeton, T. J. Meyer, *J. Am. Chem. Soc.* **2008**, *130*, 16462-16463.
[148] J. J. Concepcion, J. W. Jurss, M. R. Norris, Z. Chen, J. L. Templeton, T. J. Meyer, *Inorg. Chem.* **2010**, *49*, 1277-1279.
[149] J. J. Concepcion, M.-K. Tsai, J. T. Muckerman, T. J. Meyer, *J. Am. Chem. Soc.* **2010**, *132*, 1545-1557.
[150] K. S. Shigeyuki Masaoka, *Chem. Lett.* **2009**, *38*, 182-183.
[151] D. J. Wasylenko, C. Ganesamoorthy, B. D. Koivisto, M. A. Henderson, C. P. Berlinguette, *Inorg. Chem.* **2010**, *49*, 2202-2209.
[152] L. Duan, A. Fischer, Y. Xu, L. Sun, *J. Am. Chem. Soc.* **2009**, *131*, 10397-10399.
[153] L. Zhang, Y. Gao, X. Ding, Z. Yu, L. Sun, *ChemSusChem* **2014**, *7*, 2801-2804.
[154] A. R. Parent, R. H. Crabtree, G. W. Brudvig, *Chem. Soc. Rev.* **2013**, *42*, 2247-2252.
[155] K. Kalyanasundaram, *Coord. Chem. Rev.* **1982**, *46*, 159-244.
[156] A. Juris, V. Balzani, F. Barigelletti, S. Campagna, P. Belser, A. von Zelewsky, *Coord. Chem. Rev.* **1988**, *84*, 85-277.
[157] B. Limburg, E. Bouwman, S. Bonnet, *ACS Catal.* **2016**, *6*, 5273-5284.
[158] U. S. Akhtar, E. L. Tae, Y. S. Chun, I. C. Hwang, K. B. Yoon, *ACS Catal.* **2016**, *6*, 8361-8369.
[159] S. Fukuzumi, J. Jung, Y. Yamada, T. Kojima, W. Nam, *Chem. – Asian J.* **2016**, *11*, 1138-1150.
[160] L.-L. Duan, Y.-H. Xu, P. Zhang, M. Wang, L.-C. Sun, *Inorg. Chem.* **2010**, *49*, 209-215.
[161] L.-X. Xue, T.-T. Meng, W. Yang, K.-Z. Wang, *J. Photochem. Photobiol., B* **2015**, *152*, 95-105.
[162] L. Duan, L. Tong, Y. Xu, L. Sun, *Energy Environ. Sci.* **2011**, *4*, 3296-3313.
[163] N. Song, J. J. Concepcion, R. A. Binstead, J. A. Rudd, A. K. Vannucci, C. J. Dares, M. K. Coggins, T. J. Meyer, *Proc. Natl. Acad. Sci. U.S.A.* **2015**, *112*, 4935-4940.
[164] R. Matheu, S. Neudeck, F. Meyer, X. Sala, A. Llobet, *ChemSusChem* **2016**, *9*, 3361-3369.
[165] E. S. Rountree, B. D. McCarthy, T. T. Eisenhart, J. L. Dempsey, *Inorg. Chem.* **2014**, *53*, 9983-10002.
[166] C. Costentin, S. Drouet, M. Robert, J.-M. Savéant, *J. Am. Chem. Soc.* **2012**, *134*, 11235-11242.
[167] E. D. Cline, S. Bernhard, *Chimia* **2009**, *63*, 709-713.
[168] L. Duan, C. M. Araujo, M. S. G. Ahlquist, L. Sun, *Proc. Natl. Acad. Sci. U.S.A.* **2012**, *109*, 15584-15588.

[169] N. D. McDaniel, F. J. Coughlin, L. L. Tinker, S. Bernhard, *J. Am. Chem. Soc.* **2008**, *130*, 210-217.

[170] H. N. Kagalwala, L. Tong, R. Zong, L. Kohler, M. S. G. Ahlquist, T. Fan, K. J. Gagnon, R. P. Thummel, *ACS Catal.* **2017**, *7*, 2607-2615.

[171] L. Duan, Y. Xu, P. Zhang, M. Wang, L. Sun, *Inorg. Chem.* **2010**, *49*, 209-215.

[172] Y. Xu, L. Duan, T. Åkermark, L. Tong, B.-L. Lee, R. Zhang, B. Åkermark, L. Sun, *Chem. – Eur. J.* **2011**, *17*, 9520-9528.

[173] L. C. Clark, Jr., R. Wold, D. Granger, Z. Taylor, *J. Appl. Physiol. (1948-1976)* **1953**, *6*, 189-193.

[174] A. Savini, A. Bucci, G. Bellachioma, L. Rocchigiani, C. Zuccaccia, A. Llobet, A. Macchioni, *Eur. J. Inorg. Chem.* **2014**, *2014*, 690-697.

[175] R. Staehle, L. Tong, L. Wang, L. Duan, A. Fischer, M. S. G. Ahlquist, L. Sun, S. Rau, *Inorg. Chem.* **2014**, *53*, 1307-1319.

[176] D. J. Wasylenko, C. Ganesamoorthy, M. A. Henderson, B. D. Koivisto, H. D. Osthoff, C. P. Berlinguette, *J. Am. Chem. Soc.* **2010**, *132*, 16094-16106.

[177] L. Duan, Y. Xu, M. Gorlov, L. Tong, S. Andersson, L. Sun, *Chem. – Eur. J.* **2010**, *16*, 4659-4668.

[178] C. J. Gagliardi, A. K. Vannucci, J. J. Concepcion, Z. Chen, T. J. Meyer, *Energy Environ. Sci.* **2012**, *5*, 7704-7717.

[179] Z. Chen, J. J. Concepcion, X. Hu, W. Yang, P. G. Hoertz, T. J. Meyer, *Proc. Natl. Acad. Sci. U.S.A.* **2010**, *107*, 7225-7229.

[180] S. Neudeck, S. Maji, I. López, S. Meyer, F. Meyer, A. Llobet, *J. Am. Chem. Soc.* **2014**, *136*, 24-27.

[181] J. L. Cape, W. F. Siems, J. K. Hurst, *Inorg. Chem.* **2009**, *48*, 8729-8735.

[182] S. Romain, F. Bozoglian, X. Sala, A. Llobet, *J. Am. Chem. Soc.* **2009**, *131*, 2768-2769.

[183] J. J. Concepcion, D. K. Zhong, D. J. Szalda, J. T. Muckerman, E. Fujita, *Chem. Commun.* **2015**, *51*, 4105-4108.

[184] J. Honta, S. Tajima, T. Sato, K. Saito, T. Yui, M. Yagi, *J. Photochem. Photobiol., A* **2015**, *313*, 126-130.

[185] A. Kimoto, K. Yamauchi, M. Yoshida, S. Masaoka, K. Sakai, *Chem. Commun.* **2012**, *48*, 239-241.

[186] Q. Daniel, P. Huang, T. Fan, Y. Wang, L. L. Duan, L. Wang, F. S. Li, Z. Rinkevicius, F. Mamedov, M. S. G. Ahlquist, S. Styring, L. C. Sun, *Coord. Chem. Rev.* **2017**, *346*, 206-215.

[187] B. Yang, X. Jiang, Q. Guo, T. Lei, L.-P. Zhang, B. Chen, C.-H. Tung, L.-Z. Wu, *Angew. Chem., Int. Ed.* **2016**, *55*, 6229-6234.

[188] D. Moonshiram, Y. Pineda-Galvan, D. Erdman, M. Palenik, R. Zong, R. Thummel, Y. Pushkar, *J. Am. Chem. Soc.* **2016**, *138*, 15605-15616.

[189] D. Moonshiram, I. Alperovich, J. J. Concepcion, T. J. Meyer, Y. Pushkar, *Proc. Natl. Acad. Sci. U.S.A.* **2013**, *110*, 3765-3770.

[190] Y. Pushkar, D. Moonshiram, V. Purohit, L. Yan, I. Alperovich, *J. Am. Chem. Soc.* **2014**, *136*, 11938-11945.

[191] C. Gimbert-Suriñach, D. Moonshiram, L. Francàs, N. Planas, V. Bernales, F. Bozoglian, A. Guda, L. Mognon, I. López, M. A. Hoque, L. Gagliardi, C. J. Cramer, A. Llobet, *J. Am. Chem. Soc.* **2016**, *138*, 15291-15294.

[192] L. Tong, Y. Wang, L. Duan, Y. Xu, X. Cheng, A. Fischer, M. S. G. Ahlquist, L. Sun, *Inorg. Chem.* **2012**, *51*, 3388-3398.

[193] E. M. Duffy, B. M. Marsh, E. Garand, *J. Phys. Chem. A* **2015**, *119*, 6326-6332.

[194] S. Xu, J. E. T. Smith, J. M. Weber, *J. Phys. Chem. A* **2016**, *120*, 7650-7658.

[195] R. Bianco, P. J. Hay, J. T. Hynes, *J. Phys. Chem. B* **2013**, *117*, 15761-15773.

[196] R. Bianco, P. J. Hay, J. T. Hynes, *J. Phys. Chem. A* **2011**, *115*, 8003-8016.
[197] R. Bianco, P. J. Hay, J. T. Hynes, *Energy Environ. Sci.* **2012**, *5*, 7741-7746.
[198] J. Nyhlén, L. Duan, B. Åkermark, L. Sun, T. Privalov, *Angew. Chem.* **2010**, *122*, 1817-1821.
[199] T. Privalov, B. Åkermark, L. Sun, *Chem. – Eur. J.* **2011**, *17*, 8313-8317.
[200] Y. Wang, M. S. G. Ahlquist, *Dalton Trans.* **2014**, *43*, 13776-13782.
[201] T. Fan, S. Zhan, M. S. G. Ahlquist, *ACS Catal.* **2016**, *6*, 8308-8312.
[202] R. Kang, J. Yao, H. Chen, *J. Chem. Theory Comput.* **2013**, *9*, 1872-1879.
[203] T. F. Hughes, R. A. Friesner, *J. Phys. Chem. B* **2011**, *115*, 9280-9289.
[204] A. Ozkanlar, A. E. Clark, *J. Chem. Phys.* **2012**, *136*, #204104.
[205] D. Balcells, in *Adv. Organomet. Chem., Vol. 65* (Ed.: J. P. Pedro), Academic Press, **2016**, pp. 115-173.
[206] A. Laio, M. Parrinello, *Proc. Natl. Acad. Sci. U.S.A.* **2002**, *99*, 12562-12566.
[207] C. Ma, S. Piccinin, S. Fabris, *ACS Catal.* **2012**, *2*, 1500-1506.
[208] B. Li, F. Li, S. Bai, Z. Wang, L. Sun, Q. Yang, C. Li, *Energy Environ. Sci.* **2012**, *5*, 8229-8233.
[209] Y. Jiang, F. Li, B. Zhang, X. Li, X. Wang, F. Huang, L. Sun, *Angew. Chem., Int. Ed.* **2013**, *52*, 3398-3401.
[210] Z. Liu, Y. Gao, M. Zhang, J. Liu, *Inorg. Chem. Commun.* **2015**, *55*, 56-59.
[211] L. L. Zhang, Y. Gao, Z. Liu, X. Ding, Z. Yu, L. C. Sun, *Dalton Trans.* **2016**, *45*, 3814-3819.
[212] R. Matheu, L. Francàs, P. Chernev, M. Z. Ertem, V. Batista, M. Haumann, X. Sala, A. Llobet, *ACS Catal.* **2015**, *5*, 3422-3429.
[213] B. Limburg, E. Bouwman, S. Bonnet, *Coord. Chem. Rev.* **2012**, *256*, 1451-1467.
[214] X. Wu, F. Li, B. Zhang, L. Sun, *J. Photochem. Photobiol., C* **2015**, *25*, 71-89.
[215] C. J. Richmond, R. Matheu, A. Poater, L. Falivene, J. Benet-Buchholz, X. Sala, L. Cavallo, A. Llobet, *Chem. – Eur. J.* **2014**, *20*, 17282-17286.
[216] L. Wang, L. Duan, Y. Wang, M. S. G. Ahlquist, L. Sun, *Chem. Commun.* **2014**, *50*, 12947-12950.
[217] F. Ding, L. Duan, Y. Gao, *Inorg. Chem. Commun.* **2016**, *70*, 129-131.
[218] A. Králík, M. Hansen, B. König, *RSC Adv.* **2016**, *6*, 5739-5744.
[219] R. Matheu, M. Z. Ertem, J. Benet-Buchholz, E. Coronado, V. S. Batista, X. Sala, A. Llobet, *J. Am. Chem. Soc.* **2015**, *137*, 10786-10795.
[220] J. L. Boyer, D. E. Polyansky, D. J. Szalda, R. Zong, R. P. Thummel, E. Fujita, *Angew. Chem., Int. Ed.* **2011**, *50*, 12600-12604.
[221] P. Wrzolek, S. Wahl, M. Schwalbe, *Catal. Today* **2017**, *290*, 28-32.
[222] P. Wrzolek, M. Schwalbe, *Eur. J. Inorg. Chem.* **2015**, *2015*, 4373-4378.
[223] Y. Xie, D. W. Shaffer, A. Lewandowska-Andralojc, D. J. Szalda, J. J. Concepcion, *Angew. Chem., Int. Ed.* **2016**, *55*, 8067-8071.
[224] M. Yoshida, M. Kondo, S. Torii, K. Sakai, S. Masaoka, *Angew. Chem., Int. Ed.* **2015**, *54*, 7981-7984.
[225] C.-C. You, R. Dobrawa, C. R. Saha-Möller, F. Würthner, in *Top. Curr. Chem., Vol. 258* (Ed.: F. Würthner), Springer-Verlag, Berlin, Heidelberg (Germany), **2005**, pp. 39-82.
[226] S. Scheerer, M. Linseis, E. Wuttke, S. Weickert, M. Drescher, O. Tröppner, I. Ivanović-Burmazović, A. Irmler, F. Pauly, R. F. Winter, *Chem. – Eur. J.* **2016**, *22*, 9843-9843.
[227] C. J. Richmond, A. Llobet, *Catal. Sci. Tech.* **2016**, *6*, 6697-6704.
[228] W.-B. Yu, Q.-Y. He, H.-T. Shi, G. Yuan, X. Wei, *Chem. – Asian J.* **2015**, *10*, 239-246.
[229] W.-B. Yu, Q.-Y. He, H.-T. Shi, X. Wei, *New J. Chem.* **2016**, *40*, 2354-2361.

[230] Y. Dong, J. Zhang, J. Ma, *Patent: CN104558050*, Shandong Normal University, **2015**.

[231] J. L. McHale, *J. Phys. Chem. Lett.* **2012**, *3*, 587-597.

[232] S. Kundu, A. Patra, *Chem. Rev.* **2017**, *117*, 712-757.

[233] A. Harriman, *Chem. Commun.* **2015**, *51*, 11745-11756.

[234] T. Brixner, R. Hildner, J. Köhler, C. Lambert, F. Würthner, *Adv. Energy Mater.*, 10.1002/aenm.201700236, 1700236-n/a.

[235] D. L. Ashford, M. K. Gish, A. K. Vannucci, M. K. Brennaman, J. L. Templeton, J. M. Papanikolas, T. J. Meyer, *Chem. Rev.* **2015**, *115*, 13006-13049.

[236] S. Berardi, L. Francàs, S. Neudeck, S. Maji, J. Benet-Buchholz, F. Meyer, A. Llobet, *ChemSusChem* **2015**, *8*, 3688-3696.

[237] A. Lewandowska-Andralojc, D. E. Polyansky, R. Zong, R. P. Thummel, E. Fujita, *Phys. Chem. Chem. Phys.* **2013**, *15*, 14058-14068.

[238] T. M. Laine, M. D. Kärkäs, R.-Z. Liao, T. Åkermark, B.-L. Lee, E. A. Karlsson, P. E. M. Siegbahn, B. Åkermark, *Chem. Commun.* **2015**, *51*, 1862-1865.

[239] L. Wang, M. Mirmohades, A. Brown, L. Duan, F. Li, Q. Daniel, R. Lomoth, L. Sun, L. Hammarström, *Inorg. Chem.* **2015**, *54*, 2742-2751.

[240] H. Junge, N. Rockstroh, S. Fischer, A. Brückner, R. Ludwig, S. Lochbrunner, O. Kühn, M. Beller, *Inorganics* **2017**, *5*, #14.

[241] M. K. Brennaman, R. J. Dillon, L. Alibabaei, M. K. Gish, C. J. Dares, D. L. Ashford, R. L. House, G. J. Meyer, J. M. Papanikolas, T. J. Meyer, *J. Am. Chem. Soc.* **2016**, *138*, 13085-13102.

[242] N. Kaveevivitchai, R. Chitta, R. Zong, M. El Ojaimi, R. P. Thummel, *J. Am. Chem. Soc.* **2012**, *134*, 10721-10724.

[243] J. J. Concepcion, J. W. Jurss, P. G. Hoertz, T. J. Meyer, *Angew. Chem., Int. Ed.* **2009**, *48*, 9473-9476.

[244] V. Balzani, F. Scandola, *Supramolecular Photochemistry*, Ellis Horwood, Chichester (U.K.), **1991**.

[245] D. L. Ashford, D. J. Stewart, C. R. Glasson, R. A. Binstead, D. P. Harrison, M. R. Norris, J. J. Concepcion, Z. Fang, J. L. Templeton, T. J. Meyer, *Inorg. Chem.* **2012**, *51*, 6428-6430.

[246] M. R. Norris, J. J. Concepcion, D. P. Harrison, R. A. Binstead, D. L. Ashford, Z. Fang, J. L. Templeton, T. J. Meyer, *J. Am. Chem. Soc.* **2013**, *135*, 2080-2083.

[247] L. Alibabaei, B. D. Sherman, M. R. Norris, M. K. Brennaman, T. J. Meyer, *Proc. Natl. Acad. Sci. U.S.A.* **2015**, *112*, 5899-5902.

[248] F. Li, Y. Jiang, B. Zhang, F. Huang, Y. Gao, L. Sun, *Angew. Chem., Int. Ed.* **2012**, *51*, 2417-2420.

[249] H. Li, F. Li, B. Zhang, X. Zhou, F. Yu, L. Sun, *J. Am. Chem. Soc.* **2015**, *137*, 4332-4335.

[250] H. Li, F. Li, Y. Wang, L. C. Bai, F. S. Yu, L. C. Sun, *ChemPlusChem* **2016**, *81*, 1056-1059.

[251] M. Hansen, F. Li, L. Sun, B. König, *Chem. Sci.* **2014**, *5*, 2683-2687.

[252] Y. Sato, S. Takizawa, S. Murata, *J. Photochem. Photobiol., A* **2016**, *321*, 151-160.

[253] M. V. Sheridan, B. D. Sherman, R. L. Coppo, D. G. Wang, S. L. Marquard, K. R. Wee, N. Y. M. Iha, T. J. Meyer, *ACS Energy Lett.* **2016**, *1*, 231-236.

[254] M. R. Norris, J. J. Concepcion, Z. Fang, J. L. Templeton, T. J. Meyer, *Angew. Chem., Int. Ed.* **2013**, *52*, 13580-13583.

[255] M. Yamamoto, L. Wang, F. Li, T. Fukushima, K. Tanaka, L. Sun, H. Imahori, *Chem. Sci.* **2016**, *7*, 1430-1439.

[256] Y. Gao, X. Ding, J. Liu, L. Wang, Z. Lu, L. Li, L. Sun, *J. Am. Chem. Soc.* **2013**, *135*, 4219-4222.

[257] Y. Gao, L. Zhang, X. Ding, L. Sun, *Phys. Chem. Chem. Phys.* **2014**, *16*, 12008-12013.

[258] M. P. Soriaga, J. H. Baricuatro, K. D. Cummins, Y.-G. Kim, F. H. Saadi, G. Sun, C. C. L. McCrory, J. R. McKone, J. M. Velazquez, I. M. Ferrer, A. I. Carim, A. Javier, B. Chmielowiec, D. C. Lacy, J. M. Gregoire, J. Sanabria-Chinchilla, X. Amashukeli, W. J. Royea, B. S. Brunschwig, J. C. Hemminger, N. S. Lewis, J. L. Stickney, *Surf. Sci.* **2015**, *631*, 285-294.

[259] B. D. Sherman, D. L. Ashford, A. M. Lapides, M. V. Sheridan, K.-R. Wee, T. J. Meyer, *J. Phys. Chem. Lett.* **2015**, *6*, 3213-3217.

[260] Z. Fang, A. Ito, H. Luo, D. L. Ashford, J. J. Concepcion, L. Alibabaei, T. J. Meyer, *Dalton Trans.* **2015**, *44*, 8640-8648.

[261] D. L. Ashford, B. D. Sherman, R. A. Binstead, J. L. Templeton, T. J. Meyer, *Angew. Chem., Int. Ed.* **2015**, *54*, 4778-4781.

[262] D. L. Ashford, A. M. Lapides, A. K. Vannucci, K. Hanson, D. A. Torelli, D. P. Harrison, J. L. Templeton, T. J. Meyer, *J. Am. Chem. Soc.* **2014**, *136*, 6578-6581.

[263] X. Ding, Y. Gao, L. Zhang, Z. Yu, J. Liu, L. Sun, *ACS Catal.* **2014**, *4*, 2347-2350.

[264] K. Hanson, D. A. Torelli, A. K. Vannucci, M. K. Brennaman, H. Luo, L. Alibabaei, W. Song, D. L. Ashford, M. R. Norris, C. R. K. Glasson, J. J. Concepcion, T. J. Meyer, *Angew. Chem., Int. Ed.* **2012**, *51*, 12782-12785.

[265] C. R. K. Glasson, W. Song, D. L. Ashford, A. Vannucci, Z. Chen, J. J. Concepcion, P. L. Holland, T. J. Meyer, *Inorg. Chem.* **2012**, *51*, 8637-8639.

[266] F. Li, K. Fan, B. Xu, E. Gabrielsson, Q. Daniel, L. Li, L. Sun, *J. Am. Chem. Soc.* **2015**, *137*, 9153-9159.

[267] V. Kunz, J. O. Lindner, M. Schulze, M. I. S. Röhr, D. Schmidt, R. Mitrić, F. Würthner, *Energy. Environ. Sci.* **2017**, DOI: 10.1039/c7ee01557g.

[268] J. O. Lindner, Master Thesis, Julius-Maximilians-Universität Würzburg (Würzburg), **2016**.

[269] C. Tard, C. J. Pickett, *Chem. Rev.* **2009**, *109*, 2245-2274.

[270] J. Esselborn, C. Lambertz, A. Adamska-Venkatesh, T. Simmons, G. Berggren, J. Noth, J. Siebel, A. Hemschemeier, V. Artero, E. Reijerse, M. Fontecave, W. Lubitz, T. Happe, *Nat. Chem. Biol.* **2013**, *9*, 607-609.

[271] G. Berggren, A. Adamska, C. Lambertz, T. R. Simmons, J. Esselborn, M. Atta, S. Gambarelli, J. M. Mouesca, E. Reijerse, W. Lubitz, T. Happe, V. Artero, M. Fontecave, *Nature* **2013**, *499*, 66-69.

[272] D. R. Weinberg, C. J. Gagliardi, J. F. Hull, C. F. Murphy, C. A. Kent, B. C. Westlake, A. Paul, D. H. Ess, D. G. McCafferty, T. J. Meyer, *Chem. Rev.* **2012**, *112*, 4016-4093.

[273] S. Hammes-Schiffer, A. A. Stuchebrukhov, *Chem. Rev.* **2010**, *110*, 6939-6960.

[274] S. Hammes-Schiffer, *J. Am. Chem. Soc.* **2015**, *137*, 8860-8871.

[275] L. Vigara, M. Z. Ertem, N. Planas, F. Bozoglian, N. Leidel, H. Dau, M. Haumann, L. Gagliardi, C. J. Cramer, A. Llobet, *Chem. Sci.* **2012**, *3*, 2576-2586.

[276] V. Kunz, M. Schulze, D. Schmidt, F. Würthner, *ACS Energy Lett.* **2017**, *2*, 288-293.

[277] I. P. Evans, A. Spencer, G. Wilkinson, *J. Chem. Soc., Dalton Trans.* **1973**, 204-209.

[278] C. L. Donnici, D. H. Máximo Filho, L. L. C. Moreira, G. T. d. Reis, E. S. Cordeiro, I. M. F. d. Oliveira, S. Carvalho, E. B. Paniago, *J. Braz. Chem. Soc.* **1998**, *9*, 455-460.

[279] F. Li, B. Zhang, X. Li, Y. Jiang, L. Chen, Y. Li, L. Sun, *Angew. Chem., Int. Ed.* **2011**, *50*, 12276-12279.

[280] H. Wang, X. Gu, B. Zhang, H. Su, M. Hu, *Acta Crystallogr., Sect. E* **2012**, *68*, m290-m291.

[281] H. Wang, X. Gu, B. Zhang, H. Su, *Acta Crystallogr., Sect. E* **2012**, *68*, m411-m412.

[282] H. Wang, H. Su, J. Xu, F. Bai, Y. Gao, *Acta Crystallogr., Sect. E* **2009**, *65*, m352-m353.

[283] R. Chakrabarty, P. S. Mukherjee, P. J. Stang, *Chem. Rev.* **2011**, *111*, 6810-6918.

[284] E. A. K. James E. Huheey, Richard L. Keiter, *Inorganic Chemistry: Principles of Structure and Reactivity*, 4th ed., HarperCollins College Publishers, New York, **1993**.

[285] L. Helm, A. E. Merbach, *Chem. Rev.* **2005**, *105*, 1923-1960.

[286] W. Hillier, T. Wydrzynski, *Biochim. Biophys. Acta, Bioenerg.* **2001**, *1503*, 197-209.

[287] F. Basolo, R. G. Pearson, in *Mechanisms of Inorganic Reactions: A Study of Metal Complexes in Solution*, 2nd ed. (Ed.: W. I. Stephen), J. Wiley and Sons, New York, **1967**.

[288] J. Reedijk, *Platinum Met. Rev.* **2008**, *52*, 2-11.

[289] P. V. Grundler, G. Laurenczy, A. E. Merbach, *Helv. Chim. Acta* **2001**, *84*, 2854-2867.

[290] N. Aebischer, G. Laurenczy, A. Ludi, A. E. Merbach, *Inorg. Chem.* **1993**, *32*, 2810-2814.

[291] D. De Vito, H. Sidorenkova, F. P. Rotzinger, J. Weber, A. E. Merbach, *Inorg. Chem.* **2000**, *39*, 5547-5552.

[292] R. A. Leising, J. S. Ohman, K. J. Takeuchi, *Inorg. Chem.* **1988**, *27*, 3804-3809.

[293] G. A. Lawrance, *Adv. Inorg. Chem.* **1989**, *34*, 145-194.

[294] L. Tong, R. P. Thummel, *Chem. Sci.* **2016**, *7*, 6591-6603.

[295] O. Piovesana, J. Selbin, *J. Inorg. Nucl. Chem.* **1969**, *31*, 443-447.

[296] C. Janiak, T. Klapötke, H.-J. Meyer, R. Alsfasser, E. Riedel, *Moderne Anorganische Chemie*, 3rd ed., De Gruyter, Berlin, Boston, **2008**.

[297] A. Garci, S. Marti, S. Schurch, B. Therrien, *RSC Adv.* **2014**, *4*, 8597-8604.

[298] J. Mola, I. Romero, M. Rodríguez, F. Bozoglian, A. Poater, M. Solà, T. Parella, J. Benet-Buchholz, X. Fontrodona, A. Llobet, *Inorg. Chem.* **2007**, *46*, 10707-10716.

[299] J. M. Santos, C. Cipriano, R. B. Faria, J. D. Figueroa-Villar, *Can. J. Chem.* **1997**, *75*, 890-898.

[300] E. Alessio, G. Balducci, M. Calligaris, G. Costa, W. M. Attia, G. Mestroni, *Inorg. Chem.* **1991**, *30*, 609-618.

[301] M. Abe, Y. Sasaki, A. Nagasawa, T. Ito, *Bull. Chem. Soc. Jpn.* **1992**, *65*, 1411-1414.

[302] M. Abe, A. Mitani, A. Ohsawa, M. Herai, M. Tanaka, Y. Sasaki, *Inorg. Chim. Acta* **2002**, *331*, 158-167.

[303] M. Abe, M. Tanaka, K. Umakoshi, Y. Sasaki, *Inorg. Chem.* **1999**, *38*, 4146-4148.

[304] D. K. Chand, K. Biradha, M. Kawano, S. Sakamoto, K. Yamaguchi, M. Fujita, *Chem. – Asian J.* **2006**, *1*, 82-90.

[305] F. A. Pereira, T. Fallows, M. Frank, A. Chen, G. H. Clever, *Z. Anorg. Allg. Chem.* **2013**, *639*, 1598-1605.

[306] T. R. Cook, P. J. Stang, *Chem. Rev.* **2015**, *115*, 7001-7045.

[307] D. Moonshiram, J. W. Jurss, J. J. Concepcion, T. Zakharova, I. Alperovich, T. J. Meyer, Y. Pushkar, *J. Am. Chem. Soc.* **2012**, *134*, 4625-4636.

[308] J. A. Stull, T. A. Stich, J. K. Hurst, R. D. Britt, *Inorg. Chem.* **2013**, *52*, 4578-4586.

[309] N. Planas, L. Vigara, C. Cady, P. Miró, P. Huang, L. Hammarström, S. Styring, N. Leidel, H. Dau, M. Haumann, L. Gagliardi, C. J. Cramer, A. Llobet, *Inorg. Chem.* **2011**, *50*, 11134-11142.

[310] D. Erdman, Y. Pineda-Galvan, Y. Pushkar, *Catalysts* **2017**, *7*, 39.

[311] L. Duan, L. Wang, A. K. Inge, A. Fischer, X. Zou, L. Sun, *Inorg. Chem.* **2013**, *52*, 7844-7852.

[312] Z. Chen, A. K. Vannucci, J. J. Concepcion, J. W. Jurss, T. J. Meyer, *Proc. Natl. Acad. Sci. U.S.A.* **2011**, *108*, E1461-E1469.

[313] Q. Daniel, L. Wang, L. Duan, F. Li, L. Sun, *Dalton Trans.* **2016**, *45*, 14689-14696.
[314] J. An, L. Duan, L. Sun, *Faraday Discuss.* **2012**, *155*, 267-275.
[315] B. Zhang, F. Li, R. Zhang, C. Ma, L. Chen, L. Sun, *Chem. Commun.* **2016**, *52*, 8619-8622.
[316] Y. Tsubonouchi, S. Lin, A. R. Parent, G. W. Brudvig, K. Sakai, *Chem. Commun.* **2016**, *52*, 8018-8021.
[317] F. P. Rotzinger, S. Munavalli, P. Comte, J. K. Hurst, M. Grätzel, F. J. Pern, A. J. Frank, *J. Am. Chem. Soc.* **1987**, *109*, 6619-6626.
[318] M. K. Nazeeruddin, F. P. Rotzinger, P. Comte, M. Grätzel, *J. Chem. Soc., Chem. Commun.* **1988**, 872-874.
[319] J. A. Gilbert, D. S. Eggleston, W. R. Murphy, D. A. Geselowitz, S. W. Gersten, D. J. Hodgson, T. J. Meyer, *J. Am. Chem. Soc.* **1985**, *107*, 3855-3864.
[320] J. W. Jurss, J. J. Concepcion, J. M. Butler, K. M. Omberg, L. M. Baraldo, D. G. Thompson, E. L. Lebeau, B. Hornstein, J. R. Schoonover, H. Jude, J. D. Thompson, D. M. Dattelbaum, R. C. Rocha, J. L. Templeton, T. J. Meyer, *Inorg. Chem.* **2012**, *51*, 1345-1358.
[321] J. P. Zobel, J. J. Nogueira, L. González, *J. Phys. Chem. Lett.* **2015**, *6*, 3006-3011.
[322] M. J. G. Peach, P. Benfield, T. Helgaker, D. J. Tozer, *J. Chem. Phys.* **2008**, *128*, #044118.
[323] V. Kunz, V. Stepanenko, F. Würthner, *Chem. Commun.* **2015**, *51*, 290-293.
[324] N. Sutin, C. Creutz, in *Inorganic and Organometallic Photochemistry, Vol. 168*, American Chemical Society, **1978**, pp. 1-27.
[325] F. Puntoriero, A. Sartorel, M. Orlandi, G. La Ganga, S. Serroni, M. Bonchio, F. Scandola, S. Campagna, *Coord. Chem. Rev.* **2011**, *255*, 2594-2601.
[326] H. Lv, J. Song, Y. V. Geletii, J. W. Vickers, J. M. Sumliner, D. G. Musaev, P. Kögerler, P. F. Zhuk, J. Bacsa, G. Zhu, C. L. Hill, *J. Am. Chem. Soc.* **2014**, *136*, 9268-9271.
[327] W. Rabten, M. D. Kärkäs, T. Åkermark, H. Chen, R.-Z. Liao, F. Tinnis, J. Sun, P. E. M. Siegbahn, P. G. Andersson, B. Åkermark, *Inorg. Chem.* **2015**, *54*, 4611-4620.
[328] M.-T. Zhang, T. Irebo, O. Johansson, L. Hammarström, *J. Am. Chem. Soc.* **2011**, *133*, 13224-13227.
[329] N. Iordanova, S. Hammes-Schiffer, *J. Am. Chem. Soc.* **2002**, *124*, 4848-4856.
[330] D. K. Bediako, B. H. Solis, D. K. Dogutan, M. M. Roubelakis, A. G. Maher, C. H. Lee, M. B. Chambers, S. Hammes-Schiffer, D. G. Nocera, *Proc. Natl. Acad. Sci. U.S.A.* **2014**, *111*, 15001-15006.
[331] J. S. Kretchmer, T. F. Miller, *Inorg. Chem.* **2016**, *55*, 1022-1031.
[332] D. J. Cárdenas, J. M. Cuerva, M. Alías, E. Buñuel, A. G. Campaña, *Chem. – Eur. J.* **2011**, *17*, 8318-8323.
[333] H. Zhu, M. Sommerhalter, A. K. L. Nguy, J. P. Klinman, *J. Am. Chem. Soc.* **2015**, *137*, 5720-5729.
[334] A. Monti, J. M. de Ruiter, H. J. M. de Groot, F. Buda, *J. Phys. Chem. C* **2016**, *120*, 23074-23082.
[335] C. Capello, U. Fischer, K. Hungerbuhler, *Green Chem.* **2007**, *9*, 927-934.
[336] D. Preston, A. Fox-Charles, W. K. C. Lo, J. D. Crowley, *Chem. Commun.* **2015**, *51*, 9042-9045.
[337] P. Raboisson, C. L. Manthey, M. Chaikin, J. Lattanze, C. Crysler, K. Leonard, W. Pan, B. E. Tomczuk, J. J. Marugán, *Eur. J. Med. Chem.* **2006**, *41*, 847-861.
[338] J. Hood, D. M. Wallace, S. K. KC, *Patent: US 8703794 B2*, Samumed, Llc, **2009**.
[339] Y. Jiang, F. Li, F. Huang, B. Zhang, L. Sun, *Chin. J. Catal.* **2013**, *34*, 1489-1495.
[340] L. Tong, A. K. Inge, L. Duan, L. Wang, X. Zou, L. Sun, *Inorg. Chem.* **2013**, *52*, 2505-2518.

[341] T. J. Meyer, *Acc. Chem. Res.* **1989**, *22*, 163-170.

[342] J. H. Alstrum-Acevedo, M. K. Brennaman, T. J. Meyer, *Inorg. Chem.* **2005**, *44*, 6802-6827.

[343] S. Zhang, H. Wang, M. Li, J. Han, S. Inagaki, X. Liu, *Dalton Trans.* **2017**, 10.1039/C7DT02026K.

[344] R. Brimblecombe, G. C. Dismukes, G. F. Swiegers, L. Spiccia, *Dalton Trans.* **2009**, 9374-9384.

[345] C. Wang, J.-L. Wang, W. Lin, *J. Am. Chem. Soc.* **2012**, *134*, 19895-19908.

[346] B. Nepal, S. Das, *Angew. Chem., Int. Ed.* **2013**, *52*, 7224-7227.

[347] L. Li, L. Duan, Y. Xu, M. Gorlov, A. Hagfeldt, L. Sun, *Chem. Commun.* **2010**, *46*, 7307-7309.

[348] J. Chen, P. Wagner, L. Tong, D. Boskovic, W. Zhang, D. Officer, G. G. Wallace, G. F. Swiegers, *Chem. Sci.* **2013**, *4*, 2797-2803.

[349] K. Okeyoshi, R. Yoshida, *Adv. Funct. Mater.* **2010**, *20*, 708-714.

[350] Z. Chen, A. Lohr, C. R. Saha-Möller, F. Würthner, *Chem. Soc. Rev.* **2009**, *38*, 564-584.

[351] B. Rybtchinski, *ACS Nano* **2011**, *5*, 6791-6818.

[352] J. Hu, W. Kuang, K. Deng, W. Zou, Y. Huang, Z. Wei, C. F. J. Faul, *Adv. Funct. Mater.* **2012**, *22*, 4149-4158.

[353] C. Huang, S. Barlow, S. R. Marder, *J. Org. Chem.* **2011**, *76*, 2386-2407.

[354] F. Würthner, *Chem. Commun.* **2004**, 1564-1579.

[355] M. Schulze, M. Philipp, W. Waigel, D. Schmidt, F. Würthner, *J. Org. Chem.* **2016**, *81*, 8394-8405.

[356] R. Samudrala, X. Zhang, R. M. Wadkins, D. L. Mattern, *Bioorg. Med. Chem.* **2007**, *15*, 186-193.

[357] D. Görl, X. Zhang, F. Würthner, *Angew. Chem., Int. Ed.* **2012**, *51*, 6328-6348.

[358] M. R. Hansen, T. Schnitzler, W. Pisula, R. Graf, K. Müllen, H. W. Spiess, *Angew. Chem., Int. Ed.* **2009**, *48*, 4621-4624.

[359] R. Kota, R. Samudrala, D. L. Mattern, *J. Org. Chem.* **2012**, *77*, 9641-9651.

[360] X.-D. Chen, H.-F. Wu, X.-H. Zhao, X.-J. Zhao, M. Du, *Cryst. Growth Des.* **2007**, *7*, 124-131.

[361] J. H. Wynne, J. M. Jones-Meehan, A. W. Snow, L. J. Buckley, *Patent: US 8436083 B2*, The United States Of America, As Represented By The Secretary Of The Navy, **2008**.

[362] J. Kelber, H. Bock, O. Thiebaut, E. Grelet, H. Langhals, *Eur. J. Org. Chem.* **2011**, *2011*, 707-712.

[363] M. Sadrai, L. Hadel, R. R. Sauers, S. Husain, K. Krogh-Jespersen, J. D. Westbrook, G. R. Bird, *J. Phys. Chem.* **1992**, *96*, 7988-7996.

[364] F. Würthner, *Pure Appl. Chem.* **2006**, *78*, 2341-2349.

[365] L. M. Levine, D. Holten, *J. Phys. Chem.* **1988**, *92*, 714-720.

[366] A. Prodi, C. Chiorboli, F. Scandola, E. Iengo, E. Alessio, R. Dobrawa, F. Würthner, *J. Am. Chem. Soc.* **2005**, *127*, 1454-1462.

[367] V. L. Gunderson, E. Krieg, M. T. Vagnini, M. A. Iron, B. Rybtchinski, M. R. Wasielewski, *J. Phys. Chem. B* **2011**, *115*, 7533-7540.

[368] S. Ghosh, X.-Q. Li, V. Stepanenko, F. Würthner, *Chem. – Eur. J.* **2008**, *14*, 11343-11357.

[369] J. K. Gallaher, E. J. Aitken, R. A. Keyzers, J. M. Hodgkiss, *Chem. Commun.* **2012**, *48*, 7961-7963.

[370] Z. Chen, U. Baumeister, C. Tschierske, F. Würthner, *Chem. – Eur. J.* **2007**, *13*, 450-465.

[371] K. Park, G. Bae, J. Moon, J. Choe, K. H. Song, S. Lee, *J. Org. Chem.* **2010**, *75*, 6244-6251.

[372] R. Iden, G. Seybold, *Patent: DE3434059A1*, BASF A.G., **1985**.

[373] G. Sheldrick, *Acta Crystallogr., Sect. A* **2008**, *64*, 112-122.

[374] A. Spek, *Acta Crystallogr., Sect. A* **1990**, *46*, c34.

[375] V. V. Pavlishchuk, A. W. Addison, *Inorg. Chim. Acta* **2000**, *298*, 97-102.

[376] A. J. Fry, in *In Laboratory Techniques in Electroanalytical Chemistry*, 2nd ed. (Eds.: P. T. Kissinger, W. R. Heineman), Marcel Dekker Inc., New York, **1996**, pp. 469-486.

[377] S. Gawęda, G. Stochel, K. Szaciłowski, *J. Phys. Chem. C* **2008**, *112*, 19131-19141.

[378] J. P. Perdew, K. Burke, M. Ernzerhof, *Phys. Rev. Lett.* **1996**, *77*, 3865-3868.

[379] F. Weigend, R. Ahlrichs, *Phys. Chem. Chem. Phys.* **2005**, *7*, 3297-3305.

[380] D. Andrae, U. Häußermann, M. Dolg, H. Stoll, H. Preuß, *Theor. Chim. Acta* **1990**, *77*, 123-141.

[381] TURBOMOLE, V6.3, a development of University of Karlsruhe and Forschungszentrum Karlsruhe GmbH, 1989-2007, TURBOMOLE GmbH, since 2007; available from http://www.turbomole.com.

[382] W. L. Jorgensen, J. Chandrasekhar, J. D. Madura, R. W. Impey, M. L. Klein, *J. Chem. Phys.* **1983**, *79*, 926-935.

[383] J. W. Ponder, F. M. Richards, *J. Comput. Chem.* **1987**, *8*, 1016-1024.

[384] W. L. Jorgensen, D. S. Maxwell, J. Tirado-Rives, *J. Am. Chem. Soc.* **1996**, *118*, 11225-11236.

[385] A. K. Rappe, C. J. Casewit, K. S. Colwell, W. A. Goddard, W. M. Skiff, *J. Am. Chem. Soc.* **1992**, *114*, 10024-10035.

[386] T. Yanai, D. P. Tew, N. C. Handy, *Chem. Phys. Lett.* **2004**, *393*, 51-57.

[387] M. J. Frisch, G. W. Trucks, H. B. Schlegel, G. E. Scuseria, M. A. Robb, J. R. Cheeseman, G. Scalmani, V. Barone, G. A. Petersson, H. Nakatsuji, X. Li, M. Caricato, A. Marenich, J. Bloino, B. G. Janesko, R. Gomperts, B. Mennucci, H. P. Hratchian, J. V. Ortiz, A. F. Izmaylov, J. L. Sonnenberg, D. Williams-Young, F. Ding, F. Lipparini, F. Egidi, J. Goings, B. Peng, A. Petrone, T. Henderson, D. Ranasinghe, V. G. Zakrzewski, J. Gao, N. Rega, G. Zheng, W. Liang, M. Hada, M. Ehara, K. Toyota, R. Fukuda, J. Hasegawa, M. Ishida, T. Nakajima, Y. Honda, O. Kitao, H. Nakai, T. Vreven, K. Throssell, J. A. M. Jr., J. E. Peralta, F. Ogliaro, M. Bearpark, J. J. Heyd, E. Brothers, K. N. Kudin, V. N. Staroverov, T. Keith, R. Kobayashi, J. Normand, K. Raghavachari, A. Rendell, J. C. Burant, S. S. Iyengar, J. Tomasi, M. Cossi, J. M. Millam, M. Klene, C. Adamo, R. Cammi, J. W. Ochterski, R. L. Martin, K. Morokuma, O. Farkas, J. B. Foresman, D. J. Fox, *Gaussian-09 Revision D.01. Gaussian Inc. Wallingford CT* **2009**.

CHAPTER A APPENDIX

A.1 Supporting Information to Chapter 3.1

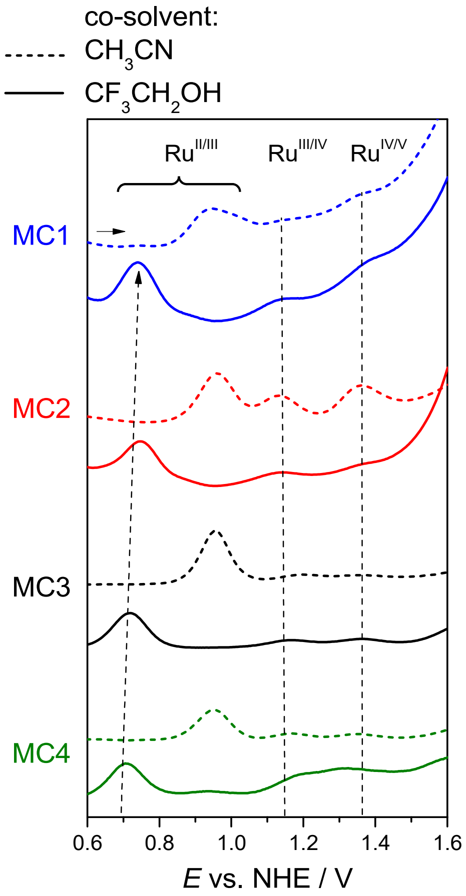

Figure A1: Differential pulse voltammograms (DPVs) for all macrocycles with two different co-solvents (solid lines = 2,2,2-trifluoroethanol, dotted lines = acetonitrile) in a 1:1 mixture with water (pH 1, acid: CF_3SO_3H).

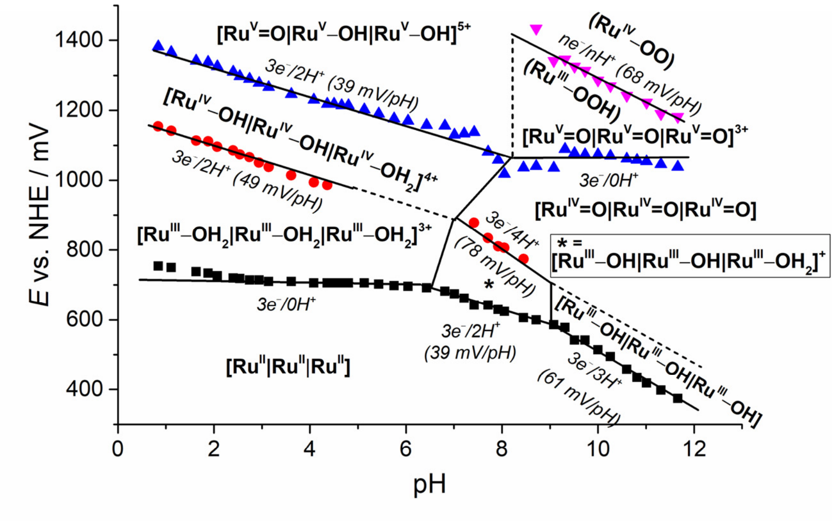

Figure A2: Pourbaix diagram of **MC1**. The potentials were obtained from differential pulse voltammetry at certain pH values which were adjusted by stepwise addition of NaOH solutions to a 1:1 CF_3CH_2OH/H_2O (pH 1, acid: CF_3SO_3H) solution.

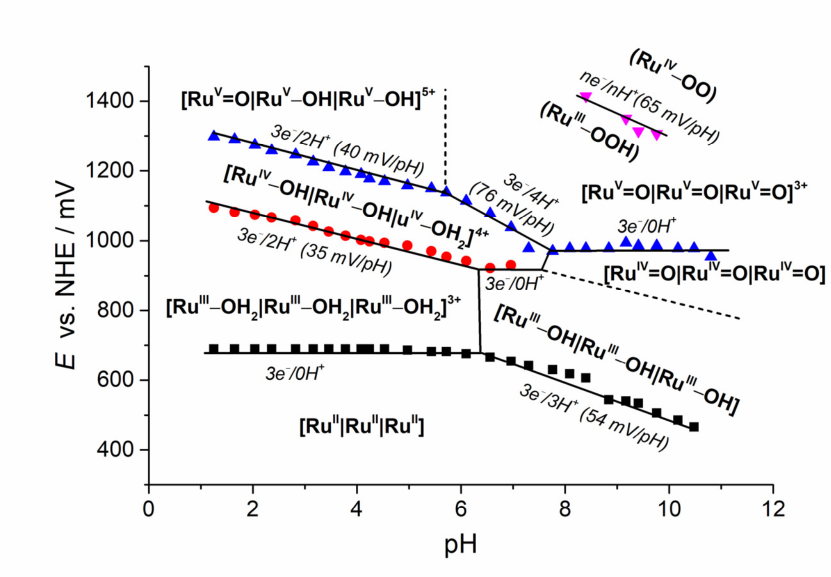

Figure A3: Pourbaix diagram of **MC3**. The potentials were obtained from differential pulse voltammetry at certain pH values which were adjusted by stepwise addition of NaOH solutions to a 1:1 CF_3CH_2OH/H_2O (pH 1, acid: CF_3SO_3H) solution.

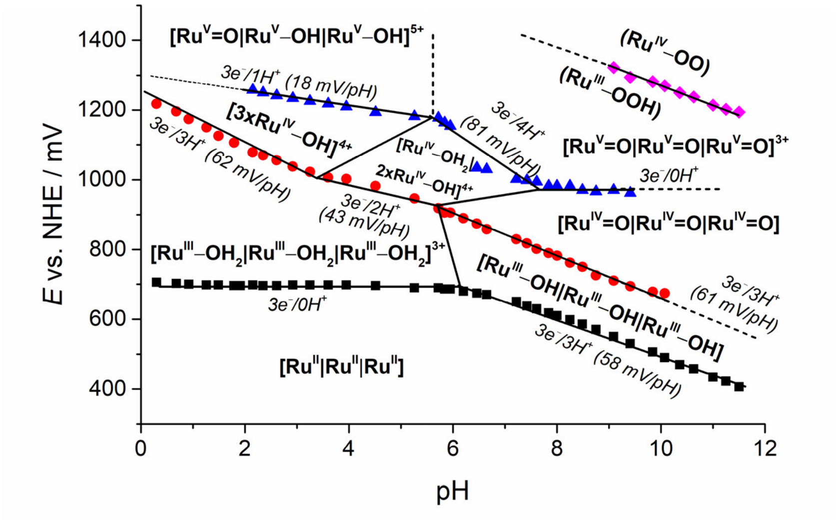

Figure A4: Pourbaix diagram of **MC4**. The potentials were obtained from differential pulse voltammetry at certain pH values which were adjusted by stepwise addition of NaOH solutions to a 1:1 CF_3CH_2OH/H_2O (pH 1, acid: CF_3SO_3H) solution.

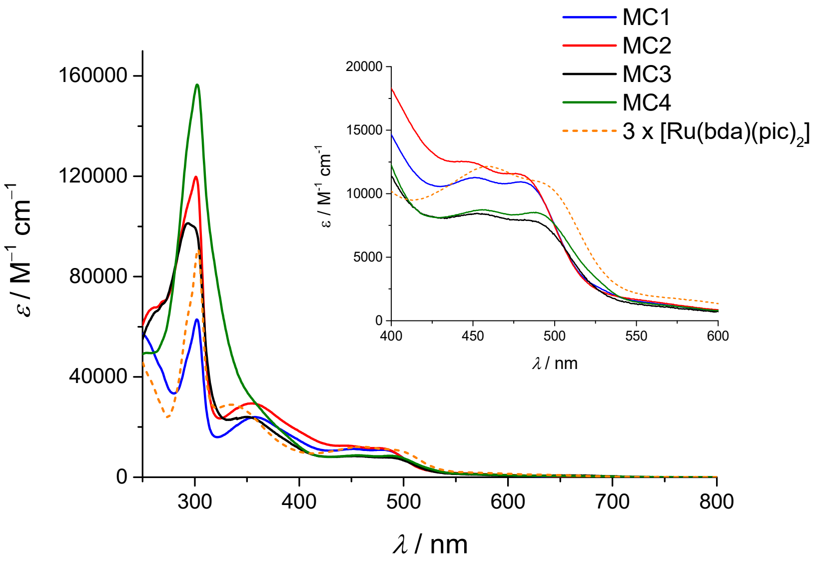

Figure A5: UV/Vis spectra of all macrocycles **MC1**–**MC4** and the mononuclear reference complex [Ru(bda)(pic)$_2$] in the Ru(II) oxidation state measured in CH_3CN/H_2O (pH 1, acid: CF_3SO_3H) 1:1 at a concentration of 10^{-5} M.

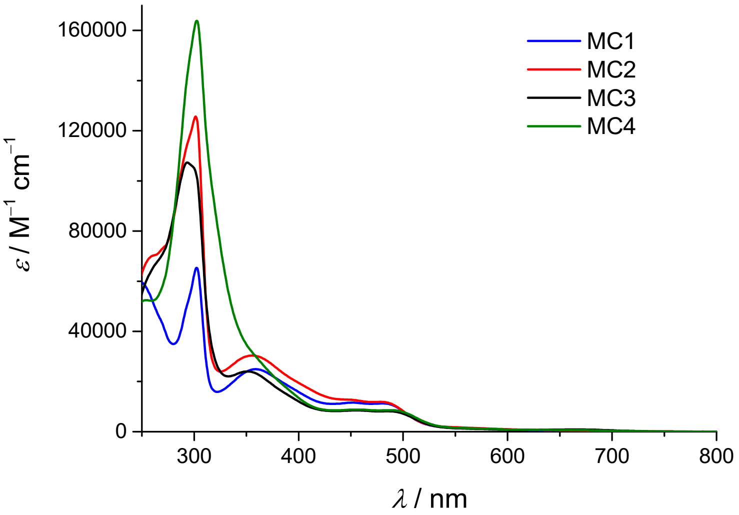

Figure A6: UV/Vis spectra of all macrocycles **MC1**–**MC4** in the Ru(II) oxidation state measured in CH_3CN/H_2O (pH 1, acid: CF_3SO_3H) 4:1 at a concentration of 10^{-5} M.

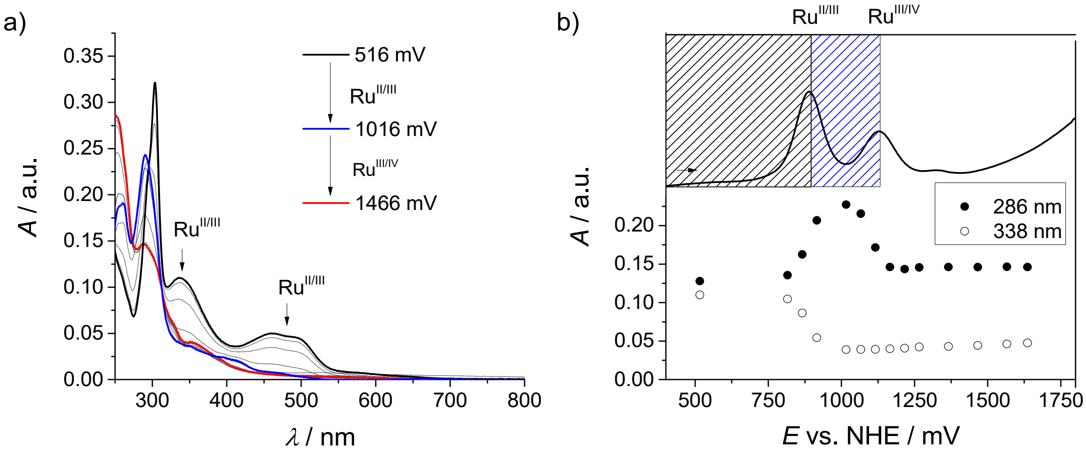

Figure A7: (a) Spectroelectrochemistry measurement for $[Ru(bda)(pic)_2]$ in 1:1 CH_3CN/H_2O (pH 1, acid: CF_3SO_3H). (b) DPV in the same solvent mixture and monitoring of different absorption wavelengths over the applied potential derived from the spectroelectrochemistry.

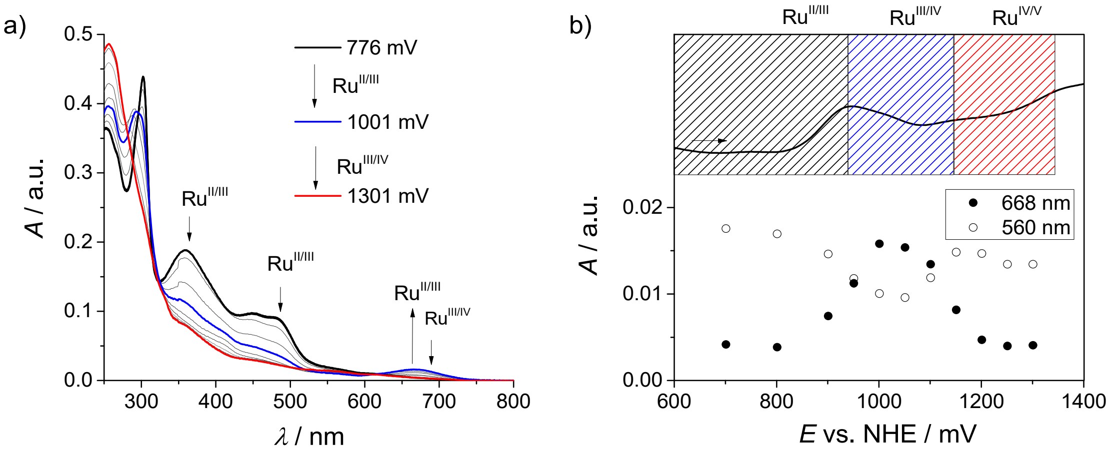

Figure A8: (a) Spectroelectrochemistry measurement for **MC1** in 1:1 CH_3CN/H_2O (pH 1, acid: CF_3SO_3H). (b) DPV in the same solvent mixture and monitoring of different absorption wavelengths over the applied potential derived from the spectroelectrochemistry.

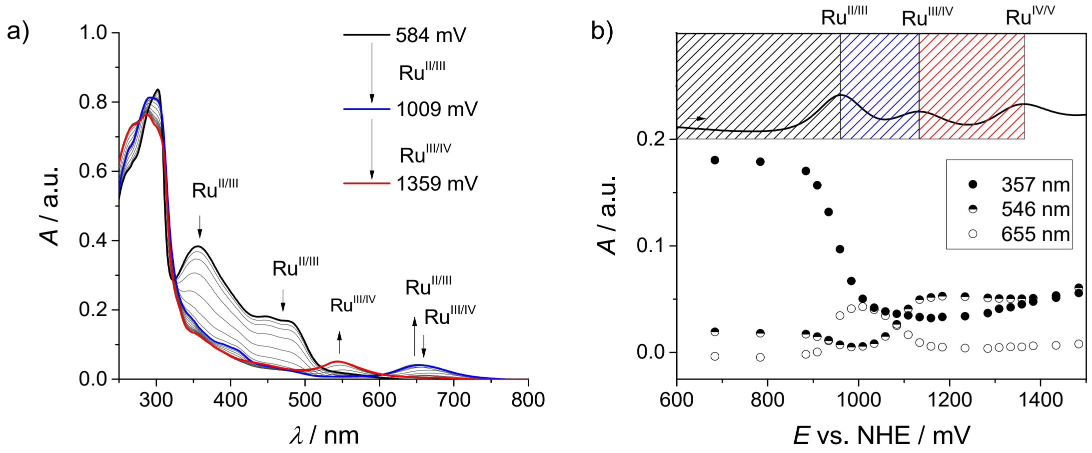

Figure A9: (a) Spectroelectrochemistry measurement for **MC2** in 1:1 CH_3CN/H_2O (pH 1, acid: CF_3SO_3H). (b) DPV in the same solvent mixture and monitoring of different absorption wavelengths over the applied potential derived from the spectroelectrochemistry.

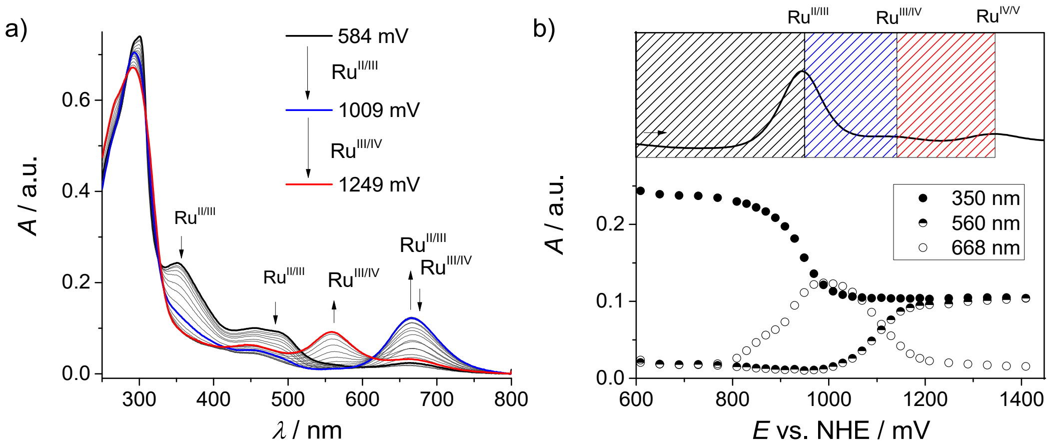

Figure A10: (a) Spectroelectrochemistry measurement for **MC3** in 1:1 CH_3CN/H_2O (pH 1, acid: CF_3SO_3H). (b) DPV in the same solvent mixture and monitoring of different absorption wavelengths over the applied potential derived from the spectroelectrochemistry.

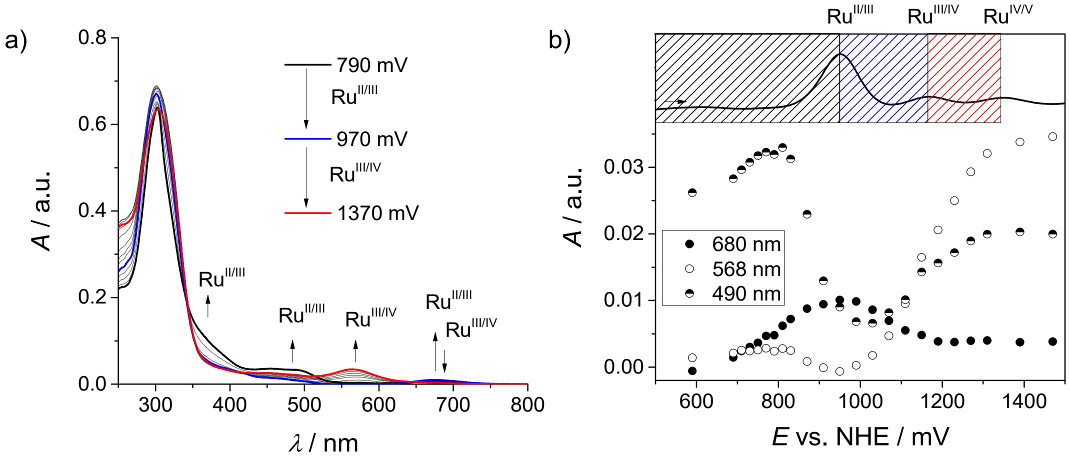

Figure A11: (a) Spectroelectrochemistry measurement for **MC4** in 4:1 CH_3CN/H_2O (pH 1, acid: CF_3SO_3H). (b) DPV in the same solvent mixture and monitoring of different absorption wavelength over the applied potential derived from the spectroelectrochemistry.

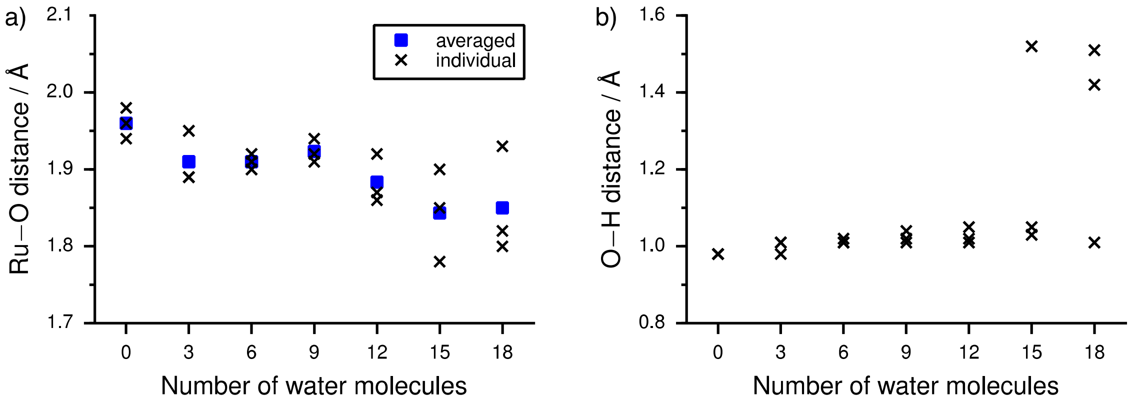

Figure A12: Influence of the amount of explicit water molecules on important properties of **MC3** in the Ru^{IV} state. (a) Ru–OH distance against the number of water molecules for each individual center and averaged. (b) RuO–H distance against the number of water molecules.

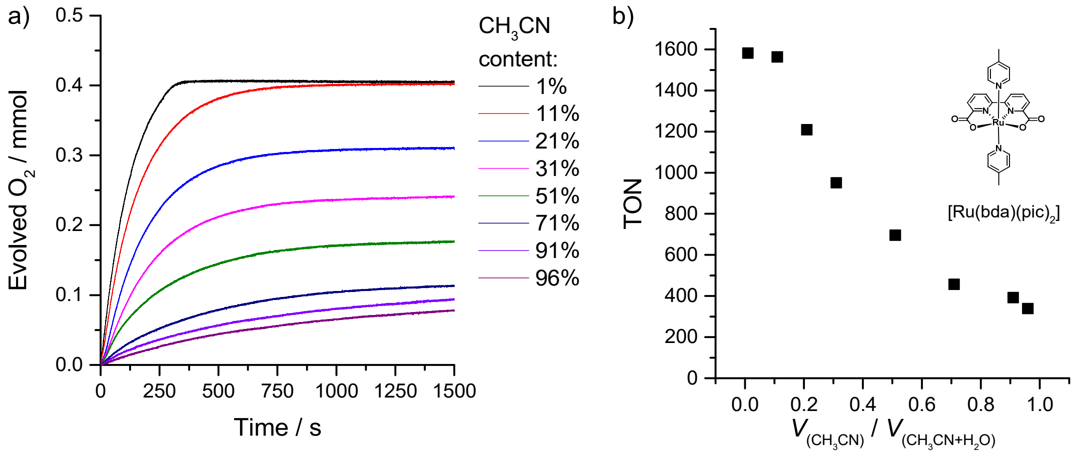

Figure A13: (a) Oxygen evolution over time using reference [Ru(bda)(pic)$_2$] (c = 75.5 µM) as catalyst depending on the acetonitrile content in the reaction mixture. (b) The TONs that are reached as a function of the acetonitrile content. The catalyst solution (400 µL, acetonitrile/water (pH 7) 1:9) was injected into a reaction vial filled with 1.0 g (1.82 mmol) CAN dissolved in 3.0 mL of the corresponding acetonitrile/water (pH 1) mixture.

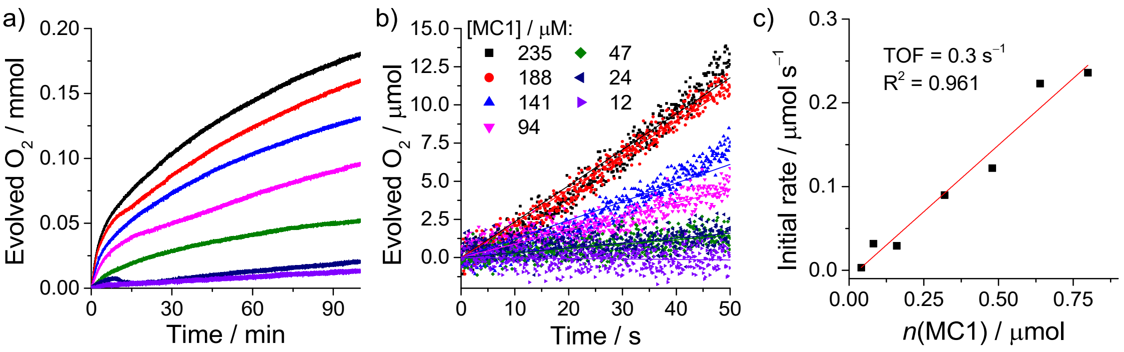

Figure A14: (a) Concentration-dependent oxygen evolution over time for **MC1** as catalyst with 80% (v/v) acetonitrile as co-solvent at 20 °C. (b) Linear regressions through the first 50 s, and (c) the of the initial rates vs. the catalyst concentration. (1.0 g CAN was dissolved in 3.0 mL CH_3CN/H_2O (pH 1, acid: CF_3SO_3H) 4:1 and 400 µL of catalyst solution in CH_3CN/H_2O (pH 1) 4:1 have been injected).

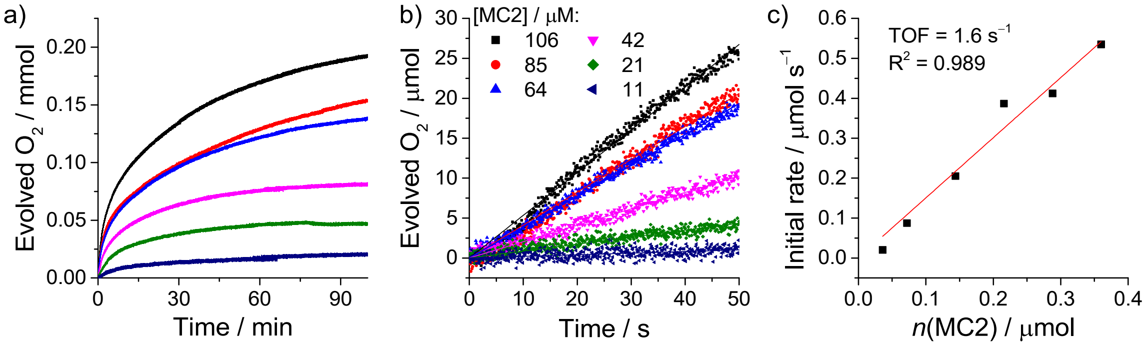

Figure A15: (a) Concentration-dependent oxygen evolution over time for **MC2** as catalyst with 80% (*v*/*v*) acetonitrile as co-solvent at 20 °C. (b) Linear regressions through the first 50 s, and (c) plot of the initial rates vs. the catalyst concentration. (1.0 g CAN was dissolved in 3.0 mL CH_3CN/H_2O (pH 1, acid: CF_3SO_3H) 4:1 and 400 µL of catalyst solution in CH_3CN/H_2O (pH 1) 4:1 have been injected).

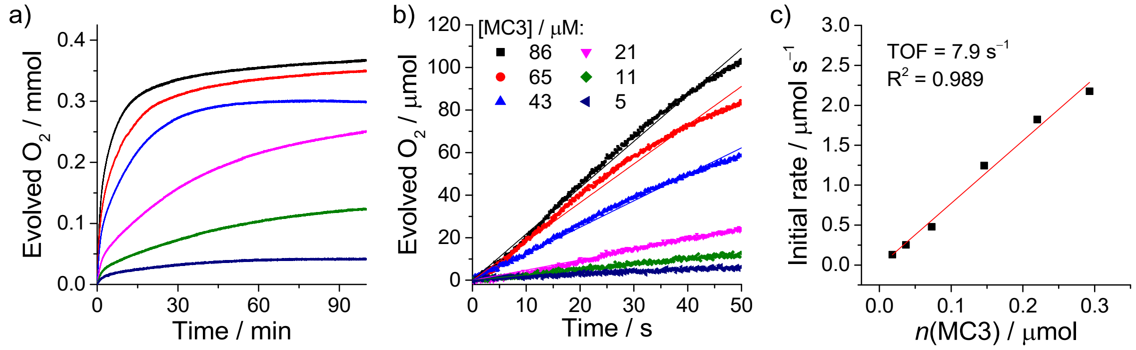

Figure A16: (a) Concentration-dependent oxygen evolution over time for **MC3** as catalyst with 80% (*v*/*v*) acetonitrile as co-solvent at 20 °C. (b) Linear regressions through the first 50 s, and (c) plot of the initial rates vs. the catalyst concentration. (1.0 g CAN was dissolved in 3.0 mL CH_3CN/H_2O (pH 1, acid: CF_3SO_3H) 4:1 and 400 µL of catalyst solution in CH_3CN/H_2O (pH 1) 4:1 have been injected).

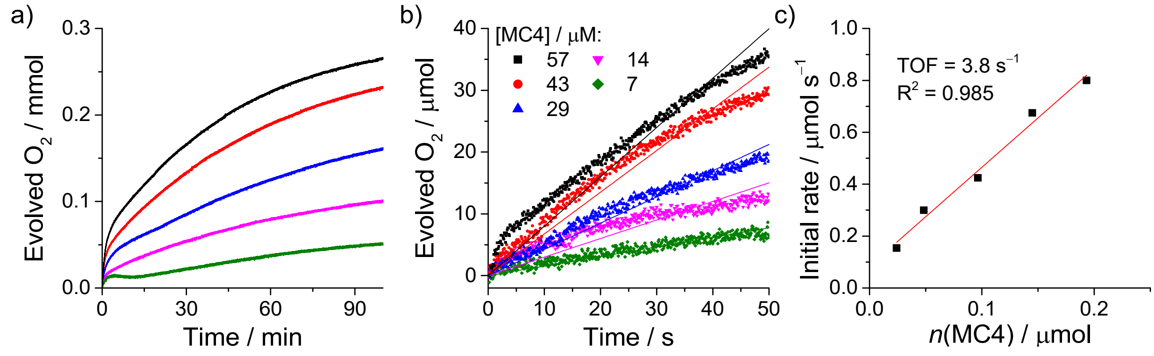

Figure A17: (a) Concentration-dependent oxygen evolution over time for **MC4** as catalyst with 80% (*v*/*v*) acetonitrile as co-solvent at 20 °C. (b) Linear regressions through the first 50 s, and (c) plot of the initial rates vs. the catalyst concentration. (1.0 g CAN was dissolved in 3.0 mL CH_3CN/H_2O (pH 1, acid: CF_3SO_3H) 4:1 and 400 µL of catalyst solution in CH_3CN/H_2O (pH 1) 4:1 have been injected).

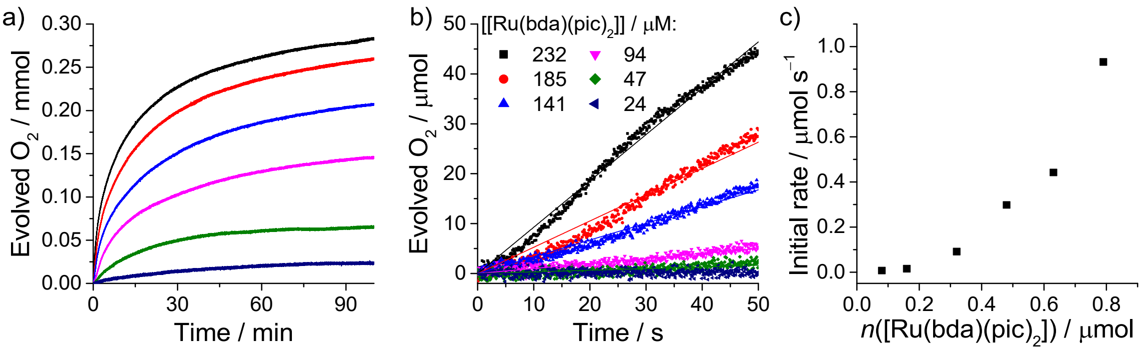

Figure A18: (a) Concentration-dependent oxygen evolution over time for [Ru(bda)(pic)$_2$] as catalyst with 80% (*v*/*v*) acetonitrile as co-solvent at 20 °C. (b) Linear regressions through the first linear part, and (c) plot of the initial rates vs. the catalyst concentration. (1.0 g CAN was dissolved in 3.0 mL CH_3CN/H_2O (pH 1, acid: CF_3SO_3H) 4:1 and 400 µL of catalyst solution in CH_3CN/H_2O (pH 1) 4:1 have been injected).

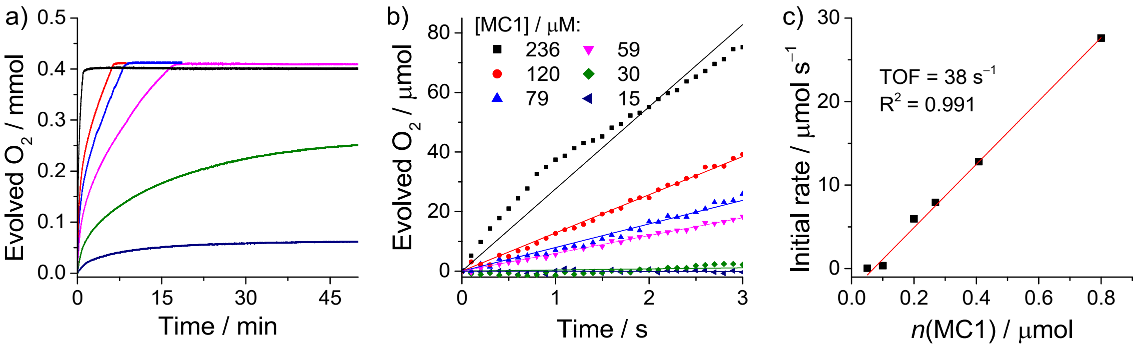

Figure A19: (a) Concentration-dependent oxygen evolution over time for **MC1** as catalyst with 2% (*v*/*v*) acetonitrile as co-solvent at 20 °C. (b) Linear regressions through the first linear part, and (c) plot of the initial rates vs. the catalyst concentration. (1.0 g CAN was dissolved in 3.0 mL H_2O (pH 1, acid: CF_3SO_3H) and 400 µL of catalyst solution in CH_3CN/H_2O (pH 7) 1:9 have been injected).

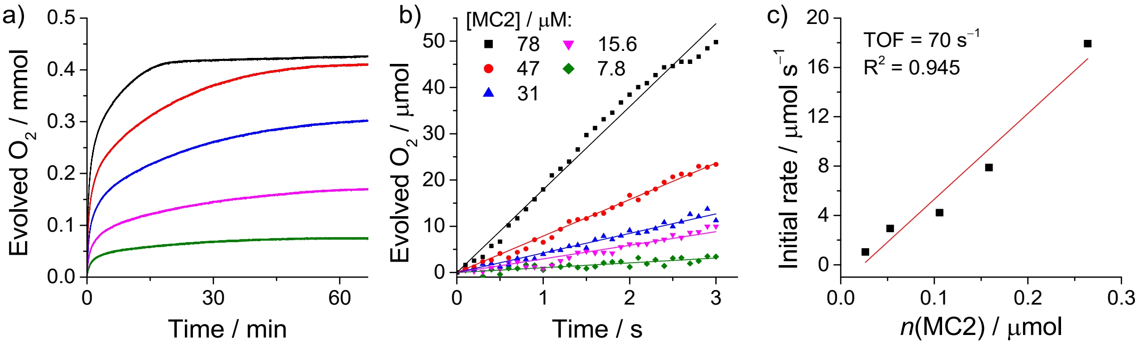

Figure A20: (a) Concentration-dependent oxygen evolution over time for **MC2** as catalyst with 50% (*v*/*v*) acetonitrile as a co-solvent at 20 °C. (b) Linear regressions through the first linear part, and (c) plot of the initial rates vs. the catalyst concentration. (1.0 g CAN was dissolved in 3.0 mL CH_3CN/H_2O (pH 1, acid: CF_3SO_3H) 1:1 and 400 µL of catalyst solution in CH_3CN/H_2O (pH 7) 1:1 have been injected).

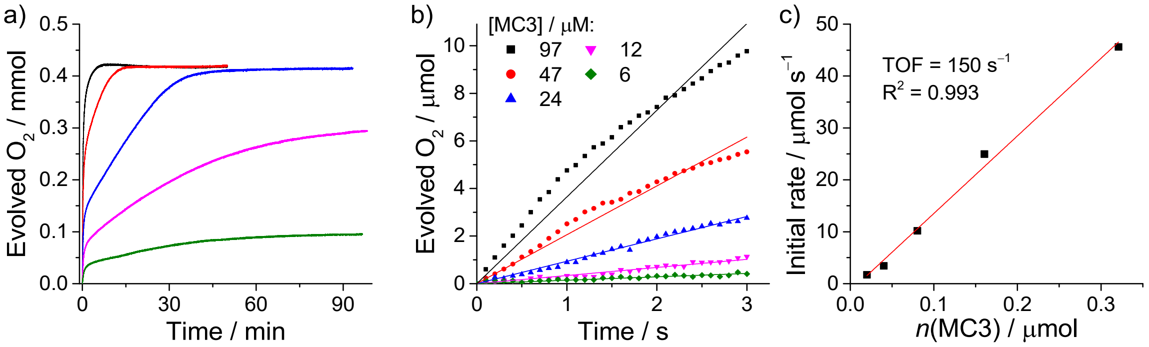

Figure A21: (a) Concentration-dependent oxygen evolution over time for **MC3** as catalyst with 60% (*v*/*v*) acetonitrile as a co-solvent at 20 °C. (b) Linear regressions through the first linear part, and (c) plot of the initial rates vs. the catalyst concentration. (1.0 g CAN was dissolved in 3.0 mL CH_3CN/H_2O (pH 1, acid: CF_3SO_3H) 3:2 and 400 µL of catalyst solution in CH_3CN/H_2O (pH 7) 3:2 have been injected).

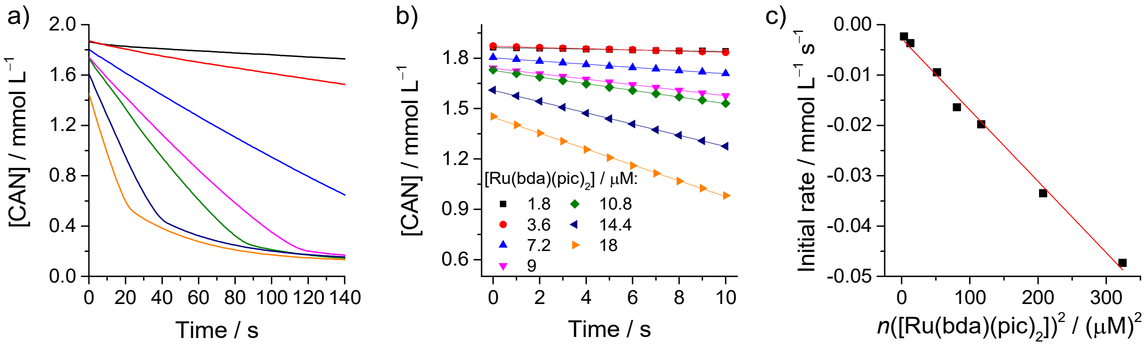

Figure A22: (a) CAN absorbance decay at 360 nm depending on different $[Ru(bda)(pic)_2]$ concentrations over 140 s, (b) between 0 and 10 s, and (c) plot of the initial rates vs. the catalyst concentration. Conditions: [CAN] = 2.0 mM in 2.0 mL 1:1 CH_3CN/H_2O (pH 1) at 25 °C.

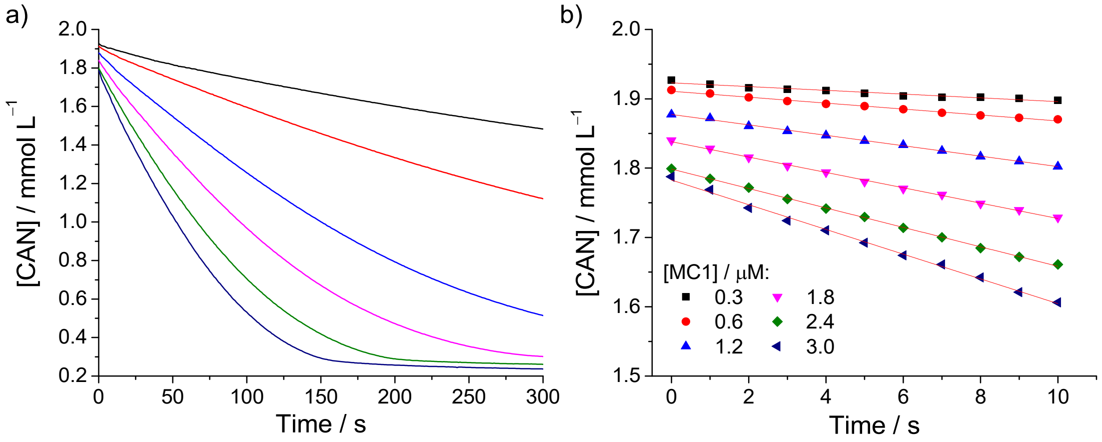

Figure A23: (a) CAN absorbance decay at 360 nm depending on different **MC1** concentrations over 300 s, and (b) between 0 and 10 s. Conditions: [CAN] = 2.0 mM in 2.0 mL 1:1 CH_3CN/H_2O (pH 1) at 25 °C.

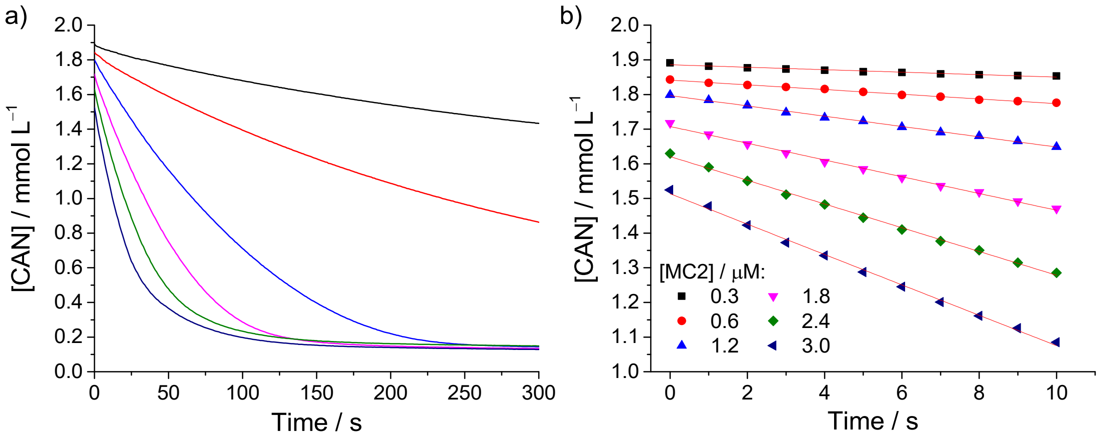

Figure A24: (a) CAN absorbance decay at 360 nm depending on different **MC2** concentrations over 300 s, and (b) between 0 and 10 s. Conditions: [CAN] = 2.0 mM in 2.0 mL 1:1 CH_3CN/H_2O (pH 1) at 25 °C.

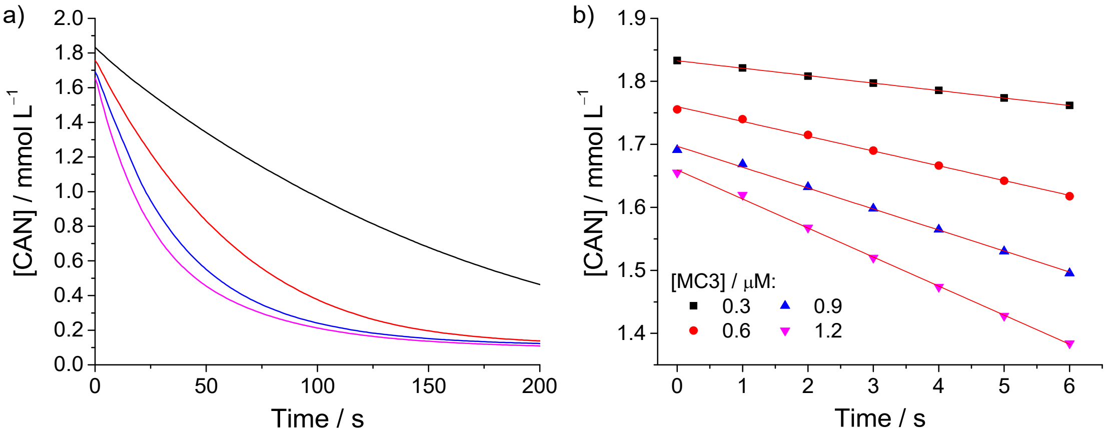

Figure A25: (a) CAN absorbance decay at 360 nm depending on different **MC3** concentrations over 200 s, and (b) between 0 and 6 s. Conditions: [CAN] = 2.0 mM in 2.0 mL 1:1 CH_3CN/H_2O (pH 1) at 25 °C.

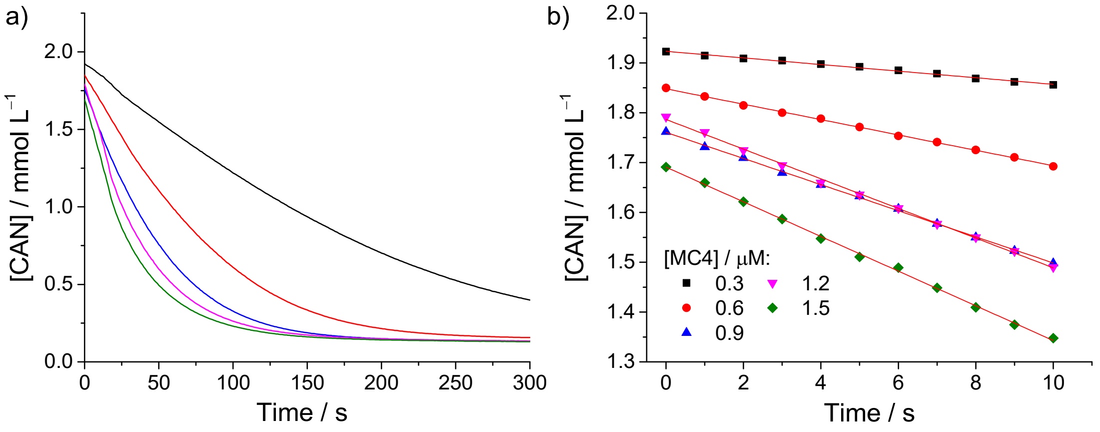

Figure A26: (a) CAN absorbance decay at 360 nm depending on different **MC4** concentrations over 300 s, and (b) between 0 and 10 s. Conditions: [CAN] = 2.0 mM in 2.0 mL 1:1 CH_3CN/H_2O (pH 1) at 25 °C.

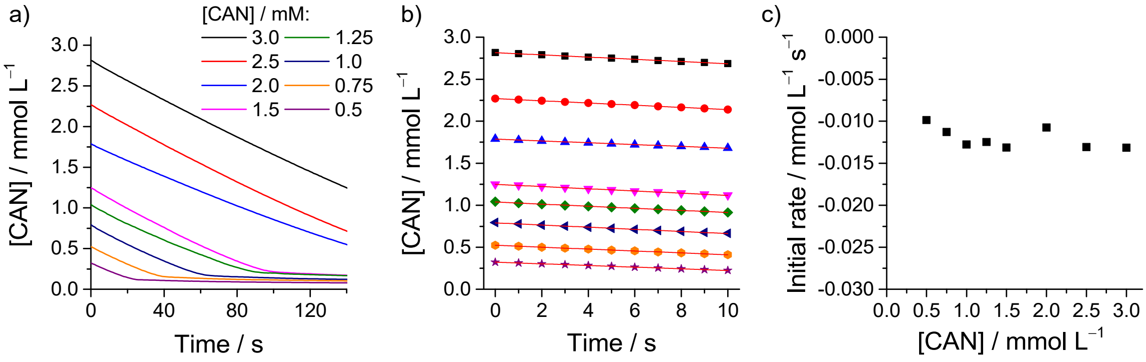

Figure A27: (a) CAN absorbance decay at 360 nm, for [Ru(bda)(pic)$_2$] as catalyst, depending on different CAN concentrations over 140 s, (b) between 0 and 10 s, and (c) plot of the initial rates vs. the catalyst concentration. Conditions: [Ru(bda)(pic)$_2$] = 9.0 µM in 2.0 mL 1:1 CH_3CN/H_2O (pH 1) at 25 °C.

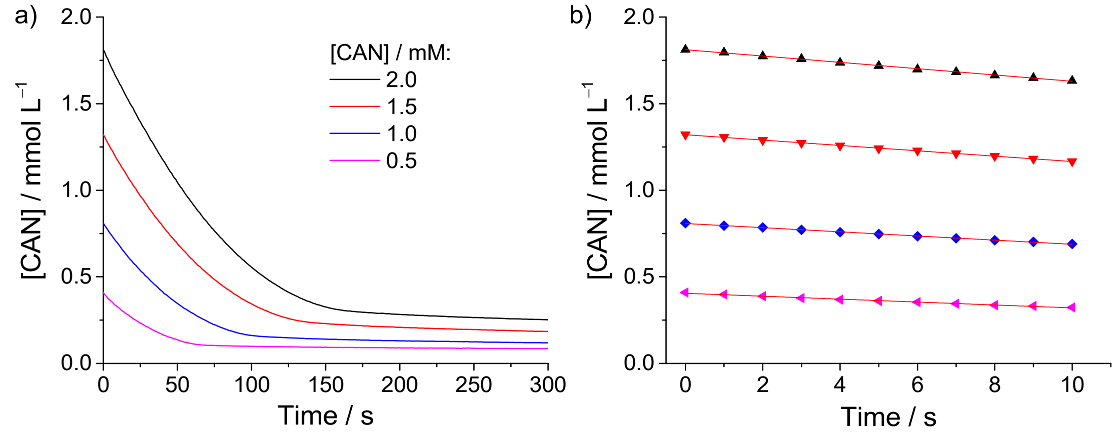

Figure A28: (a) CAN absorbance decay at 360 nm depending on different CAN concentrations with **MC1** as catalyst over 300 s, and (b) between 0 and 10 s. Conditions: [MC1] = 3.0 µM in 2.0 mL 1:1 CH_3CN/H_2O (pH 1) at 25 °C.

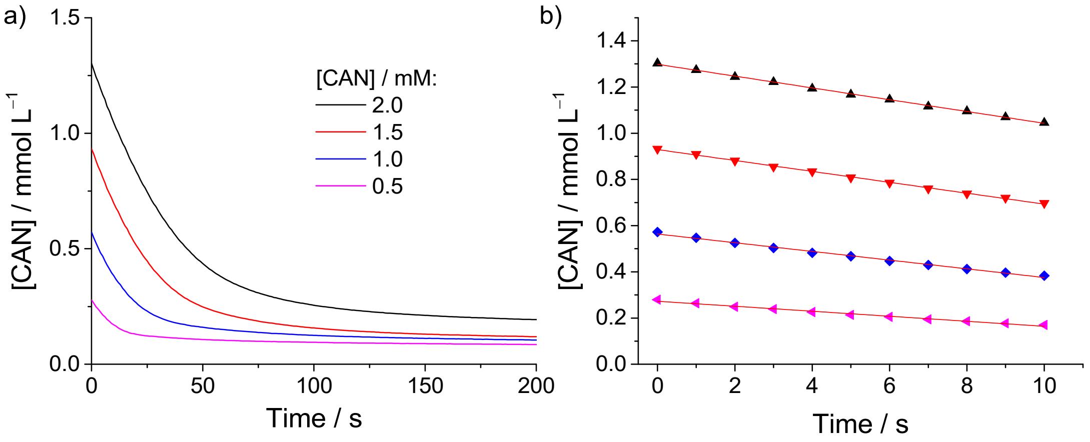

Figure A29: (a) CAN absorbance decay at 360 nm depending on different CAN concentrations with **MC2** as catalyst over 200 s, and (b) between 0 and 10 s. Conditions: [MC2] = 3.0 µM in 2.0 mL 1:1 CH_3CN/H_2O (pH 1) at 25 °C.

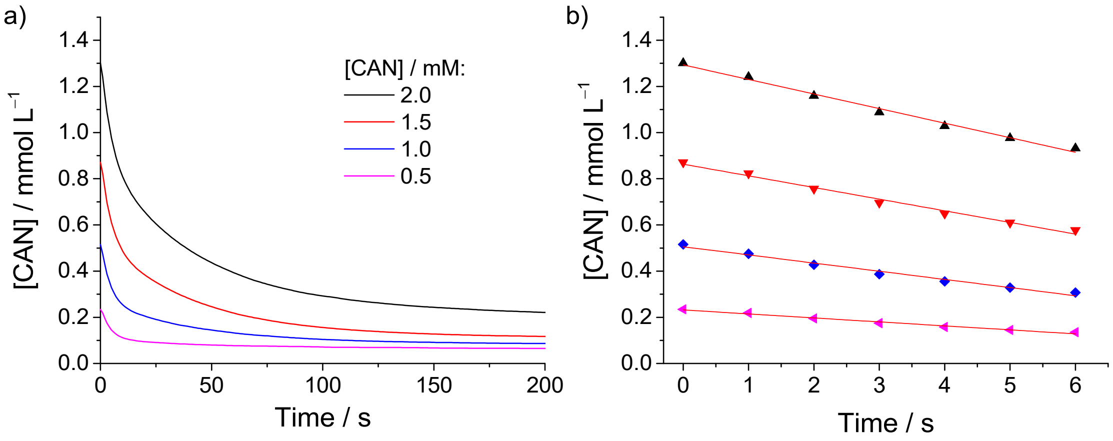

Figure A30: (a) CAN absorbance decay at 360 nm depending on different CAN concentrations with **MC3** as catalyst over 200 s, and (b) between 0 and 6 s. Conditions: [MC3] = 3.0 µM in 2.0 mL 1:1 CH_3CN/H_2O (pH 1) at 25 °C.

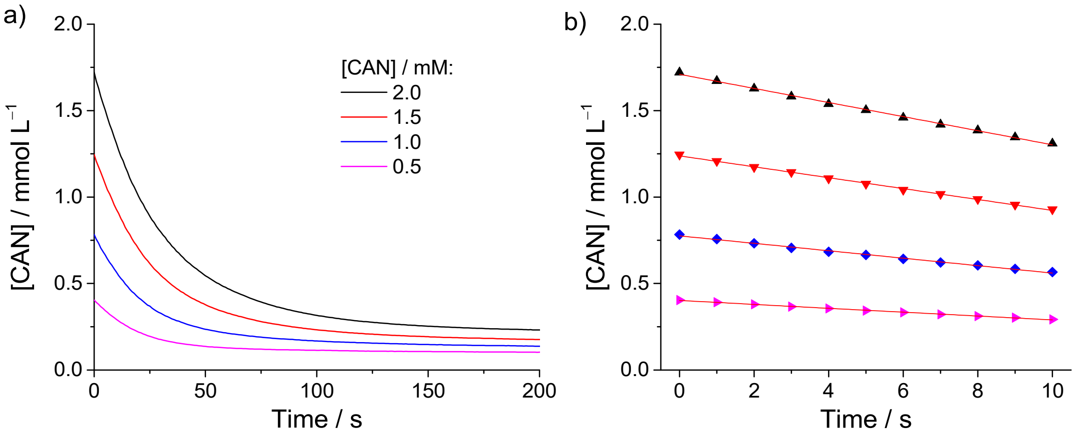

Figure A31: (a) CAN absorbance decay at 360 nm depending on different CAN concentrations with **MC4** as catalyst over 150 s, and (b) between 0 and 10 s. Conditions: [MC4] = 3.0 µM in 2.0 mL 1:1 CH_3CN/H_2O (pH 1) at 25 °C.

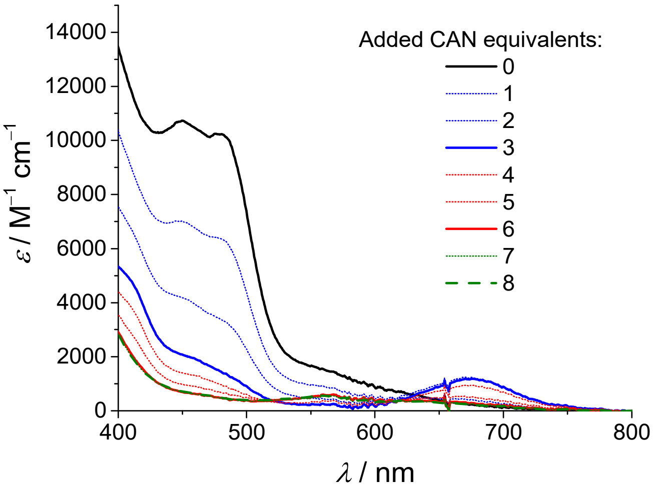

Figure A32: UV/Vis spectra of **MC1** (10^{-4} M in 1:1 CH_3CN/H_2O (pH 1, acid: CF_3SO_3H)) after the successive addition of CAN equivalents.

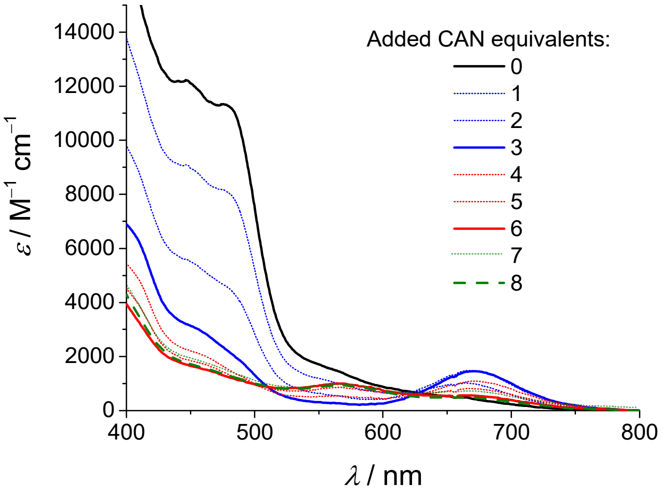

Figure A33: UV/Vis spectra of **MC2** (10^{-4} M in 1:1 CH_3CN/H_2O (pH 1, acid: CF_3SO_3H)) after the successive addition of CAN equivalents.

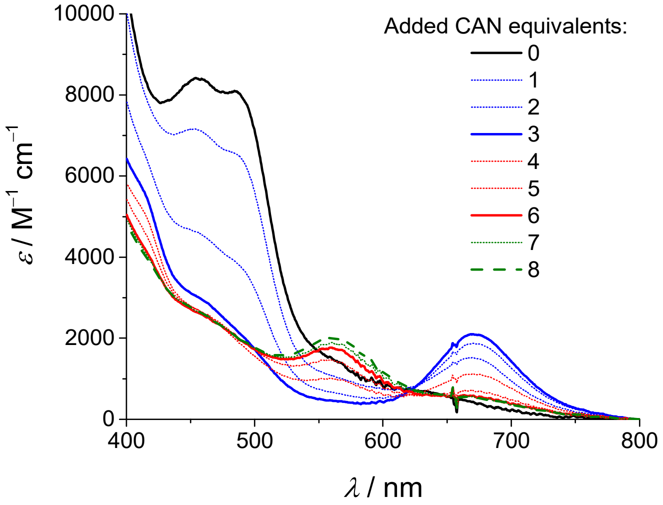

Figure A34: UV/Vis spectra of **MC3** (10^{-4} M in 1:1 CH_3CN/H_2O (pH 1, acid: CF_3SO_3H)) after the successive addition of CAN equivalents.

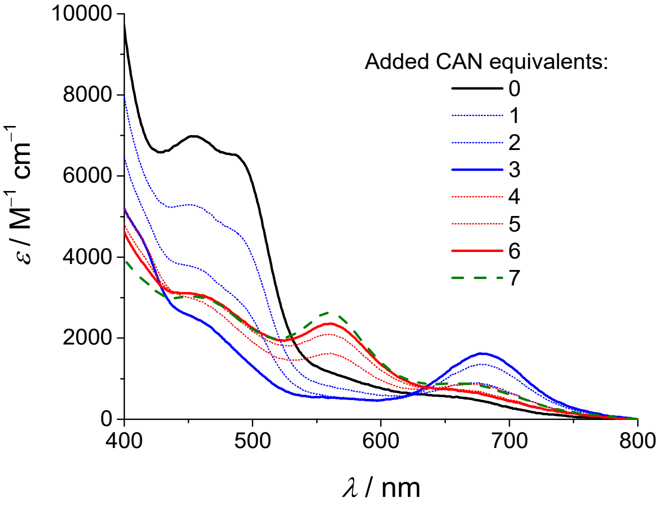

Figure A35: UV/Vis spectra of **MC4** (10^{-4} M in 1:1 CH_3CN/H_2O (pH 1, acid: CF_3SO_3H)) after the successive addition of CAN equivalents.

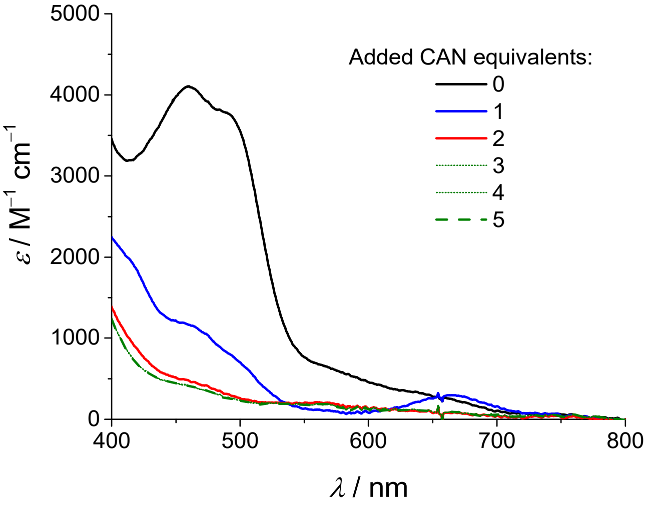

Figure A36: UV/Vis spectra of [Ru(bda)(pic)$_2$] (10^{-4} M in 1:1 CH_3CN/H_2O (pH 1, acid: CF_3SO_3H)) after the successive addition of CAN equivalents.

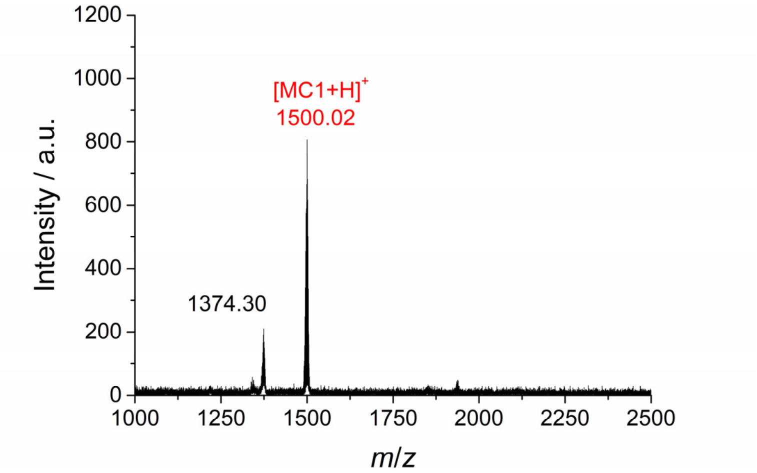

Figure A37: MALDI mass spectrum of **MC1** after 33 catalytic cycles (after the reduction with ascorbic acid).

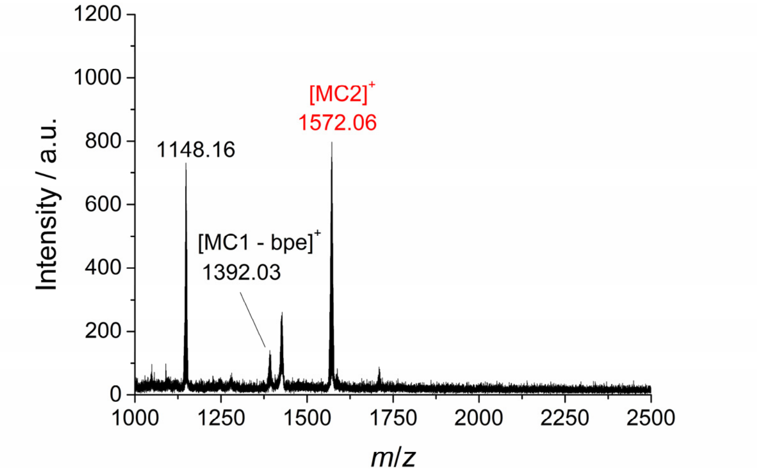

Figure A38: MALDI mass spectrum of **MC2** after 33 catalytic cycles (after the reduction with ascorbic acid).

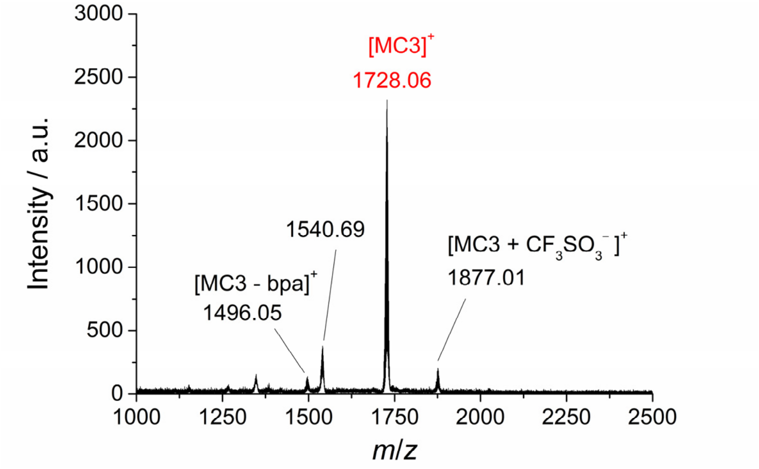

Figure A39: MALDI mass spectrum of **MC3** after 33 catalytic cycles (after the reduction with ascorbic acid).

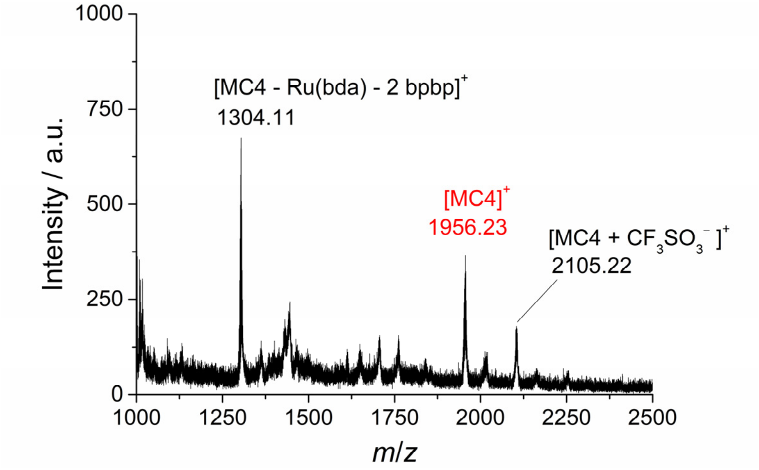

Figure A40: MALDI mass spectrum of **MC4** after 33 catalytic cycles (after the reduction with ascorbic acid).

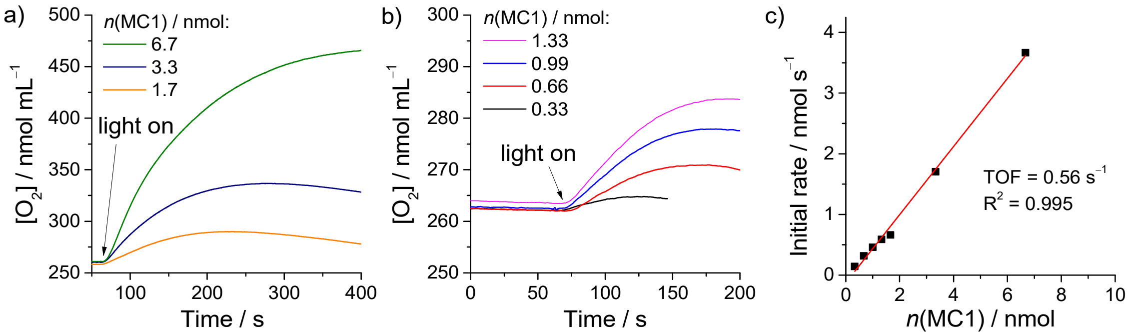

Figure A41: (a,b) Oxygen evolution curves of the photocatalytic water oxidation with varying **MC1** concentrations measured with a Clark-type electrode setup in 2.0 mL 1:1 CH_3CN/H_2O (pH 7.2, buffer: phosphate) solution, and (c) plot of the initial rates vs. the catalyst concentration. ($[Na_2S_2O_8]$ = 37 mM, $[[Ru(bpy)_3]Cl_2]$ = 1.5 mM, λ_{irr} > 380 nm with 230 mW/cm^2)

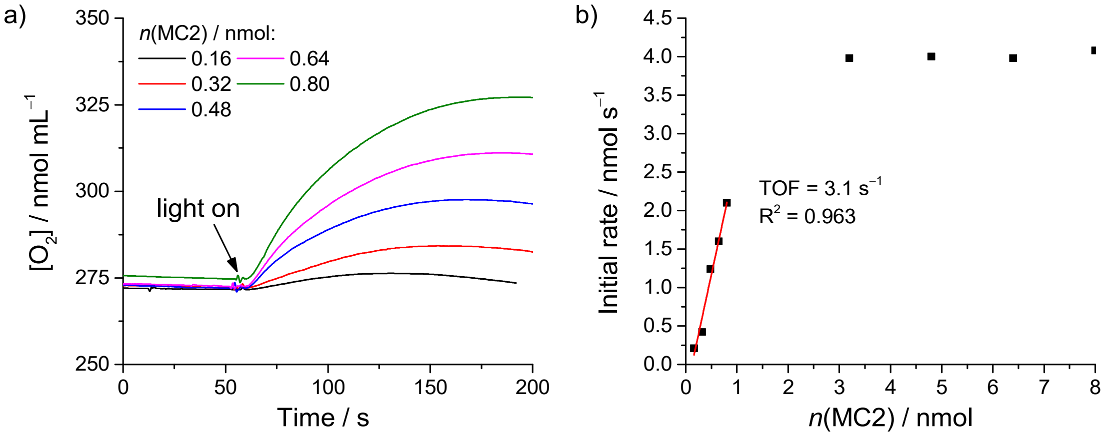

Figure A42: (a) Oxygen evolution curves of the photocatalytic water oxidation with varying **MC2** concentrations measured with a Clark-type electrode setup in 2.0 mL 1:1 CH_3CN/H_2O (pH 7.2, buffer: phosphate) solution, and (b) plot of the initial rates vs. the catalyst concentration. ($[Na_2S_2O_8]$ = 37 mM, $[[Ru(bpy)_3]Cl_2]$ = 1.5 mM, λ_{irr} > 380 nm with 230 mW/cm^2).

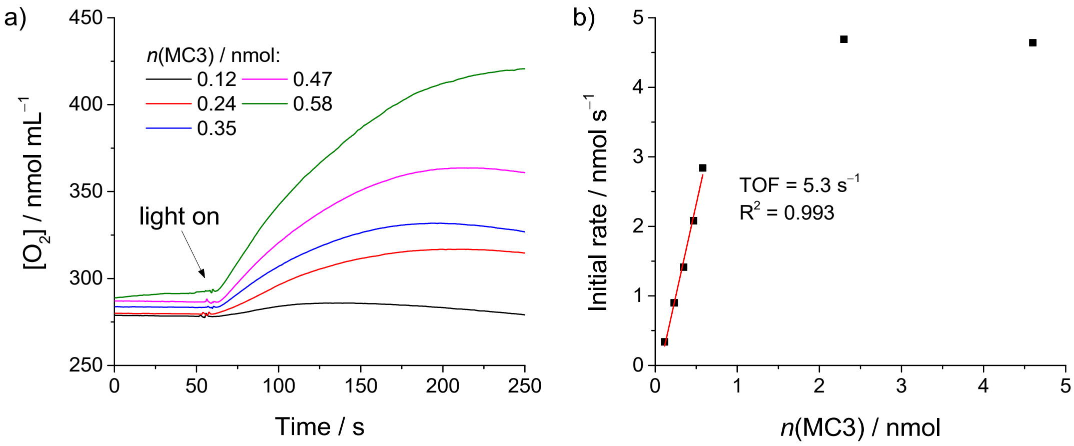

Figure A43: (a) Oxygen evolution curves of the photocatalytic water oxidation with varying **MC3** concentrations measured with a Clark-type electrode setup in 2.0 mL 1:1 CH_3CN/H_2O (pH 7.2, buffer: phosphate) solution, and (b) plot of the initial rates vs. the catalyst concentration. ([$Na_2S_2O_8$] = 37 mM, [[Ru(bpy)$_3$]Cl$_2$] = 1.5 mM, λ_{irr} > 380 nm with 230 mW/cm^2).

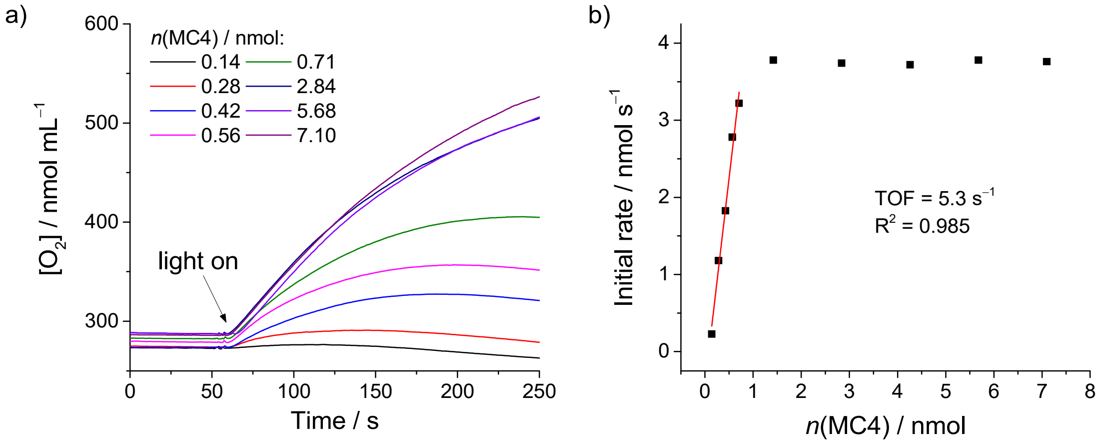

Figure A44: (a) Oxygen evolution curves of the photocatalytic water oxidation with varying **MC4** concentrations measured with a Clark-type electrode setup in 2.0 mL 1:1 CH_3CN/H_2O (pH 7.2, buffer: phosphate) solution, and (b) plot of the initial rates vs. the catalyst concentration. ([$Na_2S_2O_8$] = 37 mM, [[Ru(bpy)$_3$]Cl$_2$] = 1.5 mM, λ_{irr} > 380 nm with 230 mW/cm^2).

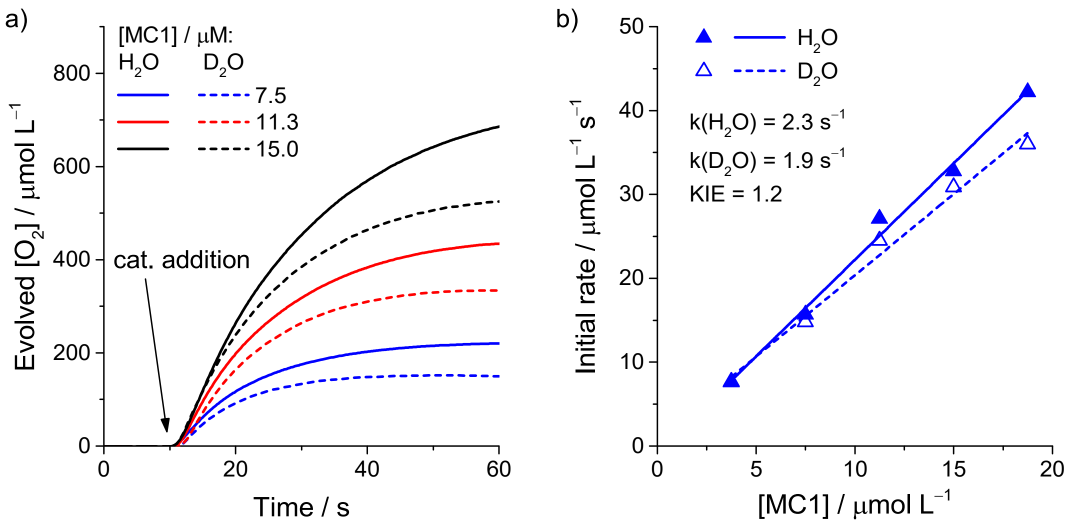

Figure A45: (a) Oxygen evolution vs. time during water oxidation with **MC1** as catalyst at varying catalyst concentrations in 2.0 mL aqueous pH 1 solutions (H_2O or D_2O) with 50% CH_3CN (*v*/*v*) as co-solvent using CAN (0.525 M) as sacrificial oxidant. Measured with a Clark-type electrode setup at 20 °C. (b) Plot of initial catalytic rates vs. **MC1** concentration, with corresponding linear regression fits to determine reaction rates *k*(H_2O) and *k*(D_2O).

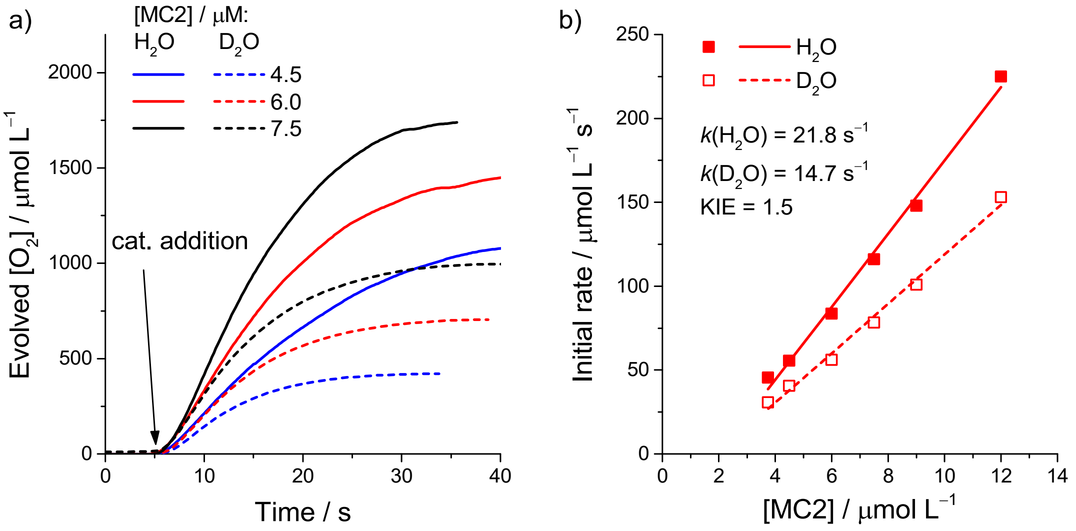

Figure A46: (a) Oxygen evolution vs. time during water oxidation with **MC2** as catalyst at varying catalyst concentrations in 2.0 mL aqueous pH 1 solutions (H_2O or D_2O) with 50% CH_3CN (*v*/*v*) as co-solvent using CAN (0.525 M) as sacrificial oxidant. Measured with a Clark-type electrode setup at 20 °C. (b) Plot of initial catalytic rates vs. **MC2** concentration, with corresponding linear regression fits to determine reaction rates *k*(H_2O) and *k*(D_2O).

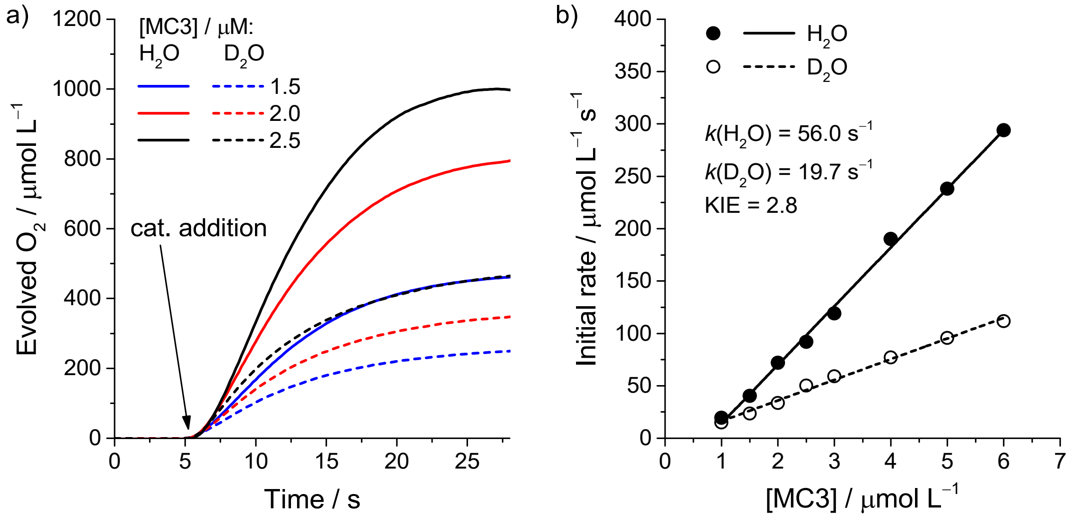

Figure A47: (a) Oxygen evolution vs. time during water oxidation with **MC3** as catalyst at varying catalyst concentrations in 2.0 mL aqueous pH 1 solutions (H_2O or D_2O) with 50% CH_3CN (*v*/*v*) as co-solvent using CAN (0.525 M) as sacrificial oxidant. Measured with a Clark-type electrode set-up at 20 °C. (b) Plot of initial catalytic rates vs. **MC3** concentration, with corresponding linear regression fits to determine reaction rates $k(H_2O)$ and $k(D_2O)$.

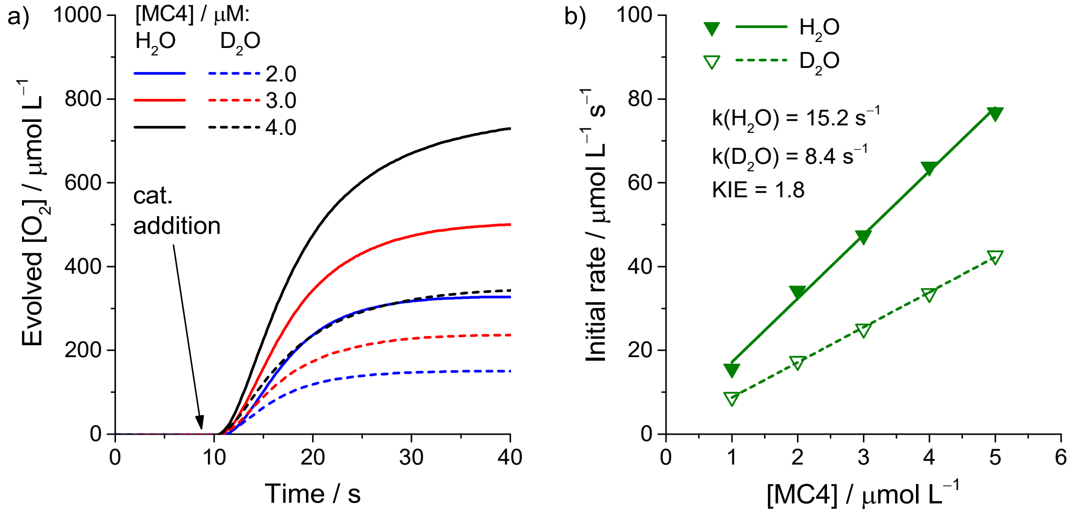

Figure A48: (a) Oxygen evolution vs. time during water oxidation with **MC4** as catalyst at varying catalyst concentrations in 2.0 mL aqueous pH 1 solutions (H_2O or D_2O) with 50% CH_3CN (*v*/*v*) as co-solvent using CAN (0.525 M) as sacrificial oxidant. Measured with a Clark-type electrode set-up at 20 °C. (b) Plot of initial catalytic rates vs. **MC4** concentration, with corresponding linear regression fits to determine reaction rates $k(H_2O)$ and $k(D_2O)$.

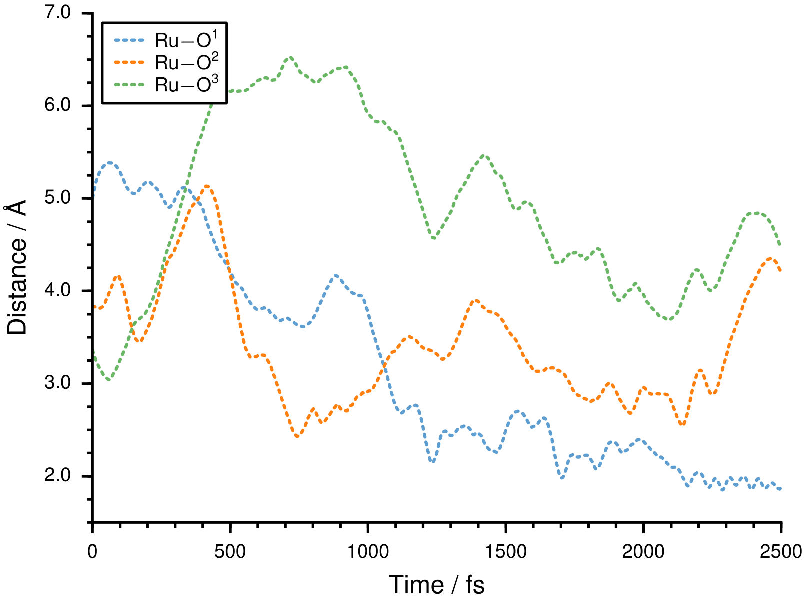

Figure A49: Results from the oxidation simulation from Ru^{II} to Ru^{III} for **MC3**. Depicted are the Ru–O distances from each Ru atom to the respective closest water molecule.

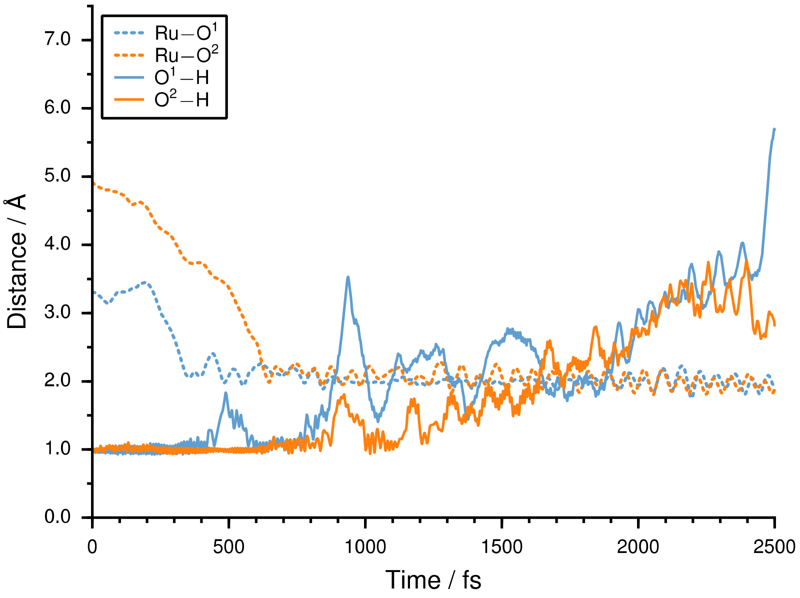

Figure A50: Results from the oxidation simulation from Ru^{III} to Ru^{IV} for **MC3**. Depicted are the Ru–O distances from each reacting Ru atom to the respective closest water molecule, as well as the O–H distances that are elongated during the propagation.

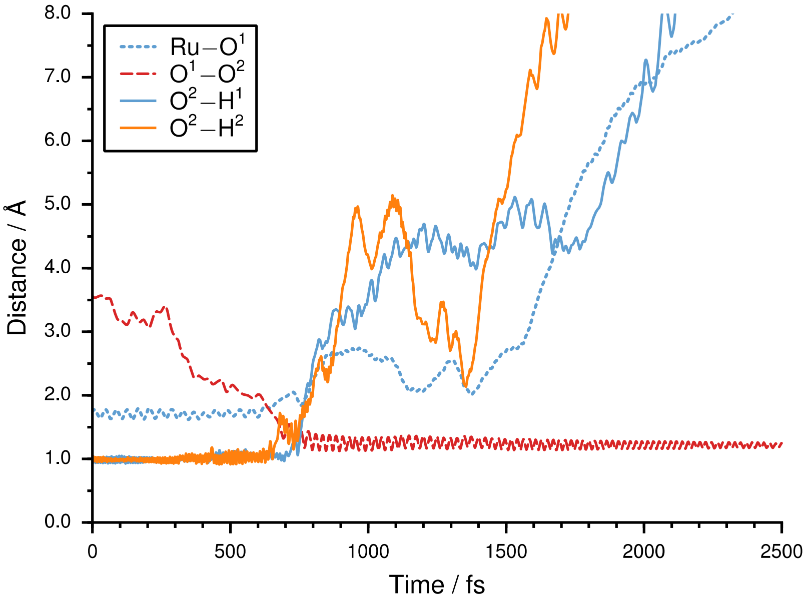

Figure A51: Results from the oxidation simulation from Ru^{V} with subsequent O–O bond formation for **MC3**. The electronic state was switched from singlet to triplet after 672 fs. Depicted are the Ru–O, O–O and O–H distances of the atoms that are involved in the reaction.

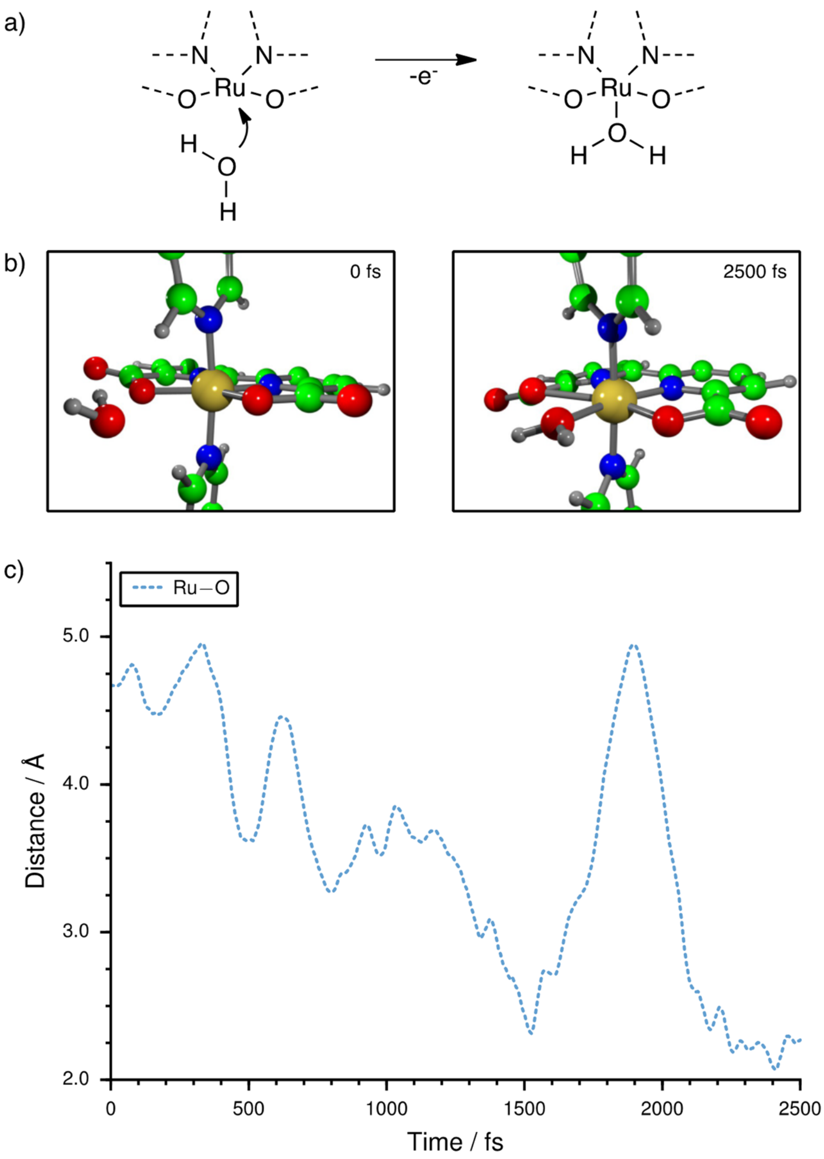

Figure A52: Results from the oxidation simulation from Ru^{II} to Ru^{III} for $[Ru(bda)(pic)_2]$. In addition to the reaction scheme (a) and the corresponding structures from the MD simulation (b), the Ru–O distance to the water molecule is depicted in (c). For the sake of clarity, additional solvent molecules are omitted in (b). (green = carbon, grey = hydrogen, red = oxygen, blue = nitrogen, yellow = ruthenium)

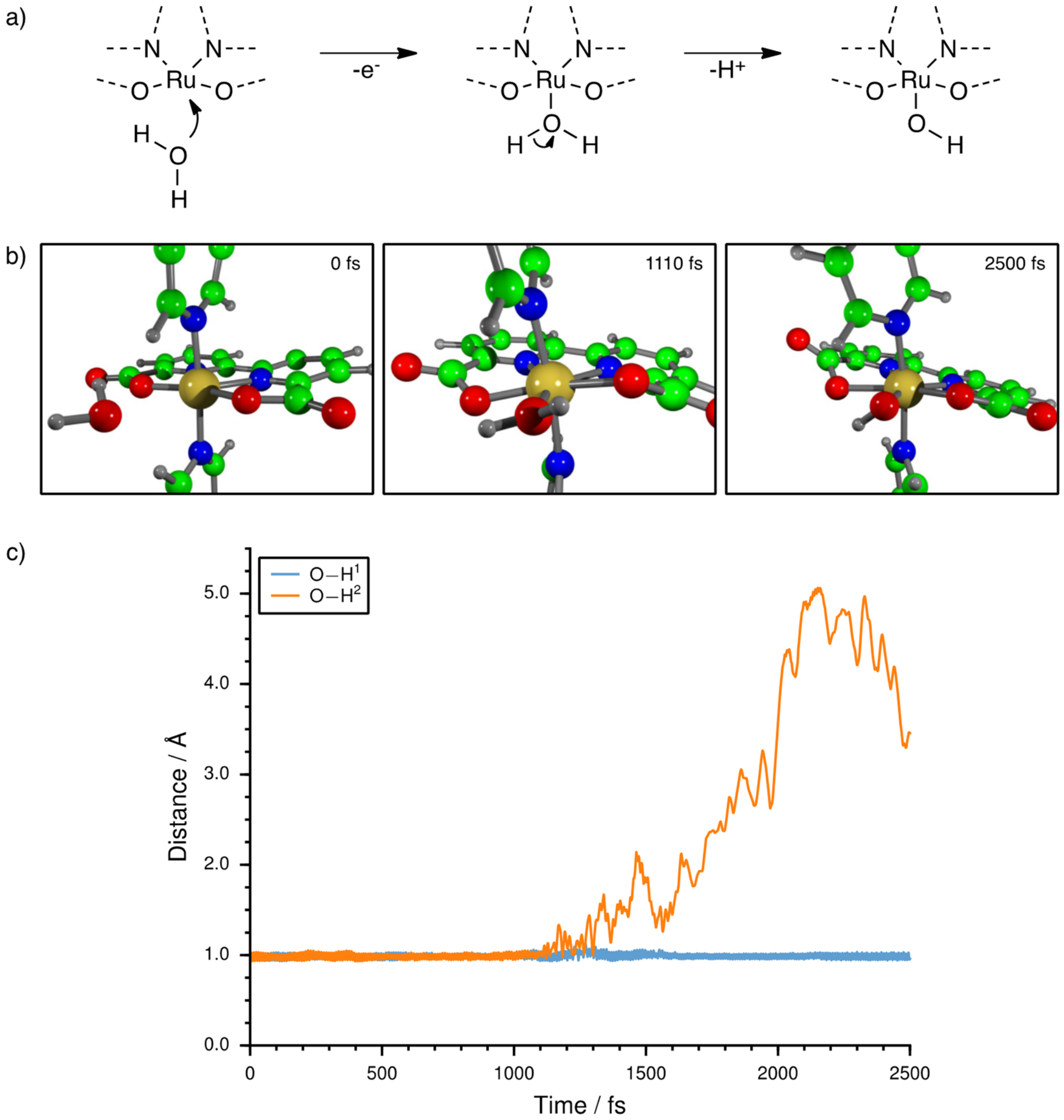

Figure A53: Results from the oxidation simulation from $\mathrm{Ru^{III}}$ to $\mathrm{Ru^{IV}}$ for $[\mathrm{Ru(bda)(pic)_2}]$. In addition to the reaction scheme (a) and the corresponding structures from the MD simulation (b), the O–$\mathrm{H^1}$ and O–$\mathrm{H^2}$ distances within the coordinating water molecule are depicted in (c). For the sake of clarity, additional solvent molecules are omitted in (b). (green = carbon, grey = hydrogen, red = oxygen, blue = nitrogen, yellow = ruthenium)

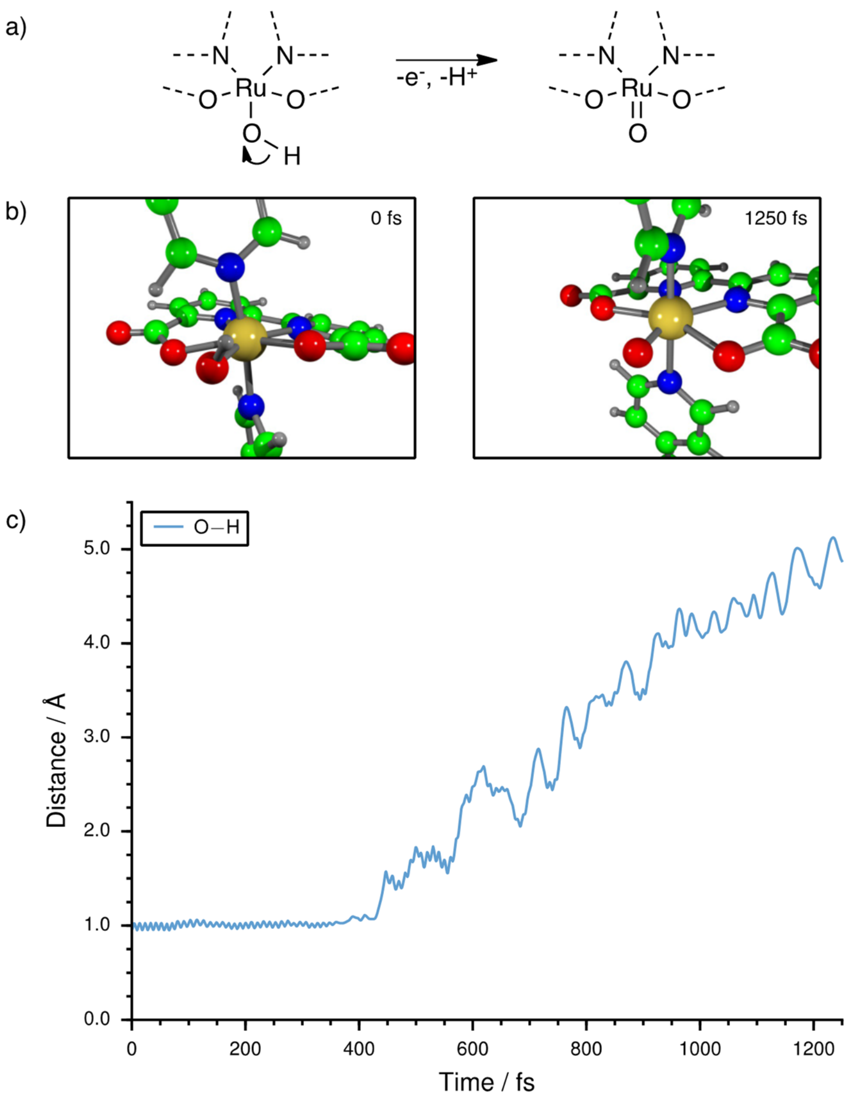

Figure A54: Results from the oxidation simulation from Ru^{IV} to Ru^{V} for $[Ru(bda)(pic)_2]$. In addition to the reaction scheme (a) and the corresponding structures from the MD simulation (b), the O–H distance of the OH-ligand is depicted in (c). For the sake of clarity, additional solvent molecules are omitted in (b). (green = carbon, grey = hydrogen, red = oxygen, blue = nitrogen, yellow = ruthenium)

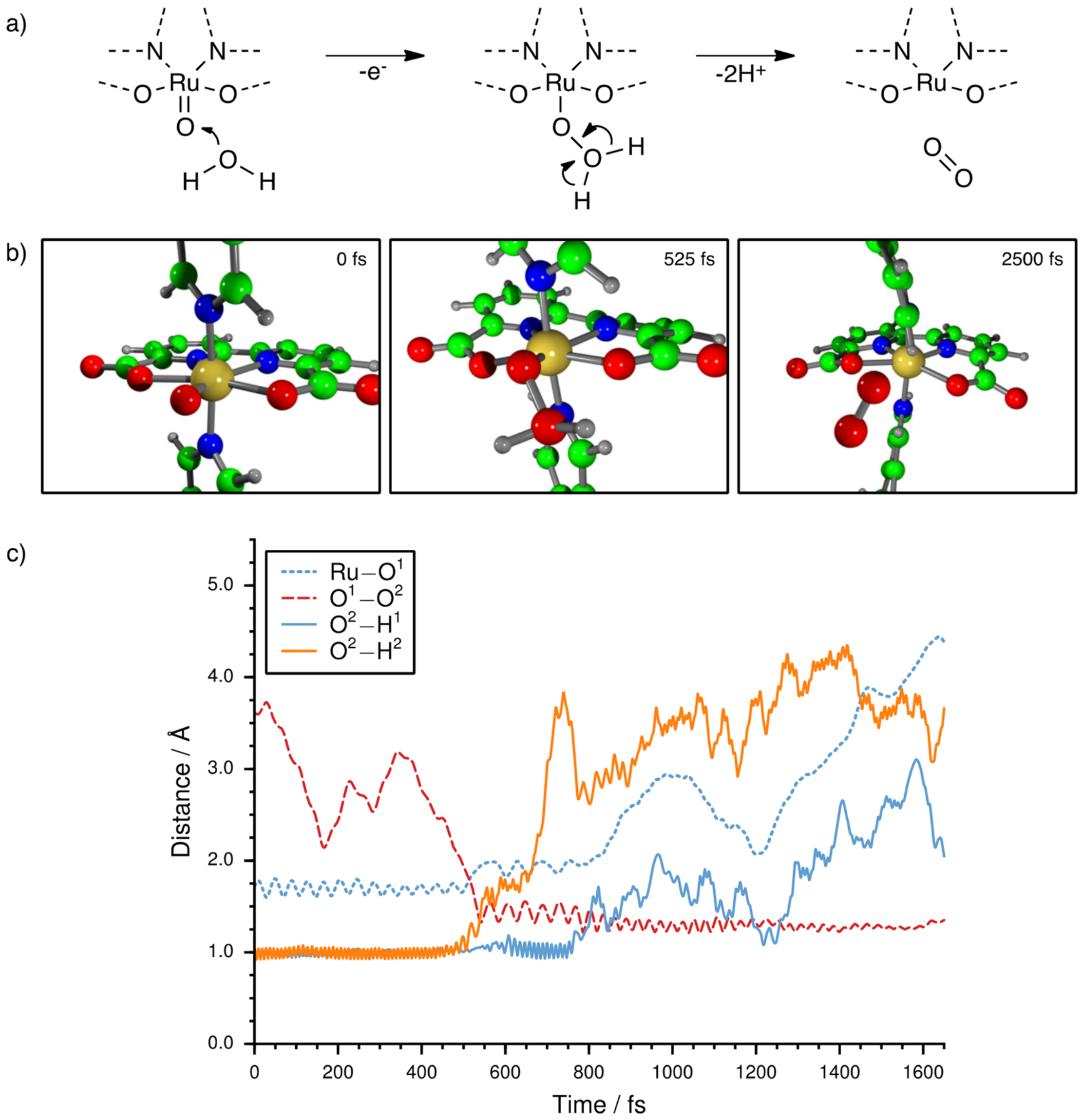

Figure A55: Results from the oxidation simulation from Ru^V with subsequent O–O bond formation for [Ru(bda)(pic)$_2$]. The electronic state was switched from singlet to triplet after 525 fs. In addition to the reaction scheme (a) and the corresponding structures from the MD simulation (b), the Ru–O^1 distance, the O^1– O^2 distance of the evolving bond and both the O^2–H distances are depicted in (c). For the sake of clarity, additional solvent molecules are omitted in (b). (green = carbon, grey = hydrogen, red = oxygen, blue = nitrogen, yellow = ruthenium)

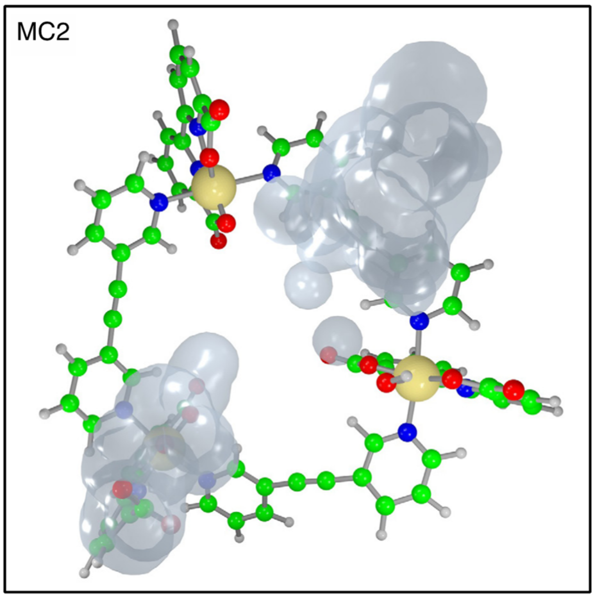

Figure A56: Dynamic proton delocalization cavities of **MC2** calculated based on the reaction MD from Ru^{IV} to Ru^{V} in the time interval from 0 to 1715 fs. The given structures are taken from the last simulation step. The solvent is not displayed for clarity. (green = carbon, grey = hydrogen, red = oxygen, blue = nitrogen, yellow = ruthenium)

A.2 Supporting Information to Chapter 3.2

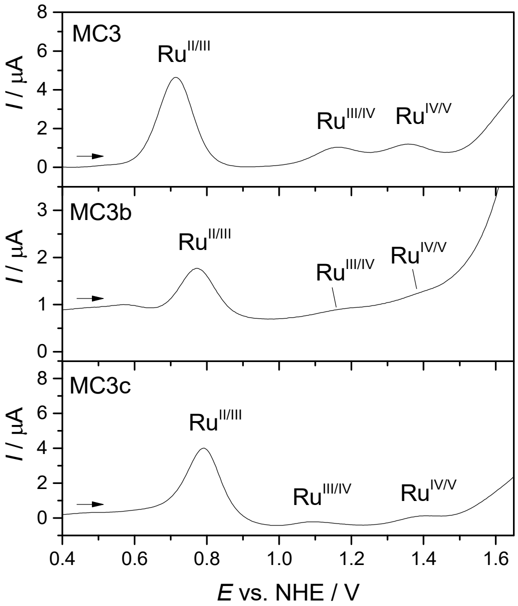

Figure A57: Differential pulse voltammograms of **MC3** and **MC3b** in H_2O/CF_3CH_2OH 1:1 and **MC3c** in H_2O, all at pH 1 (acid: CF_3SO_3H).

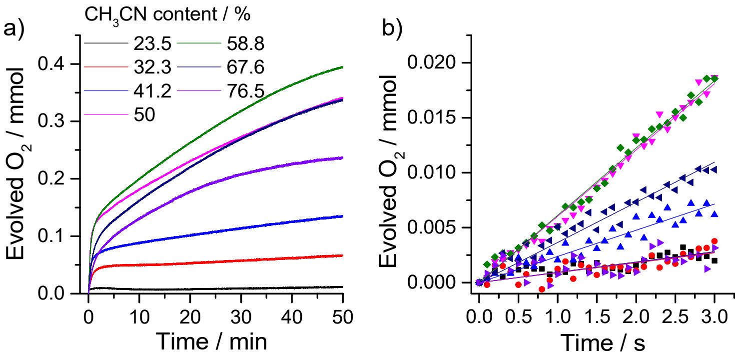

Figure A58: (a) Oxygen evolution over time using **MC3** as catalyst for different CH_3CN/H_2O (pH 1, CF_3SO_3H) mixtures (total volume: 3.4 mL) at fixed catalyst concentration (24.3 µM) and CAN concentration (0.535 M). For each solvent composition 1.0 g of CAN was dissolved in 3.0 mL of the solvent mixture and 400 µL of the catalyst solution (in CH_3CN/H_2O (pH 1, acid: CF_3SO_3H) 1:1) were injected through a septum. (b) Initial O_2 evolution rates were determined by linear regression for the first 3 s of catalysis.

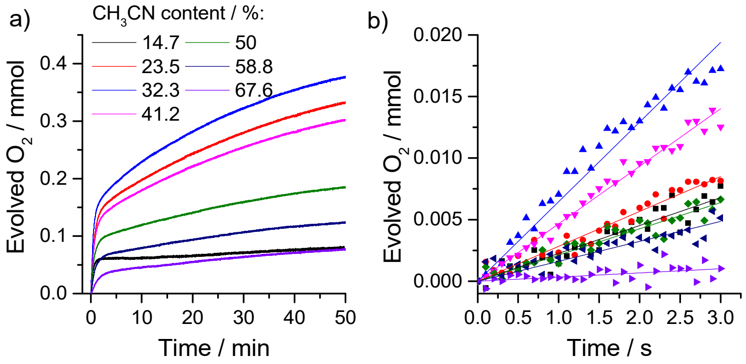

Figure A59: (a) Oxygen evolution over time using **MC3b** as catalyst for different CH_3CN/H_2O (pH 1, CF_3SO_3H) mixtures (total volume: 3.4 mL) at fixed catalyst concentration (24.3 µM) and CAN concentration (0.535 M). For each solvent composition 1.0 g of CAN was dissolved in 3.0 mL of the solvent mixture and 400 µL of the catalyst solution (in CH_3CN/H_2O (pH 1, acid: CF_3SO_3H) 1:1) were injected through a septum. (b) Initial O_2 evolution rates were determined by linear regression for the first 3 s of catalysis.

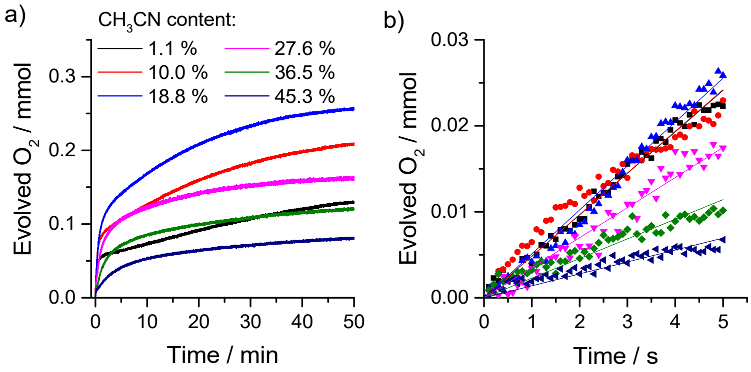

Figure A60: (a) Oxygen evolution over time using **MC3c** as catalyst for different CH_3CN/H_2O (pH 1, CF_3SO_3H) mixtures (total volume: 3.4 mL) at fixed catalyst concentration (24.3 µM) and CAN concentration (0.535 M). For each solvent composition 1.0 g of CAN was dissolved in 3.0 mL of the solvent mixture and 400 µL of the catalyst solution (in CH_3CN/ H_2O (pH 1, acid: CF_3SO_3H) 1:9) were injected through a septum. (b) Initial O_2 evolution rates were determined by linear regression for the first 3 s of catalysis.

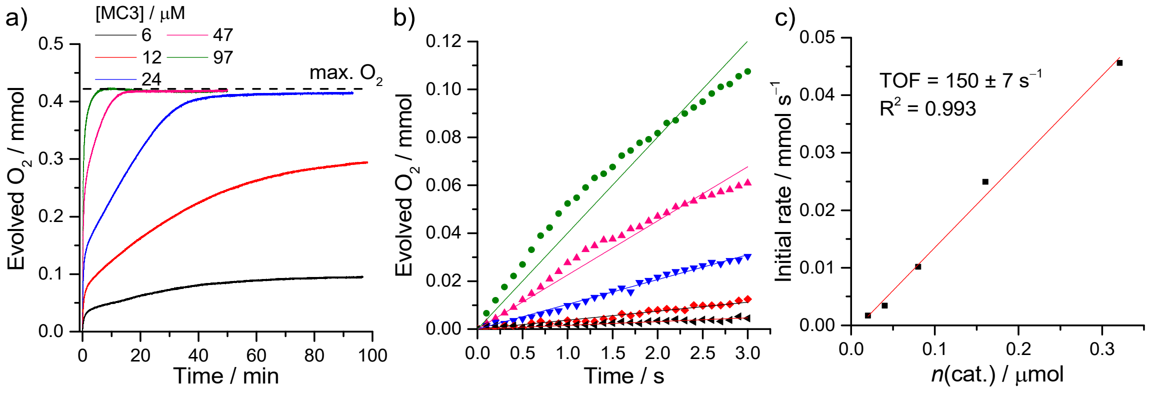

Figure A61: (a) Oxygen evolution over time using **MC3** as catalyst for various catalyst concentrations with fixed CAN concentration (0.535 M) in 3.4 mL of a CH_3CN/H_2O 6:4 mixture (pH 1, acid: CF_3SO_3H). (b) Initial O_2 evolution rates were determined by linear regression for the first 3 s of catalysis. (c) The TOF was determined by plotting the initial rate versus the catalyst concentration.

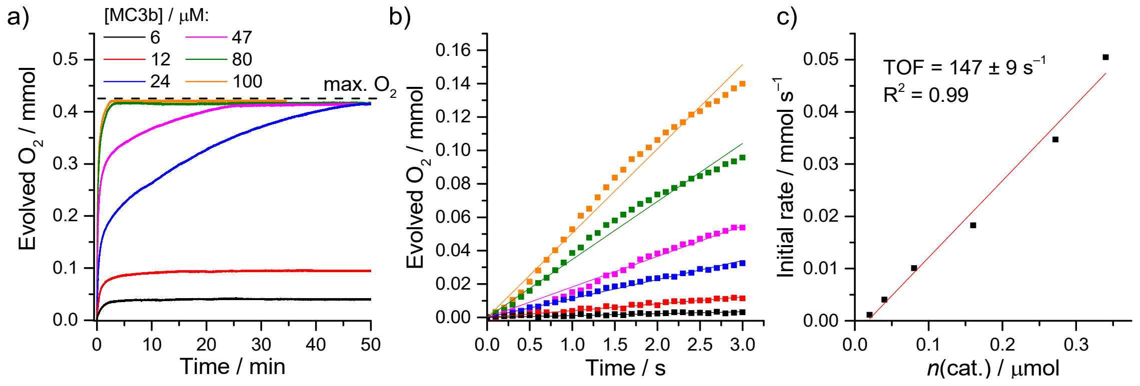

Figure A62: (a) Oxygen evolution over time using **MC3b** as catalyst for various catalyst concentrations with fixed CAN concentration (0.535 M) in 3.4 mL of a CH_3CN/H_2O 3:7 mixture (pH 1, acid: CF_3SO_3H). (b) Initial O_2 evolution rates were determined by linear regression for the first 3 s of catalysis. (c) The TOF was determined by plotting the initial rate versus the catalyst concentration.

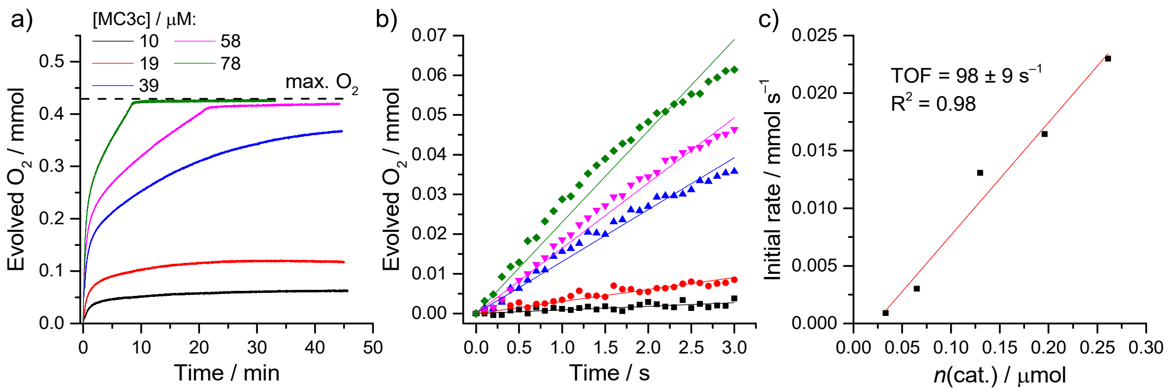

Figure A63: (a) Oxygen evolution over time using **MC3c** as catalyst for various catalyst concentrations with fixed CAN concentration (0.535 M) in 3.4 mL of a CH_3CN/H_2O 2:8 mixture (pH 1, acid: CF_3SO_3H). (b) Initial O_2 evolution rates were determined by linear regression for the first 3 s of catalysis. (c) The TOF was determined by plotting the initial rate versus the catalyst concentration.

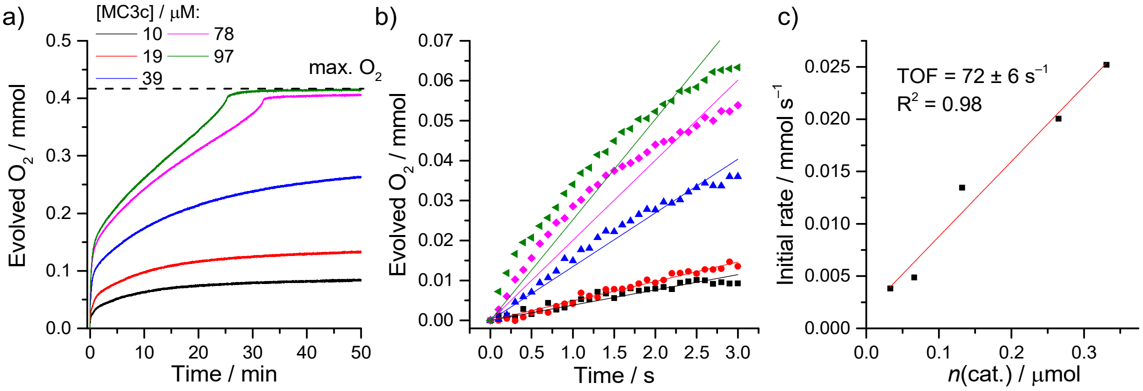

Figure A64: (a) Oxygen evolution over time using **MC3c** as catalyst for various catalyst concentrations with fixed CAN concentration (0.535 M) in 3.4 mL of H_2O (pH 1, acid: CF_3SO_3H). (b) Initial O_2 evolution rates were determined by linear regression for the first 3 s of catalysis. (c) The TOF was determined by plotting the initial rate versus the catalyst concentration.

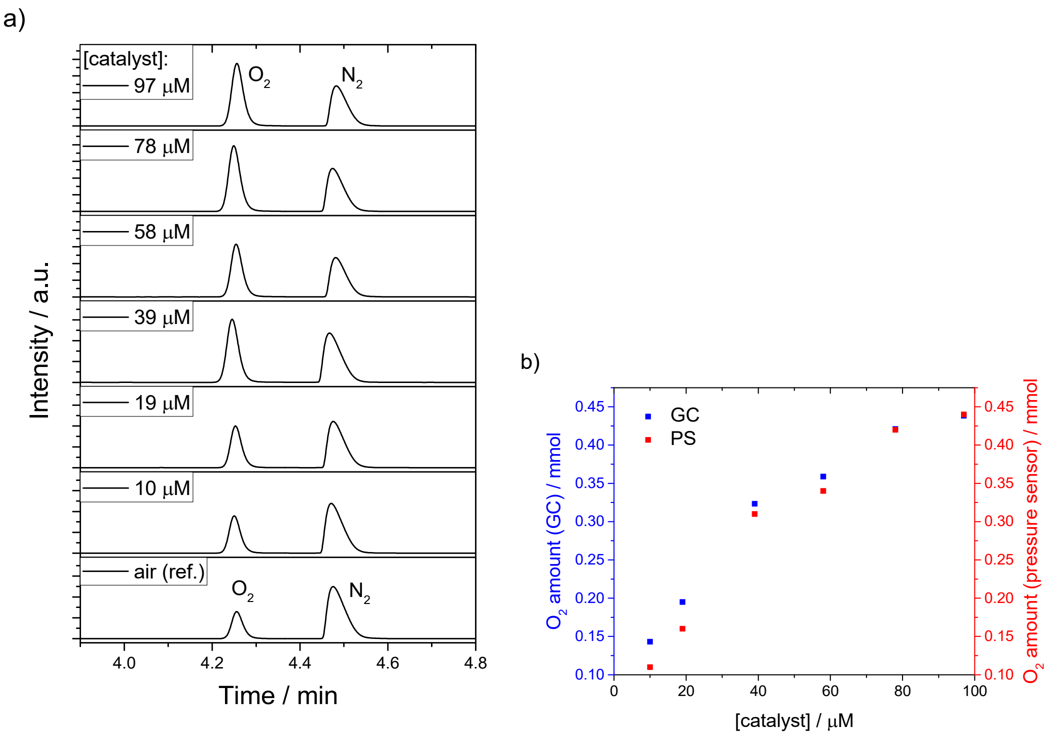

Figure A65: (a) GC chromatograms obtained by the injection of 0.5 mL of the reaction headspace after the completed water oxidation reaction with catalyst **MC3c** for different catalyst concentrations and fixed CAN concentration (0.535 M) in 3.4 mL of H_2O (pH 1, CF_3SO_3H). (b) Comparison of the amount of evolved oxygen as determined by GC or by the pressure transducers.

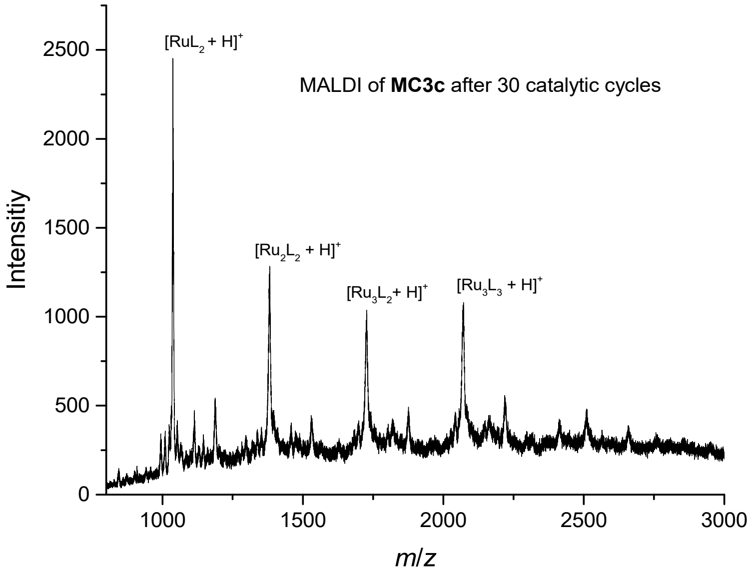

Figure A66: MALDI-ToF mass spectrum of **MC3c** after water oxidation (30 catalytic cycles, 10 per Ru(bda) center) with CAN as oxidant in 1:1 CH_3CN/H_2O (pH 1, acid: CF_3SO_3H) mixture. Before the mass spectrometric measurement, the sample was reduced with ascorbic acid (matrix: SDHB in methanol, mode: linear, positive).

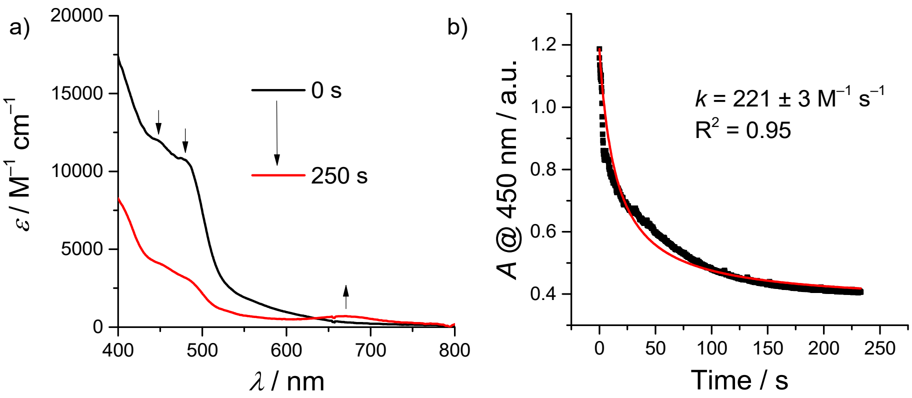

Figure A67: Redox Titration with **MC3c** as catalyst. To the catalyst dissolved in a CH_3CN/H_2O (pH 1) 3:7 mixture (2.0 mL, 10^{-4} M), a solution of CAN in the same solvent mixture (10 µL, 6×10^{-2} M) was titrated. (a) Initial and final UV/Vis absorption spectrum. (b) Changes of the MLCT absorption band at 450 nm over time after the addition of CAN and the corresponding fit to determine the rate constant (*k*) for the oxidation process.

A.3 Supporting Information to Chapter 3.3

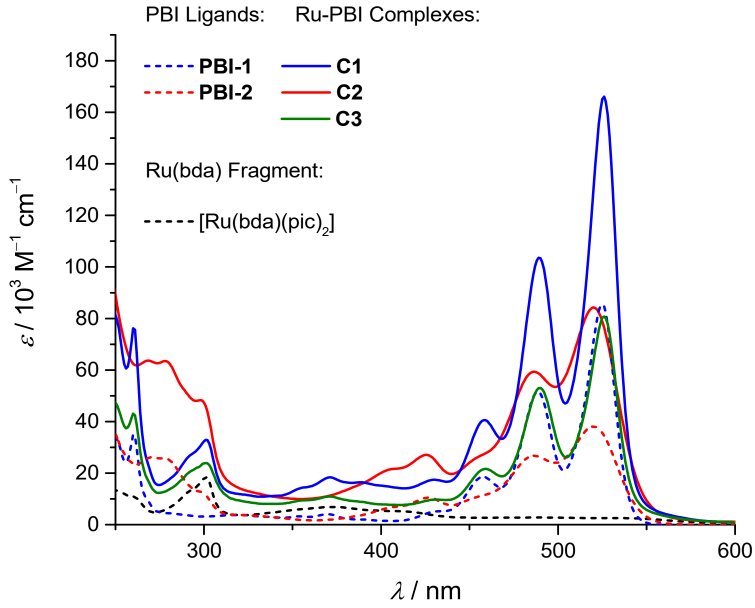

Figure A68: Comparison of all UV/Vis absorption spectra measured in dichloromethane ($c = 10^{-5}$ M).

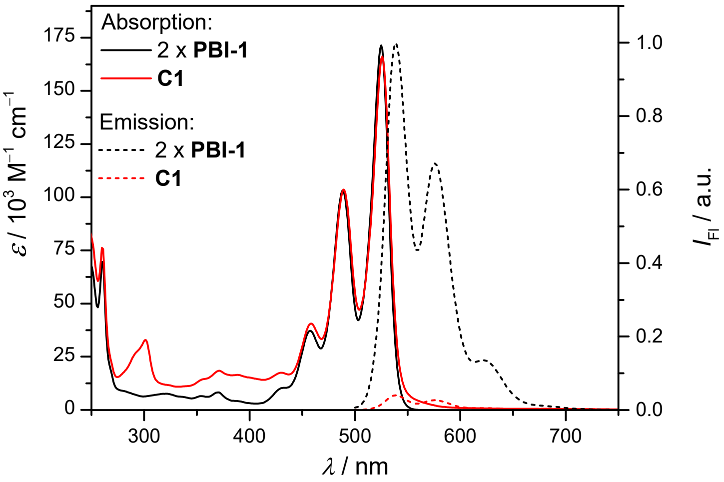

Figure A69: UV/Vis absorption (solid lines, $c = 10^{-5}$ M) and fluorescence emission (dotted lines, $c = 10^{-6}$ M) spectra of the ligand **PBI-1** and the respective complex **C1** in dichloromethane.

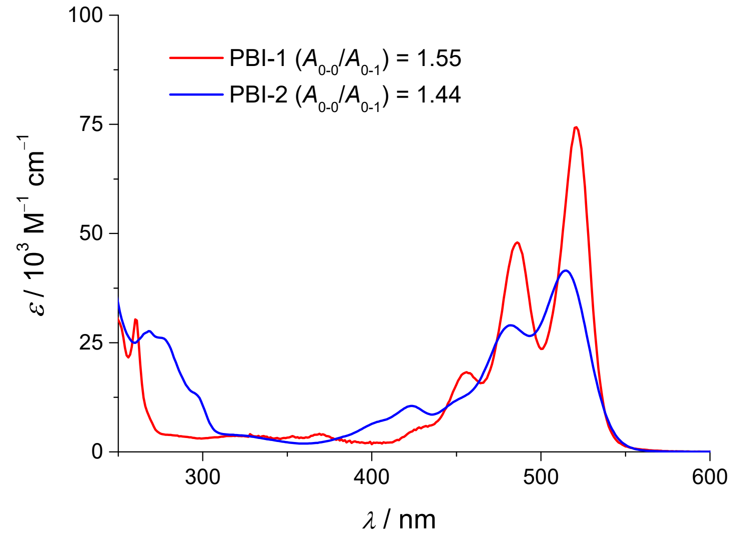

Figure A70: UV/Vis absorption spectra of **PBI-1** and **PBI-2** in acetonitrile at ($c = 10^{-5}$ M).

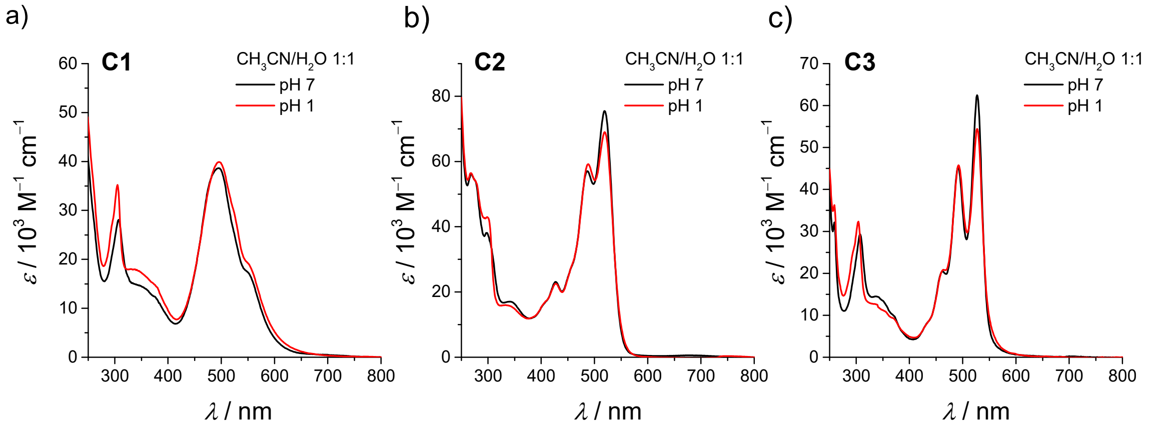

Figure A71: UV/Vis absorption spectra of hydrophilic ruthenium complexes (a) [Ru(bda)(PBI-1)$_2$] (**C1**), (b) [Ru(bda)(PBI-2)$_2$] (**C2**), and (c) [Ru(bda)(PyO)(PBI-1)] (**C3**) in various aqueous solvent mixtures at a concentration of 10^{-5} M (black = CH_3CN/H_2O (pH 7) 1:1 and red = CH_3CN/H_2O (pH 1, acid: CF_3SO_3H) 1:1).

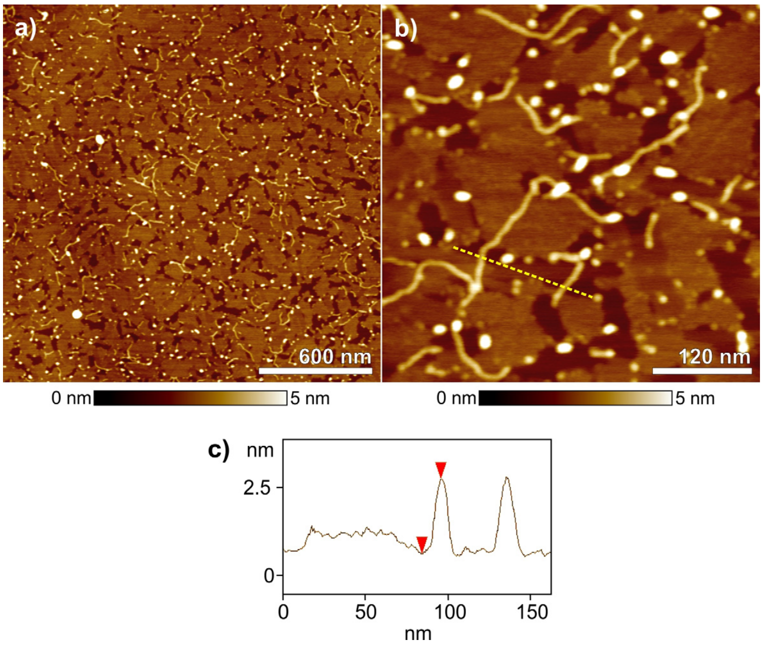

Figure A72: AFM height images of a sample obtained by spin-coating solutions of **C1** in CH_3CN onto HOPG ($c = 10^{-5}$ M).

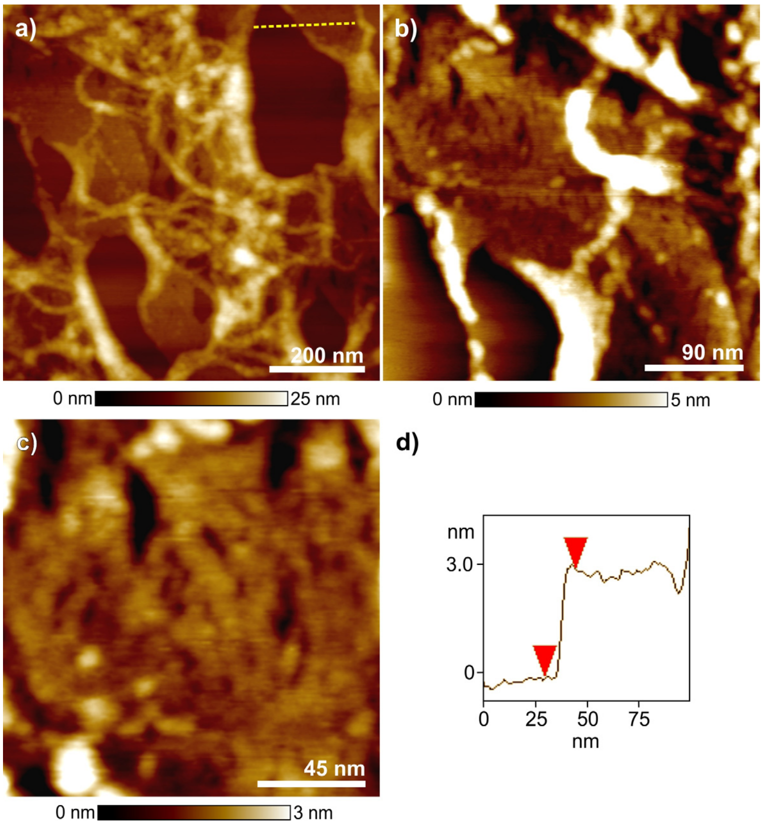

Figure A73: AFM height images of a sample obtained by spin-coating solutions of **C1** in a 1:1 CH_3CN/H_2O (pH 7) mixture onto HOPG ($c = 10^{-5}$ M).

DANKSAGUNG

Ich danke Prof. Dr. Frank Würthner für die freundliche Aufnahme in seine Arbeitsgruppe, die Bereitstellung des interessanten Themas und dafür, mir die Freiheiten zur Entwicklung dieses Projektes zu gewährt zu haben.

Ich danke darüber hinaus Prof. Dr. Roland Mitrić, Dr. Merle I. S. Röhr und Joachim O. Lindner für die umfangreichen Berechnungen, die erheblich zum Verständnis der von mir synthetisierten Verbindungen beigetragen haben. Besonderer Dank gebührt Dr. David Schmidt, der mich all die Jahre exzellent betreut hat und mir eine große Hilfe beim Anfertigen von Manuskripten war. Auch Chantu Saha-Möller gebührt Dank für seine Unterstützung beim Erstellen von Manuskripten. Dr. Peter Frischmann danke ich für die Betreuung während meines ersten Jahres und die ergiebige Zusammenarbeit an supramolekularen Tetraedern. Meinem langjährigen Laborpartner Marcus Schulze, danke ich für die großartige Zusammenarbeit auf dem Gebiet der Wasseroxidationskatalyse und all den gemeinsamen Spaß, der den Laboralltag bereichert hat.

Bei Dr. Vladimir Stepanenko bedanke ich mich für die zahlreichen AFM- und Elektronenmikroskopie-Messungen und für die gemeinsame Betreuung des Fluoreszenzspektrometers. Bei Ana-Maria Krause und Dr. David Schmidt bedanke ich mich für die Messung von Kristallstrukturen, bei Michael Moos für die Unterstützung beim Messen der Spektroelektrochemie, bei Dr. Matthias Stolte, Michael Ramold und Bernd Brunner für Hilfe bei dem Aufbau von Messständen, bei Joachim Bialas und Petra Seufert-Baumbach für die Unterstützung bei der Synthese und bei Dorothee Schindler und Ana-Lucía Meza für die hoffentlich erfolgreiche Fortführung des Katalyse-Themas. Christiana Toussaint gebührt Dank für die Unterstützung in allen offiziellen Belangen. Ich bedanke mich darüber hinaus bei meinen Bachelorstudenten Paul Adamski und Kai Oberdorf für ihre motivierte Mitarbeit und bei allen Praktikanten, die mich über die Jahre unterstützt haben: Melanie Achsnich, Maria Krebs, Vanessa Maier, Michael Philipp, Max Rang, Carl Schiller und Pascal Seufert.

Zudem danke ich dem gesamten Arbeitskreis Würthner für eine angenehme Arbeitsatmosphäre und schöne gemeinsame vier Jahre. Dazu zählt unter anderem der regelmäßige Stammtisch und besonderer Dank gebührt all jenen die zu dessen Organisation beigetragen haben.

Zuletzt möchte ich meiner Familie danken, die mir immer ein starker Rückhalt war und ist.

LIST OF PUBLICATIONS

11 V. Kunz, J. O. Lindner, M. Schulze, M. I. S. Röhr, D. Schmidt, R. Mitrić, F. Würthner, *Energy Environ. Sci.* **2017**, DOI: 10.1039/c7ee01557g.

10 V. Kunz, D. Schmidt, M. I. S. Röhr, R. Mitrić, F. Würthner, *Adv. Energy Mat.* **2017**, *7*, #1602939.

9 V. Kunz, M. Schulze, D. Schmidt, F. Würthner, *ACS Energy Lett.* **2017**, *2*, 288–293.

8 M. Schulze, V. Kunz, P. D. Frischmann, F. Würthner, *Nat. Chem.* **2016**, *8*, 576–583.

7 P. D. Frischmann, V. Kunz, F. Würthner, *Angew. Chem., Int. Ed.* **2015**, *54,* 7285–7289.

6 P. D. Frischmann, V. Kunz, V. Stepanenko, F. Würthner, *Chem. Eur. J.* **2015**, *21,* 2766–2769.

5 V. Kunz, V. Stepanenko, F. Würthner, *Chem. Commun.* **2015**, *51*, 290–293.

4 T. Heinrich, C. H.-H. Traulsen, M. Holzweber, S. Richter, V. Kunz, S. Kastner, S. O. Krabbenborg, J. Huskens, W. E. S. Unger, C. A. Schalley, *J. Am. Chem. Soc.* **2015***, 137,* 4382–4390.

3 M. Holzweber, T. Heinrich, V. Kunz, S. Richter, C. H.-H. Traulsen, C. A. Schalley, W. E. S. Unger, *Anal. Chem.* **2014**, *86*, 5740–5748.

2 D. Trawny, V. Kunz, H.-U. Reißig, *Eur. J. Org. Chem.* **2014**, *28*, 6295–6302.

1 C. H.-H. Traulsen, V. Kunz, T. Heinrich, S. Richter, M. Holzweber, A. Schulz, L. K. S. von Krbek, U. T. J. Scheuschner, J. Poppenberg, W. E. S. Unger, C. A. Schalley, *Langmuir* **2013**, *29*, 14284–14292.

OVERVIEW NEWLY SYNTHESIZED COMPOUNDS

Bridging ligands

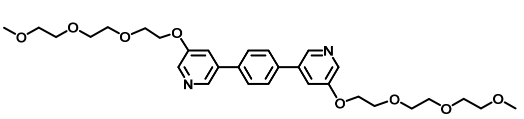

53

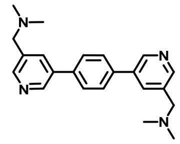

54

{Ru(bda)} Macrocycles

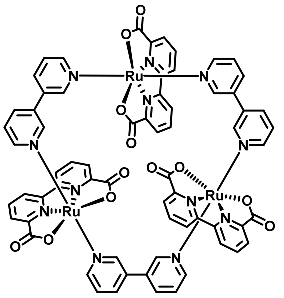

MC1

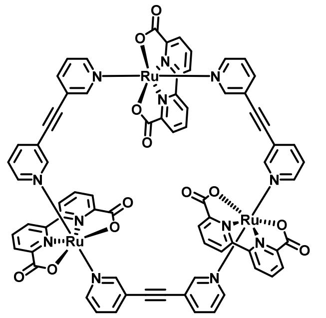

MC2

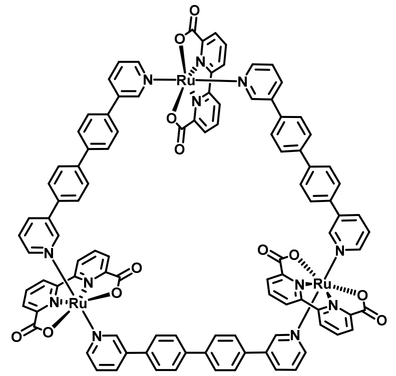

MC4

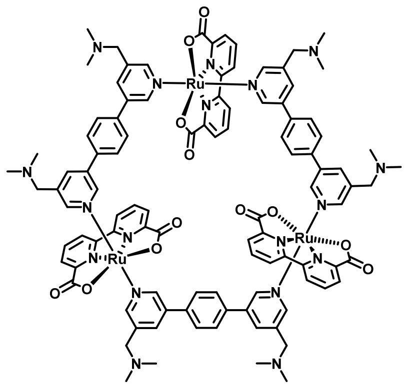

MC3b

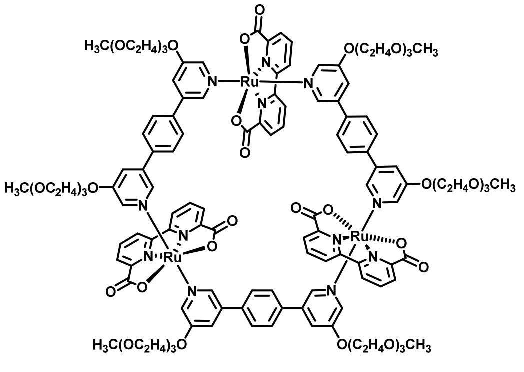

MC3c

Other {Ru(bda)} Complexes

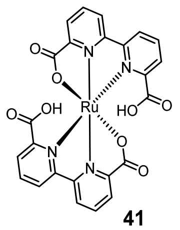

41

(PBI) Ligands

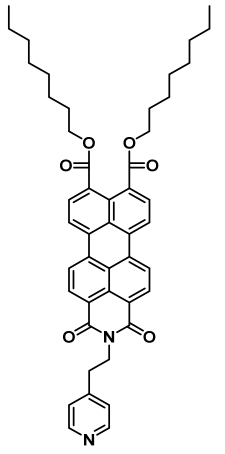

58

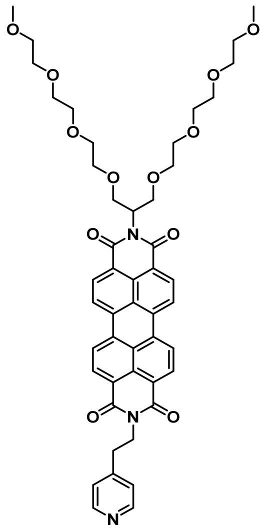

PBI-1

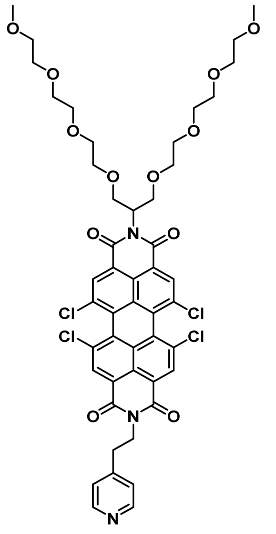

PBI-2

{Ru(bda)}-PBI Complexes

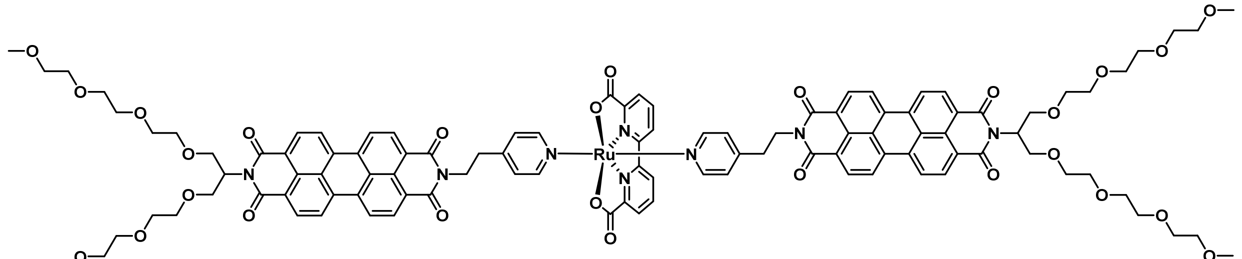

C1

[Ru(bda)(PBI-1)$_2$]

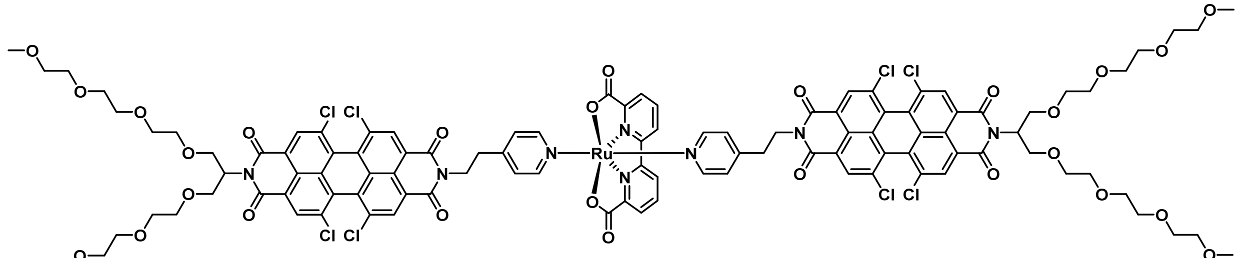

C2

[Ru(bda)(PBI-2)$_2$]

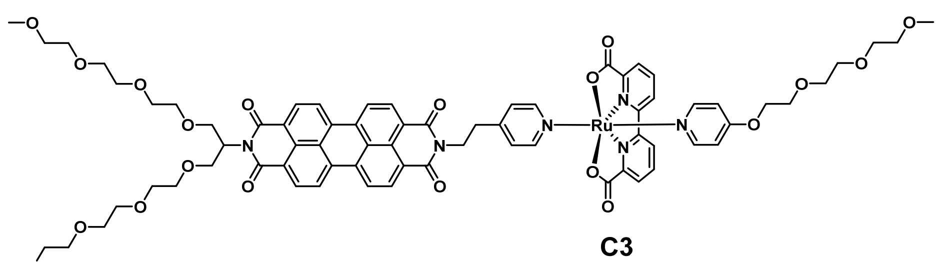

C3

[Ru(bda)(PyO)(PBI-1)]